Design and characterization of Silicon Photonic structures for third order nonlinear effects

Samuel Felipe Serna Otálvaro

▶ To cite this version:

Samuel Felipe Serna Otálvaro. Design and characterization of Silicon Photonic structures for third order nonlinear effects. Optics [physics.optics]. Université Paris Saclay (COmUE), 2016. English. ⟨NNT : 2016SACLS409⟩. ⟨tel-01474981⟩

HAL Id: tel-01474981

https://theses.hal.science/tel-01474981v1

Submitted on 23 Feb 2017

NNT : 2016SACLS409

THESE DE DOCTORAT
DE L'UNIVERSITE PARIS-SACLAY

préparée à

L'UNIVERSITE PARIS SUD
CENTRE DE NANOSCIENCES ET DE NANOTECHNOLOGIES

et à

L'INSTITUT D'OPTIQUE GRADUATE SCHOOL

ÉCOLE DOCTORALE N° 575
Electrical, Optical, Bio - physics and Engineering (EOBE)

Spécialité de doctorat : Physique

par

Samuel Felipe SERNA OTÁLVARO

Design and characterization of Silicon Photonic structures for third order nonlinear effects

Thèse présentée et soutenue à Orsay, le 28 novembre 2016

Composition du jury :

Mme MAITRE, Agnès	Institut des NanoSciences de Paris	Présidente du Jury
M. De ROSSI, Alfredo	Thales-TRT	Rapporteur
M. HOUDRÉ, Romuald	École Polytechnique Fédérale de Lausanne	Rapporteur
M. CLUZEL, Benoît	Institut Carnot de Bourgogne	Examinateur
M. LEVENSON, Ariel	Centre de Nanosciences et de Nanotechnologies	Examinateur
M. CASSAN, Éric	Centre de Nanosciences et de Nanotechnologies	Directeur de thèse
M. DUBREUIL, Nicolas	Laboratoire Charles Fabry - IOGS	Co-encadrant

A thought for the victims of the Colombian conflict...
We want the truth no matter what it has been.

Qu'un vaincu de Paris, qu'un homme de la réunion dite Commune, que Paris a fort peu élue et que, pour ma part, je n'ai jamais approuvée, qu'un de ces hommes, fût-il mon ennemi personnel, surtout s'il est mon ennemi personnel, frappe à ma porte, j'ouvre. Il est dans ma maison. Il est inviolable.
Victor Hugo

Acknowledgments

Let me be clear. I understand very little and the text in front of the reader is one small step in a very specific topic from the vast scientific world: nonlinear effects in waveguiding structures. I can only think of two reasons for reading this manuscript: the first is that you are a scientist interested in the same challenges that occupied my days during this research; the second (and more rare) is a personal attachment. In any case, this work is an honest effort to condensate most of the work done during the last three years.

I do not conceive any human campaign without political insights and consequences. This is why I feel grateful of having the opportunity to work for a public university inspired by the motto: "Comprendre le monde, construire l'avenir" (Understand the world, build the future).

First of all, I would like to start expressing my immense gratitude to the examiners Dr. Alfredo de Rossi and Dr. Romuald Houdré for taking the time of reading carefully my manuscript and writing a report about it. I felt honored that two researchers that enlightened me through their published work were interested in our developments.

Secondly to the other members of the jury, which we have asked to participate in the process due to their knowledge in the field. Dr. Agnès Maître, president of the jury; Dr. Ariel Levenson and Dr. Benoît Cluzel. Their questions and comments during the defense showed me how discussion enriches the research. It was my pleasure to share such a moment with researchers I admire.

I acknowledge my supervisors Dr. Eric Cassan and Dr. Nicolas Dubreuil. Eric has given me the freedom to explore new paths by always being next to me whenever I needed advise regardless his busy schedule. He didn't hesitate in supporting me during the master, the PhD or after. Nicolas was a beacon to me, not only in the scientific aspect but also in my personal sphere; he was always willing to debate about politics, history, music, life...

Dr. Laurent Vivien, Dr. Delphine Marris-Morini and Dr. Philippe Delaye were always ready to discuss with me and in many occasions even letting other compromises aside. I extend my deep gratitude to them.

My odyssey, up to this point, would not be possible without the support of professor Román Castañeda, that showed me the possibility to "create darkness by adding light". Then my colleagues in Colombia and the people I met during the master, particularly Luis, Víctor, Peter, Can, Lorenz, Mateusz and Edgar. In their way, they have made this text possible.

The groups that helped me in the two laboratories were the two pillars of my research. They showed me that there are different ways and interests when "doing science". The group in C2N - MINAPHOT, with the Spanish (sub-)team Elena, Carlos, Diego and Joan-Manel and, in chronological order, Mohamed, Melisa, Papichaya, Pedro, Nhung, Vladyslav, Matthias, Guillaume, Daniel, Lazhar, Dorian, Phuong, Qiankun and Xin. I let intentionally some names out of the list, particularly Cam and Weiwei that due to our common PhD conditions allowed me to establish a close personal relation. I thank them for listening and discussing always without prejudices. I am also grateful with Charles that paves part of my way after his PhD work and Pierre from whom I have learn different characterization techniques. Finally, from the Orsay-site, I have a very special thought to Adrien that nevertheless the short period of time we shared, is always there to listen. His patience and honesty gave me hope in times I needed it. I acknowledge also the CTU engineers particularly to Xavier Le Roux and Jean-Rene Coudevylle for giving me the confidence in testing novel techniques.

I had also a home in LCF with the MANOLIA group. I acknowledge Gilles, Mireille, Jérèmy, Margaux, Mihn-Châu, Sylvie, Thibault, Abderrahim and Aliénor. Even though my time was very limited in IOGS, they were always welcoming. The quality of this work was greatly improved thanks to the collaborators around the world, the frame of the collaboration will be mentioned through the manuscript.

I acknowledge also the teaching team at IUT-Orsay, Sergio and Bastien trained me and gave me the freedom to teach according to my preferences. Nathalie helped me a lot and was always confident with my use of the equipment.

Luckily, life does not only consist in work, so I had the chance to expand my knowledge with the SCOP (Student Chapter of Optics-Paris) where I have been president. With these activities I could meet great people such as Valérie, Benjamin, Paul and Lijo.

My family played an important role, particularly my parents, my grandmother and my sister. Having an ocean in between is not easy, so I thank them for their unconditional support.

Finally, to my most important personal support during this journey, Luna. She is next to me transcending barriers of space. I count on her, as always...

Samuel
12-2016

Contents

Introduction

The intriguing nature of light has fascinated philosophers-scientists since early stages in history. The demonstration of the wave nature of light by Augustin Fresnel in the French academy of Science has started a revolution that last until our days. Later, the dual nature of photons opened even further perspectives for light. In particular, the light-matter interactions have changed the scientific landscape by offering a set of phenomena that are crucial in our days, for instance spectroscopy or the invention of bulbs, microscopes and telescopes have changed the understanding of our environment.

After the developments of Maxwell, Hertz and Marconi (among others), light has been used as an information carrier, it has brought another radical change, empowering photonics as a required field to solve the bottlenecks of pure electronics becoming one of the fundamental pillars of modern communication. All-optical solutions can provide both: faster processing speed and lower power consumption, since the optical-electrical-optical conversion is cut-out of these schemes. For instance, electronics limits the switching rates to around 50 GHz.

The most promising effects for all-optical signal processing are offered by higher order phenomena, which are referred as **nonlinear optics**. For instance, most all-optical regeneration techniques, including self phase modulation (SPM), four-wave mixing and cross-phase modulation are based on Kerr nonlinearity (a third order nonlinear effect). To get a sufficient light-matter interactions (through higher order polarization terms) for the desired effect, one can have different choices: use a material with high nonlinear third order susceptibilities ($\chi^{(3)}$) or to increase the pump intensity. For the latter, one can either use pulsed lasers or decrease the mode field area. In this view, micrometer scale or sub-micrometer scale integrated waveguides can be used to exploit the refereed higher order effects. The ultimate goal is to reduce the size of all-optical signal processing devices by choosing highly nonlinear materials and appropriate structures for high mode confinement requiring lower powers and allowing low-cost and fast signal processing techniques that can be integrated on CMOS compatible wafers for mass production.

The measurement of third order nonlinear properties for telecommunication applications operate in the near infrared window (1.55 μm to 1.60 μm) has been a subject of intense study. One of the key point related to nonlinear materials, and that will be addressed in this work, concerns the precise measurement and characterization of the guided structures. As an illustration, we show in Fig. 1 a plot of the two photon absorption coefficient, on a semi-logarithmic scale, as a function of year published in the literature for GaAs. It has been established that these large differences (around two orders of magnitude) are not exclusively due to differences in the materials, but are due to experimental problems and interpretation errors [1].

Although related to old results, this matter of fact highlights a specific picture: accurate and stable experimental characterization of nonlinear integrated materials is difficult to realize in most often conditions. In the context of this PhD work, that is centered on the study nonlinear optical effects in high index contrast silicon nanowaveguides with cross-section areas around 0.1 μm^2 and cladding materials with possible giant nonlinear properties, fully experimental characterization of the effective waveguide nonlinear parameters is an even further challenging but important task.

Silicon microphotonics benefits from the well known material properties and the mature fabrication methods associated with the strong microelectronics industry. The dimensions and fabrication processes have allowed the integration of a large number of photonic functions on a single chip. However, optical properties of silicon face limits in the nonlinear regime, especially in the telecommunication waveband that is addressed in this text. On one hand the nonlinear refractive index, is very high. On the other hand, the two-photon absorption coefficient is also very large, which is responsible for the generation of free carriers that modify the signal in intensity (absorption-FCA) and phase (refraction-FCR) [2]. Even with these limitations, many nonlinear optical effects have been demonstrated in silicon photonic wires. Liu et.al. have shown wavelength conversion by four wave mixing [3] and Espinola et.al. [4] demonstrated Raman amplification using only 20.5mW pump power and ~1mW signal power.

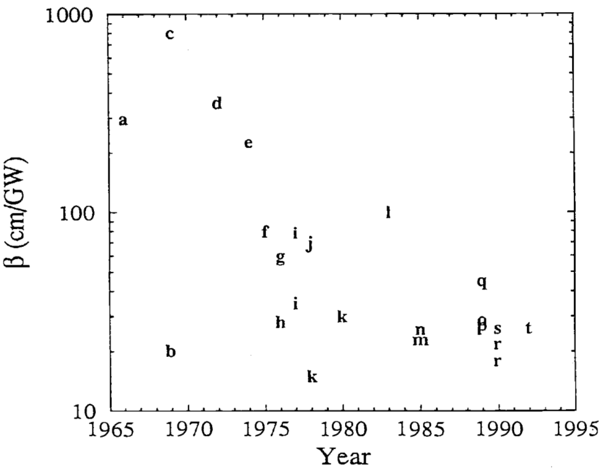

Figure 1: The Two photon absorption coefficient as a function of year published for GaAs [1].

To overcome the free carrier and two-photon absorption in silicon, other nonlinear materials have being investigated for microphotonics. One choice is to fabricate waveguides with materials from the III-V group, chalcogenides, amorphous crystals or nitrides. Another one is to explore hybrid silicon platforms by covering silicon-on-insulator (SOI) waveguides with high performance soft matter compounds.

Furthermore, there are two ways to localize the light in a nonlinear medium: **optical microcavities** and **slow light** waveguides. Semiconductor photonic crystal cavities have been demonstrated with very small volumes and ultrahigh Q factors of the order of 10^6, making them suitable for small footprint all-optical operations. The slowing down effect of light can be achieved in photonic crystal waveguides which are in the same time highly dispersive. Consequently, their geometry controls the behavior of the light propagating into the structure an takes over by several orders of magnitude the natural material dispersion.

In this context, the present thesis is devoted to the design and characterization of integrated waveguides and cavities for third order nonlinear effects in silicon photonic field-enhanced structures operating in the telecommunication waveband. The manuscript is organized as follows:

Chapter 1 recalls the required concepts to understand the physics of specific nonlinear quantities to be targeted, then the basics of waveguides and cavities are summarized. Next, we present the procedures employed on silicon and silicon nitride to fabricate integrated devices, followed by the linear measurements of these waveguides and others realized in the frame of collaborations. Finally, we develop the vectorial nonlinear wave equation and the traditional methods used to quantify effective third order nonlinear waveguide parameters.

Chapter 2 presents a novel single beam non-destructive method to characterize the effective nonlinearities of integrated structures: bi-directional top-hat Dispersive Scan (D-Scan). The technique is a temporal analogue to the top-hat Z-Scan with a double side injection that allows the critical measurement of the coupling efficiencies. The technique is validated in a SOI waveguide and applied to other integrated materials, where some of them have never been explored in the nonlinear regime around 1550 nm.

Chapter 3 explores a technique to enhance light-matter interactions in a microcavity in the nonlinear regime. It consists in a coherent excitation of the resonator by a properly shaped pulse that set in phase the excitation pulse and the resonant frequency drift induced by free carrier refraction. The idea is proved in a SOI cavity made with two Bragg mirrors and ps shaped pulses, consisting in the first experimental nonlinear coherent excitation of microcavities.

Chapter 4 is devoted to the study of Slot Photonic Crystal Waveguides (SPhCW). The design of dispersion engineered structures is performed in the first stage, being followed by their fabrication in our facilities. Next, the characterization of the group delay is performed via external and internal interferometric techniques demonstrating the presence of a usable slow light bandwidth. These structures are thoroughly studied in the linear regime with different refractive cladding material indices. The chapter ends with a simulation effort to optimize silicon hybrid nonlinear devices and preliminary measurements of silicon photonic crystal waveguides in the nonlinear regime.

Finally, a **summary** restates the key results within the three directions of this work and provides **perspectives** to exploit the characterization methods and to enhance device performances of coupled and hybrid microcavities and slow light filled SPhCW.

1 Third order nonlinear waveguide structures

In this chapter we will introduce the general concepts of the nonlinear phenomena to be studied in this thesis. Then, we present the physical principles of waveguiding and resonant integrated structures such as strip, slot, photonic crystal waveguides and resonators. Next, the fabrication steps of silicon structures are presented followed by the materials used along this manuscript. Under this context, we refine the nonlinear expressions to settle down the quantities to be measured and introduce a figure of merit. In the last part, a brief introduction to the historical techniques to characterize third order nonlinear parameters is stated.

Contents

“Miedo a la brutalidad de lo real(...) miedo a sentirse aislado, no reconocido y no aplaudido”.

Mario Mendoza, La locura de nuestro tiempo.

1.1 Introduction

Soon after the invention of the laser [5], the nonlinear effects [6] have attracted the attention of researchers. In integrated systems, due to the advance in lithography and material structuring, nonlinear processes have been explored to open the possibility of all-optical on-chip systems. In particular, third order nonlinear effects promise to play an important role in functions requiring generation of new frequencies or logic operations. The objective of this chapter is to introduce the concepts of third order nonlinear effects in integrated structures. First, a general development is performed. Then, an explanation of physical principles and materials of integrated waveguide structures is introduced. Finally, the nonlinear effects are considered in waveguides to end with a brief introduction of common methods to quantify the third order nonlinear coefficients in materials. In Fig. 1.1 (a), we show a scheme of an electromagnetic field inducing a dipole oscillation in a media, in particular, we will be interested in these kinds of light-matter interactions in integrated waveguides. We depicted also an energy level diagram of two of the most relevant nonlinear effects treated in this manuscript. (b) Self-phase modulation (SPM) which is a contribution to the refractive index changes and (c) two-photon absorption (TPA) effect.

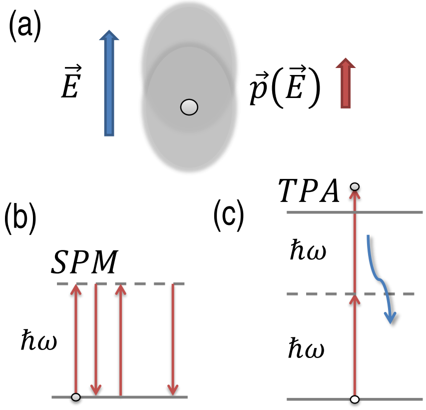

Figure 1.1: (a) An electromagnetic wave at frequency ω with an electric field $\vec{E}$, inducing a dipole oscillation in an atom. Third-order nonlinear dipole transitions, showing (b) self-phase modulation (SPM) and (c) two-photon absorption (TPA).

1.2 Nonlinear Optics

Hereafter the nonlinear wave equation is first derived in the scalar approximation. We assume bulk materials and transversal (diffraction) effects negligible. The deduction can start from the macroscopic Maxwell's equations for dielectric non-magnetizable media:

$$\nabla \times \vec{E}(\vec{r},t) = -\mu_0 \frac{\partial \vec{H}(\vec{r},t)}{\partial t}, \qquad \nabla \times \vec{H}(\vec{r},t) = \frac{\partial \vec{D}(\vec{r},t)}{\partial t} \tag{1.1}$$

In the necessary constitutive equation, we split the polarization into linear and nonlinear contributions:

$$\vec{D}(\vec{r},t) = \varepsilon_0 \vec{E}(\vec{r},t) + \vec{P}(\vec{r},t) = \varepsilon_0 \vec{E}(\vec{r},t) + \vec{P}^L(\vec{r},t) + \vec{P}^{NL}(\vec{r},t) \tag{1.2}$$

To derive the wave equation, the two curl equations are combined to obtain:

$$\nabla \times \nabla \times \vec{E}(\vec{r},t) = -\mu_0 \frac{\partial^2 \vec{D}(\vec{r},t)}{\partial t^2} \tag{1.3}$$

Assuming weak guidance approximation, one can consider [7]:

$$\nabla \cdot \vec{E}(\vec{r},t) = -\frac{1}{\varepsilon_0} \nabla \cdot \vec{P}(\vec{r},t) = 0 \tag{1.4}$$

With $\varepsilon_{ij}(\omega) = \delta_{ij} + \chi_{ij}^{(1)}(\omega)$, the nonlinear Helmholtz equation in the Fourier domain can be written down:

$$\Delta \hat{E}_i(\vec{r},\omega) + \frac{\omega^2}{c^2} \sum_j \varepsilon_{ij}(\omega) \hat{E}_j(\vec{r},\omega) = -\mu_0 \omega^2 \hat{P}_i^{NL}(\vec{r},\omega) \tag{1.5}$$

The nonlinear polarization can be seen as a source term in the equation, and is responsible for the generation of new frequencies. In the following, we will discuss special solutions to this equation, particularly for $\chi^{(3)}$ effects. The third order nonlinearity is a universal property, found in any material regardless of its spatial symmetry. This is the lowest order nonvanishing nonlinearity for a broad class of materials, remarkably some in the CMOS compatible platform such as Si, for which all the even-order nonlinear susceptibilities are identically equal to zero for symmetry reasons (they present a natural centrosymmetric lattice).

Third-order nonlinear susceptibility effects include a vast variety of processes, which are extensively used for frequency conversion and powerful methods for nonlinear microscopy and spectroscopy. During this manuscript we will focus our attention in the (quasi-)instantaneous (electronic Kerr and TPA) effects and their consequences, such as the self-phase modulation or the free carrier generation in integrated structures. In the following we will assume a field that propagates in the z direction and we will be interested in its transverse profile, we will use the scalar approximation so that:

$$\Rightarrow \hat{E}(\vec{r},z,\omega_0) = A(\vec{r},z)e^{ik_0 z} \qquad \text{with } k_0 = \frac{\omega_0^2}{c^2}\varepsilon(\omega_0) \tag{1.6}$$

Now, assuming the slowly varying envelope approximation (SVEA): $|\frac{\partial^2 A}{\partial z^2}| \ll |k_0 \frac{\partial A}{\partial z}|$, we can re-write the propagation wave equation as:

$$\frac{\partial A(x,y)}{\partial z} = i\frac{(\partial_x^2+\partial_y^2)}{2k_0}A(x,y) + i\frac{\omega_0^2}{2k_0\varepsilon_0 c^2}P_{\omega_0}^{NL}e^{-ik_0 z} \tag{1.7}$$

It is possible to derive a simplified version if only considering the third order nonlinear effects:

$$P_{\omega_0}^{NL} = 3\varepsilon_0\chi^{(3)}\left|E_{\omega_0}\right|^2 E_{\omega_0} = 3\varepsilon_0\chi^{(3)}\left|A_{\omega_0}\right|^2 Ae^{ik_0 z} \tag{1.8}$$

$$\boxed{\frac{\partial A}{\partial z} = i\frac{1}{2k_0}(\partial_x^2+\partial_y^2)A + i\frac{\omega_0}{c}\frac{3\chi^{(3)}}{2n_0}\left|A\right|^2 A} \tag{1.9}$$

This is the 2D (two-dimensional, in x and y) nonlinear wave equation, which could be reformulated in terms of intensity as $I = 2n_0\varepsilon_0 c|A|^2$, with the normalization of the amplitude $u = \sqrt{2n_0\varepsilon_0 c}A \Rightarrow |u|^2 = I$.

$$\boxed{\frac{\partial u}{\partial z} = i\frac{1}{2k_0}(\partial_x^2+\partial_y^2)u + i\frac{\omega_0}{c}n_2\left|u\right|^2 u} \tag{1.10}$$

The components of the third-order susceptibility tensor relates the the electric field amplitudes to the nonlinear polarization components:

$$P_i(\omega_o+\omega_n+\omega_m) = \varepsilon_0\sum_{jkl}\sum_{mno}\chi_{ijkl}^{(3)}(\omega_o+\omega_n+\omega_m;\omega_o,\omega_n,\omega_m)\times E_j(\omega_o)E_k(\omega_n)E_l(\omega_m) \tag{1.11}$$

where i,j,k and l refer to the cartesian components of the field. The summation over m,n and o contains the frequency combination such that the quantity $\omega_o+\omega_n+\omega_m$ is kept equal (energy conservation). Using intrinsic permutation symmetry, we can rewrite the nonlinear polarization:

$$P_i(\omega_o+\omega_n+\omega_m)=\varepsilon_0 D\sum_{jkl}\chi^{(3)}_{ijkl}(\omega_o+\omega_n+\omega_m;\omega_o,\omega_n,\omega_m)\times E_j(\omega_o)E_k(\omega_n)E_l(\omega_m) \tag{1.12}$$

where the degeneracy factor D represents the number of distinct permutations of the frequencies ω_o, ω_m and ω_n, such that:

$$\begin{aligned} &D=6,\ \text{for}\ \omega_1\neq\omega_2\neq\omega_3\\ &D=3,\ \text{for}\ \omega_1=\omega_2\neq\omega_3\\ &D=1,\ \text{for}\ \omega_1=\omega_2=\omega_3 \end{aligned} \tag{1.13}$$

$\chi^{(3)}_{ijkl}$ is a fourth-rank tensor, containing 81 elements. In general, for crystalline solids with low symmetry all the elements are independent and non-zero but for materials with a higher degree of spatial symmetry (as the ones studied through this research), the number of independent elements could be significantly reduced. If the material is isotropic, the tensor elements are zero except if indices appear in even numbers, as the response in all directions is equivalent. After considering the equivalence of coordinate axes and the possibility of rotation, the nonzero elements are governed by the equation:

$$\chi_{ijkl}=\chi_{1122}\delta_{ij}\delta_{kl}+\chi_{1212}\delta_{ik}\delta_{jl}+\chi_{1221}\delta_{il}\delta_{jk} \tag{1.14}$$

which is based on three independent elements in case of arbitrary field frequencies. $\chi^{(3)}_{ijkl}$ is a complex quantity, so we will study the effects of the real part $\mathbb{Re}\{\chi^{(3)}\}$ associated with an optical Kerr contribution and $\mathbb{Im}\{\chi^{(3)}\}$ with two-photon absorption (TPA).

1.2.1 Optical Kerr effect

Briefly, if we want to consider the optical Kerr effect, where $\omega_1=\omega_2=-\omega_3=\omega$, then $\chi^{(3)}_{ijkl}(\omega;\omega,\omega,-\omega)$ by intrinsic permutation symmetry becomes: $\chi^{(3)}_{1122}(\omega;\omega,\omega,-\omega)=\chi^{(3)}_{1212}(\omega;\omega,\omega,-\omega)\neq\chi^{(3)}_{1221}(\omega;\omega,\omega,-\omega)$, meaning $\chi^{(3)}_{ijkl}=\chi^{(3)}_{1212}(\delta_{ij}\delta_{kl}+\delta_{ik}\delta_{jl})+\chi^{(3)}_{1221}\delta_{il}\delta_{jk}$, so only two independent elements remain. Introducing this result into equation (1.12) leads to:

$$\begin{aligned} P_i(\omega)&=3\varepsilon_0\sum_{jkl}\chi^{(3)}_{ijkl}(\omega;\omega,\omega,-\omega)E_j(\omega)E_k(\omega)E_l(-\omega)\\ &=6\varepsilon_0\chi_{1122}(\vec{E}\cdot\vec{E}^*)E_i+3\varepsilon_0\chi_{1221}(\vec{E}\cdot\vec{E})E_i^* \end{aligned} \tag{1.15}$$

Or, equivalently

$$\vec{P}(\omega) = 6\varepsilon_0\chi_{1122}(\vec{E}\cdot\vec{E}^*)\vec{E} + 3\varepsilon_0\chi_{1221}(\vec{E}\cdot\vec{E})\vec{E}^* \tag{1.16}$$

Due to intrinsic permutation valid for nonresonant electronic response: $\chi^{(3)}_{1122}(\omega;\omega,\omega,-\omega) = \chi^{(3)}_{1221}(\omega;\omega,-\omega,\omega)$, so that:

$$\vec{P}(\omega) = 2\varepsilon_0\chi^{(3)}\left|\vec{E}\right|^2\vec{E} + \varepsilon_0\chi^{(3)}(\vec{E}\cdot\vec{E})\vec{E}^* \tag{1.17}$$

with $\chi^{(3)} \equiv \chi^{(3)}_{1111} = 3\chi^{(3)}_{1122}$. The nonlinear polarization consists of two contributions that have very different physical characters, since the first contribution corresponds to a nonlinear induced index change whereas the second will be responsible for a nonlinear induced polarization rotation of the field along the propagation (only linearly or circularly polarized light are transmitted with their state of polarization unchanged).

In the case of linearly polarized light (we will study mainly the fundamental TE mode): $E_1 = E, E_2 = E_3 = 0$, the nonlinear polarization is reduced to: $P_1^{NL} = 3\varepsilon_0\chi^{(3)}\left|E\right|^2 E$, so the total polarization is then described by a linear and a nonlinear parts:

$$P_1 = \varepsilon_0\chi^{(1)}E + 3\varepsilon_0\chi^{(3)}\left|E\right|^2 E = \varepsilon_0\chi_{eff}E \tag{1.18}$$

Reminding the refractive index definition: $n = \sqrt{1+\chi_{eff}}$, that in the linear regime is $n_0 = \sqrt{1+\mathbb{R}\mathbf{e}\{\chi^{(1)}\}}$, we can find a variation induced by the nonresonant $\chi^{(3)}$ effect ($\mathbb{R}\mathbf{e}\{\chi^{(3)}\}$):

$$\begin{aligned} n(|E|^2) = \sqrt{1+\mathbb{R}\mathbf{e}\{\chi^{(1)}\}+3\mathbb{R}\mathbf{e}\{\chi^{(3)}\}|E|^2} &\approx \sqrt{1+\mathbb{R}\mathbf{e}\{\chi^{(1)}\}} + \frac{3\mathbb{R}\mathbf{e}\{\chi^{(3)}\}|E|^2}{2\sqrt{1+\mathbb{R}\mathbf{e}\{\chi^{(1)}\}}} \\ &= n_0 + \frac{3\mathbb{R}\mathbf{e}\{\chi^{(3)}\}|E|^2}{2n_0} \end{aligned} \tag{1.19}$$

from where we can define the nonlinear refractive (optical Kerr) index n_2 (in units of m^2/W), such that $n = n_0 + n_2 I$ where I stands for the electric field intensity, that is related to the electric field component as $I = 2n_0\varepsilon_0 c|E|^2$, so the refractive index could be rewritten as $n = n_0 + n_2 2n_0\varepsilon_0 c|E|^2$. Relating this definition with equation (1.19), the expression for the nonlinear refractive index is:

$$\boxed{n_2 = \frac{3}{4n_0^2\varepsilon_0 c}\mathbb{R}\mathbf{e}\{\chi^{(3)}\}} \tag{1.20}$$

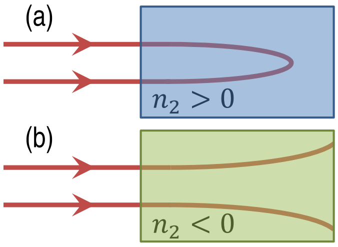

Figure 1.2: (a) Self focusing and (b) defocusing of light.

At telecom wavelengths around 1550 nm, the values of n_2 in semiconductors are very large compared to that of silica. For instance, the nonlinear refractive index is 200 times larger in silicon. One of the processes that can occur as a result of the intensity dependent refractive index n_2 is self-focusing when n_2 0 and defocusing when n_2 0, which is illustrated in Fig. 1.2 (a) and (b) respectively. These processes can occur when a beam of light having a nonuniform transverse intensity distribution propagates through a material for which $n_2 \neq 0$. The material effectively acts as a lens [8].

Analytical approach to estimate n_2

By means of a two band model and the Kramers-Krönig (KK) relations (principle of causality), Sheik-Bahae and co-workers [9] have deduced an expression for the bound electronic nonlinear refractive index n_2 in **semiconductors** and wide-gap optical solids. This expression will be used in the next chapter to model novel materials and hybrid waveguides that are not reported in the literature. The expression is given by:

$$\boxed{n_2(\omega) = \frac{40\pi\sqrt{E_p}}{c n_0^2 E_g^4} K' G_2\left(\frac{\hbar\omega}{E_g}\right)} \tag{1.21}$$

where E_g is the gap energy, n_0 the material index of refraction, $E_p = 21$ eV is the Kane energy and K' is a numerical fitting coefficient that takes values of the order of 1.5×10^{-8} if the energies are in eV. The function G_2 describe the contributions from different physical origins: two-photon transitions (TPA and Raman (R)), linear Stark (LS), quadratic Stark (QS) and a divergent term (DT). They are related as:

$$G_2(x) = G_{\text{TPA}}(x) + G_{\text{R}}(x) + G_{\text{LS}}(x) + G_{\text{QS}}(x) - G_{\text{DT}}(x) \tag{1.22}$$

with

$$\begin{aligned} G_{\text{TPA}}(x) = \frac{1}{(2x)^6}\Big[&-\frac{3}{8}x^2(1-x)^{-1/2} + 3x(1-x)^{1/2} - 2(1-x)^{3/2} \\ &+ 2\mathcal{H}(1-2x)(1-2x)^{3/2}\Big] \end{aligned} \tag{1.23}$$

$$G_{\mathrm{R}}(x) = \frac{1}{(2x)^6}\left[-\frac{3}{8}x^2(1+x)^{-1/2} + 3x(1+x)^{1/2} - 2(1+x)^{3/2} + 2(1+2x)^{3/2}\right] \tag{1.24}$$

$$G_{\mathrm{LS}}(x) = \frac{1}{(2x)^6}\left[2 - (1-x)^{3/2} - (1+x)^{3/2}\right] \tag{1.25}$$

$$G_{\mathrm{QS}}(x) = \frac{1}{(4x)^5}\left[(1-x)^{-1/2} - (1+x)^{-1/2} - \frac{x}{2}(1-x)^{-3/2} + \frac{x}{2}(1+x)^{-3/2}\right] \tag{1.26}$$

$$\begin{aligned} G_{\mathrm{DT}}(x) = \frac{1}{(2x)^6}\,\Big[& -2 - \frac{35x^2}{8} + \frac{x}{8}(3x-1)(1-x)^{-1/2} - 3x(1-x)^{1/2} + (1-x)^{3/2} \\ & + \frac{x}{8}(3x+1)(1+x)^{-1/2} + 3x(1+x)^{1/2} + (1+x)^{3/2}\Big] \end{aligned} \tag{1.27}$$

where $\mathcal{H}(x)$ is the Heaviside or step function. Eq (1.21) has only one variable quantity: G_2, so we plot in Fig. 1.3-Left, the different contributions and the overall shape in red as function of $h\nu/E_g$. Fig. 1.3-Right shows the evolution for three bandgap materials of the calculated n_2 with operating energy normalized to the material bandgap. Interestingly, the n_2 values are expected to strongly vary nearby $h\nu{>}0.7E_g$. We have chosen as example typical gap energies of integrated semiconductors (for Si, E_g=1.12 eV). We have assume a linear index of n=3 for all the cases. It could be seen that for the same excitation wavelength (1580 nm), the expected n_2 is not inversely proportional to E_g. The maximum nonlinearity is expected for the material with intermediate E_g. In our work, these theoretical predictions will be used to understand some nonlinear refractive index measured values and to estimate its magnitude for diverse wavelength ranges.

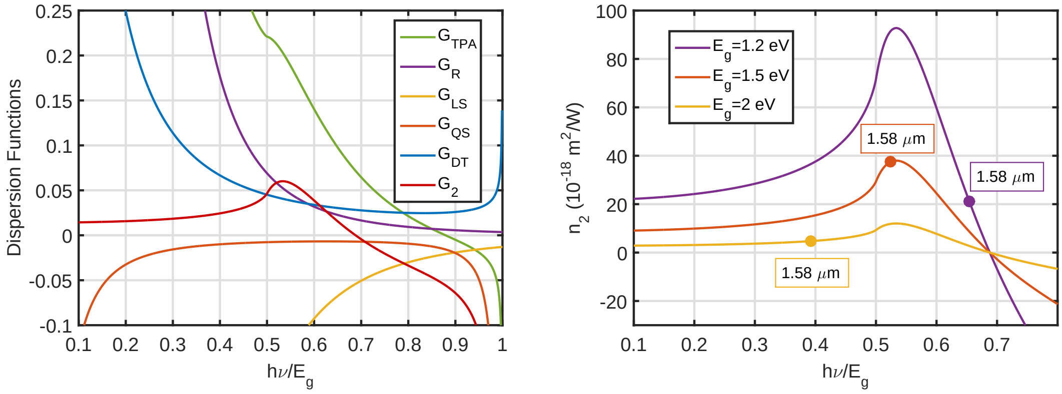

Figure 1.3: Left: Frequency dependence of the various contributions to the nonlinear refractive index. Right: Kerr coefficient evolution as a function of $h\nu/E_g$ for artificial materials with n=3. The dots corresponds to a photon energy at $\lambda = 1.58$ μm.

Self Phase Modulation: SPM

The Kerr effect has an interesting and very important consequence in the optical pulse: the self-phase modulation (SPM). This phenomenon introduces a symmetrical spectral broadening in the pulse. We will use this effect to measure the induced nonlinear phase shift and quantify the magnitude and sign of the real part of the third order nonlinear susceptibility. As a first approximation we can use a simplified version of the propagation Eq. (1.10):

$$\frac{\partial u(z,t)}{\partial z} = i\frac{2\pi}{\lambda_0} n_2 I(t) u(z,t) \tag{1.28}$$

assuming a purely real $\chi^{(3)}$ (lossless) material, the equation shows that the field derivative undergoes a phase shift. Following the non-depleted approximation, one can assume that $I(z) \approx$ constant, so, enabling to integrate the previous differential equation:

$$u(z,t) = u(0)\exp\left(i\frac{2\pi}{\lambda_0} n_2 I(t) z\right) \qquad \Rightarrow\ \phi_{NL}(z,t) = \frac{2\pi}{\lambda_0} n_2 I(t) z \tag{1.29}$$

This is the self-induced phase shift, that follows the temporal intensity envelope and increases proportionally with the propagated distance z. We can introduce the instantaneous variation of the pulse frequency or instantaneous pulsation as $\delta\omega(t) = -d\phi_{NL}(t)/dt$, so its shape is governed by the temporal derivative of the intensity as illustrated in Fig. 1.4. The self-phase modulation does not change the temporal pulse envelope but creates a chirp. In Fig. 1.4 we display two envelopes (dashed lines) and their respective derivatives (solid lines) for positive n_2: a gaussian (blue) and sinus cardinal squared (orange), the former for pedagogical reasons and the later because it coincides with the temporal shape in our nonlinear experiments. In the gaussian case it is easier to understand that the front of the pulse is shifted towards lower frequencies while the end of the pulse is shifted towards higher frequencies when n_2 is positive, the opposite will occur if n_2 is negative. The unchanged envelope and chirped pulses in the case of sinus cardinal pulse are depicted in Fig. 1.4 for the two signs after a generic propagation length.

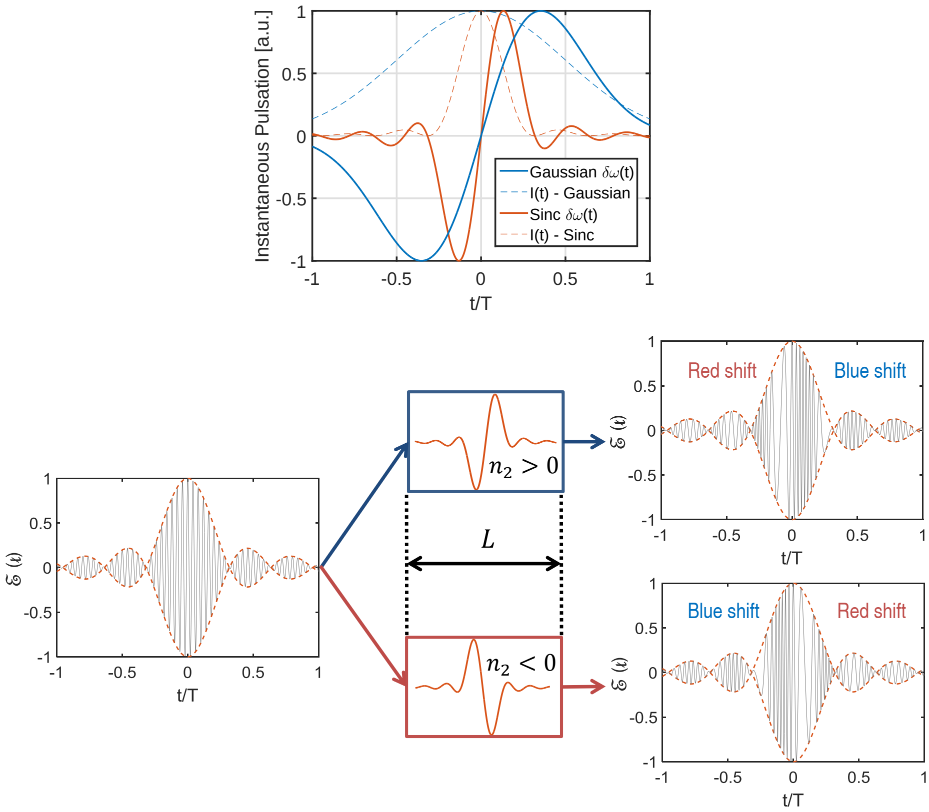

Figure 1.4: Up: Temporal shape of the pulse envelope (dashed lines) and its respective induced frequency shift (solid lines) for gaussian (blue) and sinus cardinal (orange) cases. Down: Schematics of the invariance of the envelope and the induced chirp when a pulse crosses a positive or a negative Kerr material with length L.

1.2.2 Two Photon Absorption

The real part of the third order nonlinear susceptibility is directly associated with the phase changes of the high intensity beams. On the other hand, the imaginary part induces a nonlinear modification of the material absorption. We are interested in semiconductors transparent in the telecommunication window. But in some cases, the gap energy is smaller than that of two photons, so if the density of energy is large enough, a two-photon transition can be achieved from the valence to the conduction band. In practice, it means that the delay between two photons should be smaller than the lifetime of a virtual intermediate state. So finally, two photons can promote an electron to the conduction band, leaving a hole in the valence band. This effect is proportional to the imaginary part of the nonlinear third order susceptibility such that:

$$\boxed{\beta_{\text{TPA}} = \frac{3\omega}{2\varepsilon_0 c^2 n^2} \mathbb{Im}\left\{\chi^{(3)}\right\}} \tag{1.30}$$

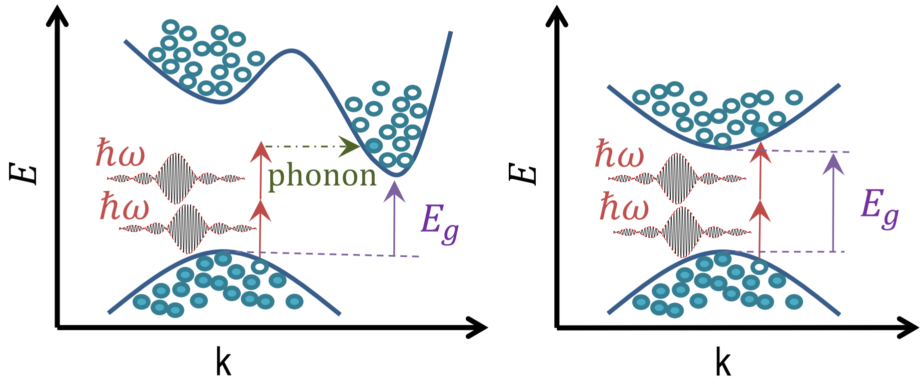

Figure 1.5: TPA scheme for an indirect and a direct gap material.

As it could be seen from Fig. 1.5, to excitation of one electron to a higher real energy state requires the annihilation of two photons, implying an additional losses source.

Neglecting higher order than two-photon transitions, the variation of the intensity is governed by:

$$\frac{dI}{dz} = -(\alpha + \alpha_{\text{TPA}})I = -\alpha I - \beta_{\text{TPA}} I^2 \tag{1.31}$$

where α corresponds to the linear propagation losses and $\alpha_{\text{TPA}} = \beta_{\text{TPA}} I$, the two photon absorption. So the nonlinear losses are an intensity dependent quantity.

Analytical approach to estimate β_{TPA}

Similarly to the real susceptibility effect, Sheik-Bahae et al. [9] have derived an analytical expression to estimate the TPA coefficient in semiconductors and wide-gap solids by applying the causality principle (KK relations):

$$\boxed{\beta_{\text{TPA}}(\omega) = \frac{K'\sqrt{E_p}}{n_0^2 E_g^3} F_2\left(\frac{\hbar\omega}{E_g}\right)} \tag{1.32}$$

where K' can be again considered to be a single free parameter, that here we will set as previously equals to 1.5×10^{-8}. The universal function F_2 is:

$$F_2(x) = \frac{(2x-1)^{3/2}}{(2x)^5} \qquad \text{for } x > \tfrac{1}{2} \tag{1.33}$$

and $F_2(x) = 0$ otherwise. This restriction means that the TPA process vanishes for

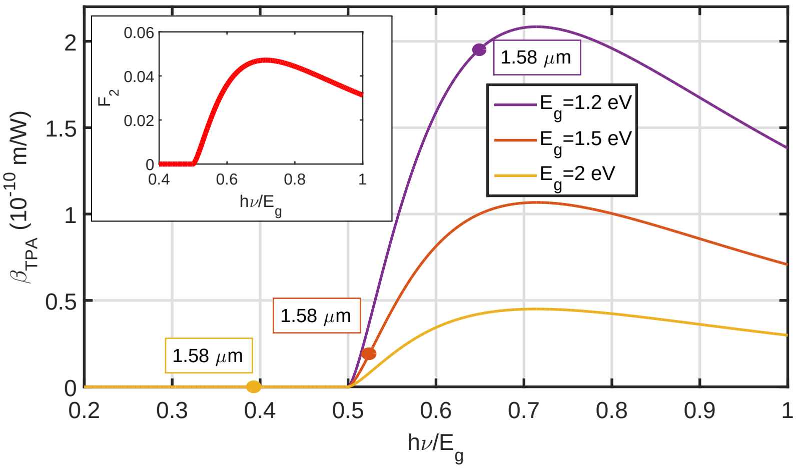

Figure 1.6: Theoretical variation of the two-photon absorption coefficient (β_{TPA}) with photon energy for 3 materials with bandgaps 1.2 eV, 1.5 eV and 2 eV and refractive index n=3. Inset: Variation of the function F_2 which vanishes for photon energy smaller than half of the energy gap. The predicted β_{TPA} is marked for the three materials at a wavelength of 1580 nm.

$\hbar\omega < E_g/2$. As previously, we illustrate in Fig. 1.6 the predicted trends for three artificial materials with $n = 3$.

Interestingly, this model predicts that the two-photon absorption probability does not increase monotonically with the photon energy but reaches a maximum at $\hbar\omega/E_g \approx 0.7$, in the region where the Kerr coefficient is expected to vanish and change in sign. The material exhibiting the largest n_2 at $\lambda = 1580$ nm ($E_g = 1.5$ eV) shows a low β_{TPA}, instead the material with larger gap do not present TPA but exhibits a n_2 one order of magnitude lower, so it is important to consider all the variables for the design of nonlinear devices.

1.2.3 Free Carrier Effects

As can be seen from Fig. 1.5, direct and indirect gap materials generate an electron-hole pair after the absorption of two photons. As a consequence of TPA, the generation of free carriers modifies the population density in the valence and the conduction bands which conducts to a modification of the material susceptibilities. The master equation that describes the density of carriers is given by:

$$\frac{\mathrm{d}}{\mathrm{d}t} N_{FC} = -\frac{1}{\tau_e} N_{FC} + \beta_{TPA} \frac{I^2}{2\hbar\omega} \tag{1.34}$$

The first right side term describes the evolution of the carrier population weighted by the recombination time τ_e. This corresponds to a relaxation time of the electrons from the conduction band decaying into the valence band. The second term of the right hand expression relates the rates of generated carriers by TPA, which is proportional to the TPA coefficient and the energy of two photons. This effect is proportional to the square of the intensity. Physically, this term corresponds to the creation of an electron-hole pair by the annihilation of two photons.

Conversely to the Kerr and TPA processes that could be considered as instantaneous, the free carrier effect has a dynamic nature meaning that carriers could be accumulated for high enough intensities or sufficiently short duty cycles.

In fact, the relevance of free carriers is such that they change the effective susceptibility of the medium, through a variation of the real part of the effective susceptibility called free carrier refraction (FCR) and of the imaginary part called free carrier absorption (FCA). This modification can be expressed as [10]:

$$\chi = \chi^{(1)} + \Delta\chi^{(1)} \text{ with } \Delta\chi^{(1)} = \chi_{FC} = 2n_0 \left(\sigma_n(\omega) N_{FC} + i\frac{c}{2\omega}\sigma_a(\omega) N_{FC}\right) \tag{1.35}$$

where n_0 is the linear refractive index at the frequency ω, the quantities $\sigma_n(\omega)$ and $\sigma_a(\omega)$ can be expressed in terms of the effective masses and mobilities of electrons and holes [11]:

$$\sigma_n(\omega) = -\frac{q^2}{2\varepsilon_0 n_0 \omega^2}\left(\frac{1}{m_e} + \frac{1}{m_h}\right)\frac{E_g^2}{E_g^2 - (\hbar\omega)^2} \tag{1.36}$$

$$\sigma_a(\omega) = \frac{q^3}{c\varepsilon_0 n_0 \omega^2}\left(\frac{1}{\mu_e m_e^2} + \frac{1}{\mu_h m_h^2}\right)\frac{E_g^2}{E_g^2 - (\hbar\omega)^2} \tag{1.37}$$

where E_g is the semiconductor gap energy, q is the elementary electron charge equals to 1.602×10^{-19} C. m_e, m_h, μ_e and μ_h are the effective masses and mobilities of electrons and holes, respectively. We have assumed that the number of holes and electrons are equivalent (they are always in pairs).

In summary, the generated pairs affect the phase (refraction) and the intensity (absorption) of the propagating wave. Generally the carrier recombination time is in the order of nanoseconds for the materials treated in this manuscript. In the next chapter, as we will be working with picosecond pulses with repetition rate of 50 MHz, these effects will be negligible. For instance in silicon, the carrier lifetime is in the order of few nanoseconds. As the free carrier density is driven by $\int \frac{I^2}{\hbar\omega}dt$, at our operating intensities the temporal separation between each pulse (~ 20 ns) is enough for the FC relaxation.On the contrary, in chapter 3, we will further explain and exploit the free carrier refraction (FCR) to increase the transmission efficiency of cavities.

We have described up to now, the basic relations for the phenomena that will be used later. There are many other additional nonlinear effects that have been investigated and exploited in integrated platforms during recent years but they are out of this thesis scope.

1.3 Optical waveguides and cavities

Optical signals are transfered by the use of transparent media that could confine the light. Optical fibers have been largely used at research and industrial scales showing the potential of using light waves for long distance information transmission. Usually, single mode fibers use a low index variation to confine the light, allowing the propagation of the fundamental mode over a wide spectral band and large distances with few losses. In high refractive index contrast structures such as silicon-on-insulator (SOI) wires, generically known as optical waveguides, the mode can be tightly confined. These small areas limits the propagation distance due to optical losses but strongly increases light-matter interactions, comprising the nonlinear effects.

The relative size between optical waveguides and single mode fibers can be appreciated in Fig. 1.7, where we have also shown the index variations. Propagation losses, in general terms, can be studied regarding two main physical origins: intrinsic losses (i.e. carrier absorption in doping based waveguides) and extrinsic losses (i.e. sidewall scattering due to fabrication imperfections and radiative losses into the substrate). The later will be the subject of study as it requires optimization of the fabrication and design process.

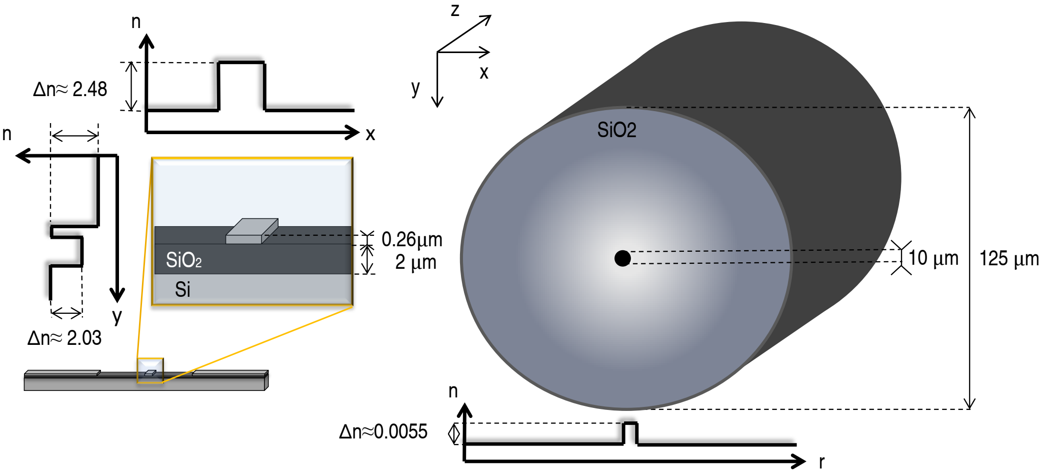

Figure 1.7: Scaled comparison between the size and refractive index profiles of a monomode fiber and a single mode SOI waveguide.

1.3.1 Enhancement of nonlinear effects in highly confined structures

In the previous sections we have introduced the basic relations for nonlinear optics in infinite and diluted materials and a brief description of optical waveguides. Now, we will see the effect of light confinement in light-matter interactions [12]. The electric field and the polarization considered at the moment were external quantities that do not describe all the dipole interactions required in dense media or highly localized light. Indeed, as seen in Fig. 1.7, integrated waveguides allows the light confinement in sub-micrometer sizes. One approach to fully describe our guided scenario is to consider a classic electrostatic approximation and calculate the local field experienced by each dipole. It can be expressed as the sum of the applied external field and the specific electric field generated by the surrounding dipoles ($\vec{E}_{\text{loc}} = \vec{E}_{\text{ext}} + \vec{E}_{\text{dip}}$), the latest being estimated through a perfect empty sphere surrounding each dipole : $\vec{E}_{\text{dip}} = \vec{P}^{(1)}/(3\varepsilon_0)$. In isotropic media, $\vec{P}^{(1)}$ could be calculated by taking into account the number of dipoles: $\vec{P}^{(1)} = N\alpha\vec{E}_{\text{loc}}$, so we can find a relation between the local field and the macroscopic field that we measure; enabling to give a relation between the susceptibility (a macroscopic quantity) and the polarizability (a microscopic quantity):

$$\vec{E}_{\text{loc}}(\omega) = f(\omega)\vec{E}(\omega), \qquad \text{with} \qquad f(\omega) = \frac{1}{1 - \frac{N\alpha}{3\varepsilon_0}} \tag{1.38}$$

To estimate the correction factor effect, we can relate the local field factor correction ($f(\omega)$) and the relative permittivity ($\varepsilon_r(\omega)$):

$$\varepsilon_r(\omega) = 1 + \chi^{(1)}(\omega), \qquad f(\omega) = \frac{2 + \varepsilon_r(\omega)}{3} \tag{1.39}$$

In dielectric materials $\varepsilon_r(\omega) > 1$, then the correction factor is always larger than 1, therefore we call it enhancement factor. It can be further shown that the correction factor scales with the susceptibility order, in such manner that the n^{th} order susceptibility contains a product of $n+1$ local field factors. If $n > 1$ and all the frequencies are the same (degenerated case):

$$\chi^{(n)}_{eff}(\vec{r},\omega) = f^{n+1}(\omega)\chi^{(n)}(\vec{r},\omega) \tag{1.40}$$

In table 1.1, we have summarized the nonlinear order susceptibility effects treated in this manuscript and their corresponding expected enhancement effects.

While the local field factor corrections are included in the nonlinear susceptibility values for bulk materials, we will next use this approach in order to take into account for

Nonlinear effect	order	Factor
Kerr	3	f^4
Two photon absorption (TPA)	3	f^4
Free carrier refraction (FCR)	5	f^6
Free carrier absorption (FCA)	5	f^6

Table 1.1: Enhancement factors and effective order of the main nonlinear effects under study.

the nonlinear enhancement effects that are observed in slow mode waveguides and/or microcavities. In the first case, we will find a relation with the group velocity [13] and in the second with the quality factor. Indeed, experimentally, one faces the difficulty of relating the intensity of an electromagnetic wave inside a high contrast waveguide to the intensity measured outside the waveguide. By demonstrating the group velocity ($\nabla_{\vec{k}}$) and Poynting (Π) vectors collinearity, we can rely the wave intensity to the Poynting vector average:

$$f = \frac{|E_1|}{|E_0|} = \sqrt{\frac{I_1}{I_0}} = \sqrt{\frac{\langle||\Pi_1||\rangle}{\langle||\Pi_0||\rangle}} = \sqrt{\frac{\langle||\nabla_{\vec{k}1}(\omega)||\rangle}{\langle||\nabla_{\vec{k}0}(\omega)||\rangle}} = \sqrt{\frac{v_{g0}}{v_{g1}}} = \sqrt{\frac{n_{g1}}{n_{g0}}} \tag{1.41}$$

Using this relation to measure the nonlinearity in structured materials, we will have a relation between the group index inside the structure and the bulk index material. Dealing with powers (proportional to the squared of the electric field), we will introduce another parameter $\mathbf{S = f^2 = n_g/n_0}$, called the **slow down factor**. So, the optical Kerr and TPA effects will scale with S^2.

1.3.2 Strip waveguide

Strip and ridge waveguides are the basic building blocks of photonic integrated circuits. They exploit the high refractive index contrast between different planar materials. The refractive index map for silicon-on-insulator (SOI) waveguides is depicted in Fig. 1.7. The waveguide dimensions are smaller than the excitation wavelength ($\lambda \sim 1550$ nm). The optical mode is found by solving the Maxwell equations (eigenvalue problem). In Fig. 1.8 (a), we depict the different components of the fundamental TE electromagnetic mode (electric and magnetic fields) in a SOI strip (fully etched) waveguide. The silicon thickness was 220 nm and the width 360 nm. It is noteworthy that the E_x is dominant component. It can be seen the interaction with the waveguide walls, highlighting the importance of proper fabrication quality. In Fig. 1.8 (b), we show the $|\vec{E}|^2 = |\vec{E_x}|^2 + |\vec{E_y}|^2 + |\vec{E_z}|^2$ of a SOI ridge waveguide.

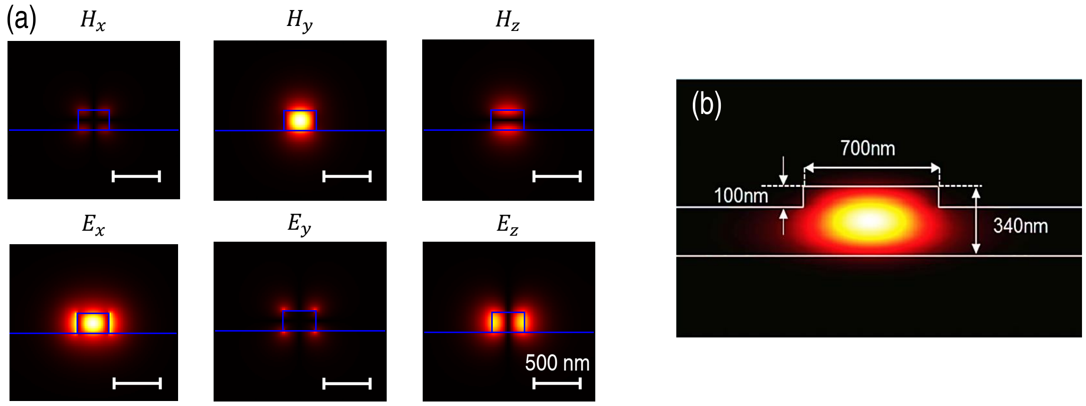

Figure 1.8: (a) Magnetic and electric field components of the fundamental TE mode in a SOI strip waveguide. (b) $|\vec{E}|^2$ fundamental TE mode in a ridge SOI waveguide.

1.3.3 Slot waveguide

Integrated materials have the advantage of confining light in sub-micrometer dimensions. Nevertheless the electronic properties of some semiconductors (particularly silicon) limit the nonlinear waveguide performances. Taking advantage of the high contrast of structures, slot waveguides were conceived to confine the light within a gap between semiconductor rails [14]. A typical slot geometry is depicted in Fig. 1.9 for the case of silicon. In order to keep the mode confined, the refractive index filling material must be smaller than the refractive index of the rails. Its operational principle is based in the continuity of the displacement electric field at interfaces. This means that for a strong change in the refractive index, the electric field amplitude should suffer a very strong discontinuity. For the case of TE mode, the displacement continuity applies to the normal vectorial component implies:

$$\vec{D}^N_{\text{Si}} = \vec{D}^N_{\text{Clad}} \quad \Longrightarrow \quad \varepsilon_{\text{Si}}\vec{E}^N_{\text{Si}} = \varepsilon_{\text{Clad}}\vec{E}^N_{\text{Clad}} \quad \Longrightarrow \quad \vec{E}^N_{\text{Clad}} = \frac{\varepsilon_{\text{Si}}}{\varepsilon_{\text{Clad}}}\vec{E}^N_{\text{Si}} \tag{1.42}$$

So, the electric field amplitude inside the cladding (i.e. slot) region increases proportionally to the ratio between the dielectric permittivities of the materials, meaning a stronger effect for higher index contrast scenario. This structure allows a very intense guided mode localized in the low refractive index medium, being confined in the low-refractive-index slot region. Typical values for power confinement ratio in silicon slot monomode waveguides filled with materials around the index of silica is 30% of the total power[15].

Given that the width of the slot is comparable to the decay length of the field, the electrical field remains high across the slot, resulting in a dielectric power density larger in the slot than in the silicon rails, as could be seen in Fig. 1.9. The extreme light confinement possible in slot waveguides also results in significantly enhanced propagation losses due

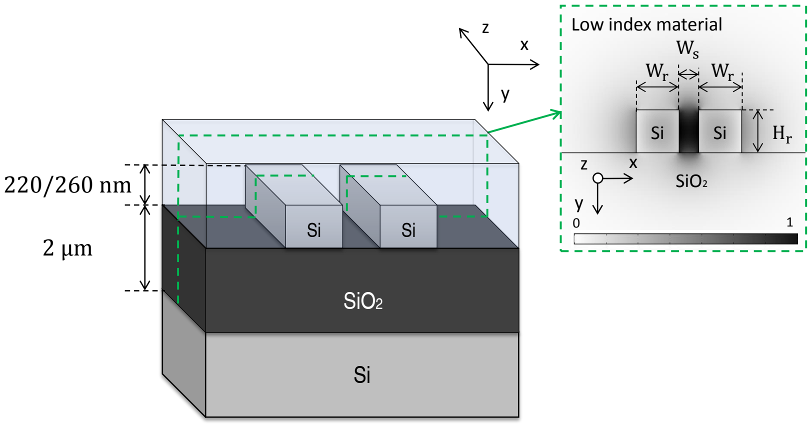

Figure 1.9: Schematics of a silicon slot waveguide covered with a material with refractive index n=1.46. The fundamental TE mode is displayed at 1580 nm. In the simulation case the rails are squares of 220 nm.

to increased interaction of the waveguiding mode with the sidewall surface roughness. Extensive experimental studies have shown that surface roughness is responsible for high propagation losses, which can become prohibitive for building dense integrated circuits.

1.3.4 Photonic crystal waveguides

A photonic crystal is a periodic arrangement at the wavelength scale of optical media with different refractive indices. The particularity of this kind of periodic arrays is the generation of energy bands where the light of specific frequencies is restricted to propagate in some particular or in all directions of the crystal. This effect is analogous to the electronic band diagrams in semiconductor crystals. In this manuscript we will focus the attention on 1D and 2D photonic crystals. In the case of 2D photonic crystals, when the lattice is shaped hexagonally, the energetic bandgap for the TE mode is omnidirectional, so the light at specific wavelengths is restricted to travel through the material (photonic bandgap). To exploit this feature, several kind of defects could be introduced in the crystal in order to create cavities or waveguides. In a silicon on insulator wafer, one can fabricate an periodic arrangement of holes. If one of the rows is not present, we introduce a linear defect in the 2D crystal where light can be confined, this kind of waveguides are named W1 as only one row was omitted. In Fig. 1.10, we display a scheme with the layers used to fabricate SOI photonic crystals. The direction of light propagation is shown with a red arrow. The use of high index contrast materials ensures the confinement in the third dimension (y in the scheme) through total internal reflection.

There are three main limitations in photonic crystals that will be treated in further detail: the highly dispersive nature of the defect bands that requires the understanding and proper design of slow light modes; the injection in the photonic crystal which requires a

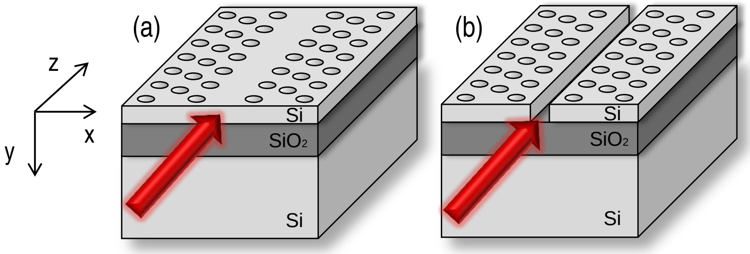

Figure 1.10: Scheme indicating the light propagation direction in a hexagonal 2D (a) W1 photonic crystal waveguide (W1-PhCW) and (b) Slot photonic crystal waveguide (SPhCW).

careful account of the spatial mode distribution, for instance from strip to slot, from slot to photonic crystal, within the photonic crystal between the different regimes of reduced group velocity and the correspondent at the output. All these impedance mismatches require the engineering of proper modal adapters. And finally a more statistical problem, regarding the propagation losses of the waveguide in different regimes of the energy band.

In Fig. 1.11, we present a typical band diagram of a W1 PhCW. There are different modes that appear after adding a defect in the crystal. They present different symmetry properties so we classify them as even and odd modes [16], we also highlight the presence of a light cone, that defines a limit for guided modes. As the even modes will be of central importance, we have plotted its group index (proportional to the inverse of the first derivative of the band) as a function of k. It is interesting to notice that as the frequency approaches the $k = \pi/a$ point, the group velocity vanishes. The n_g values presented are just to illustrate the dispersion profile of mode, but in reality it is not useful to target group indices larger than 50, mainly due to fabrication limitations. Specific details about the design, losses and dispersion of these structures will be given in following chapters.

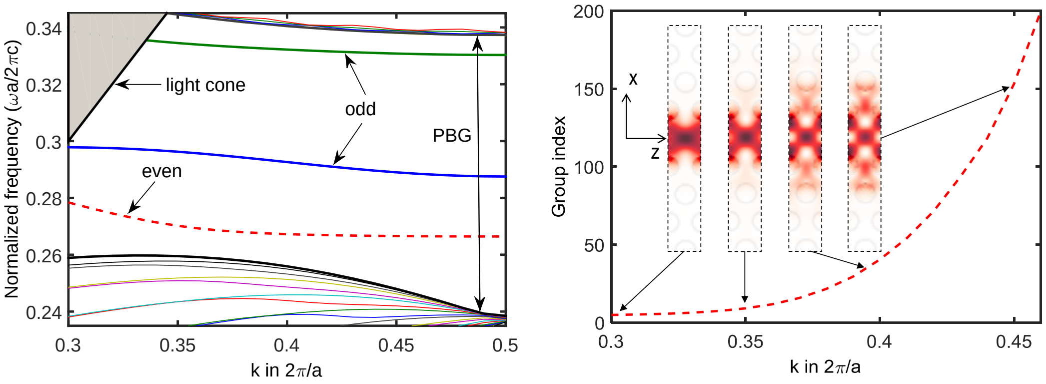

Figure 1.11: Left: Band diagram of the TE-like states for a waveguide formed by one missing row of holes (W1). PGB: Photonic Bandgap. Right: Group index of the even mode with the squared of the electric field profile at different k points.

This effect is accompanied by a mode spreading. For this particular map, the period is a = 410 nm and the ratio $r/a = 0.30$, so the wavelengths of the even mode are around 1520 nm.

Slot photonic crystal waveguide

Following the arguments to design slot waveguides, to have semiconductor photonic crystal waveguides could limit the nonlinear performances at $\lambda \sim 1550$ nm. So, it will be necessary to explore hybrid approaches able to exploit the slot and the slow light effects with a low-index highly nonlinear material filling the slot. In Fig. 1.10, we display a schematics of a photonic crystal in which a thin slot has been etched in the center of the missing row of holes. Previously, slot photonic crystal waveguides (SPhCW) and cavities have been proposed and used for sensing and nonlinear proposes [17, 18, 19].

The most interesting property of these kind of waveguides is the possibility to confine two even modes. One being called the W1-like mode that follows similar characteristics to that of the non-slotted photonic crystals (see Fig. 1.12). This mode will be extensively exploited and systematically compared to the W1 waveguide-counterpart. Another even mode is called true-slot mode (see Fig. 1.12) and follows a more specific dispersion curve. It is mainly excited in large slot size waveguides (in silicon: $W_{\text{slot}} > 150$ nm).

By comparing the band diagrams of a W1 and a SPhCW (Fig. 1.11 and 1.12), we can analyze the main changes introduced by the slot. In general terms, the shape of the forbidden gap is not affected in contrast with the guided modes inside the bandgap. In the W1 waveguide, there are two odd and one even modes for the described geometry. The latter gets strongly perturbed by the presence of the slot and the related reduction of the effective index results in an increase of the frequency. The larger the slot width,

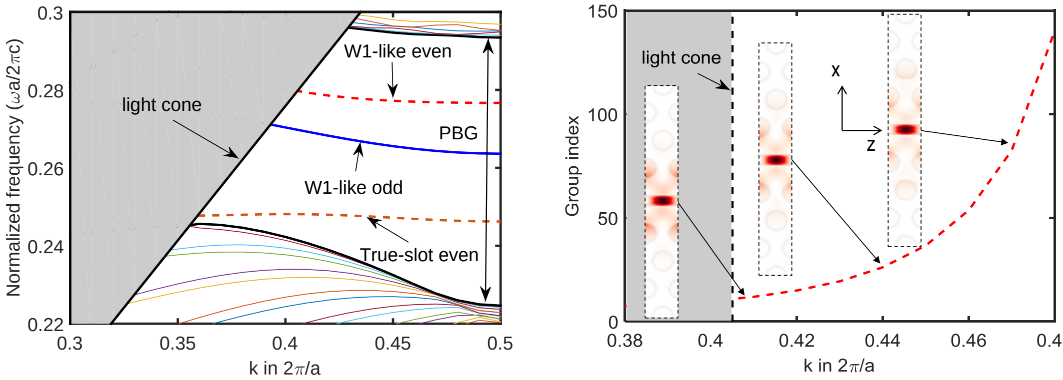

Figure 1.12: Left: Band structure of a SPhCW. PGB: Photonic Bandgap. Right: Group index (first derivative of the band) of the W1-like even mode with the squared of the electric field at different k points and shading the light cone position.

the smaller the effective index, so the W1-like even mode can be excluded from the bandgap towards the mode continuum. Another even mode appears, corresponding to the fundamental slot mode projected into the bandgap [20]. Inversely, a decrease in the slot width will correspond to smaller eigenfrequencies for the true-slot mode reaching the limit of the bulk modes continuum.

In the two even modes (W1-like and true-slot), light is strongly confined inside the slot. But as the interest in the last chapter will be centered in the W1-like mode, we have displayed the group index curve as a function of the wavevector. It can be remarked that conversely to a W1 waveguide, light do not spread as the group velocity decreases but instead tends to be more confined. The light cone is defined by the index of silica, it means that we are not working in membrane structures. Under such approach, the mechanical stability is largely increased and the possibility of working with low index materials ($1.40<n<1.80$) become straight-forward. On the other hand the main drawback is the limitation of the bandwidth. As it can be seen, the available frequency bandwidth for a given mode is significantly diminished. Furthermore, the dispersion engineering of non-membrane modes is more difficult.

There are many engineering issues to be treated, mainly the dispersion, the losses and the coupling into and from photonic crystal waveguides. The last chapter will be dedicated to the study of dispersion and potentials for nonlinear proposes of these kind of waveguides fabricated in silicon.

1.3.5 Optical Cavities and optical resonators

We have seen up to now that the light matter interactions could be reinforced by means of highly confined structures and waveguides operating at wavelengths presenting large group indices. But indeed, another way to increase these interactions (and in particular the nonlinear ones) is the use of optical cavities. In their integrated version, these resonant structures are intrinsically small and reach volumes close to the diffraction limit. A common expression to normalize the effective mode volume is given by: $V_{eff} = \frac{\int \varepsilon|\vec{E}|^2 d^3r}{\varepsilon_{max}\max[|\vec{E}|^2]}\left(\frac{2n}{\lambda}\right)^3$, being $\left(\frac{2n}{\lambda}\right)^3$ the diffraction limit. In addition to the reduction of the interaction volume to enhance light-matter interactions [21], the photon lifetime (τ) inside the cavity. It is directly evaluated through the quality factor defined as: $Q = \omega_0\tau/2 = \omega_0/\Delta\omega$, where ω_0 is the frequency of the resonance and $\Delta\omega$ the cavity linewidth.

During the last years, there has been a race to improve the figure of merit Q/V_{eff}. An incredible advance not just in the demonstration of passive microresonators such as disks, rings or photonic crystal cavities but also in specific applications such as lasing, all optical memories, silicon high-speed modulation, optical trapping, sensing and quantum processes relying on these structures have proven their potential for enhancing light-matter interaction phenomena. In particular, 1D and 2D photonic crystal cavities have been fabricated with quality factors on the order of one million with mode volumes smaller than $(\lambda/n)^3$ [22]. For instance, the use of photonic crystal cavities has allowed the demonstration of devices with record performance such as ultra-fast commutators consuming less than 1 fJ/bit [23], and the bistability effect has shown potential for all-optical memories [24, 25].

Even though during this thesis we have experimentally worked with many types of cavities and resonators for different applications, such as sensing or coupling testing [26, 27, 28, 29], we will focus our attention in the bandwidth problem when using high power optical beams. To study this phenomena, we have chosen a 1D photonic crystal cavity (also called nanobeam cavity) [30] depicted in Fig. 1.13 (b) consisting in two adapted Bragg mirrors. Due to its modeling simplicity (compared to other cavities) and the fabrication tolerance allowing to easily reach quality factors of few thousands, they have been used for laser with direct modulation speeds exceeding 100 GHz[31], quantum applications and hybrid platforms [32, 33]. Nanobeam cavities have been fabricated in several integrated materials such as Si [34], Si_3N_4[35] and SiO_2[36].

Hereafter, we introduce a general model based on the coupled mode theory to describe the temporal evolution of a (close to resonance) field confined in a microcavity [37]. We define the intracavity field amplitude as: $u(t) = \sqrt{P_u(t)\tau_R}e^{i\phi_u(t)}$ with $P_u(t)$ the intracavity power, $\phi_u(t)$ the field phase and τ_R the cavity round trip time. Next, we define the temporal evolution of such a field in the linear regime:

$$\frac{du(t)}{dt} = -\frac{1}{\tau}u(t) + i\omega_{res_0}u(t) + \sqrt{\frac{2}{\tau_e}}s_{in}(t) \tag{1.43}$$

where $|s_{in}(t)|^2$ is the instantaneous power of the input signal and ω_{res_0} the cavity resonance frequency. The linear cavity photon lifetime $\tau/2$ corresponds to $1/\tau = 1/\tau_0 + 1/\tau_e$, where $\tau_0/2$ and $\tau_e/2$ are the photon lifetimes related to the intrinsic cavity linear losses and to the coupling constant between the waveguide and the cavity respectively. It can be seen that the volume and the quality factor are implicit in the equation through the cavity mode and the photon lifetime τ, respectively. $Q = \omega_0\tau/2$ can be separated in two contributions: $Q_0 = \omega_0\tau_0/2$ related to the losses (intrinsic) and $Q_e = \omega_0\tau_e/2$ to the waveguide-cavity coupling (extrinsic), such that: $1/Q = 1/Q_0 + 1/Q_e$. We can also find an expression for the output field: $s_{out}(t) = -s_{in}(t) + \sqrt{2/\tau_e}u(t)$[38]. The previous model is applicable to coupled cavities, such as the case (a) from Fig. 1.13. In the nanobeam case (b), we will have an additional coupling that we could model as a second (add-drop) waveguide. By including a coupling lifetime to the second waveguide τ_d, the photon lifetime will have three components: $1/\tau = 1/\tau_0 + 1/\tau_e + 1/\tau_d$ and assuming no input from the add port (equivalently, only one side injection of the nanobeam cavity): $s_{drop}(t) = \sqrt{2/\tau_d}u(t)$. So we end up with three equations that models the linear temporal

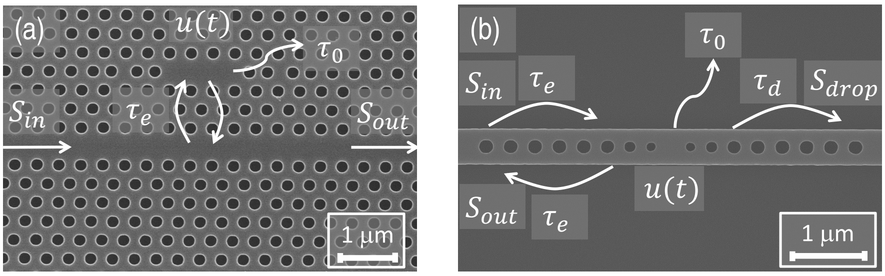

Figure 1.13: SEM images for (a) L3 coupled cavity and (b) nanobeam cavity by displaying the different terms used to generally model resonant systems.

evolution of the cavities that will be studied later on.

In chapter 3, we will introduce the general concepts of the intra-field evolution in optical microcavities under strong peak powers, i.e. the nonlinear regime and use it to calculate the resonance drift and the bandwidth limitation. We will offer a solution to overcome this issue with experimental and numerical results.

1.4 Integrated photonics: materials and linear properties

The optical principles presented above were introduced without particular care of the specific materials that can be used. Instead, it was a presentation of generic guiding principles. In order to study precise light-matter interactions and quantify the different phenomena, we should take into account the specific materials under study. Fig. 1.14 presents the chemical elements in their relative position in the periodic table that will be of interest in this work.

Recalling some basic chemistry, tendency for chemical reactions of an atom is determined by the electrons in “valence” (outermost) shell. For instance, Argon has a filled outer shell (eight electrons) and has no tendency for chemical activity. On the other hand, materials with only few electrons (one or two) ready to relinquish them, can react easily with materials that are eager to receive them (with almost full outer shells). In between those two extreme cases, there are interesting materials that are neither inert nor volatile, among them, the well known Group IV, where we could find elements that have been extensively used in integrated circuits (electrical and optical) such as carbon (nanotubes, graphene, diamond,...), silicon (SOI, strain-Si, Si-PhC,...) and germanium (SiGe,...). We have also the III-V materials such as Al, Ga, As, In and P that are successfully used in the development of sources, detectors and modulators. Finally, Chalcogenide glasses, composed by heavier materials in these III-VI region such as S, Sb, Te and Se, have been proposed and later demonstrated as a suitable material to enhance third order nonlinearities. Silicon dioxide (commonly known as Silica) and Silicon Nitride are also interesting materials for integrated optics. The values presented in Fig. 1.14 were extracted from Ref [39].

These materials have very unique electric conductive behavior. In terms of the quantum states for electrons associated with the electronic band structure, they have "partially" filled states. This concept is quantified via the bandgap, corresponding to the energy required for an electron to be promoted from the valence band towards the conduction band, generating an electron-hole pair. This bandgap energy is a fundamental property of the material and can be used to estimate the facility to emit or absorb photons (transparency window) and the instantaneous nonlinear third order effects as seen in section 1.2. An important difference between semiconducting materials is their electronic band distribution. The material bandgap can be direct or indirect. For instance, in silicon, its indirect gap makes it not suitable for active components (no laser).

In table 1.2, we present some of the bandgap energies for the materials that will be used to fabricate waveguides. In order to facilitate the comparison it is convenient to remind that the energy of one photon at 1550 nm is around 0.80 eV.

Nowadays the material sciences have a growing interest towards novel potential compounds for nonlinear integrated proposes such as sensing, microscopy, all-optical data processing and quantum information. For instance, polymers, nano and micro engineered artificial materials and degenerate or amorphous semiconductors have proven unseen nonlinear effects achievable with moderated powers.

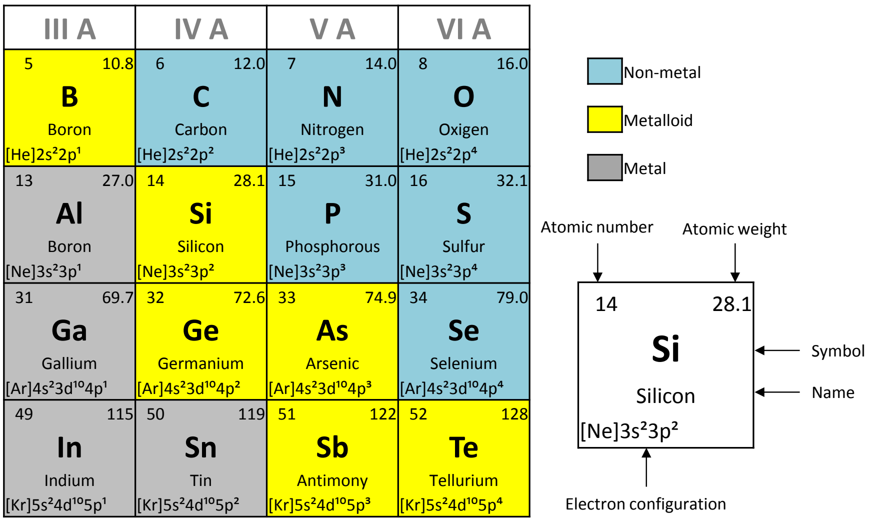

Figure 1.14: Section of the periodic table with the basic information regarding the electron configuration. The group number corresponds to the quantity of electrons in the outer "shell".

Material	E_g [eV] at 300K	**Gap type**	$\omega_{cut-off}$ [PHz]	$\lambda_{cut-off}$ [μm]
Silicon	1.12	indirect	1.70	1.108
	3.2	direct	4.86	0.388
Germanium	0.67	indirect	1.02	1.852
	0.8	direct	1.22	1.551
Silicon Nitride (Si_3N_4)	5	indirect	7.60	0.248
Silicon dioxide (SiO_2)	9	indirect	13.67	0.138

Table 1.2: Main materials to be used in this work with their respective gap energy and cut-off wavelength which defines one of the transparency window limits.

1.4.1 Fabrication

This section introduces the fabrication concepts for structures simulated and prepared in GDSII masks (comprehensible by the lithographic machines). All the SOI and silicon nitride waveguides in this manuscript (strip, slot, photonic crystal waveguides and cavities), were fabricated in the CTU (*Centrale Technologique Universitaire*), clean room of the former IEF (*Institut d'Electronique Fondamentale*), now C2N (*Centre de Nanosciences et de Nanotechnologies*), under the supervision of Ing. Xavier Le Roux from MINAPHOT team.

After the simulation of the structures, we proceed by designing some GDSII masks for the electronic lithography; in this task several software tools were used, for instance L-Edit, KLayout, CleWin and a Python extension. SOITEC wafers were used with 2 different nominal silicon thickness: (221.7 ± 8.1) nm and (260.0 ± 20.5) nm and 2.0 μm buried oxide layer. Mainly the 260 nm was used due to disposal. The crystal orientation was <100>.

We have used a 80 keV electronic lithography machine: Nanobeam Ltd. nb4. We have optimized the ICP (inductively Coupled Plasma) etching. The structures are formed in a positive resist, so, it is required to define them by inversion (Fig. 1.15). After the resist cleaning, there is a mechanical cleaving leaving measurable samples around 5 mm long that include tapers and access waveguides.

The positive resist (ZEP 520-A) consists of a polymer chain sensitive to electronic exposition. The exposed chains then react differently during the development. The mentioned resist exhibits good selectivity and high resolution (<2 nm), making it adequate to deal with our structures. For instance, typical minimum fully etched slot sizes of around 60 nm are achieved.

Two parameters are critical to ensure the proper electron penetration that will determine the etching quality: the deposited thickness and its homogeneity. To optimize this procedure, the resist is diluted in methoxybenzene and deposited by spin-coating (6000 turns/min), with a final thickness of 90 nm. Finally, the sample with the resist is deposed

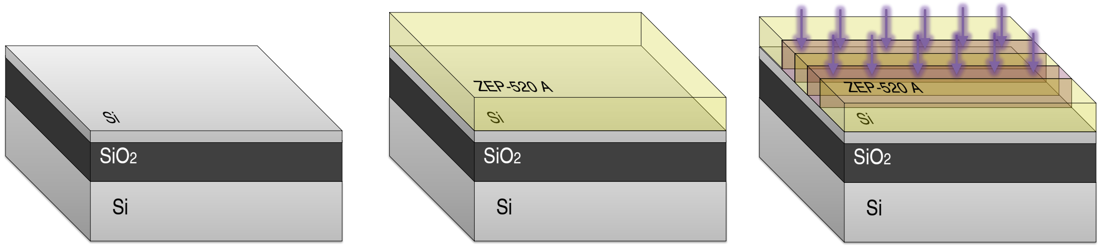

a) 260 nm/220nm SOI wafer with 2μm buried oxide layer

b) Use of a positive EB resist (ZEP 520-A)

c) Electron Beam Lithography (nb4 system)

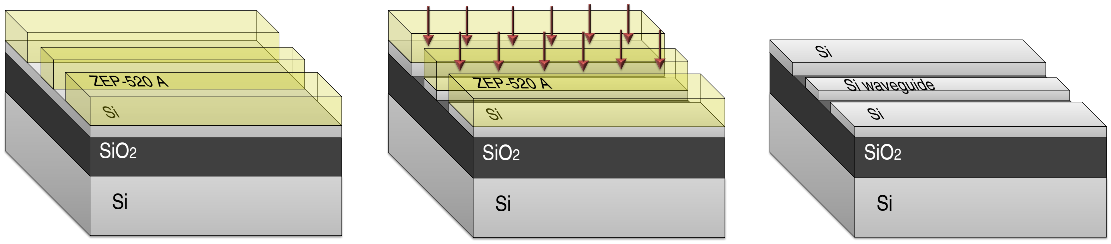

d) Development of the resist in a MIBK

e) Silicon etching with the system ICP-STS

f) Cleaning of the resist with piranha solution and plasma O2

Figure 1.15: Schematic representation of the different fabrication steps followed in the clean room to fabricate silicon structures (strip, slot, PhC and cavities).

in a heated surface at 170°C during 2 minutes. In Fig. 1.15, we summarize the fabrication steps. We will briefly describe the different procedures followed to fabricate more complex devices in a special subsection in the last chapter.

e-beam lithography

The .gds masks are treated in the nb4 softwares to define the electronic writing fields. Depending on the kind of structures, the main and sub fields are optimized. Indeed, the subfield center is more accurate than the extremes (where the electronic beam should deflect), so the smallest motives should be located preferentially in the central area. Next, the .gds are fragmented in the format .npf, where the machine drift should be verified in order not to exceed the practical limit (47 MHz).

The e-beam lithography offers a good compromise between written surface and precision, required for long photonic crystals. Even though, lithography is limited by diffraction, the main advantage of eBL over optical lithography is that electrons are orders of magnitude smaller than photons, so a higher resolution is achieved (maximum of 2 nm in our case), and smaller features could be patterned. In the $Nanobeam4$, the electrons accelerate from an electron gun with an energy of 80 keV. This potential reduces the electron retro-diffusion in the resist, limiting proximity effects. The electron beam scans across the surface point by point following the compromises coded in the .npf. Depending on the complexity of the mask, it could take from some tenths of minutes until one day of writing.

The pattern is divided into several main writing fields. Inside each main field, the sample stage is fixed at the center and the beam is deflected by a coil to insolate the rest. To avoid the minimum beam aberrations the choice would be to decrease the main field size but this approach increases the stitching errors (defined by the accuracy of the line continuity, maintained by a laser interferometer), which corresponds to the limit between main fields. In other words, as we increase the number of stage displacements, we also increase the probability of mechanical errors. We should take into account also that the larger is the displacement, the larger is the error probability, so the choice of main field size is not evident.

Indeed, we have worked with large main fields (300x300 μm^2) when the whole structure could be contained inside that area, such as short photonic crystals or cavities. In other cases, we have opted for larger number of smaller stitching errors with main fields of 50x50 μm^2. We should keep in mind that the limit sizes for the main field are 1000x1000 μm^2 and 50x50 μm^2. Inside a main field, the electron beam scans the surface following some sub-field distribution. Inside this sub-field, a second coil generates a finer deflection. The limits for the sub-field are 25x25 μm^2 and 5x5 μm^2. For a maximum precision we have chosen the smallest sub-field, even though it increases the total time. We should note that the stitching errors from the sub-field are negligible with respect to the main field ones. In Fig. 1.16, we show different scanning electron microscope (SEM) images with common fabrication errors. In (a) we depicted the covering ZEP-520A resist on top of the silicon layer. In (c), a common stitching error when changing main fields, generating a source of strong scattering losses.

The resolution does not only depend on the acceleration energy or the main and sub field elections, but also on the resist and the amount of dose of secondary and scattered electrons that the resist can tolerate before being exposed. Finally, the development is made with ZED-N50 during 40 seconds followed by 30 seconds treatment with MIBK and isopropanol and then another 30s with isopropanol. Finally the sample is dried under a nitrogen flow.

Etching

The step e) in Fig 1.15 is as important as the lithographic writing: the feature transfer. Indeed, we should remove the non-protected silicon to obtain the desired depth structures. This removal process is called etching and it can be done in two ways: wet chemical etching (isotropic and very selective if a proper solution is chosen) and dry chemical etching (using reacting gases). We have chosen to etch via ICP (inductively coupled plasma), a highly anisotropic technique where plasma ionizes the SF_6 and C_4F_8. The

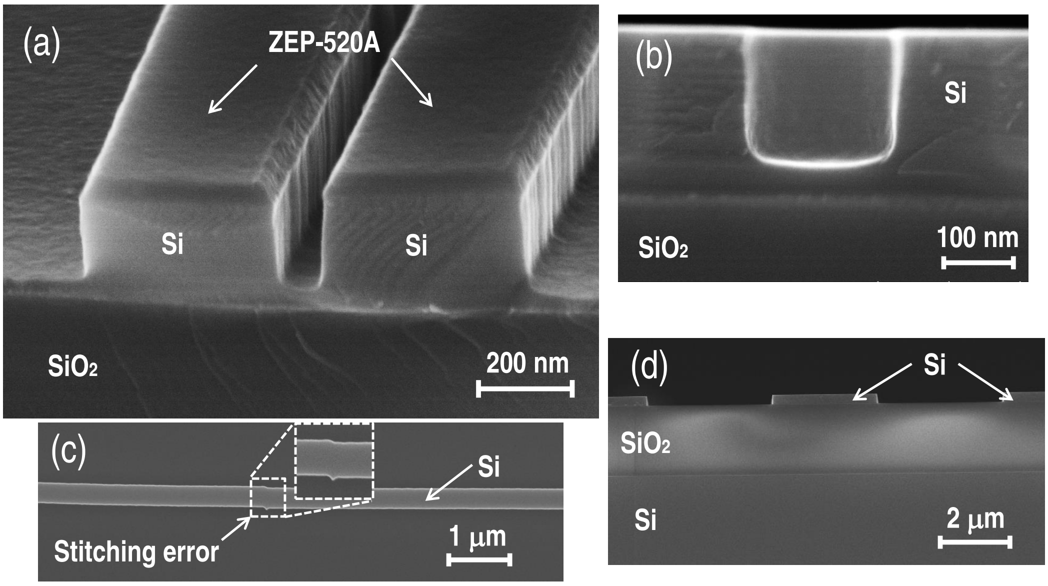

Figure 1.16: Scanning electron microscope (SEM) images to illustrate different fabrication results. (a) Waveguide after etching process and before the cleaning stage (f) from Fig. 1.15, in this case the sample is under-etched. (b) Under-etching of a hole. (c) Typical stitching error from a main field in a strip waveguide with a inset zoom. (d) Properly etched 3 μm width waveguide with an isolation of 3 μm in each side. The 2 μm buried oxide and the silicon under are also clear.

first one produces radicals that react with the material to be removed, forming volatile products and the second creates a film that smooth the etched walls.

The process has been optimized, taking into account the different coils, the injected gas flux and the etching time. As in silicon, we have worked in strip-ridge (not strip-loaded) waveguides, the under-etching could be a problem with respect to the designed structure. Finally, the remaining resist is removed with "piranha" (a halved mix of sulfuric acid and hydrogen peroxide) immersion during 4 hours and a last step of plasma O_2 that removes the thin C_4F_8 film. In Fig. 1.16 (a) and (b), we show an under-etched slot waveguide and photonic crystal hole respectively. It creates imperfections that affect the light propagation and the bandgap in PhC.

As the followed optical injection methodology consists in butt-coupling technique, we have mechanically cleaved the samples by two different approaches: creating a defect that is propagated though the silicon crystallographic axis or by cutting the sample with a diamond saw. The final sample length in the light propagation direction is typically of 5 mm.

1.4.2 Linear optical properties of waveguides with different integrated materials

We have introduced interesting materials that can be exploited in the optical domain around 1550 nm, particularly CMOS compatible compounds. In this section we will introduce some waveguiding structures that can be fabricated in those platforms and particularly the ones that will be characterized in the nonlinear regime. The aim is to briefly explain their linear properties and the fabrication processes performed in our facilities. The photonic and slotted photonic crystal waveguide fabrication will be treated independently in the final chapter as non-conventional procedures were tested.

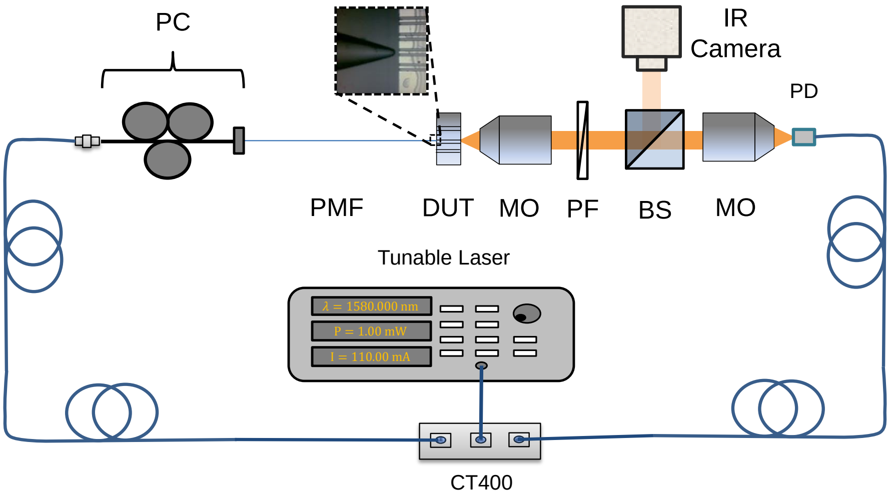

Figure 1.17: Schematics of the linear measurement set-up. CT400: Component Tester, PC: (Fibered) Polarization control, PMF: Polarization maintaining fiber, DUT: Divice under test, MO: Microscope objective, PF: Polarization filter, BS: Beam splitter, PD: Photodetector. A camera view provides the image of the lensed fiber output and the sample.

In Fig. 1.17, we present a schematic drawing of the set-up used for waveguide characterization. By using a component tester CT400 connected to a computer, we can control and collect the transmission over more than 300 nm bandwidth (from 1280 nm until 1640 nm). After the optimization of the set-up, we obtain a transmission without sample (fiber to PD) of around -13 dBm with an injection of 1 mW (0 dBm).

Strip and slot SOI waveguides

We have isolated the guides by 3 μm etching from both sides. The access waveguides have a width of 3 μm (unless specified) to ease the injection and collection from/to objectives or micro-lensed fibers. After, a mode adapter of 300 μm long is added to couple the light in a strip monomode waveguide. In the case of slot waveguides, and additional coupler is required. We will deal with these optimizations in the last chapter. A typical output

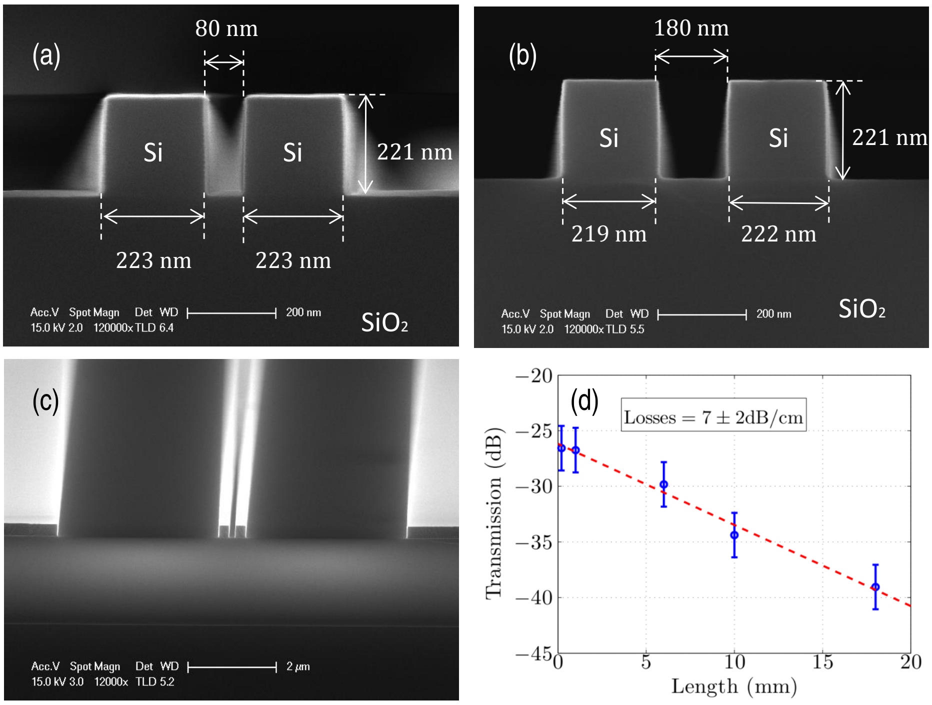

Figure 1.18: (a) and (b) SEM images for 220 nm width slot waveguides. The etching quality could be appreciated. (c) SEM image showing the isolation of the waveguide and the buried box below. (d) Cut back method for waveguides with 80 nm slot width (a), calculated at 1530 nm [40].

power value of a monomode strip waveguide after propagation through all the set-up components is of around -33 dBm (We recall that the reference transmission without sample is of around -13dBm). By using the cut-back method, we have found typical losses of 2-3 dB/cm of the TE mode.

Considering a total length of 5 mm and assuming that both facets have around the same coupling efficiency, we can have an order of magnitude of the efficiencies that we will be dealing with, in both the linear and nonlinear regime. The coupling losses are estimated around 10 dB losses per facet, meaning injection and collection efficiencies are in the order of 10%.

In Fig. 1.18, we show different SEM images of fabricated slot waveguide cross sections in 220 nm Si thickness platform. We highlight the etching quality for different slot sizes as depicted in (a) and (b). The targeted slot rails were 220 nm × 220 nm, so the fabrication process is properly calibrated. In (c), we show the waveguide isolation and in (d) the cut-back method is applied to waveguides with slot size of 80 nm. The transmission measurement for different lengths allows the estimation of the losses from the slope.

Slot Width [nm]	Losses at 1530 nm [dB/cm]
80 ± 10	7 ± 2
130 ± 10	8 ± 2
180 ± 10	15 ± 1

Table 1.3: Summary of waveguide losses for three different slot widths at 220 nm height and applying the cut-back method considering 5 lengths filled with a liquid with n=1.45.

After applying the cut-back method to different slot width waveguides we have obtained typical propagation losses given in table 1.3. These values remain acceptable, taking into account that not further optimization was performed, i.e. oxidation and removal or coating by atomic layer deposition to decrease the wall roughness [41].

Silicon-Germanium

SOI technology is in the core of on-chip applications targeting mass production. Nevertheless, Germanium is also an interesting material for integrated proposes. It has been extensively used due to its reliable properties to develop Si integrated photonic circuits. Both Si and Ge exhibit large third order nonlinear susceptibilities, so they are interesting for all-optical functionalities exploiting small confinement areas. Nevertheless, Ge has gap properties that discourage its use as waveguiding structure at 1550 nm. However, it has been exploited in applications to realize light sources [42, 43], modulators [44, 45] and photodetectors [46, 47]. It is interesting to tune the energetic properties of Si and Ge by fabricating devices with $\mathrm{Si}_{1-\mathrm{x}}\mathrm{Ge}_{\mathrm{x}}$ alloys [48]. In particular Ge rich $\mathrm{Si}_{1-\mathrm{x}}\mathrm{Ge}_{\mathrm{x}}$ (x>70%) waveguides have not been experimentally explored in the nonlinear regime. Taking into account that both materials exhibit large n_2 coefficients, it is interesting to characterize their alloys and explore potential applications in different frequency bands.

Ge and $\mathrm{Si}_{1-\mathrm{x}}\mathrm{Ge}_{\mathrm{x}}$ alloy are group IV materials (see Fig. 1.14) which structure is organized as a diamond crystal. In the alloy case, the repartition of Si and Ge atoms is homogeneous but random by respecting the crystal stoichiometry, so there are no preferential planes [49].

For a $\mathrm{Si}_{1-\mathrm{x}}\mathrm{Ge}_{\mathrm{x}}$ alloy, the evolution of the energy bands has been experimentally evaluated by Weber et al. [50] and gives an interesting point at around 85 % Ge concentration. For smaller concentrations, the minimum of the conduction band is located in the valley X, after overpassing this critical point, the minimum will be in the valley L. The underwritten analytical expressions are deduced from the experimental data:

$$E_{\mathrm{g,ind}}^{\Gamma\Delta} = 1.155 - 0.43x + 0.206x^2 (\mathrm{eV}) \qquad \text{for } x < 0.85 \tag{1.44}$$

$$E_{\mathrm{g,ind}}^{\Gamma L} = 2.010 - 1.270x(\mathrm{eV}) \qquad \text{for } x > 0.85 \tag{1.45}$$

Instead, the direct energy gap follows a linear energetic decrease from the value of the direct energy gap of silicon ($E_{\mathrm{g,dir}}^{Si}$ ∼4.1 eV) towards the direct energy gap of germanium ($E_{\mathrm{g,dir}}^{Ge}$ ∼0.8 eV)[50]:

$$E_{\mathrm{g,dir}} = 4.185 - 3.296x(\mathrm{eV}) \tag{1.46}$$

In Fig. 1.19, we plot the expected evolution of the bandgap energy for the direct and indirect gap as a function of different Ge concentrations. We show in the right vertical axis the corresponding wavelength. In Fig. 1.20, we show the absorption properties reported in Ref. [51] for rich Ge (x>64%) SiGe alloys in bulk. It should be noticed that when the concentration is closer to pure germanium (0% Si), the losses increases by orders of magnitudes for wavelengths around $\lambda \sim 1550$ nm.

From theoretical predictions, as closer the wavelength is to the bandgap, the larger is the third order susceptibility. So in our group MINAPHOT, Dr. Delphine Marris-Morini has led efforts to develop a platform of Ge-rich $\mathrm{Si_{1-x}Ge_x}$ [48]. Using wafers grown by a collaborative group of L-NESS from the Politechnico di Milano (Prof. G. Isella), my colleague V. Vakarin has fabricated diverse ridge waveguides with different widths that will be characterized in the nonlinear regime.

In Fig. 1.21, we present the general form of the buffer. Light is vertically confined in a 2 μm-thick relaxed $\mathrm{Si_{1-x}Ge_x}$ layer on top of a graded buffer that begins with a Si wafer up to a layer of $\mathrm{Si_{1.01-x}Ge_{x-0.01}}$. The Ge concentration x of the graded buffer is linearly increased from 0 (Si wafer) up to x − 0.01 over a thickness of 11μm. The linear refractive

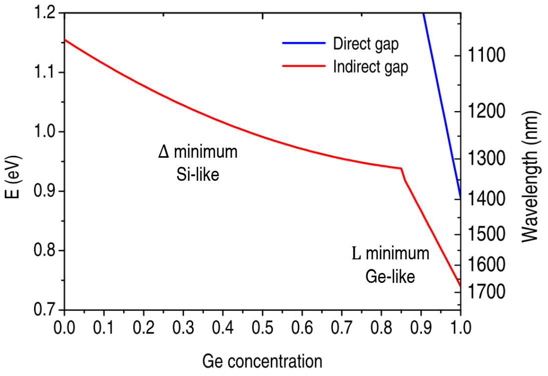

Figure 1.19: Direct and indirect gap evolution for different Ge concentration in the infrared wavelength window.

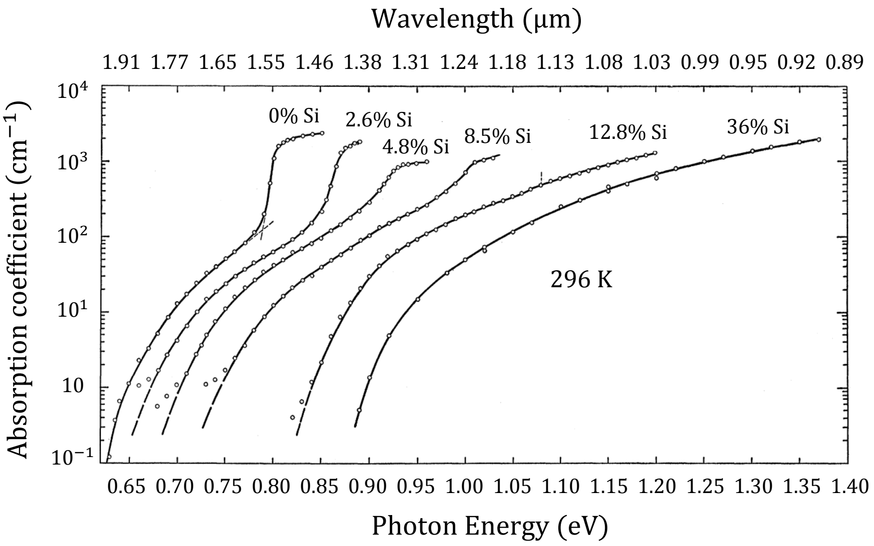

Figure 1.20: Intrinsic absorption spectra in a series of Ge-rich Ge-Si alloys at 296 K. Figure adapted from [51].

index variation is estimated by linearly interpolating the proportions of Si and Ge. We have considered refractive indices for Si and Ge at a wavelength of 1.55 μm: 3.48 and 4.28 respectively.

Low energy plasma enhanced chemical vapor deposition (LEPECVD) was used for the growth of the SiGe stack. Patterning was made by deep UV lithography followed by inductive plasma (ICP) etching set to 1 μm to fabricate rib waveguides [52]. In Fig. 1.21, we show a scheme with the described dimensions. To limit the sidewall roughness

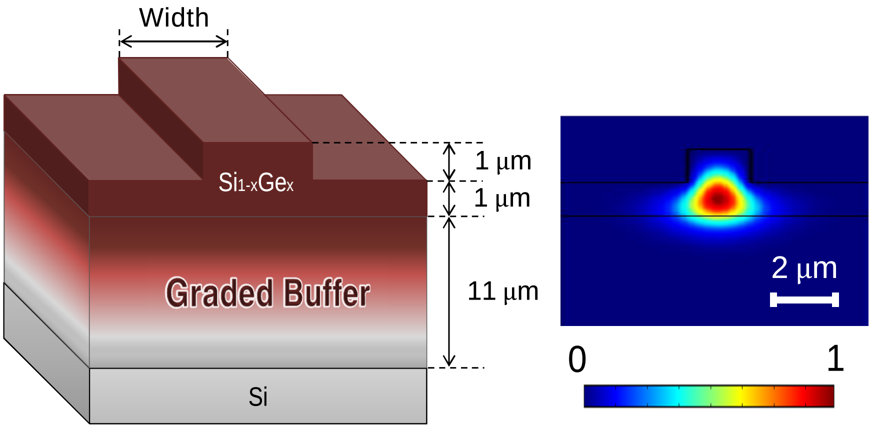

Figure 1.21: Left: $Si_{1-x}Ge_x$ rib waveguides $Si_{1-x}Ge_x$ with 1μm etching. The graded buffer has a total thickness of 11μm. Right: Normalized fundamental TE mode profile for a 1.6 μm width ridge waveguide for $x = 0.80$ ($Si_{0.20}Ge_{0.80}$) at 1550 nm.

post treatment with hydrogen peroxide (H_2O_2) was performed. Finally, a diamond saw cutting allowed to obtain devices of around 7 mm long. In the sample, three series of identical waveguides were fabricated by changing the width. We have focused on TE monomode waveguides, corresponding to widths between 1.4 μm and 4 μm. In particular for the nonlinear comparison, 1.6 μm will be privileged. In Fig. 1.21 right, we show the fundamental TE mode for a $Si_{0.20}Ge_{0.80}$ ridge waveguide with the chosen width at a wavelength of $\lambda = 1550$ nm.

In accordance with the dependence of the absorption coefficient with Ge concentration shown in Fig. 1.20, the waveguide propagation loss varies with the Ge quantity present in the sample. For higher concentrations, the losses are larger. Using the cut-back method, waveguide propagation losses around $\lambda \sim 1550$ nm have been estimated to 8-12 dB/cm for a 70% Ge concentration, 10-16 dB/cm for a 80% and 20-26 dB/cm for a 90%.

Chalcogenide

Apart of Si and Ge, other materials are interesting for hybrid waveguide applications. In this chapter we will introduce a particular kind of chalcogenide which are a class of amorphous semiconductors. Chalcogenide glasses have been used for waveguiding proposes since long ago, first in fibers and later on in integrated platforms [53]. They are based on the chalcogen elements S, Se, and Te; then the glasses are formed with the addition of other elements such as Ge, Sb or As. They exhibit interesting properties such as the ability to switch between states making them suitable for optical memory proposes, a large variety of third order nonlinear figure of merits depending on the particular composition, low-phonon-energy materials and broad transparency in the visible and infrared wavelengths. Therefore, they could be used for all-optical functionalities and will be a part of study in this manuscript.

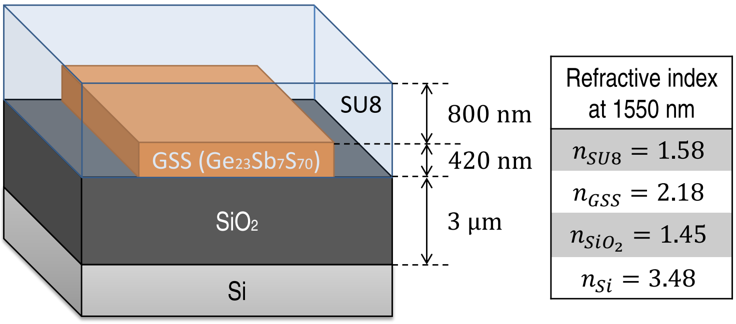

Figure 1.22: Index and layer thickness of the different layers of GSS chalcogenide on insulator.

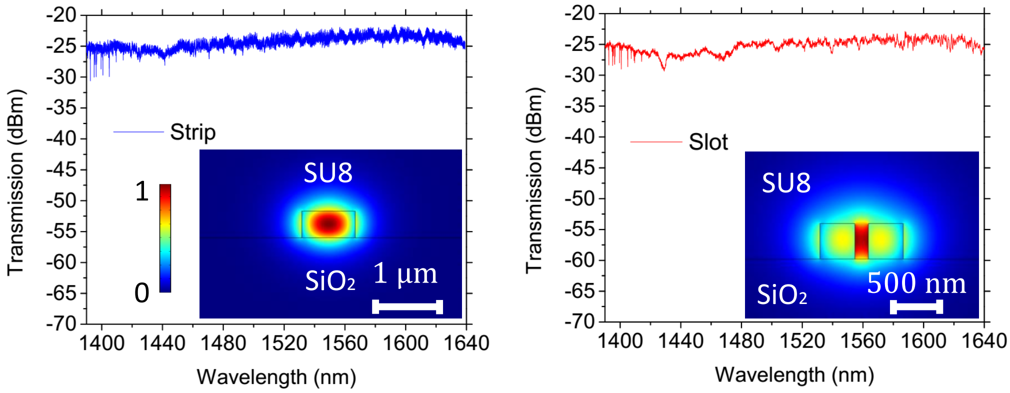

Figure 1.23: Broadband linear transmission of a strip and slot chalcogenide waveguides. The insets display the mode at 1580 nm. The optical transmission level corresponds to the measured values from fiber to fiber (in all the set-up).

In a collaboration with the research group in glass for advance photonics from MIT, we have characterized GSS ($Ge_{23}Sb_7S_{70}$) chalcogenide waveguides in the near infrared. The partner group is specialized in glasses for midIR applications and flexible photonics [54]. In Fig. 1.22, we depict a schematics with the size and refractive indices of the platform. The chalcogenide is deposited by evaporation on an oxide coated silicon wafer and patterned using UV contact lithography. Finally, SU-8 polymer is spin-coated on the wafer. After some simulations, given the index maps of the structures, we have provided the .gds masks to be used in the fabrication made by Prof. Juejun Hu MIT-group. The specific details on the material and fabrication flow could be find in Ref. [55]. The collaborators have sent the samples that were used to measure the real and imaginary third order susceptibilities. Several structures have been fabricated to be butt-coupled, among them, different strip waveguides in the monomode regime around 1580 nm, varying the width from 500 nm until 1000 nm. In order to check the influence on different confinement modes, we have also fabricated several slot waveguides, so, in principle, as a large part of the mode is expected to be confined in the SU8 layer, the measured nonlinearity should decrease.

In Fig. 1.23 we show the measured transmission for strip and slot chalcogenide waveguides and their respective calculated TE mode profiles. It is noteworthy that the index contrast and fabrication quality allows a low loss mode propagation over the 5 mm length of the waveguides and in a large wavelength band.

Silicon nitride

Finally, we have fabricated waveguides in silicon nitride as it has been extensively used in integrated optics, we will characterize the nonlinear response of waveguides around 1580 nm where nitride does not present TPA.

The use of stoichiometric silicon nitride (Si_3N_4) as a waveguiding material on silicon oxide has attracted a lot of attention in recent years. Among others, due to the low scattering losses, the wide transparency window, and the compatibility with Si microelectronic technology. During this work we have started using this material, so the wafer and machines calibration were required. Even though the e-beam, resist thickness and etching times are different from Si, the fabrication steps and physical principles behind remain the same.

The optical properties of silicon nitride for manufacturing proposes are less well known than for SiO_2 and Si, so we have performed some ellipsometric and SEM measurements to determine the refractive index and the slab thickness. Rather than absorption from the bulk, surface roughness is the main source of losses of Si_3N_4 therefore enabling a path for achieving ultra low loss devices by simply addressing surface quality. Absorption loss is mainly due to O-H bonds in SiO_2, and N-H and Si-H bonds in Si_3N_4. Scattering loss comes primarily from the interaction of light with the roughness of all the surfaces in a high confinement waveguide.

Due to a lower index compared to silicon and negligible TPA nonlinear losses around 1550 nm (generally the bandgap between 4.5 and 5 eV depends on deposition conditions[56]), silicon nitride has become an interesting material for linear and nonlinear integrated functionalities. For instance a non-volatile all optical memory has been demonstrated with nitride as host [57]. Regarding its nonlinear properties, we will measure and establish

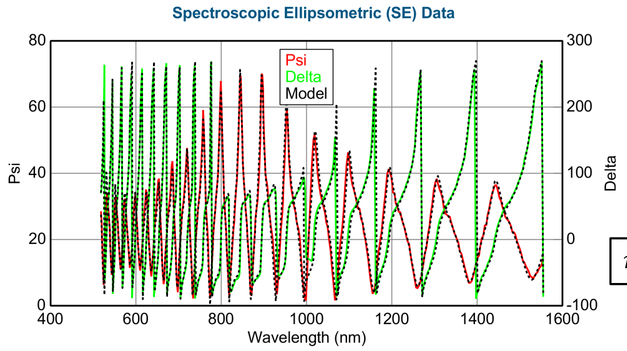

$$n(\lambda) = A + \frac{B}{\lambda^2} + \frac{C}{\lambda^4}$$

$$\text{with } A = 1.975 \pm 0.0105$$
$$B = 0.147 \pm 0.008$$
$$C = -0.021 \pm 0.002$$

$$\boxed{n_{Si_3N_4}(@1580\text{nm}) = 1.98 \pm 0.01}$$

Figure 1.24: Ellipsometric measurement of the nitride wafer. Next, the Cauchy parameters with the given uncertainties after the data analysis and the calculated refractive index at 1580 nm. The refractive index should be calculated with λ in Angström.

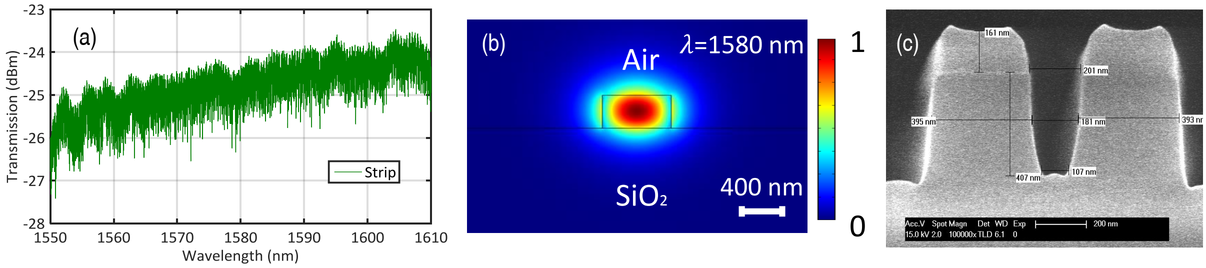

Figure 1.25: (a) Optical transmission of a strip nitride waveguide with 407 nm x 800 nm. (b) Simulation of the mode for an index map corresponding to the strip waveguide (400 nm x 800 nm). (c) Etching test of a nitride slot waveguide, the thickness is estimated at around 407 nm.

the potentialities of nitride. Fig 1.24 shows the ellipsometric measurement of the nitride waveguide with an index of 1.98±0.01 at 1580 nm in extremely good accordance with literature values.

In Fig. 1.25, we show the transmission and TE fundamental mode of a strip silicon nitride waveguide. In (c) we show an SEM image of a testing structure to calibrate the fabrication. Some missing resist could be appreciated at the top, the shape showing that the process is good but still to be optimized. The transmission level ($\sim$ -25 dBm) shows a proper injection of light and low propagation losses around the wavelengths that we will use in the nonlinear regime. The propagation losses are estimated to be around 1-2 dB/cm and, as the index is lower than Silicon, the losses per facet are of 5-6 dB. This will improve the injection efficiency for the nonlinear regime.

1.5 Vectorial Nonlinear wave equation

As explained in previous sections, optical nanostructures offer the possibility of engineering diverse properties, allowing the structure optimization for given effects in specific spectral bandwidths. This engineering process is mainly governed by the geometry and its related refractive index structure. This will determine the fabrication requirements and the guiding properties.

Regarding the nonlinear performance, the equations given at the beginning of this manuscript are valid for low index contrast structures, for instance, silica optical fibers, where the nonlinear susceptibility is constant over the entire cross-section, so the assumption $\vec{\nabla} \cdot \vec{\mathscr{E}}(\vec{r},t) = \varepsilon \nabla \cdot \vec{\mathscr{D}}(\vec{r},t) = 0$ remains valid. Nevertheless, in high index contrast structures such as those of integrated optics, this approximation is not valid and a vectorial derivation is required.

In this section we will introduce the parameters to be used, particularly to be determined experimentally, such as the real and imaginary γ effective nonlinear parameters, the effective lengths and the effective area. This will be a robust platform to compare the performance of different structures and the case of hybrid waveguides where only parts of the cross section are nonlinear or have different nonlinearities.

We will assume that the field is composed only by guided modes, neglecting the existence of radiative mode fields. The electric and magnetic fields can be expressed as a superposition of guided modes.

$$\vec{\mathscr{E}}\left(\vec{r}_\perp, z, t\right) = \frac{1}{2}\sum_{p,\omega}\left[\vec{E}_p\left(\vec{r}_\perp, z, \omega\right)e^{-i\omega t} + c.c.\right] \tag{1.47}$$

$$\vec{\mathscr{H}}\left(\vec{r}_\perp, z, t\right) = \frac{1}{2}\sum_{p,\omega}\left[\vec{H}_p\left(\vec{r}_\perp, z, \omega\right)e^{-i\omega t} + c.c.\right] \tag{1.48}$$

where *c.c.* stands for complex conjugation. The sum is made over a discrete number of frequencies corresponding to a finite normalization "volume" T in the temporal domain [58]. By considering only the forward propagating modes (unidirectional pulse propagation [59]), one can express each field components as:

$$\vec{E}_p\left(\vec{r}_\perp, z, \omega\right) = a_p\left(z, \omega\right)\vec{e}_p\left(\vec{r}_\perp, \omega\right)e^{i\beta_p(\omega)z} \tag{1.49}$$

$$\vec{H}_p\left(\vec{r}_\perp, z, \omega\right) = a_p\left(z, \omega\right)\vec{h}_p\left(\vec{r}_\perp, \omega\right)e^{i\beta_p(\omega)z} \tag{1.50}$$

where $\beta_p(\omega)$ corresponds to the propagation constant at the frequency ω. The power of a given mode p measured at the output of the waveguide is set to $P_p(z \mapsto \infty, \omega) = \left|a_p(z \mapsto \infty, \omega)\right|^2$. So, to fulfill this relation, we introduce orthonormal modes by calculating the power flow for one specific mode [7].

$$\begin{aligned} P_p(z,\omega) &= \frac{1}{2}\int\int_{-\infty}^{+\infty} \mathbb{R}\mathrm{e}\left[\vec{E}_p \times \vec{H}_p^*\right]\cdot \vec{z}\, d^2r \\ &= \frac{\left|a_p(z,\omega)\right|^2}{2}\int\int_{-\infty}^{+\infty} \mathbb{R}\mathrm{e}\left[\vec{e}_p \times \vec{h}_p^*\right]\cdot \vec{z}\, d^2r = \left|a_p(z,\omega)\right|^2 \mathscr{N}_p \end{aligned} \tag{1.51}$$

Where $\mathscr{N}_p$ is a normalization factor. Therefore, we can introduce an orthonormal set of eigensolutions for our problem:

$$\hat{e}_p = \frac{\vec{e}_p}{\sqrt{\mathscr{N}_p}}, \qquad \hat{h}_p = \frac{\vec{h}_p}{\sqrt{\mathscr{N}_p}} \tag{1.52}$$

Then, the general orthonormality condition for two forward propagating modes is:

$$\int\int_{-\infty}^{+\infty} \mathbb{R}\mathrm{e}\left[\hat{e}_p \times \hat{h}_r^* - \hat{h}_p \times \hat{e}_r^*\right] \cdot \vec{z}\; d^2r = 2\delta_{p,r} \tag{1.53}$$

with $\delta_{p,r}$ equals to 1 if $p = r$ and 0 otherwise. Now, taking into account the presence of a nonlinear source term along the waveguide, and assuming that this source is weak enough to still consider $\hat{e}_p$ and $\hat{h}_p$ as a set of orthonormal modes of the waveguide in the nonlinear regime, we have to assume that the modal power (or the power flow carried by each mode) may vary with z.

$$\vec{E}(\vec{r}_\perp, z, \omega) = \sum_{p,\omega} a_p(z)\hat{e}_p(\vec{r}_\perp, \omega)e^{i\beta_p(\omega)z} = \sum_{p,\omega} \phi_p(z,\omega)\hat{e}_p(\vec{r}_\perp, \omega) \tag{1.54}$$

$$\vec{H}(\vec{r}_\perp, z, \omega) = \sum_{p,\omega} a_p(z)\hat{h}_p(\vec{r}_\perp, \omega)e^{i\beta_p(\omega)z} = \sum_{p,\omega} \phi_p(z,\omega)\hat{h}_p(\vec{r}_\perp, \omega) \tag{1.55}$$

The nonlinear wave equation can be derived from the linear one by adding a polarization term as already shown at the beginning of the chapter. Starting from Maxwell's equations in frequency domain and considering a high-index contrast propagating media:

$$\vec{\nabla} \times \vec{E}\left(\vec{r}_\perp, z, \omega\right) = i\omega\mu_0\vec{H}\left(\vec{r}_\perp, z, \omega\right) \tag{1.56}$$

$$\vec{\nabla} \times \vec{H}\left(\vec{r}_\perp, z, \omega\right) = -i\omega\left(\varepsilon_0\varepsilon(\vec{r}_\perp, \omega)\vec{E}\left(\vec{r}_\perp, z, \omega\right) + \vec{P}_{NL}\left(\vec{r}_\perp, z, \omega\right)\right) \tag{1.57}$$

Using a set of solutions for the unperturbed system ($\vec{P}_{NL} = 0$):

$$\vec{\nabla} \times \vec{H}(\vec{r}_\perp, z, \omega) = \sum_p \vec{\nabla} \times \left(\phi_p(z,\omega)\hat{h}_p(\vec{r}_\perp, \omega)\right) = \frac{1}{2}\sum_p \phi_p\left(\vec{\nabla} \times \hat{h}_p\right) + \vec{\nabla}(\phi_p) \times \hat{h}_p \tag{1.58}$$

Knowing that

$$\vec{\nabla}(\phi_p) = \nabla_z(\phi_p)\vec{z} = i\beta_p\phi_p\vec{z} \tag{1.59}$$

and using the expression (1.57):

$$\phi_p\left(\vec{\nabla} \times \hat{h}_p\right) + i\beta_p\phi_p\vec{z} \times \hat{h}_p = -i\omega\varepsilon_0\varepsilon\phi_p\hat{e}_p \Longrightarrow \left(\vec{\nabla} \times \hat{h}_p\right) + i\beta_p\vec{z} \times \hat{h}_p = -i\omega\varepsilon_0\varepsilon\hat{e}_p \tag{1.60}$$

And analogously for (1.56):

$$\left(\vec{\nabla}\times\hat{e}_p\right)+i\beta_p\vec{z}\times\hat{e}_p=i\omega\mu_0\hat{h}_p \tag{1.61}$$

Now, we will find a nonlinear wave equation via a perturbative approach ($\vec{P}_{NL}\neq 0$). Taking into account the dispersion: $\beta_p(\omega)=\beta_p^{(0)}+\Delta\omega\beta_p^{(1)}+\frac{\Delta\omega^2}{2}\beta_p^{(2)}+\cdots$ and the z dependence of the field amplitude term $a_p(z)$, meaning that:

$$\vec{\nabla}(\phi_p)=i\beta_p(\omega)\phi_p\vec{z}+\frac{\partial a_p}{\partial z}\exp\left(i\beta_p(\omega)z\right)\vec{z} \tag{1.62}$$

We can re-write the expressions (1.60) and (1.61) after a scalar product with $\hat{e_p^*}$ and $\hat{h_p^*}$:

$$\sum_p\left[\frac{\partial a_p}{\partial z}+i\Delta\omega\beta_p^{(1)}a_p+i\frac{\Delta\omega^2}{2}\beta_p^{(2)}a_p\right](\vec{z}\times\hat{h}_p)\cdot\hat{e_p^*}=-i\omega\exp\left(-i\beta_p(\omega)z\right)\vec{P}_{NL}\cdot\hat{e_p^*} \tag{1.63}$$

$$\sum_p\left[\frac{\partial a_p}{\partial z}+i\Delta\omega\beta_p^{(1)}a_p+i\frac{\Delta\omega^2}{2}\beta_p^{(2)}a_p\right](\vec{z}\times\hat{e}_p)\cdot\hat{h_p^*}=0 \tag{1.64}$$

where $(\vec{z}\times\hat{h}_p)\cdot\hat{e_p^*}=-\vec{z}\cdot(\hat{e_p^*}\times\hat{h}_p)$ and $(\vec{z}\times\hat{e}_p)\cdot\hat{h_p^*}=\vec{z}\cdot(\hat{e}_p\times\hat{h_p^*})$, so by adding these last two expressions and integrating over the waveguide cross-section:

$$\begin{aligned}\left[\frac{\partial a_p}{\partial z}+i\Delta\omega\beta_p^{(1)}a_p+i\frac{\Delta\omega^2}{2}\beta_p^{(2)}a_p\right]&\int\!\!\int[(\hat{e_p^*}\times\hat{h}_p)+(\hat{e_p}\times\hat{h}_p^*)]\cdot\vec{z}\;d^2\vec{r}\\&=+i\omega e^{-i\beta_p(\omega)z}\int\!\!\int\vec{P}_{NL}\cdot\hat{e_p^*}d^2\vec{r}\end{aligned} \tag{1.65}$$

$$\begin{aligned}\left[\frac{\partial a_p}{\partial z}+i\Delta\omega\beta_p^{(1)}a_p+i\frac{\Delta\omega^2}{2}\beta_p^{(2)}a_p\right]&\underbrace{\frac{1}{2}\int\!\!\int\mathbb{R}\mathrm{e}(\hat{e}_p\times\hat{h}_p^*)\cdot\vec{z}\;d^2\vec{r}}_{1}\\&=+i\omega\frac{e^{-i\beta_p(\omega)z}}{4}\int\!\!\int\vec{P}_{NL}\cdot\hat{e_p^*}d^2\vec{r}\end{aligned} \tag{1.66}$$

$$\boxed{\frac{\partial a_p}{\partial z}+i\Delta\omega\beta_p^{(1)}a_p+i\frac{\Delta\omega^2}{2}\beta_p^{(2)}a_p=+i\omega\frac{e^{-i\beta_p(\omega)z}}{4}\int\!\!\int\vec{P}_{NL}\cdot\hat{e}_p^*d^2\vec{r}} \tag{1.67}$$

This is the nonlinear vectorial propagation equation. Now, we can use this expression to find the different parameters to be measured afterwards with a clear meaning regarding the mode and material properties. We will consider non-crossed effects even though their inclusion in the calculation is straight forward.

The nonlinear polarization could be written as:

$$\vec{P}_{NL}(\vec{r},\omega) = \frac{3}{4}\varepsilon_0 \chi^{(3)} \vec{E}_p(\omega)\vec{E}_p(-\omega)\vec{E}_p(\omega) = \frac{3}{4}\varepsilon_0 \chi^{(3)} |a_p|^2 a_p \hat{e}_p \hat{e}_p^* \hat{e}_p e^{i\beta(\omega)z} \tag{1.68}$$

So, the propagation equation (1.67) ignoring the dispersion terms reads:

$$\frac{\partial a_p}{\partial z} = +i\omega \frac{3\varepsilon_0}{16} |a_p|^2 a_p \int\int \chi^{(3)} \hat{e}_p \hat{e}_p^* \hat{e}_p \hat{e}_p^* d^2\vec{r} \tag{1.69}$$

Next, we will consider $\chi^{(3)}$ homogeneous and scalar in each integration section (in particular, the waveguide material). And recalling that $\hat{e}_p = \vec{e}_p / \sqrt{\mathcal{N}_p}$:

$$\frac{\partial a_p}{\partial z} = +i\omega \frac{3\varepsilon_0}{16} \chi^{(3)} |a_p|^2 a_p \frac{\int\int_{S_{NL}} |\vec{e}_p|^4 \ d^2\vec{r}}{\left(\frac{1}{2}\int\int \mathbb{Re}\left[\vec{e}_p \times \vec{h}_p^*\right] \cdot \vec{z} \ d^2\vec{r}\right)^2} \tag{1.70}$$

We can decompose the envelope expression in terms of amplitude and phase: $a_p = \sqrt{P_p} e^{i\phi_p}$, so its derivative is given by: $\frac{\partial a_p}{\partial z} = \left[\frac{1}{2\sqrt{P_p}}\frac{\partial P_p}{\partial z} + i\sqrt{P_p}\frac{\partial \phi_p}{\partial z}\right] e^{i\phi_p}$, we can write the real and the imaginary part in the expression (1.70) independently, by using $\chi^{(3)} = f^4 \chi^{(3)}_{\text{mat}} = S^2 \mathbb{Re}[\chi^{(3)}_{\text{mat}}] + i \ S^2 \mathbb{Im}[\chi^{(3)}_{\text{mat}}] = S^2 \chi^{(3)'}_{\text{mat}} + i \ S^2 \chi^{(3)''}_{\text{mat}}$. First for the real part (that will correspond to the imaginary part of the susceptibility):

$$\frac{1}{2\sqrt{P_p}}\frac{\partial P_p}{\partial z} = -\omega S^2 \frac{3\varepsilon_0}{16} \mathbb{Im}[\chi^{(3)}] P_p \sqrt{P_p} \frac{\int\int_{S_{NL}} |\vec{e}_p|^4 \ d^2\vec{r}}{\left(\frac{1}{2}\int\int \mathbb{Re}\left[\vec{e}_p \times \vec{h}_p^*\right] \cdot \vec{z} \ d^2\vec{r}\right)^2} \tag{1.71}$$

$$\begin{aligned} \frac{\partial P_p}{\partial z} &= -S^2 \omega \frac{3\varepsilon_0}{2} \mathbb{Im}[\chi^{(3)}_{\text{mat}}] \frac{\int\int_{S_{NL}} |\vec{e}_p|^4 \ d^2\vec{r}}{\left(\int\int \mathbb{Re}\left[\vec{e}_p \times \vec{h}_p^*\right] \cdot \vec{z} \ d^2\vec{r}\right)^2} P_p^2 \\ &= -S^2 \underbrace{\frac{3\omega}{2\varepsilon_0 c^2 n_0^2} \mathbb{Im}[\chi^{(3)}_{\text{mat}}]}_{\beta_{\text{TPA}}} \underbrace{\varepsilon_0^2 c^2 n_0^2 \frac{\int\int_{S_{NL}} |\vec{e}_p|^4 \ d^2\vec{r}}{\left(\int\int \mathbb{Re}\left[\vec{e}_p \times \vec{h}_p^*\right] \cdot \vec{z} \ d^2\vec{r}\right)^2}}_{\frac{1}{A_{NL}}} P_p^2 \qquad (1.72) \\ &= -\frac{S^2 \beta_{\text{TPA}}}{A_{NL}} P_p^2 = -\gamma_{\text{TPA}}^{wg} P_p^2 \end{aligned}$$

So, we have found valid expressions for high index contrast structures for the nonlinear effective area and the β_{TPA} coefficient. Finally, for the imaginary part (corresponding to the real part of the susceptibility):

$$\begin{aligned}\frac{\partial \phi_p}{\partial z} &= S^2 \omega \frac{3\varepsilon_0}{4} \mathbb{R}\mathrm{e}[\chi^{(3)}_{\mathrm{mat}}] \frac{\int\int_{S_{NL}} |\vec{e}_p|^4 \ d^2\vec{r}}{\left(\int\int \mathbb{R}\mathrm{e}\left[\vec{e}_p \times \vec{h}^*_p\right] \cdot \vec{z}\ d^2\vec{r}\right)^2} P_p \\ &= S^2 k_0 \underbrace{\frac{3}{4\varepsilon_0 n_0^2 c} \mathbb{R}\mathrm{e}[\chi^{(3)}_{\mathrm{mat}}]}_{n_2} \underbrace{\varepsilon_0^2 c^2 n_0^2 \frac{\int\int_{S_{NL}} |\vec{e}_p|^4 \ d^2\vec{r}}{\left(\int\int \mathbb{R}\mathrm{e}\left[\vec{e}_p \times \vec{h}^*_p\right] \cdot \vec{z}\ d^2\vec{r}\right)^2}}_{\frac{1}{A_{NL}}} P_p \\ &= \frac{S^2 k_0 n_2}{A_{NL}} P_p = \gamma^{wg} P_p\end{aligned} \tag{1.73}$$

Finally we will introduce a figure of merit that will take into account the nonlinear losses and the kerr effect, either in the waveguide (taking into account the slowing down factor and the effective area) or in the bulk material:

$$\boxed{FOM_{\mathrm{TPA}} = \frac{|\gamma^{wg}|}{2\pi \gamma^{wg}_{\mathrm{TPA}}}} \tag{1.74}$$

This relation is valid for waveguides. If we assume the same material over the effective area, we retrieve the classical third order figure of merit for bulk materials:

$$\boxed{FOM_{\mathrm{TPA}} = \frac{|\mathbb{R}\mathrm{e}[\chi^{(3)}_{\mathrm{mat}}]|}{4\pi \mathbb{I}\mathrm{m}[\chi^{(3)}_{\mathrm{mat}}]} = \frac{|n_2|}{\lambda_0 \beta_{\mathrm{TPA}}}} \tag{1.75}$$

This definition has been made based on 2π generated nonlinear phase shift. Hence $|\phi^{crit}_{NL}| = 2\pi = S^2 k_0 |n_2| I^{crit}_0 L_{\mathrm{eff}}$, but the required intensity will also generate proportional nonlinear losses. So, we define a general criterion for avoiding large losses such that $S^2 \beta_{\mathrm{TPA}} I^{crit}_0 L_{\mathrm{eff}} < 1$. By combining those two relations, we have a figure of merit that is geometry-independent: $\frac{|n_2|}{\lambda_0 \beta_{\mathrm{TPA}}} > 1$. The reader should be aware that this criteria is different by a factor of two from the one proposed by [60] as they have chosen a shift of 4π to characterize a nonlinear material. This other FOM is also used in the literature so, we will pay particular attention when comparing data from the state of the art. Such a difference does not represent a change on the definition of the material properties.

1.6 Characterization methods for nonlinear third order effects

The third order nonlinear properties lead to an interesting variety of phenomena, particularly in integrated optics where an intrinsic small area of interaction and strong confinements are possible. These effects can be also used inversely to measure the nonlinear parameters of a given waveguiding structure, not just the bulk. In most of the relations hereafter and above, the linear properties of the devices such as the refractive index, waveguide dispersion or propagation losses should be also known by means of linear measurement methods.

In the nonlinear regime new materials are being engineered, under such context, a proper technique to measure the optical nonlinearities is required for systematic material optimization [61], particularly when considering optical waveguides, where **effective nonlinearities depend not only in the $\chi^{(3)}$ values of the bulk material but also in the confinement properties**. Among the techniques for characterizing nonlinear materials the most common ones are:

1) Z- Scan
2) Degenerate four wave mixing (DFWM)
3) Interferometric methods
4) Third harmonic generation (THG)
5) Nonlinear absorption - 1/T technique

Z-Scan

Among the techniques for measuring the effective complex third-order nonlinearities, one of the simplest and preferred by experimentalists is the Z-Scan method[62]. The latter is not only simple in the experiences but also in its interpretation. Z-scan allows to determine, in sign and magnitude, the intensity dependent nonlinear changes in index (Fig. 1.2) and absorption in bulk materials . Its simplest approach (closed aperture) requires for implementation a single beam, a translation stage, a small structure and a far field detector (Fig. 1.26 (a)). The transmittance is determined as a function of the sample position (Z) measured with respect to the focal plane. The induced modifications in the transversal beam profile, by nonlinear absorption and refraction are used to estimate the nonlinear parameters of the sample.

As an example, assume a sample with negative nonlinear refractive index located in a very negative Z position (i.e. close to the lens). In that case, the irradiance is low and the nonlinear induced refractive index change is negligible, so the normalized transmittance remains close to unity near this position (see Fig. 1.26 (b)). As the sample is brought closer to focus, the beam irradiance increases leading to self-defocusing (focusing in the

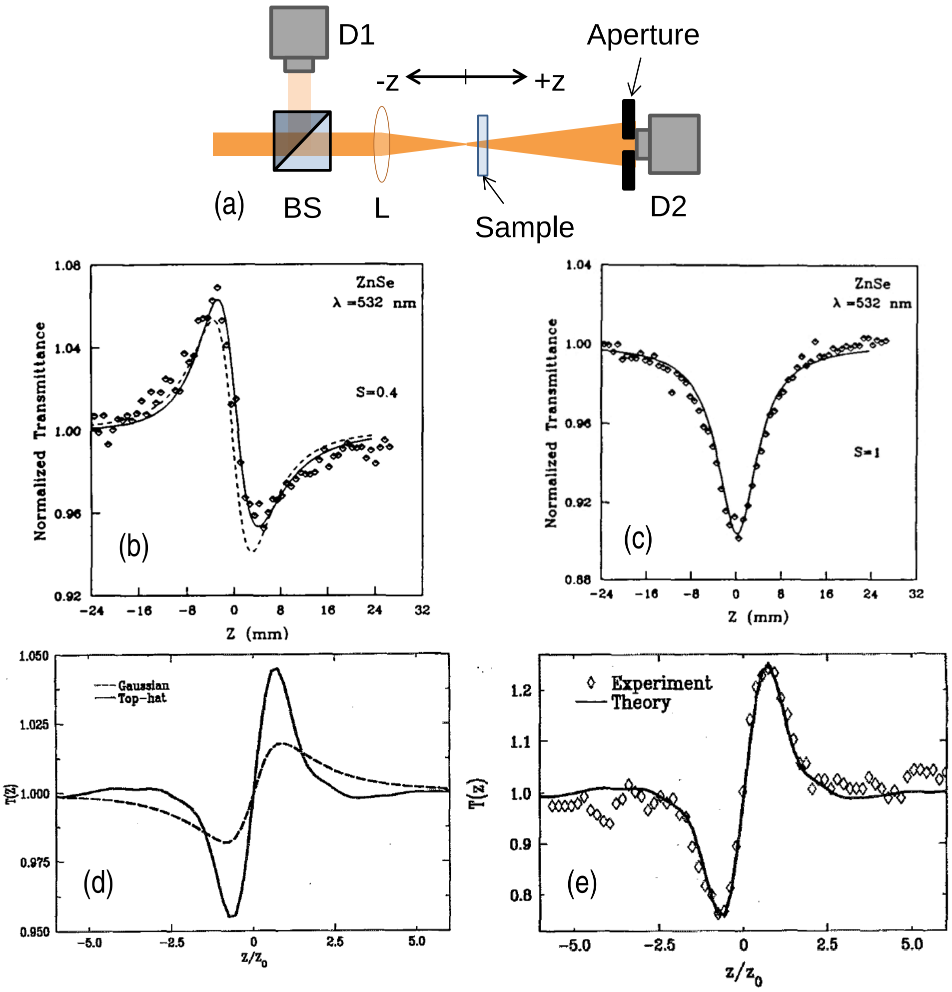

Figure 1.26: (a) Z-scan experimental apparatus in which the ratio D2/D2 is recorded as a function of the sample position z. BS: Beam Splitter, L: Lens, D: detector. (b-c) Normalized Z-scan transmittance of ZnSe measured using picosecond pulses at $\lambda = 532$ nm. The solid lines are the theoretical results. The S factor corresponds to the opening of the aperture, in (b) at 40% and in (c) at 100% (no aperture)[62]. (c-d) Top-hat beams compared to the gaussian counterpart and experimental results for a CS$_2$ sample at S=0.09 at $\lambda = 532$ nm [63].

case of a positive nonlinear refractive index Fig. 1.26 (d)). This negative nonlinear refraction moves the focal point closer to the aperture increasingly collimating the beam and resulting in enhanced transmittance through the aperture. As the sample is moved past the focus, self-defocusing causes greater beam divergence in the far field, though reducing the transmittance through the aperture. Finally, translating the sample further toward the detector reduces the irradiance to the linear regime and returns the normalized transmittance to unity. So if the peak is in the negative distances and the dip in the positive, we can immediately deduce the sign of the Kerr coefficient as negative (Fig.

1.26 (b)). In the positive case, one finds exactly the opposite: a peak in the positive Z and a dip in the negative (Fig. 1.26 (d)).

Now, if we assume that the material presents nonlinear absorption, it has been shown that in Z-Scan measurements two-photon absorption will suppress the peak and enhance the valley of the dispersive curve. If nonlinear absorption and refraction are present simultaneously, a numerical fitting procedure can be used to extract both the nonlinear refractive and absorption coefficients. Alternatively, a second Z-scan with the open aperture, so all the light could be collected, can independently determine the transmittance losses for different irradiances (as a function of the Z position). Considering TPA only, the Z-scan traces out a symmetric Lorentzian shape as the one shown in Fig. 1.26 (c). The nonlinear absorption quantification is possible because we can collect the full pulse energy and detect the output power as a function of the focusing in the sample.

This original approach has been refined by different methods to enhance the sensitivity[64, 65]. This method have also some drawbacks. For instance, as it is sensitive to any nonlinear mechanism, it is rather difficult to identify the particular physical processes that gave rise to the change of the refractive index or the absorption coefficient. Then, series of measurements are required to separate diverse physical mechanisms. The necessary scan range in an experiment depends on experimental factors such as the beam properties (width of the pulse and frequencies) or the sample thickness L. However, the z-scan method is not applicable to optical waveguides, as seen before, the mode remains confined via a fixed refractive index profile.

Top hat Z-Scan

As a particular case of Z-scan and of high importance to this manuscript as a source of analogy, there is the technique called top hat Z-scan. It is base in the same physical principles of Z-scan but the sensitivity is improved due to the use of top-hat (double truncated) beams. As any spectral broadening becomes easier to measure, sensitivity can be improved by a factor of 2.5 compared to the gaussian beam counterpart [63, 66]. In Fig. 1.26 (d), we show a comparison between two dispersion traces, one for a gaussian beam and the other for top-hat beams for the same conditions. The contrast between peak and valley allow an easier quantification of the nonlinear phase shift.

Four wave mixing (FWM)

The wave mixing techniques are pump-probe based experiences, often referred to Transient Absorption Spectroscopy (TAS) and commonly used for resolving the time dynamics of absorption processes [67]. In particular, Four-wave mixing is a reliable technique for determining the third-order nonlinear susceptibility $\chi^{(3)}$, especially in waveguides. Determination of $\mathbb{I}\mathrm{m}\ \{\chi^{(3)}\}$ and $|\chi^{(3)}|$ involves measurement of the pump-induced probe power loss and the efficiency of coherent signal wave generation. Strictly speaking, the two quantities represent different physical processes: $\mathbb{Im}[\chi^{(3)}_{\text{mat}}(\omega_2 = \omega_1 + \omega_2 - \omega_1)]$ describes two-photon absorption, whereas $|\chi^{(3)}(\omega_3 = \omega_1 + \omega_1 - \omega_2)|$ represents frequency generation. In order to extract the sign of the real part, this technique must be supplemented with another measurement. One advantage of this technique is the possibility to monitor the nonlinear dynamics or in other words, the time dependence of the nonlinearities. As this technique relies on the phase matching of several beams, the sensitivity of the alignment is restrictive as the angles and overlaps must be carefully controlled.

The ability to resolve the time dynamics by adjusting the delay between the pump and probe beams is particularly useful. It has been applied to numerous materials such as semiconductors [68] and organic compounds [69]. In addition to adjusting the delay, polarization between pulses can also be adapted, allowing for examination of $\chi^{(3)}$ off diagonal components [70].

In particular, the third-order nonlinear process of FWM in integrated waveguides has raised particularly intense research due to its potential for a wavelength-tunable method of signal amplification, conversion and regeneration in an integrated platform [71, 72, 73, 74, 75]. The main difficulty too exploit this effect is the phase matching condition of beams separated in energy, typically by some tenths of nm, requiring a waveguide dispersion management (tune the waveguide modal dispersion with the geometry). This task is not obvious in highly dispersive structures such as photonic crystals. We will explore this optimization in the last chapter of this manuscript.

Nearly degenerate three-wave mixing

When two of the used waves have the same frequency, the four wave mixing is called nearly degenerate three-wave mixing. It consists of a strong pump at ω that interacts with a weak beam at $\omega - \Delta\omega$ to generate a new wave at $2\omega - (\omega - \Delta\omega) = \omega + \Delta\omega$. Considering a very small frequency difference ($\Delta\omega \ll \omega$): $\chi^{(3)}_{xxxx}(-\omega;\omega,\omega,-\omega) \simeq \chi^{(3)}_{xxxx}(-\omega - \Delta\omega;\omega,\omega,-\omega + \Delta\omega)$. As the beams are energetically close, this technique is nearly phase-matched for forward collinear propagation, simplifying the beam alignment.

Interferometric methods

Many experimental methods rely on interferometers to characterize the nonlinear refractive index of materials inserted in one of the arms. In the simplest case of a Mach-Zehnder interferometer[76], one of the arms is set with a reference material with a known nonlinear index and in the other arm the sample to be characterized. The set-up is then aligned and compensated at low powers to be finally tested at high powers. Both materials will experience a nonlinear phase shift and then the reference arm could be compensated with neutral density filters until getting the same phase. More complex interferometric configurations have been proposed and demonstrated [77, 78, 79].

Third harmonic generation (THG)

Usually the characterization of a nonlinear third order medium based on the specific interaction to be studied or exploited. For instance, in the previous methods, the study was focused on the nonlinear variation of the refractive index as it is one of the most interesting effects to exploit in nonlinear integrated circuits.

One way to characterize the pure electronic behavior of a material consists in studying the third harmonic generation (THG) [80]. Such a high frequency oscillation requires the intervention of a pure nonresonant electron cloud distortion. To develop this technique, several problems need to be addressed. For instance at large enough powers, air could generate third harmonics. In particular, for silicon, the third harmonic frequency is absorbed, so it is not possible to efficiently propagate it in a waveguide. Nevertheless, Dr. Monat and co-workers demonstrated in a photonic crystal waveguide that by coupling to the continuum of radiation modes above the light line, the quasi-phase matched condition between the third-harmonic signal (visible range) and the fundamental mode (NIR) could be achieved. Even though Silicon absorbs at visible wavelengths (TH frequencies), by the use of slow light and out-of-plane collection, researchers have succeeded in using THG in integrated silicon waveguides [81, 82] to demonstrate a single-shot time-domain integrated optical auto-correlator [83].

Non-linear absorption - 1/T technique

In the previous subsections, we have seen some procedures to estimate the nonlinear effects in the phase of a pulse. Nevertheless, the imaginary part of the susceptibility have not been directly treated. Indeed, this quantity is easier to quantify as it requires the information of the transmission as a function of the input power. We will use a variation of this technique to properly measure the effective γ_{TPA} in waveguides and it will be a tool to characterize the coupling efficiencies in the facets.

A simple insight of this technique could be seen from basic relations. Indeed, if two photon-absorption is the dominant nonlinear losses, the optical intensity can be written as (in accordance with eq. (1.72)): $dI/dt = -\beta_{\mathrm{TPA}} I^2$. By integrating, we can find the transmitted pulse energy as a function of the peak incoming intensity, that is normalized by the transmission with the low intensity limit (T_0). When $(T - T_0)/T_0 \ll 1$ and for a gaussian shaped pulse, it is easy to show that: $T_0/T = 1 + \beta_{\mathrm{TPA}} I_{in} L_{\mathrm{eff}} / \sqrt{8}$. So it is a linear function of the intensity where, by tracing I_{in} vs. T/T_0, we can find the TPA coefficient of the material as the slope near the origin is directly proportional to this quantity. In the next chapter we will develop the experimental issues and quantities required to the proper extraction of γ_{TPA} in integrated waveguides.

1.7 Conclusion

In this chapter we have presented the basic concepts of nonlinear optics and its link with some materials and integrated waveguides. First, we have developed the general quantities to be studied in the frame of bulk materials, then we have introduced the basic concepts for waveguiding in integrated structures, such as strip, slot or photonic crystals. These physical principles were followed by a presentation of interesting materials for integrated proposes at wavelengths around $\lambda \sim$1550 nm. They are mainly components from chemical groups III-V and IV.

We have presented the principles and main problems in the fabrication methodology for our silicon and silicon nitride samples. We have optimized the writing and etching processes for 220/260 nm silicon thicknesses and for 400 nm thick silicon nitride. Also, we have presented the general fabrication steps followed by our collaborators to elaborate monomode SiGe and chalcogenide waveguides. Specifically, we have designed the masks for silicon, silicon nitride and chalcogenide and performed the linear measurements of all the samples. The work with internal and external collaborators was explicit along the section.

Finally, we have developed the nonlinear vectorial wave equation applicable to our waveguides in order to define the parameters to be measured. We have summarized the most common techniques used to measure the third order nonlinear properties of materials. Some of them are not suitable for waveguides and others are difficult to implement and interpret.

2 Bi-directional top hat D-Scan

In this chapter we present a technique to **measure the real and imaginary effective third order electronic susceptibilities** in integrated devices. To this aim, we have developed a method to measure the coupling efficiencies. After presenting a semi-analytical model, we introduce a set-up to meet the method requirements. The experimental procedure is validated in a standard silicon-on-insulator (SOI) waveguide and then applied to a series of interesting nonlinear integrated materials.

Contents

> "Every really basic quantity is defined by a measuring procedure... The mapping of the physical reality on a mathematical structure is the ultimate goal of physics"
>
> Gunter Scharf, From Electrostatics to Optics, Springer Verlag, Berlin, 1994.

2.1 Introduction

The increasing sophistication of integrated optical devices and the demands on data bandwidth in on-chip communications require the consideration of nonlinear interactions. The trade-off between losses, high material nonlinearities, tight optical mode confinement, and dispersion imposes the waveguide engineering to obtain adequate nonlinear figures of merit. One interesting way to increase the degrees of design is to envisage **hybrid** structures, designed with specific nonlinear materials covering CMOS compatible waveguides.

Previously, we have introduced some methods to characterize the third order electronic nonlinear parameters of materials. In particular and due to its simplicity the **Z-Scan** technique [62] is currently the preferred one. Nevertheless, it cannot be applied directly to waveguides. Instead, interferometric methods or phenomena requiring phase-matching between diverse waves are usually applied to characterize them. Both kind of methods require a careful alignment and present experimental constrains. In this context, there is a need for the development of simpler characterization methods capable to measure the nonlinear performances of waveguide structures, including hybrid and periodic integrated devices.

By keeping the advantage of using a single beam, the Z-Scan technique has been transposed in previous research to the temporal domain in order to characterize the nonlinear refractive indices of **optical fibers**. The technique has been referred to **D-Scan**, standing for *Dispersive Scan*, and consists in measuring the output spectral broadening of transmitted pulses for various dispersion coefficients $\phi^{(2)}$ applied to the injected pulses [84, 85].

Regarding the structures of interest in the present work, we require the development of a new technique to estimate effective nonlinear susceptibilities of **integrated structures**, presenting not only SPM effects (as silica fibers) but also the instantaneous nonlinear losses (TPA). In this chapter, we present a non-destructive single beam method, which allows the measurement of nonlinear performance of different guided geometries and materials based on the measurement of the bidirectional nonlinear transmission and the application of a D-Scan technique with top hat pulse spectra. The devices under test could present both Kerr and TPA effects. Unlike the case of optical fibers, the difficulty in integrated structures lies in assessing the real power injected into the waveguide mode. In the first section we apply the bidirectional procedure to extract the coupling coefficient values of each facet and then the $\gamma_{\mathrm{TPA}} = S^2 \beta_{\mathrm{TPA}} / A_{\mathrm{NL}}$ parameter (Eq. (1.72)), where β_{TPA} is the TPA coefficient, and A_{NL} is the nonlinear effective area of the guided mode.

Then, in a second step, we apply a D-Scan measurement, using spectrally quasi-rectangular pulses, being the analogous in the temporal domain of the *top-hat Z-Scan* [63, 86]. Irrespective of the injection and collection losses (in and out) of the guide, we measure the nonlinear third order figure of merit $FOM_{\mathrm{TPA}} = \gamma / (2\pi \gamma_{\mathrm{TPA}})$, with $\gamma = k_0 S^2 n_2 / A_{\mathrm{NL}}$ the effective Kerr parameter. The expressions take into account the nonlinear enhancement due to localization effects that are quantified as the ratio between the group index of the waveguide to the bulk index of the material $S = n_{\mathrm{g}}^{\mathrm{wg}} / n_0$ [87, 88, 89]. The technique of *top-hat D-Scan* will be explained in section 2.3. Finally, with the measured value for FOM_{TPA} and γ_{TPA}, we can measure the effective Kerr parameter of the waveguide (γ) related to the real part of the susceptibility.

The experimental set-up to stretch the pulse (i.e. vary the dispersion coefficient ϕ^2) is introduced and calibrated in section 2.4. The measurement methodology is validated in a standard SOI waveguide (section 2.5) and finally applied to series of materials potentially interesting for nonlinear integrated applications (section 2.6).

2.2 Bi-directional nonlinear transmission: measurement of γ_{TPA} and coupling coefficients

The actual intensity coupled in guiding structures is usually estimated indirectly. In optical fibers a bidirectional measurement of propagation losses has been proposed to measure the coupling efficiencies [90, 91], but this method is limited to linear regime.

As expected, the induced absorption effects are easier to determine than the phase variations, as they can be measured from a variation in the transmission as the injected power changes. In this section, we will study the instantaneous (<1ps) two-photon absorption (TPA) and use it as a monitoring quantity to estimate the coupling efficiencies in both facets of a chip.

We require an experimental set-up that measures the optical average powers of pulsed lasers independently of its pulse shape. In Fig. 2.1, we present a scheme of the set-up to be used. PM stands for powermeter, BS: Beam splitter, MO: Microscope objective, DUT: Device under test, κ_{FA} and κ_{FB}, the coupling coefficients from facets A and B, and the indices (1) and (2) correspond to each injection direction. The DUT is assumed to operate with non-negligible TPA absorption effect. It is noteworthy that the power is measured outside the waveguide, so to estimate the injected and the transmitted powers inside the waveguide, one has to assess at least two coupling coefficients (generically κ_{in} and κ_{out}), which in our case include the the transmission of the microscope objectives (MO).

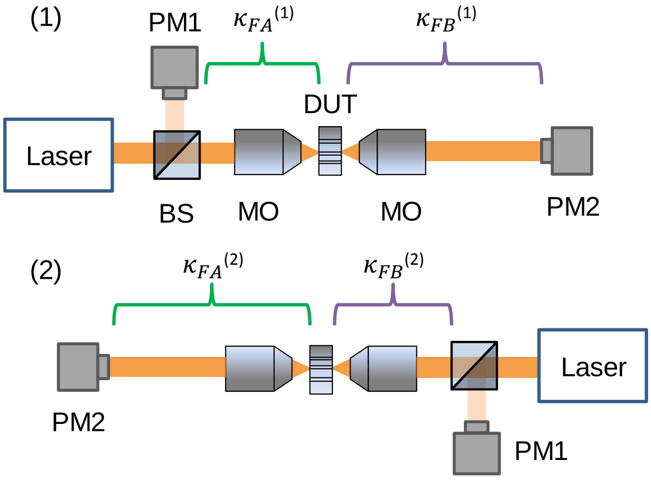

Figure 2.1: Set-up scheme to measure the coupling efficiencies and the nonlinear losses coefficients.

Even though in our scheme we use microscope objectives, the following method can be applied with injecting schemes that use gratings or lensed fibers. We start with the expression of the output power as a function of the input power in the linear regime:

$$P_{\text{out}} = \kappa_l P_{\text{in}} \tag{2.1}$$

where κ_l is the coupling coefficient of the system. This parameter could be decomposed in three terms: an input coupling coefficient (κ_{in}), which represents the amount of light that is effectively injected into the waveguide and related to the coefficients $\kappa_{\text{FA}}^{(1)}$ and $\kappa_{\text{FB}}^{(2)}$ respectively (Fig. 2.1 (1) and (2)); an output coupling coefficient (κ_{out}), representing the light collected from the output of the waveguide corresponding to $\kappa_{\text{FB}}^{(1)}$ and $\kappa_{\text{FA}}^{(2)}$ in Fig. 2.1 (1) and (2); and a term describing the (linear) propagation losses (α) inside the waveguide:

$$\kappa_l = \kappa_{\text{in}}\kappa_{\text{out}}e^{-\alpha L} = \kappa_{\text{FA}}^{(1)}\kappa_{\text{FB}}^{(1)}e^{-\alpha L} = \kappa_{\text{FB}}^{(2)}\kappa_{\text{FA}}^{(2)}e^{-\alpha L} \tag{2.2}$$

Assuming that the waveguide operates in single mode regime and that the incident free space beam is also a purely single transverse mode: $\kappa_{\text{FA}}^{(1)} = \kappa_{\text{FA}}^{(2)} = \kappa_{\text{FA}}$ and $\kappa_{\text{FB}}^{(1)} = \kappa_{\text{FB}}^{(2)} = \kappa_{\text{FB}}$. But, generally $\kappa_{\text{FA}} \neq \kappa_{\text{FB}}$ (due to cleaving, possible angles, etc.).

In general, we will work with materials presenting nonlinear losses dominated by two photon absorption (TPA). So we need to describe the depletion of the pulse intensity due to linear and nonlinear propagation losses, recalling the expression (1.31):

$$\frac{\partial I}{\partial z} = -S\alpha' I(z,t) - S^2\beta_{\mathrm{TPA}} I^2(z,t) \tag{2.3}$$

Following an integration along the waveguide length L, the output intensity is given by:

$$I(L,t) = \frac{I(0,t)e^{-S\alpha' L}}{1 + S^2\beta_{\mathrm{TPA}} I(0,t) L_{\mathrm{eff}}} \tag{2.4}$$

where the effective length of the waveguide L_{eff} is given by:

$$L_{\mathrm{eff}} = \frac{1 - e^{-S\alpha' L}}{S\alpha'} = \frac{1 - e^{-\alpha L}}{\alpha} \tag{2.5}$$

It can be seen from Eq. (2.4) that when $S^2\beta_{\mathrm{TPA}} I(0,t) L_{\mathrm{eff}} \gg 1$, the output intensity becomes $I(z) \Rightarrow \frac{1}{S^2\beta_{\mathrm{TPA}} L_{\mathrm{eff}}}$, physically meaning that regardless the input intensity, the maximum achievable value is determined by the waveguide linear (L_{eff}) and nonlinear (β_{TPA}) losses. This limiting value is a restriction to achieve arbitrarily large refractive index changes (i.e. modulation and switching), but could be exploited as a saturation intensity value to prevent high energies reaching sensitive components.

To express the described peak intensities inside the waveguide in terms of power measured with detectors, we should take into account the coupling efficiencies, so that: $I(0,t) = \kappa_{\mathrm{in}} \frac{P_{\mathrm{in}}^{\mathrm{peak}}}{A_{NL}}$ and $P_{\mathrm{out}}^{\mathrm{peak}} = \kappa_{\mathrm{out}} I(L,t) A_{NL}$, where A_{NL} is the effective mode area defined in Eq. (1.72). We can re-write Eq. (2.4) in terms of the external peak powers:

$$P_{\mathrm{out}}^{\mathrm{peak}} = \frac{\kappa_l P_{\mathrm{in}}^{\mathrm{peak}}}{1 + S^2\beta_{\mathrm{TPA}} \kappa_{\mathrm{in}} \frac{P_{\mathrm{in}}^{\mathrm{peak}}}{A_{NL}} L_{\mathrm{eff}}} = \frac{\kappa_l P_{\mathrm{in}}^{\mathrm{peak}}}{1 + \gamma_{\mathrm{TPA}}^{wg} \kappa_{\mathrm{in}} P_{\mathrm{in}}^{\mathrm{peak}} L_{\mathrm{eff}}} \tag{2.6}$$

with $\kappa_l = \kappa_{\mathrm{in}}\kappa_{\mathrm{out}} e^{-\alpha L}$. The detectors conventionally measure powers integrating over the time, so we need an additional parameter that takes into account the duration and repetition rate of the laser in order to link peak with average powers, so that $P_{\mathrm{in}}^{\mathrm{peak}} = \eta P_{\mathrm{in}} = \frac{P_{\mathrm{in}}}{\tau F}$ and analogously $P_{\mathrm{out}}^{\mathrm{peak}} = \eta P_{\mathrm{out}} = \frac{P_{\mathrm{out}}}{\tau F}$, where τ is the pulse duration in time units and F is the inverse of the repetition time in Hz. We can write Eq. (2.6) in terms of measurable powers:

$$\boxed{P_{\mathrm{out}} = \frac{\kappa_l P_{\mathrm{in}}}{1 + \gamma_{\mathrm{TPA}}^{wg} \kappa_{\mathrm{in}} \eta P_{\mathrm{in}} L_{\mathrm{eff}}}} \tag{2.7}$$

where P_{in} and P_{out} are the average powers, input and output, respectively. It can be seen that we recover the equation of the linear transmission (2.1) when the denominator tends to the unity. And we obtain a saturation power independent of the input power when $\gamma_{\text{TPA}}^{wg}\kappa_{\text{in}}\eta P_{\text{in}}L_{\text{eff}} \gg 1$ equals to $P_{\text{out}}^{\max} \Rightarrow \frac{\kappa_{\text{out}}e^{-\alpha L}}{\gamma_{\text{TPA}}^{wg}\eta L_{\text{eff}}}$. Finally, we can write this expression in a most simple way:

$$\boxed{\frac{P_{\text{in}}}{P_{\text{out}}} = \frac{1}{\kappa_l} + \frac{\gamma_{\text{TPA}}^{wg}\kappa_{\text{in}}\eta L_{\text{eff}}}{\kappa_l}P_{\text{in}} = a + bP_{\text{in}}} \tag{2.8}$$

By plotting $P_{\text{in}}/P_{\text{out}}$, we should get a linear function of P_{in} with a slope that contains the TPA coefficient. It is easy to extend this model for multiphoton absorption, which follows a quadratic dependence with P_{in} for three photon absorption (ThPA). One important parameter that we will be used constantly is the ratio between b and a, which depends on the input coupling and the linear propagation losses, the other values being given by the waveguide and the bulk material properties:

$$\boxed{\frac{b}{a} = \gamma_{\text{TPA}}^{wg}\kappa_{\text{in}}\eta L_{\text{eff}}} \tag{2.9}$$

This expression is valid regardless the direction of the injection. Now, we will inject the power from both sides to establish 2 equations with 2 unknown parameters: the coupling efficiencies in the facets A and B. From scheme of Fig. 2.1, one gets the relation:

$$\frac{b^{(1)}}{a^{(1)}} = \gamma_{\text{TPA}}^{wg}\kappa_{FA}\eta L_{\text{eff}} \qquad \frac{b^{(2)}}{a^{(2)}} = \gamma_{\text{TPA}}^{wg}\kappa_{FB}\eta L_{\text{eff}} \tag{2.10}$$

From where we can extract the ratio:

$$\frac{b^{(1)}a^{(2)}}{b^{(2)}a^{(1)}} = \frac{\kappa_{FA}}{\kappa_{FB}} \tag{2.11}$$

But we also know that $a^{(2)} = a^{(1)} = (\kappa_{FA}\kappa_{FB}e^{-\alpha L})^{-1}$, so we can determine each coefficient in terms of the experimental values a, b and the propagation losses:

$$\boxed{\kappa_{FA} = \sqrt{\frac{b^{(1)}}{b^{(2)}a^{(1)}e^{-\alpha L}}}} \qquad \boxed{\kappa_{FB} = \sqrt{\frac{b^{(2)}}{b^{(1)}a^{(2)}e^{-\alpha L}}}} \tag{2.12}$$

It is clear that those relations are only valid for $\gamma_{\text{TPA}}^{wg} \neq 0$. We have used the imaginary susceptibility to measure the coupling efficiencies that are crucial experimental parameters for the quantification of any kind of light matter interactions.

2.3 Top-hat D-Scan

The refractive effects are more difficult to quantify than the transmission ones because they are associated to phase changes. So, to obtain the material coefficients related to them, we need to rely on phenomena that induce changes in the spectral features or in the polarization of the beam. In our case, we will use self-phase modulation induced spectral broadening in pulsed regime to quantify them.

Indeed the method presented hereafter (D-Scan technique) is based on intensity-induced temporal wave-front curvatures (Fig. 2.2) that we use to characterize the effective third order nonlinear parameters of waveguide structures. We perform diverse approaches to calculate and measure the dispersion effect in a nonlinear waveguide. We present analytical and semi-analytical models that predict the spectral evolution of pulses inside waveguides with different nonlinear properties.

In Fig. 2.2, we show an input pulse in the temporal domain passing trough an **adjustable** 2nd order dispersion medium that introduces an adaptable $\phi^{(2)} = \beta_2 z$ on the pulse. At the output of the dispersive medium the pulse is broadened and exhibits a parabolic

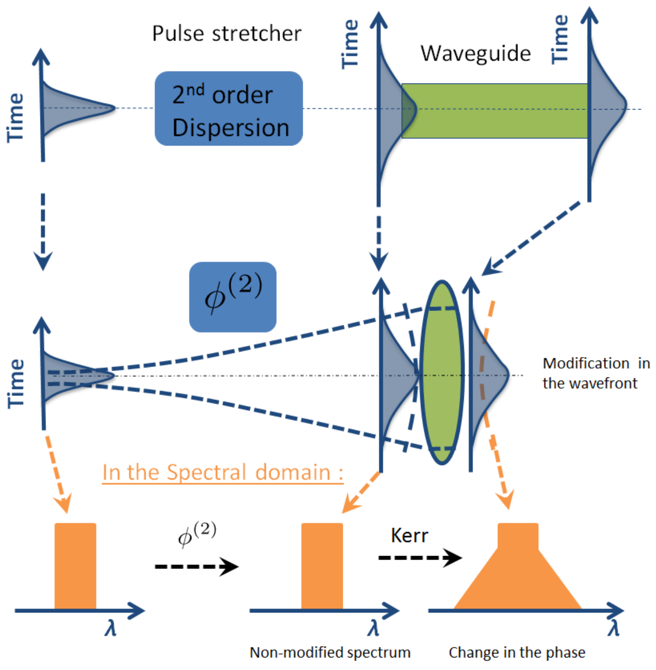

Figure 2.2: Scheme of the Top-Hat D-Scan displaying the effect of a waveguide analogous to a temporal (Kerr) lens.

temporal phase profile whose sign depends on the sign of the dispersion introduced [92], leaving the spectrum unmodified. Inside the waveguide, intensity-induced refractive effects will broaden the spectrum via self-phase modulation, acting as a temporal lens (also called Kerr lens).

2.3.1 Pure Kerr waveguides: absence of two-photon absorption

Due to their electronic properties, some materials do not present two-photon absorption at wavelengths around 1550 nm, for instance silica or silicon nitride. In this section, we will consider waveguides without nonlinear losses, so we call them "pure Kerr" as they only present intensity-dependent nonlinear refractive effects.

In appendix C, we have developed an analytical model assuming no TPA, small nonlinear phase shifts and gaussian pulse shapes. Even though the tendencies and orders of magnitude are useful to understand the physics behind a Kerr lens, we require a more refined model to quantify the third order instantaneous effects for different pulse shapes. For this matter, we will develop a semi-analytical approach to extend the analytical model and find the evolution of the spectral peak intensity as a function of $\phi^{(2)}$ for different input powers and diverse excitation pulse shapes, in presence of TPA. Z-Scan techniques appoint a relation between the peak to valley transmission variation and the nonlinear phase (ϕ_{NL}) in order to quantify the magnitude and sign of the nonlinear refractive index n_2 [62]. We will recall those concepts and adapt them to the dispersive (temporal) scan technique, leading to their extension towards integrated optical circuits.

First, we will describe the effect of a dispersive medium on a pulse through Fourier analysis. In the frequency domain, the spectrum can be written as:

$$\widetilde{U}(z_1,\nu) = \mathscr{F}\left[U(0,t)\right] e^{\frac{i\phi^{(2)}(2\pi\nu)^2}{2}} = \mathscr{F}\left[\sqrt{I_0}U(t)\right] e^{\frac{i\phi^{(2)}(2\pi\nu)^2}{2}} \tag{2.13}$$

where we have separated the maximum peak intensity (I_0) from the temporal pulse shape ($U(t)$). The temporal profiles considered in this section follow a gaussian and sinus cardinal (Sinc) temporal shapes. $\mathscr{F}$ stands for Fourier Transform and z_1 is a propagation position after the dispersive medium. It is noteworthy that $\left|\widetilde{U}(0,\nu)\right|^2 = \left|\widetilde{U}(z_1,\nu)\right|^2$, so after the dispersive medium, the pulse is unaltered in the frequency domain. Nevertheless, it implies a modification of the pulse in the temporal domain by introducing a chromatic delay, increasing the pulse duration. Fig. 2.3 [93] shows a scheme explaining the effect of a dispersive medium in a pulse for given $\phi^{(2)}$. In (a), we show an un-chirped pulse with no time delay between the spectral components. Here there is a direct Fourier relation between the temporal and the frequency domain and it coincides with the the minimum pulse duration achievable. In (b), we introduce a negative second order dispersion, so the red components of the pulse are located at the front of the pulse. This spectral phase

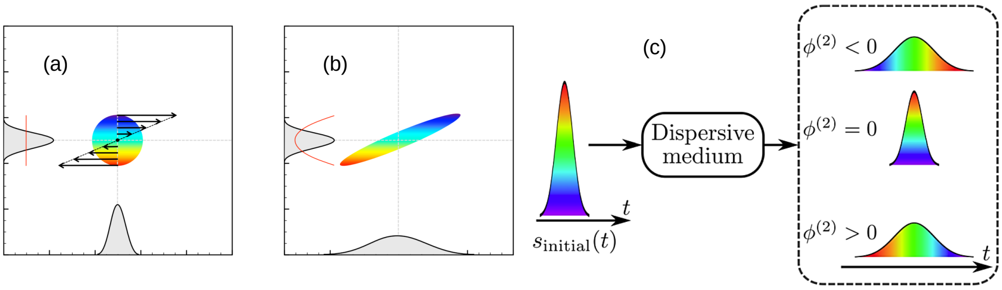

Figure 2.3: Schematics of a pulse stretching. (a) Fourier limited pulse. (b) Stretched pulse with a positive introduced dispersion ($\phi^{(2)}$>0), the red components are sent to the front of the pulse increasing its duration and changing the phase relation but leaving the spectral shape unaffected. (c) Different sign effect in the pulse duration and the relative position of the different frequencies after the dispersive effect[93].

modifies the pulse duration preserving unaltered its spectral content. In (c) we show the effect in the pulse for different dispersion signs. To find the pulse distribution in the temporal domain, we should apply an inverse Fourier Transform ($\mathscr{F}^{-1}$) to the previous expression:

$$U(z_1,t) = \mathscr{F}^{-1}\{\mathscr{F}\left[\sqrt{I_0}U(t)\right] e^{\frac{i\phi^{(2)}(2\pi\nu)^2}{2}}\} \tag{2.14}$$

In Fig. 2.4 we display a typical variation of the full width half maximum (FWHM) of the autocorrelation of a pulse (directly linked to the temporal duration) after the introduction of a second order dispersion. It should be noted that the curve is symmetric, meaning that the pulse duration is changed in the same proportion for opposite signs but the frequency order in the pulse depends on the sign (Fig. 2.3).

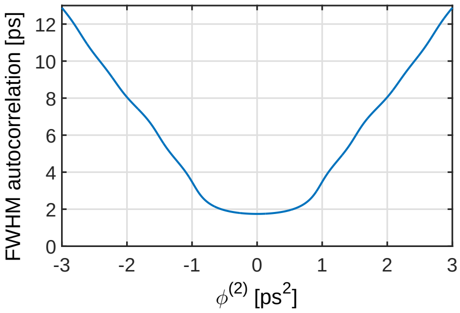

Figure 2.4: Typical variation of the full width half maximum (FWHM) of the pulse autocorrelation as a function of the introduced dispersion. Pulse duration $T_0 = 1$ ps.

Next, the effect of the nonlinear medium can be calculated without further approximations than the absence of TPA. The pulse undergoes a purely nonlinear phase shift that is proportional to an intensity temporal variation:

$$U(z_2,t) = U(z_1,t)e^{i\phi_{NL}} = U(z_1,t)e^{ik_0 n_2 I_0 L_{eff}|U(t)|^2} = U(z_1,t)e^{i\phi_{NL0}|U(t)|^2} \tag{2.15}$$

where z_2 is a propagation point after the waveguide. As the measurements will be performed in the spectral domain, we proceed by applying a Fourier Transform:

$$\boxed{\widetilde{U}(z_2,\nu) = \mathscr{F}\left[U(z_2,t)\right] = \mathscr{F}\left[U(z_1,t)e^{i\phi_{NL0}|U(t)|^2}\right]} \tag{2.16}$$

which can be implemented numerically via Fast Fourier Transform (FFT) algorithm for discrete data sets. By monitoring of the output spectrum at fixed energy for various dispersion one can expect different responses in the nonlinear regime (n_2 non negligible). Depending on the sign of the dispersion, respect to that of n_2, one expects the Kerr lens to counter-balanced the dispersion effect (in some case, a strict compensation is expected), leading to reduction of the spectral broadening observed at $\phi^{(2)}$ =0, or to further accentuate the temporal wave front distortion leading to a larger spectral broadening effect (case where n_2 and $\phi^{(2)}$ get the same sign). In other words, the waveguide can be studied as a temporal lens introducing a nonlinear phase change to the pulse (Fig. 1.2 and 2.2). Indeed, a thin lens in the spatial domain can be expressed in terms of a phase transformation.

In order to quantify the interplay between the dispersion and the Kerr lens effect, it is useful to introduce two markers: the normalized spectral peak power (NSPP) and the spectral broadening through the r.m.s. spectral linewidth $2\sigma_\lambda = 2\sqrt{\frac{\int \lambda^2 P(\lambda)d\lambda}{\int P(\lambda)d\lambda} - \left(\frac{\int \lambda P(\lambda)d\lambda}{\int P(\lambda)d\lambda}\right)^2}$ and $P(\lambda)$ the specific power at a given wavelength.

In Fig. 2.5, we show the evolution of the NSPP and the $2\sigma_\lambda$ as a function of the introduced dispersion for a temporal **gaussian** pulse with:

$$U(0,t) = U_0 e^{-\frac{t^2}{2T_0^2}} \tag{2.17}$$

where T_0 is the pulse duration in this case set to 1 ps. This value is chosen because is in the order of magnitude of the pulses to be used in experiments. We show the evolution for different nonlinear phase shifts (i.e. intensities) and materials with positive and negative nonlinear refractive indices n_2. It can be noticed that the maxima (resp. minima) of NSPP coincide with minima (resp. maxima) of the r.m.s. spectral linewidths. This can be explained through the conservation of energy. An increase in the spectral broadening

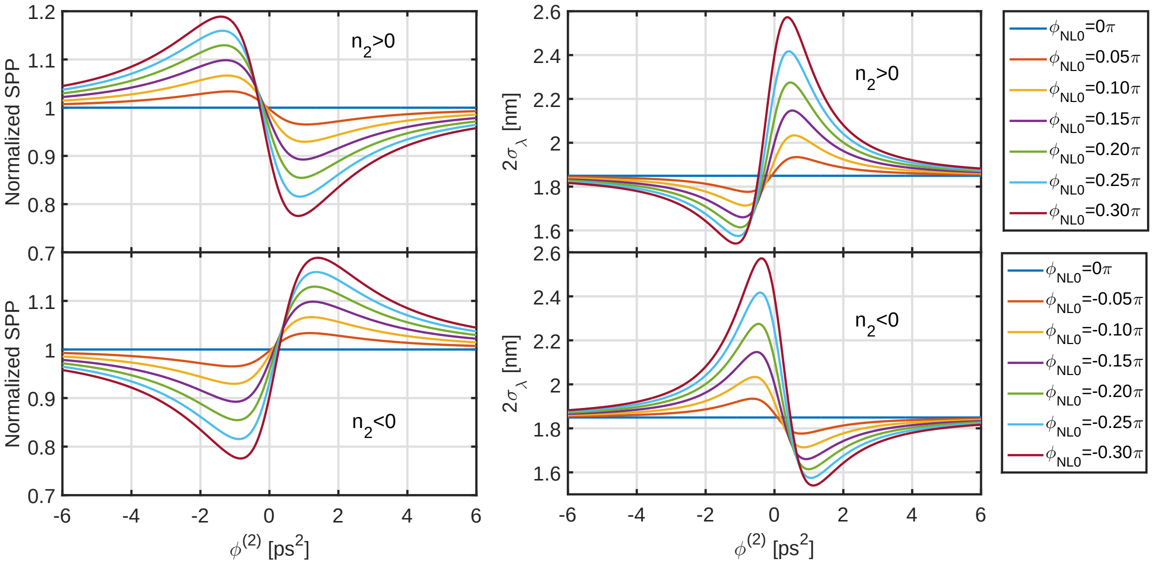

Figure 2.5: Left: Normalized Spectral Peak Power (NSPP) as a function of the second order dispersion for different nonlinear phase shifts in a pure-Kerr element under a gaussian excitation. Right:Total standard deviation as a function of the second order dispersion parameter for different ϕ_{NL0}. Pulse duration $T_0 = 1$ ps.

($2\sigma_\lambda$) necessarily implies a reduction of the spectral power density. It can be noticed also that for larger nonlinear shifts, the peak-to-valley (p-v) of both NSPP and $2\sigma_\lambda$ increases, so we can use this criteria as a characterization quantity for the strength of the material nonlinear Kerr coefficient.

To understand the behavior of the r.m.s. spectral linewidth, we have plotted in Fig. 2.6 the normalized spectra in dB for few specific $\phi^{(2)}$ values. We selected a material with n_2>0 and set the nonlinear phase to $\phi_{NL0} = 0.30\pi$. The dispersive shape of the r.m.s. linewidth obtained for D-Scan is strictly equivalent in dispersion to that obtained for Z-Scan in position. For large dispersion coefficients (either positive or negative), the pulse duration is too large to efficiently generate self-phase modulation induced spectral broadening, and the 2σ curve asymptotically tends to the spectral width of the incident pulse. For negative $\phi^{(2)}$ side of the curve, the positive temporal lensing counter-balances the dispersion effect by inducing a temporal front wave opposite in sign to that of the chirped pulse (see Fig. 2.2), which reduces the spectral width and increases the the spectral power density in the central wavelength. As the dispersion is set closer to zero, the peak power increases in the temporal domain and the spectral broadening is larger. For positive $\phi^{(2)}$, the spectral broadening increases as the Kerr lens increment the curvature of the temporal wave front of the incident chirped pulse, implying a reduction of the NSPP as the spectrum reaches its largest spectral width. It is important to note that the maximum $2\sigma(\lambda)$ point shifts towards $\phi^{(2)} = 0$ ps^2 as the power nonlinear shift

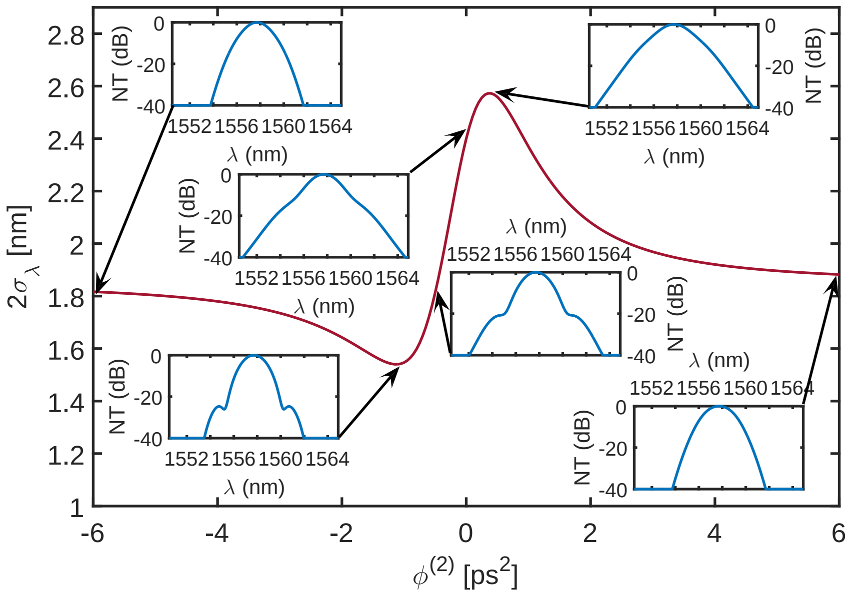

Figure 2.6: r.m.s. spectral linewidth for a pulse with temporal gaussian profile ($T_0 = 1$ps) for a nonlinear phase shift of 0.30π. Inset display the spectra at the most interesting dispersion points. NT: Normalized transmission.

increases. Finally, increasing further the dispersion decreases the peak intensity and the broadening becomes again negligible (baseline).

We can then establish a first empirical rule like in the Z-Scan technique. Regarding the shape of $2\sigma(\lambda)$ curve and reading it from negative towards positive dispersions (left to right), a valley followed by a peak is a signature for a positive nonlinear refraction (n_2>0). One finds the opposite for negative nonlinear refraction (n_2<0): a peak followed by a valley.

Finally, we can extract the peak-to-valley difference variation with the nonlinear phase experienced by the pulse. As shown in Fig. 2.7, the curve exhibits an almost linear dependence, so by knowing the injected intensity on the sample and deducing the nonlinear phase shift by measuring the $(2\sigma_\lambda)_{\mathrm{p-v}}$, the value of n_2 can be estimated. Even though in the Z-Scan empirical slopes are used to retrieve n_2 depending on the pulse shape, we will use directly the simulation curves to match both the 2σ shapes and their corresponding nonlinear phase shifts.

Analogously with the top-hat Z-Scan [63], which has been proved to increase the method sensitivity by a factor of 2.5, we will use **top-hat pulses in the frequency domain**. We can then define the pulse in time domain at $z = 0$ as a Sinc shape corresponding to

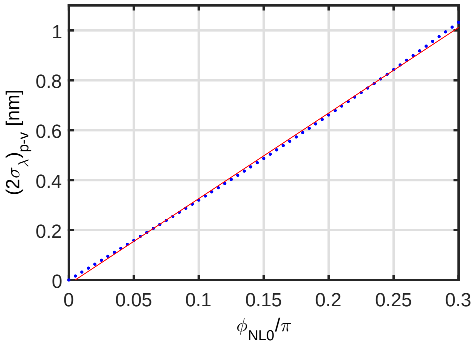

Figure 2.7: $(2\sigma_\lambda)_{\mathrm{p-v}}$ for a temporal gaussian pulse and varying ϕ_{NL0} with a linear fit in red.

the Fourier Transform of a rectangular spectral shape:

$$U(0,t) = \sqrt{I_0}U(t) = \sqrt{I_0}\ \mathrm{sinc(t)} = \sqrt{\mathrm{I}_0}\ \frac{\sin(\text{ßt})}{\text{ßt}} \tag{2.18}$$

We can directly apply the expression (2.16) to trace the $2\sigma(\lambda)$ and NSPP curves. Fig.

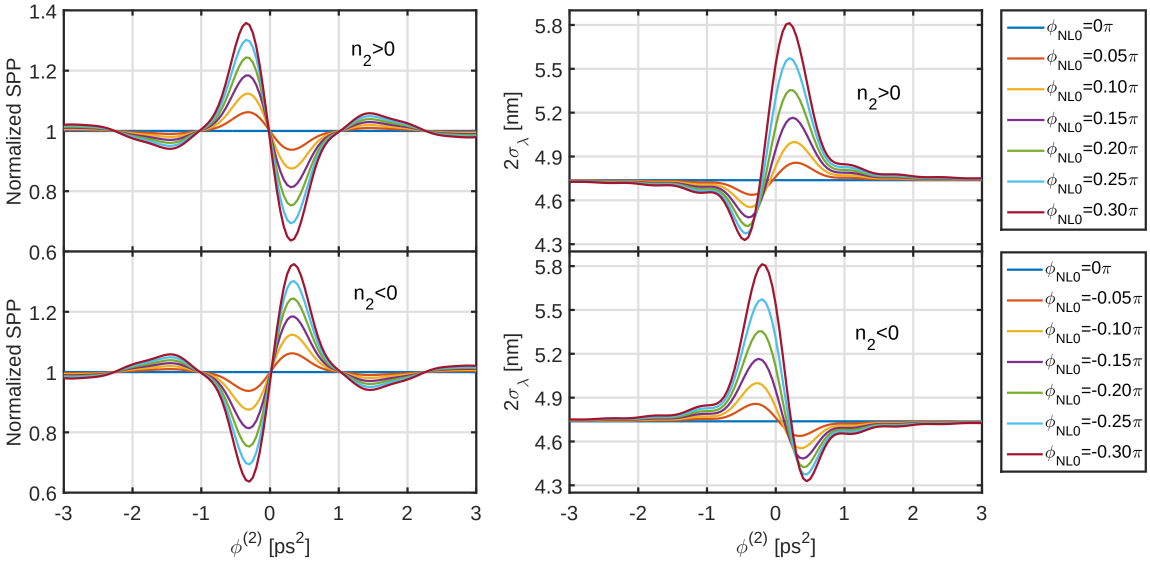

Figure 2.8: Left: Normalized Spectral Peak Power (NSPP) as a function of the second order dispersion for different nonlinear phase shifts. Right: Total standard deviation as a function of the second order dispersion parameter for different ϕ_{NL0}. Pulse duration $T_0 = 1$ ps.

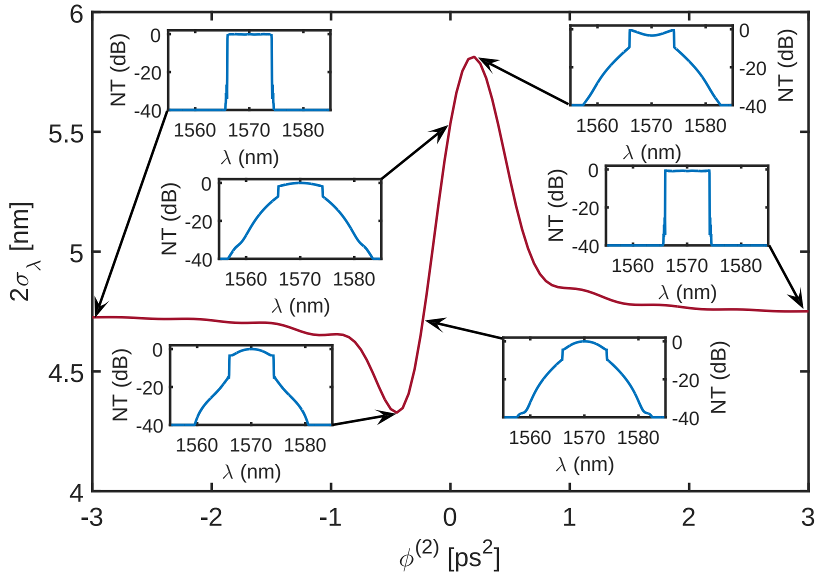

Figure 2.9: r.m.s. spectral linewidth for a pulse with temporal sinus cardinal profile ($T_0 = 1$ps) for a nonlinear phase shift of 0.30π. Inset display the spectra at the most interesting dispersion points. NT: Normalized transmission.

2.8 presents the results for a Fourier limited pulse of 1 ps duration.

By comparing with the gaussian pulses, it should be noticed that the scale for the dispersion $\phi^{(2)}$ has been decreased, as the maxima and minima are achieved with less required dispersion. Furthermore, the values of $2\sigma(\lambda)$ are larger which is understandable from rectangular-like shapes.

As done in the gaussian case, in Fig. 2.9, we have plotted the spectra for the selected dispersion values for a waveguide presenting a positive n_2 with a nonlinear phase shift of 0.30π. The trend analysis is less intuitive than in the gaussian case. For instance, the NSPP curves present several zero crossing points. We will focus our attention in the analysis of the r.m.s linewidth as it is an easier quantity to measure experimentally. If we read the spectral evolution from left to right, the analysis made for the gaussian pulse remains valid. But interestingly, the sensitivity to small nonlinear phase variation will be increased in case of top hat spectral shape pulses. Finally, when we display $(2\sigma_\lambda)_{\mathrm{p-v}}$ as a function of the induced nonlinear shift. We also show a linear trend with a different slope than the one in gaussian profiles. It is noteworthy that the corresponding $(2\sigma_\lambda)_{\mathrm{p-v}}$ for a nonlinear shift of 0.30π for a Sinc profile is 50% larger than the case of gaussian beams. One can conclude that the top-hat D-Scan presents two advantages as the dispersive shape of the 2σ curve is less extended in terms of dispersion, and as the intensity required to achieve the same $(2\sigma_\lambda)_{\mathrm{p-v}}$ is 50% smaller.

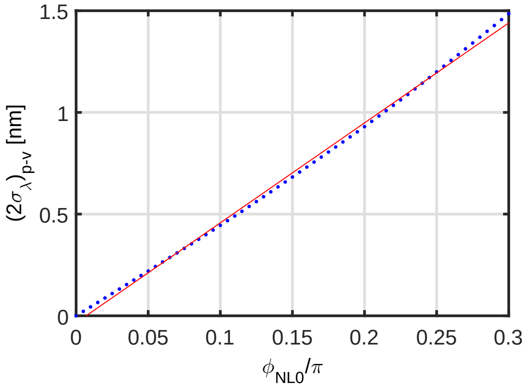

Figure 2.10: $(2\sigma_\lambda)_{\mathrm{p-v}}$ for a temporal sinus cardinal pulse and for different ϕ_{NL0} until $\phi_{NL0} = 0.3\pi$ with its respective linear tendency in red.

2.3.2 Kerr and TPA waveguides: FOM_{TPA} determination

In general, nonlinear refraction is accompanied by nonlinear absorption and transforms the temporal shape of the pulse and its intensity variation along the propagation. For general integrated components we must include both the linear and nonlinear loss effects in the wave equation. Considering the two-photon absorption (TPA) and neglecting the free carrier effects, the nonlinear phase follows the equation:

$$\frac{\partial \phi_{NL}(z,t)}{\partial z} = k_0 n_2 I(z,t) = \frac{k_0 n_2 I(0,t)}{1 + \beta_{TPA} I(0,t) z} \tag{2.19}$$

where $k_0 = \frac{2\pi}{\lambda}$. For simplicity the field enhancement factors are included in the nonlinear Kerr and TPA coefficients. Now, using the expression for the intensity evolution over the waveguide length, the accumulated phase can be written as:

$$\phi_{NL}(L,t) = k_0 \frac{n_2}{\beta_{TPA}} \ln\left(1 + \beta_{TPA} I(0,t) L\right) \tag{2.20}$$

In present relations, L coincides with the effective length accounting for the linear losses $\left(L_{eff} = \frac{1-\exp(-\alpha L)}{\alpha}\right)$. In Fig. 2.11, we show Setting the intensity and the length of the sample for which $\phi_{NL} = \phi_{NL0} = \pi$ with no TPA, we have varied the β_{TPA} coefficient and calculated the ϕ_{NL}. We have chosen values for n_2 and β_{TPA} set around the reported values for silicon. We can see that, as expected, when decreasing the TPA coefficient, the phase shift is larger. We can also appreciate that having a large n_2 could mitigate the effect of TPA. Furthermore, if the later becomes negligible ($\beta_{TPA} I(0,t) L \ll 1$), the nonlinear phase shift becomes: $\phi_{NL}(L,t) \approx k_0 n_2 I(0,t) L$.

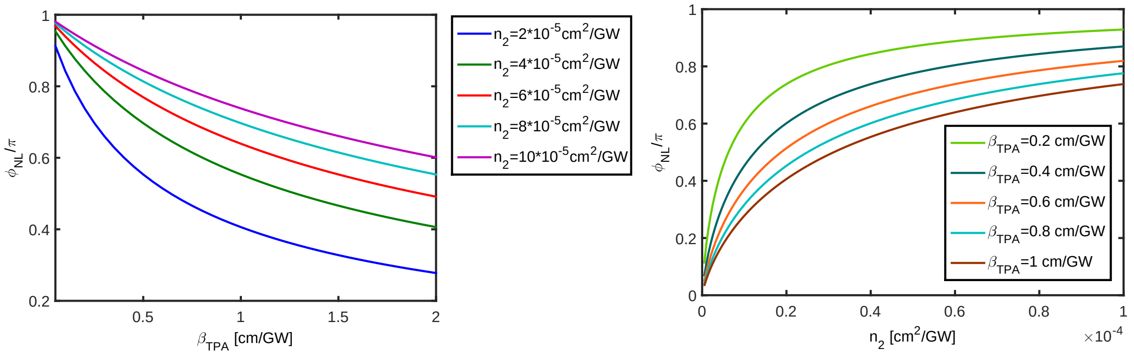

Figure 2.11: Nonlinear phase for different material parameters (around the Silicon values) at $t=0$. Left: nonlinear phase as a function of β_{TPA} for different Kerr coefficients, right: nonlinear phase as a function of Kerr coefficient for different β_{TPA}.

Now, we can modify the calculation procedure from the equation (2.15) which represents the field after the Kerr lens. It will affect the amplitude and the phase of the wave according to the previous relations:

$$\begin{aligned} U(L,t) &= \sqrt{I(L,t)}e^{i\phi_{NL}(L,t)} \\ &= \sqrt{\frac{I_0}{1+\beta_{TPA}I_0\left|U(t)\right|^2 L}}U(t)\exp\left(ik_0\frac{n_2}{\beta_{TPA}}\ln\left(1+\beta_{TPA}I_0\left|U(t)\right|^2 L\right)\right) \end{aligned} \tag{2.21}$$

where $I(0,t)=I_0\left|U(t)\right|^2$. We can express the nonlinear phase relation given in equation (2.20) as:

$$\phi_{NL}(L,t) = 2\pi FOM_{TPA}\ln\left(1+\frac{\phi_{NL0}\left|U(t)\right|^2}{2\pi FOM_{TPA}}\right) \tag{2.22}$$

with $\phi_{NL0}=k_0 n_2 I_0 L$. This expression shows that the FOM_{TPA} is the most important parameter to determine the maximum achievable phase shift. In Fig. 2.12, we can notice that for larger figures of merit, the nonlinear losses do not restrict the nonlinear phase shifts. On the opposite, for figures smaller than 1, the output shift gets saturated.

In an experimental configuration, we can re-write the equation (2.20) by using a and b values obtained with the power curves at zero dispersion (Eq. (2.9)):

$$\boxed{\phi_{NL}(L,t) = 2\pi FOM_{TPA}\ln\left(1+\frac{b}{a}P_{in}\right)} \tag{2.23}$$

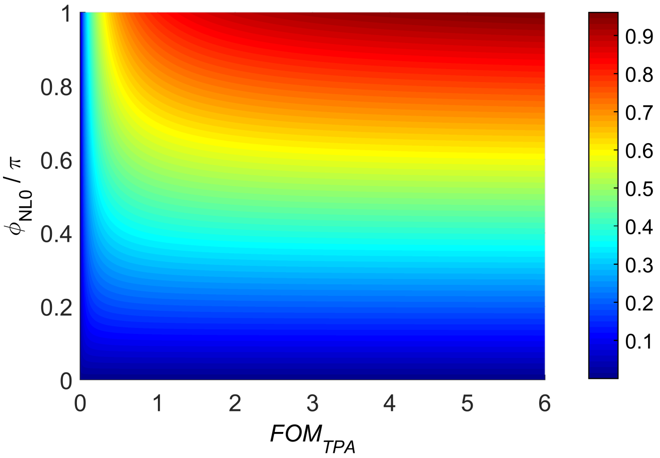

Figure 2.12: Nonlinear phase over π at $t = 0$ as a function of different material figures of merit and $\phi_{NL0}/\pi = k_0 n_2 I_0 L/\pi$ values.

So, inspired by the Z-Scan technique, we can use the peak-to-valley measurement of $2\sigma_\lambda$ to extrapolate the nonlinear phase shift for a given input power. Finally by plotting this quantity against the measured parameter $2\pi \ln\left(1+\frac{b}{a}P_{in}\right)$, we can find FOM_{TPA} as the slope of the line. It is important to notice that this procedure does not require the knowledge of the coupling efficiencies, as they are contained in the experimental ratio b/a.

Next, we will Fourier transform the expression (2.21) to analyze the spectra and the trends of 2σ and the NSPP. The resulting expression is given by:

$$\boxed{\widetilde{U}(L,\nu) = \mathscr{F}\left[\sqrt{\frac{I_0}{1+\beta_{TPA} I_0 L\,|U(t)|^2}}\,U(t)\exp\left(ik_0 \frac{n_2}{\beta_{TPA}} \ln\left(1+\beta_{TPA} I_0 L\,|U(t)|^2\right)\right)\right]} \tag{2.24}$$

This expression has no analytical solution, so we need to solve it by operating with discrete (numerical) Fourier transforms. In Fig. 2.13, we have used it to trace the trends for different FOM_{TPA} values (i.e. materials) with positive n_2 by exciting with a gaussian pulse with duration of $T_0 = 1$ ps. We have used as intensity normalization criteria the non-depleted spectral peak power at zero dispersion for each input power. The intensity step was chosen in such way that in a pure Kerr element the phase shift increases by 0.20π.

The general shapes of 2σ keeps the same trends as the ones explained in previous sections. Nevertheless, as the FOM_{TPA} decreases, the nonlinear phase shifts are smaller

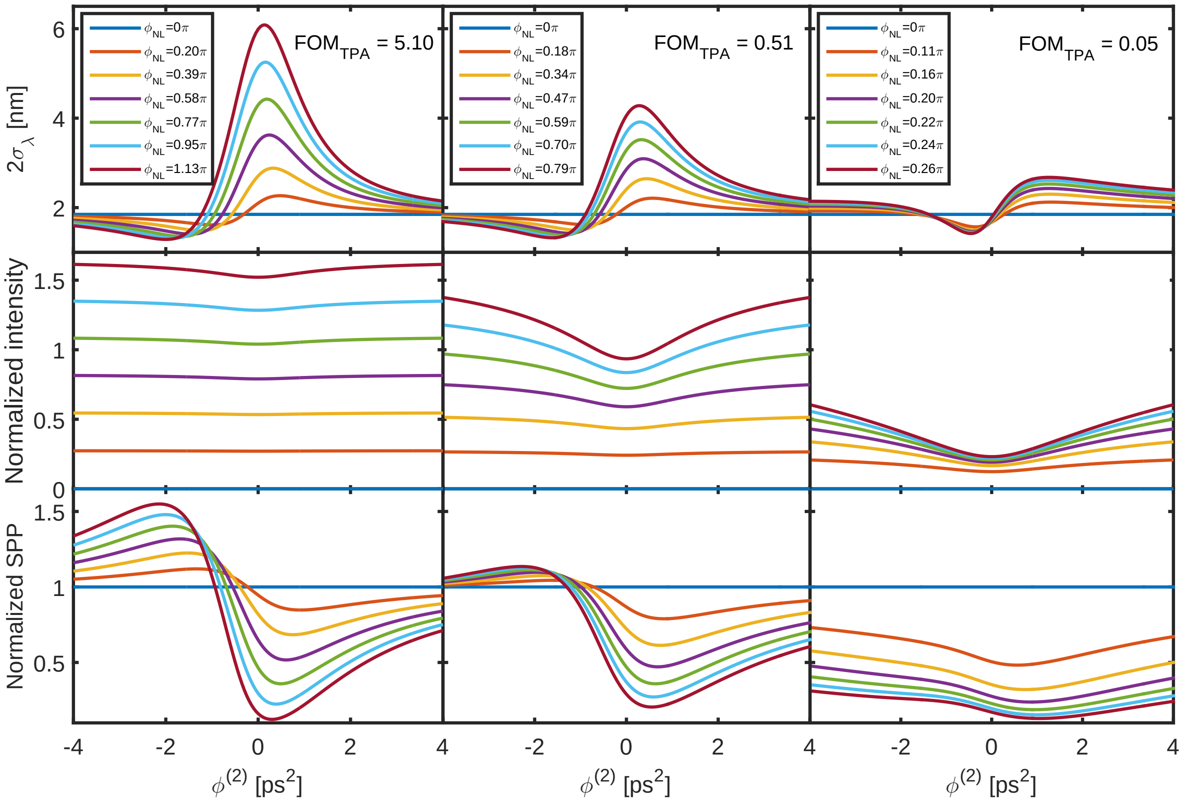

Figure 2.13: D-Scan response for different materials with one order of magnitude decrease of the FOM_{TPA}, the Kerr coefficient was maintained constant, each color correspond to the same input intensity. The gaussian pulse duration is set to 1ps (see the $2\sigma_\lambda$ baseline). The effective propagation length is of 5 mm.

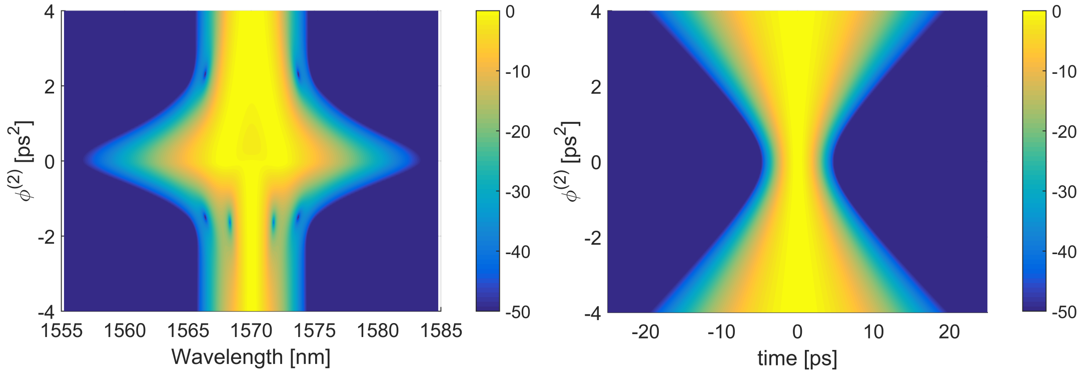

Figure 2.14: Output spectral and temporal characteristics for $\phi_{NL} = \pi$ with an input gaussian pulse. Colormap in dB.

(i.e. smaller $(2\sigma)_{\mathrm{p-v}}$). It is noteworthy that the intensity plot is symmetric, i.e. not influenced by the sign of the dispersion coefficient but from the effect on the pulse temporal duration. **The minimum transmitted power is obtained for the largest peak power, i.e. at $\phi^{(2)} = 0$ ps^2**. A given FOM_{TPA} will then give specific features under the D-Scan technique. Finally and as previously shown, a **negative Kerr material will inverse the curves with respect to the zero dispersion axis**.

In order to understand the effect in the pulse temporal and frequency domains, we have plotted in Fig. 2.14 a case where the nonlinear phase shift was set to π for a waveguide with $FOM_{TPA} = 5.10$. It can be seen that the pulse duration is symmetric with respect to the zero dispersion point where the duration is set to 1 ps. As we stretch the pulse in the time domain, the duration increases and due to energy conservation, the peak power decreases, so we can expect smaller nonlinear effects. In the spectral domain, the spectral broadening clearly decreases as the dispersion in absolute value largely increase. It can be confirmed that for **negative dispersion values close to zero**, there is a **spectral compression** which translates in larger peak power at the central frequency. Around zero dispersion the broadening starts to increase due to higher peak powers and for small positive dispersion, it can be noticed a decrease in the central peak power, even though the pulse duration for the negative counterpart is the same.

Now, we present in Fig. 2.15 the D-Scan curves in the case of a **sinus cardinal** temporal pulse. We have used a Fourier limited pulse with duration of $T_0 = 1$ ps and the same conditions used with the gaussian profile (Fig. 2.13). We have intentionally reduced the dispersion span from 4 to 3 ps^2, due to the presence of the peak and valley points for smaller dispersion values.

Some interesting features are evident, for instance in the case of $FOM_{TPA} = 0.05$, the valley in the 2σ curves overpasses the baseline and the curve tends to a symmetric shape. In the case of the intensity curves, a pronounced deep is present at zero dispersion, as expected the curve is symmetric with respect to $\phi^{(2)} = 0$ ps^2 (as the pulse duration).

In Fig. 2.16, we display the frequency evolution as a function of the dispersion for a temporal sinus cardinal pulse reaching a nonlinear phase shift of π in a waveguide with $FOM_{TPA} = 5.10$. We can see in the frequency domain a top-hat beam presenting larger broadenings around the zero dispersion point, whereas for the central wavelength (SPP), a peak in the negative and a valley in the positive regimes is more evident than in the gaussian case. It is also important to confirm that the interesting features are obtained for smaller dispersions compared to the gaussian case. In the temporal domain a sinus cardinal pulse with symmetric broadening is shown.

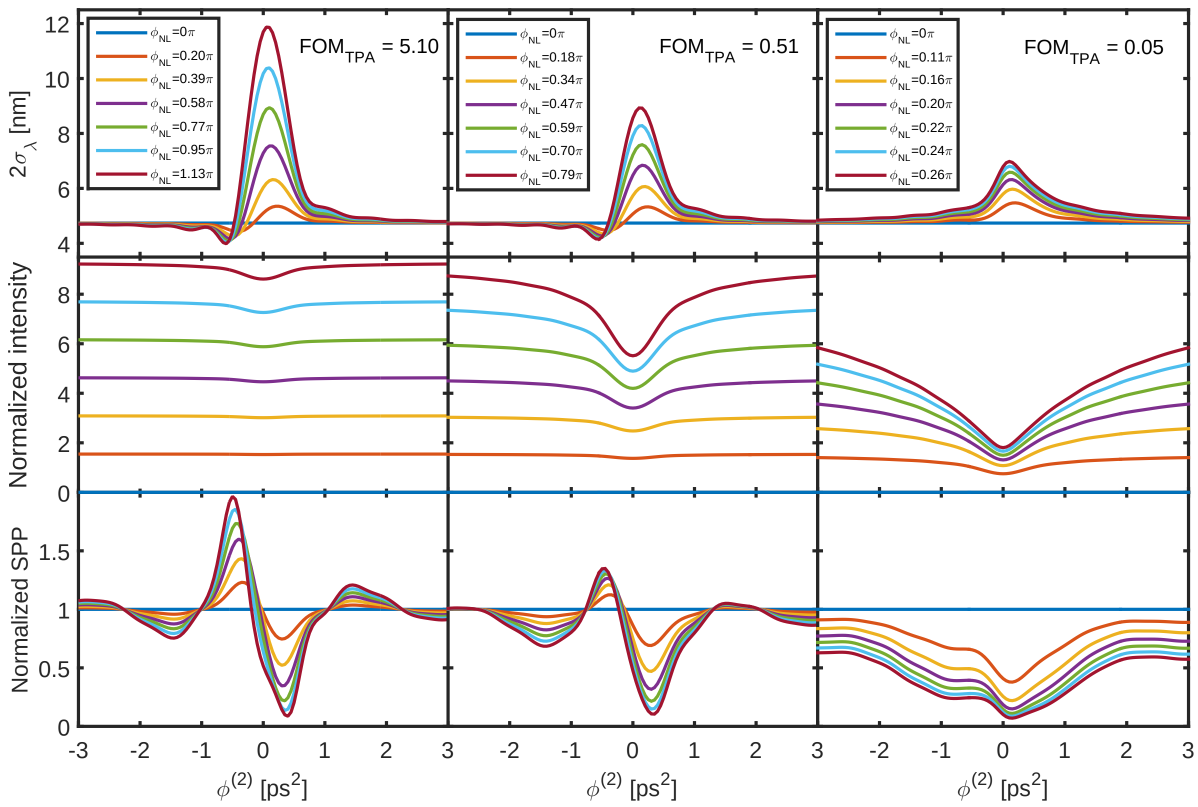

Figure 2.15: D-Scan response for different materials with one order of magnitude decrease of the FOM_{TPA}, the Kerr coefficient was maintained constant, each color correspond to the same input intensity. The sinus cardinal pulse duration is set to 1ps (see the $2\sigma_\lambda$ baseline). The effective propagation length is set to 5 mm.

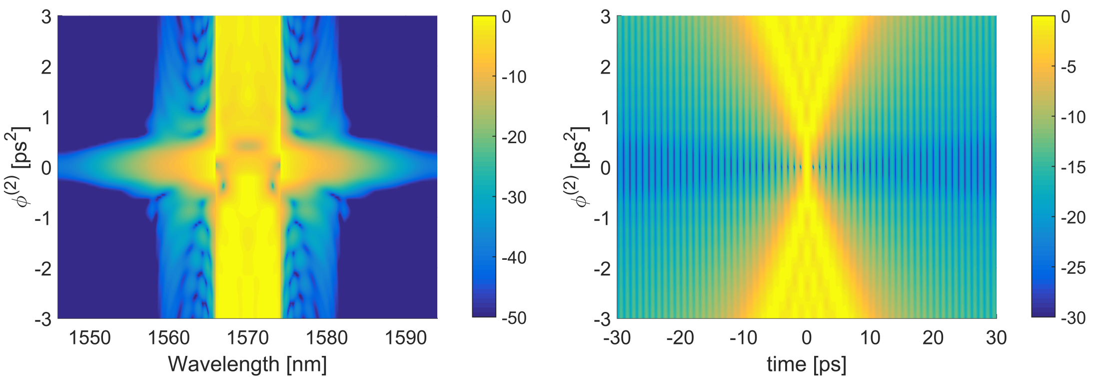

Figure 2.16: Output spectral and temporal characteristics for $\phi_{NL} = \pi$ with an input sinus cardinal pulse. Colormap in dB.

Retrieve of FOM_{TPA}

Up to now, we have presented the trends of the spectral evolution in the nonlinear regime for two different pulse shapes with the presence of TPA. **We can relate the simulation tool with experimental quantities in order to retrieve the nonlinear properties of the waveguide**. To this aim, we will use the peak-to-valley difference in the r.m.s. spectral linewidth $(2\sigma)_{\mathrm{p-v}}$. We recall Eq. (2.20) and (2.23) from where we confirm that $\beta_{\mathrm{TPA}} I_0 L_{\mathrm{eff}} = P_{\mathrm{in}} b/a$.

For each value of $(2\sigma)_{\mathrm{p-v}}$, the experimental parameter $2\pi \ln(1 + P_{in} b/a)$ can be linked to a value of ϕ_{NL} as shown in Fig. 2.17. The slope of a line between $2\pi \ln(1 + P_{in} b/a)$ vs. ϕ_{NL} gives directly the FOM_{TPA} value. The procedure then requires the knowledge of the $(2\sigma)_{\mathrm{p-v}}$ evolution for different input powers, but to determine the FOM_{TPA} does not require the knowledge of the coupling efficiencies, as their are implicit in the b/a ratio.

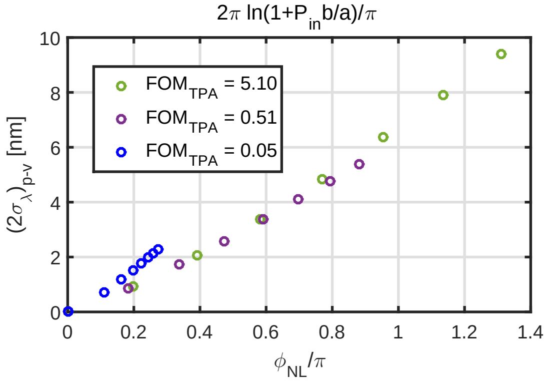

Figure 2.17: $(2\sigma)_{\mathrm{p-v}}$ for different nonlinear materials as a function of ϕ_{NL}/π. In the upper axis the corresponding experimental points given by the TPA analysis.

2.4 Experimental set-up

The experimental bench consists of a mode-locked erbium-doped fiber laser emitting pulses with a repetition rate of $F = 50$MHz, the initial pulses are Fourier limited with pulse duration of 150 fs and maximum average power of 182 mW. The output amplified pulse is collimated and sent through a grating based stretcher that will change its temporal and frequency characteristics.

Pulse shaper

The chosen stretcher configuration offers the possibility to adjust the outgoing pulse spectral linewidth and chirp coefficient. It is built with a folded system based on a diffraction grating and an optical lens to modify the dispersion sign [94]. As shown in Fig. 2.18, the pulse shaper comprises a diffraction grating followed by a doublet lens and a mirror located at the focal plane distance f. A roof prism is used as retro-reflector to fold the system. The spectral bandwidth of the pulses is adjusted by means of a slit set in front of the mirror.

The behavior of the set-up can be easily understood if we first consider that the grating and the mirror are located at the object and image focal planes of the lens respectively. Following the dispersion effect of the grating, each spectral component of the incident pulse (represented in Fig. 2.18 in the visible window) is focused in the image focal plane of the lens. The spectral components of the incoming pulse are then spatially distributed along the mirror with a constant phase relationship, meaning that no dispersion is

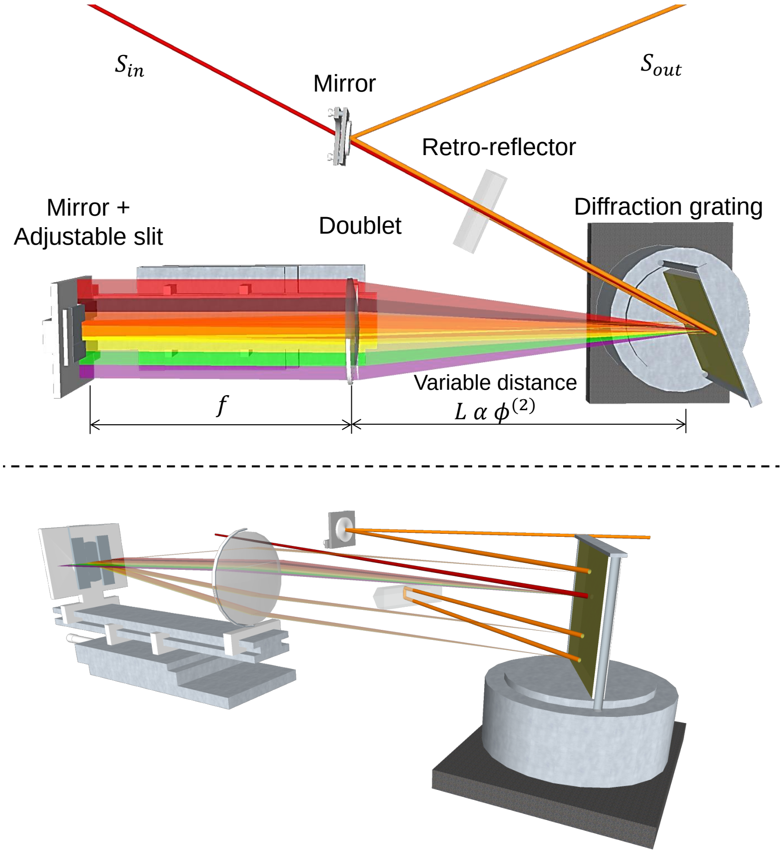

Figure 2.18: Four passages pulse shaper. View from the top, discriminating the different optical elements and the most important variables. Bottom: auxiliary tilted view to appreciate the different passages through the grating.

introduced. However, the spectral linewidth of the output pulse can be controlled by adjusting the slit width placed in front of the mirror. In order to spatially separate the outgoing pulse, the input pulse is sent above the optical axis of the lens such that the beam is reflected back to the grating at a lower height (we have added an additional tilted view in Fig. 2.18 to clarify the height difference). The beam is diffracted and reflected back into the set-up at an even lower height by means of a roof prism. By doing so, the shaped pulse exits at a height higher than the incoming beam to facilitate its extraction. This set-up is actually the folded version of the 4-f set-up introduced by C. Froehly et al. in [95].

The 2nd order dispersion coefficient $\phi^{(2)}$ is introduced by varying the distance L between the lens-mirror-slit set-up and the grating around the focal distance f using a variable mechanical stage. By doing so, a curvature of the front wave is introduced at the mirror location with a sign varying for the distance L set towards the focal distance. Because the spatial distribution of the beam at the mirror mimics its spectral distribution, the front wave distortion equivalently introduces a spectral phase of the form $e^{\imath\phi^{(2)}\omega^2}$. By either using a ray-optics based calculation or the more complete theoretical description given in [94], one can show that $\phi^{(2)} = \frac{-8\pi^2 c(L-f)}{\Lambda^2\omega^3\cos^2\theta_R}$, where Λ and θ_R are respectively the grating period and the first-order diffraction angle. It is worth noting that this formula is similar to the dispersion achieved with a pair of gratings set-up separated by a distance g (instead of $L-f$) [96]. The main difference being that the sign of the dispersion is always negative in the later, whereas it can be adjusted in the former through the sign of the quantity $L-f$.

We selected a 1200 lines/mm grating that exhibits, for TE-polarized light, a diffraction efficiency in the Littrow configuration higher than 85 % in the spectral range 1520-1580 nm. The doublet lens has a focal lens $f = 20$ cm. **Following these parameters, few ps^2 dispersion coefficient should be reached by varying the distance L towards the focal plane by a quantity around 10 mm**. A more detailed description of the optical performance of each component could be found in [93].

A typical spectrum of the outgoing pulse is reported in the Fig. 2.19 showing an almost rectangular-shaped form, in this case with a bandwidth set to 6.5 nm. The spectrum was measured with an optical spectrum analyzer (OSA) and the temporal curve was obtained with an autocorrelator. In red there is a fit of a 32$^{\text{nd}}$ order supergaussian in the spectral domain and the autocorrelation of its Fourier transform in the temporal domain.

Numerical simulation of the input chirped spectrum

As shown in Fig. 2.19, an initial super-gaussian shaped pulse properly reproduces the effect of the lossless dispersive medium in the spectral domain and retrieves the autocorrelation duration for the Fourier limited case. As the pulse spectral components

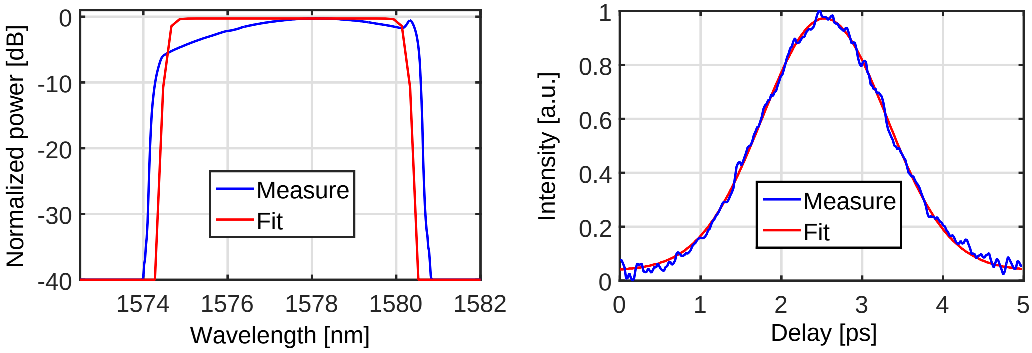

Figure 2.19: Characteristic spectrum and autocorrelation measurements with a supergaussian fit in the spectral domain and its corresponding Fourier transform in the temporal domain.

are affected by a phase $\varphi(\omega)$, it is convenient to operate in the frequency domain. The spectral phase shift introduced by a dispersive material is given by $\varphi(\omega) = \frac{n(\omega)\omega L}{c}$, where $n(\omega)$ is the refractive index and L the propagation length. So the chirped pulse following the introduced dispersion takes the form:

$$S_{\text{chirped}}(\omega) = S_{\text{initial}}(\omega) \exp\left[i\varphi(\omega)\right] \tag{2.25}$$

where $S_{\text{chirped}}(\omega) = \mathscr{F}[s_{\text{chirped}}(t)]$ and $S_{\text{initial}}(\omega) = \mathscr{F}[s_{\text{initial}}(t)]$, $\mathscr{F}$ denoting the Fourier Transform operator. Assuming the pulse spectral width small compared to the central frequency, the phase could be developed in Taylor's expansion around ω_0:

$$\varphi(\omega) = \varphi(\omega_0) + \Delta\omega \frac{d\varphi}{d\omega}\Big|_{\omega_0} + \frac{\Delta\omega^2}{2}\frac{d^2\varphi}{d\omega^2}\Big|_{\omega_0} + \frac{\Delta\omega^3}{6}\frac{d^3\varphi}{d\omega^3}\Big|_{\omega_0} + \ldots = \sum_{n=0}^{\infty} \frac{\Delta\omega^n}{n!}\frac{d^n\varphi}{d\omega^n}\Big|_{\omega_0} \tag{2.26}$$

where $\Delta\omega = \omega - \omega_0$. The notation $\varphi^{(n)} = \frac{d^n\varphi}{d\omega^n}\Big|_{\omega_0}$ will be adopted in the following. The effects of $\varphi(\omega_0)$ and $\varphi^{(1)}$ during the propagation of the pulse in the dispersive medium will be neglected, because $\varphi^{(1)}$ introduces a pure group delay. Since the second order dispersion introduced by the set-up is small, higher order dispersive effects can be neglected (unless specified), and the expression for the chirped pulsed follows:

$$S_{\text{chirped}}(\omega) = S_{initial}(\omega) \exp\left[i\frac{1}{2}\Delta\omega^2\varphi^{(2)}\right] \tag{2.27}$$

As can be appreciated in Eq. (2.27), the spectrum (in frequency domain) is multiplied by a second order phase term, so the power distribution over the frequencies is not affected. Next, a Fourier transform is performed ($s_{\text{chirped}}(t) = \mathscr{F}[S_{\text{chirped}}(\omega)] =$

$\mathscr{F}\left\{S_{initial}(\omega)\exp\left[i\frac{1}{2}\Delta\omega^2\varphi^{(2)}\right]\right\})$. A Matlab code is presented in section D.1. It was used to calculate the FWHM autocorrelation duration for a input spectrum. The calculated chirped temporal spectrum is multiplied by its complex conjugate to determine the intensity and measure the FWHM duration of its autocorrelation that is plotted as a function of the second order dispersion term in the upper axis of Fig. 2.20 and 2.21, the two figures correspond to two different pulse linewidths.

The full width at half maximum (FWHM) of the autocorrelation traces recorded experimentally for the stage positions varying over 25 mm is plotted with open circles in the Fig. 2.20 . The stage position at "0 mm" coincides with the largest separation between the grating and the lens. The symmetric shape of the curve shows that the pulses do not suffer from any nonlinear phase distortion that could have been introduced in the fiber laser module. In order to determine the relation between the stage position and the dispersion coefficient $\phi^{(2)}$, the auto-correlation traces of a linearly chirped rectangular shape pulse spectrum (with a linewidth set at the maximum and minimum slit dimension) have been numerically calculated for various $\phi^{(2)}$ values. The curve for the simulated FWHM autocorrelation width corresponding to a spectral width of around 7 nm for $\phi^{(2)}$ varying from -3 to +3 ps^2 is reported in Fig. 2.20 with red solid line. **The perfect adjustment between the measured (in blue dots) and the expected pulse durations proves that the pulses we generate respect the Fourier limit and that higher order dispersion effects are negligible**. Especially, for $\phi^{(2)} = 0\text{ps}^2$ we verify that the autocorrelation pulse duration is 2 ps, close to the Fourier-limit, which coincides to a pulse duration of 1.1 ps. We are now able to **connect the stage position with the dispersion coefficient as shown in the fits of Fig. 2.20 and 2.21, which exhibit linear dependence with slopes for the maximum and minimum slits equal to 2.25 ± 0.02 ps^2/cm and 2.38 ± 0.02 ps^2/cm respectively**. The accuracy is limited by that of the stage position control estimated to 100 μm.

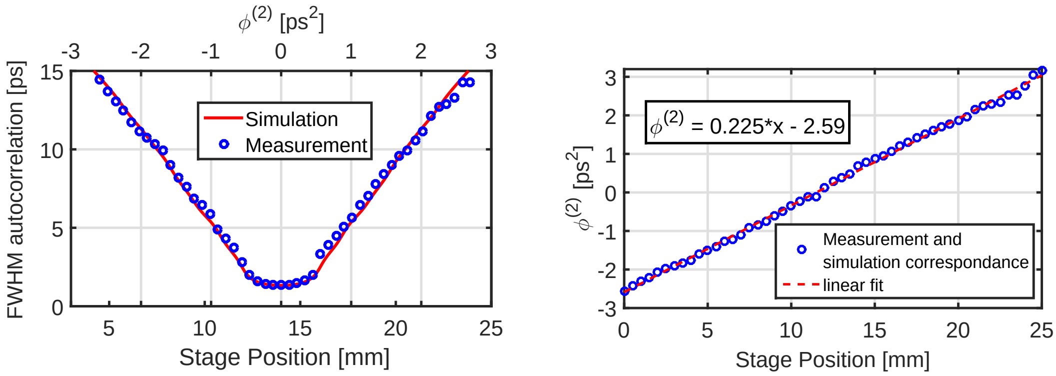

Figure 2.20: Left: Measured and simulated FWHM duration for the maximum opened slit (around 7 nm spectral width). Right: Calibration of the introduced dispersion as a function of the stage position.

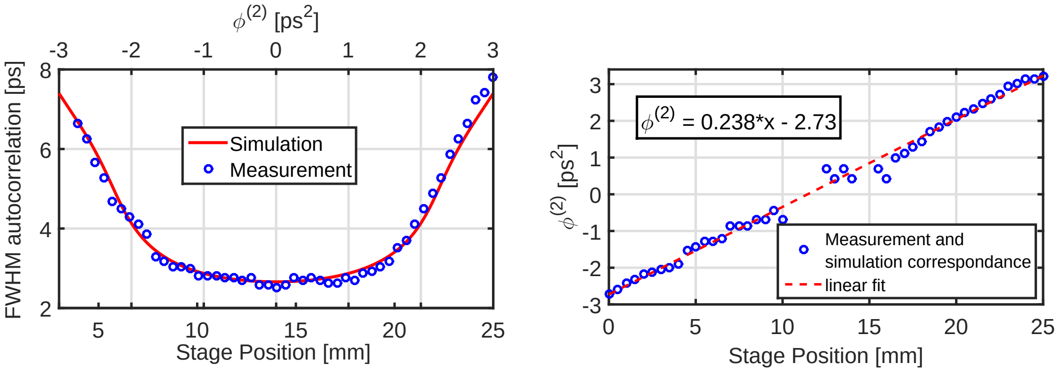

Figure 2.21: Left: Measured and simulated FWHM duration for the minimum opened slit (around 3.7 nm spectral width). Right: Calibration of the introduced dispersion as a function of the stage position.

In our case we will be interested in dispersion coefficients comprised between +3 and -3 ps^2, coinciding with the range which has been simulated for the D-Scan method in section 2.3. **This result shows that the set-up is able to introduce a very precise second order dispersion where its sign is also adjustable**.

In Fig. 2.22, we superimposed the output spectra in dBm for a second order dispersion range of 6 ps^2 following the injection of the chirped beam inside a SOI strip waveguides at low powers in order to avoid any nonlinear effect. The perfect superimposition of the output spectra demonstrate the proper alignment of the stretcher respect to the injection set-up and shows negligible variation in the coupling efficiency while varying the pulse dispersion. We present the spectra in (a) dBm to highlight the sharp edges (top-hat beam) and in (b) linear to compare the variation of power (<8%).

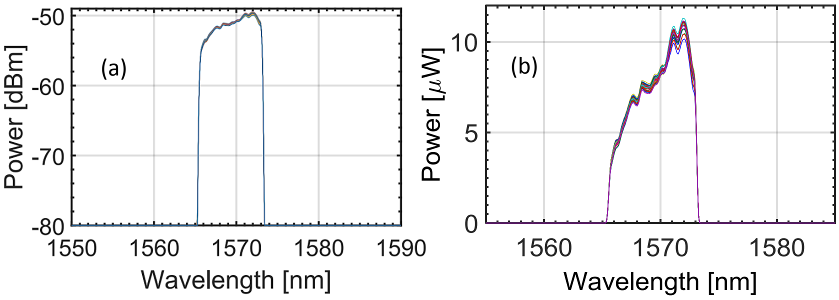

Figure 2.22: Overlap of 26 transmission spectra at low power measured trough a SOI strip waveguide varying the stage position from 0 to 25 mm with a step of 1 mm ($\phi^{(2)}$ between +3 and -3 ps^2) in (a) dBm and (b) linear scales.

2.4.1 Injection Fiber characterization

In some of the coming experiences, we will use the bi-directional method introduced in section 2.2. We have introduced polarization maintaining fibers (PMF) to guaranty a monomode operation and a symmetric set-up. First, we will characterize them in the picosecond nonlinear regime in order the quantify its contribution to the measurement. To do so, we have implemented the set-up shown in Fig. 2.23. The pulse stretcher output is injected inside the fiber with a x10 microscope objective.

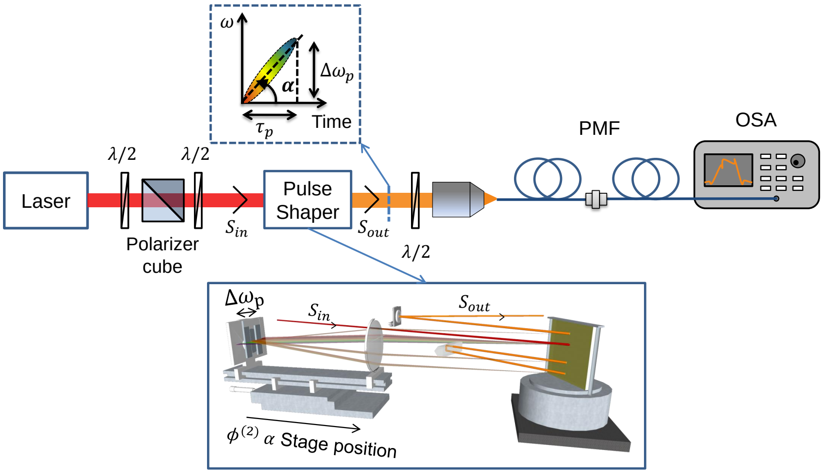

Figure 2.23: Experimental set-up injecting the light from 2 meters of polarization maintaining fibers (PMF) used for the double side injection.

We have measured the output power as a function of different input powers for 1 m and 2 m fiber lengths. In Fig. 2.24 we display the expected linear trends as there is no TPA in silica at the wavelength used ($\lambda \sim 1570$ nm).

From the slope of the lines, the efficiency could be estimated as a third of the input power (i.e. for 9 mW injected, we can expect 3 mW in the output). All of this measurements

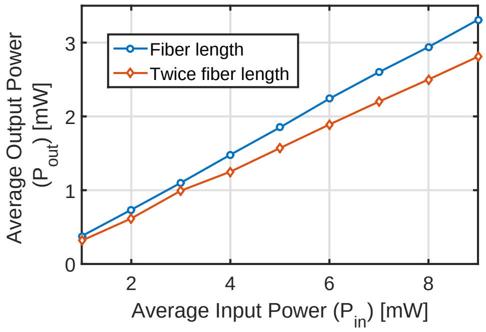

Figure 2.24: Output power as a function of the input power for two different lengths (1 m and 2 m) of polarization maintaining fibers.

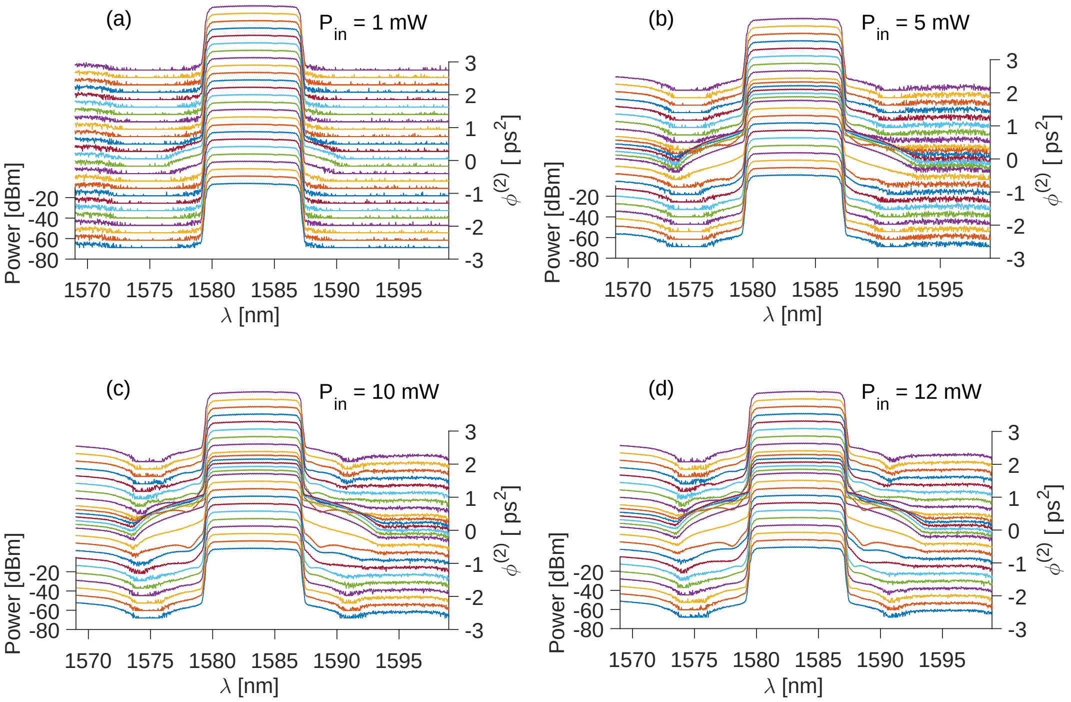

Figure 2.25: Output spectra of a two meters fiber at variable dispersion for different average input powers: (a) 1 mW, (b) 5 mW, (c) 10 mW and (d) 12 mW.

were performed at zero dispersion point ($L = f$), so with Fourier limited pulses. Although the Kerr coefficient in Silica is about 200 time smaller than that in silicon, it is necessary to evaluate the Kerr contribution of the silica fiber in the spectral broadening that will be measured with the set-up. In Fig. 2.25, we show the SPM spectral broadening measured at the output fiber for a square-like input pulse as a function of the introduced dispersion for 4 different input powers (1 mW, 5 mW, 10 mW and 12 mW). It can be noticed that a larger spectral broadening effect is observed around zero dispersion, as it coincides with shorter pulse durations. One can refer to Fig. 2.16 in order to highlight similarity in the spectral evolution as a function of the introduced dispersion.

The different spectral measurements are recorded with a resolution of 0.5 nm over a span of 30 nm in 1001 number of points (N) by using an optical spectrum analyzer (OSA) Ando AQ66317. With those values we can obtain the average output power by a discrete integration over the spectra:

$$P_{\text{out}}[\text{mW}] = \frac{Span}{Res \times \text{N}} \sum_{i=1}^{\text{N}} 10^{P_i/10}. \tag{2.28}$$

Finally, we can use the r.m.s. spectral linewidth expression to quantify the spectral

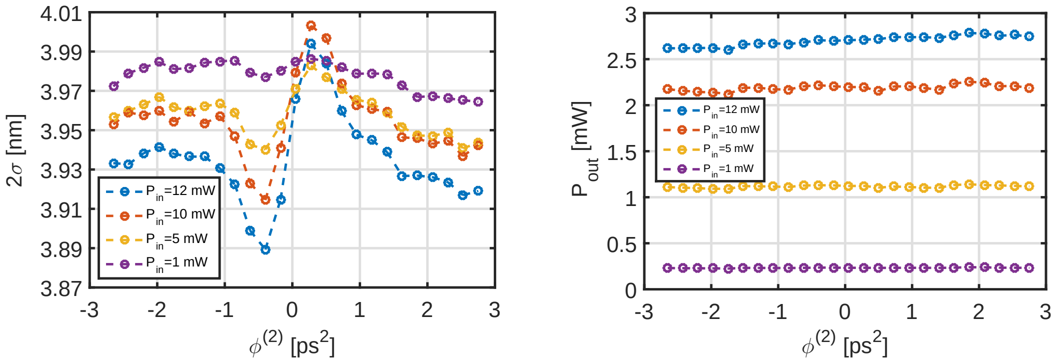

Figure 2.26: $2\sigma^{(2)}$ and P_{out} plots as a function of the dispersion for different input powers for 2 m silica fiber. The curvature show a characteristic positive Kerr material.

broadening as a function of the introduced dispersion at different powers. As it is well known, the nonlinear Kerr refractive index of silica is positive, so we would expect trends as the ones shown in Fig. 2.8.

The tendencies shown in Fig. 2.26 demonstrate the versatility of the top hat D-Scan technique, as it could be applied to fiber configurations and is able to detect Kerr coefficients as low as the one of Silica, at least one order of magnitude smaller than the typical materials used throughout this thesis. We can also estimate from the curves some uncertainties, in the case of 2σ is of around ± 0.03 nm. From the power plot, we can notice the absence of nonlinear absorption as a function of the pulse duration (chirp) as expected for silica. At the same time, the broadening contribution from the fibers will be taken into account in the following D-Scan experiments with nano-waveguides. Nevertheless, we should notice that their contribution can be neglected for middle powers and nonlinear waveguides based on silicon, chalcogenide or silicon-germanium alloys that exhibit nonlinear susceptibilities more than 5 orders of magnitude larger [97] than silica fibers, due to larger nonlinear material coefficients and smaller effective areas. On the other hand, materials with lower nonlinear effective phase shift such as silicon nitride will be more difficult to measure following this approach, and thus we will propose some variations and further numerical treatment.

2.4.2 Set-up configurations

In Fig. 2.27 and 2.28, we present the set-up for the double side injection. Microscope objectives are used to inject and collimate the light inside and outside the fibers and the waveguides, respectively with magnifications of ×10 and ×60. It can be appreciated that the fiber allows a symmetric configuration making the proposed set-up adequate to perform the techniques introduced at the beginning of the chapter. We have used the super-indices (1) and (2) to denote the two different injection directions, at the same time, the letters A and B denote the two facet sides of the sample.

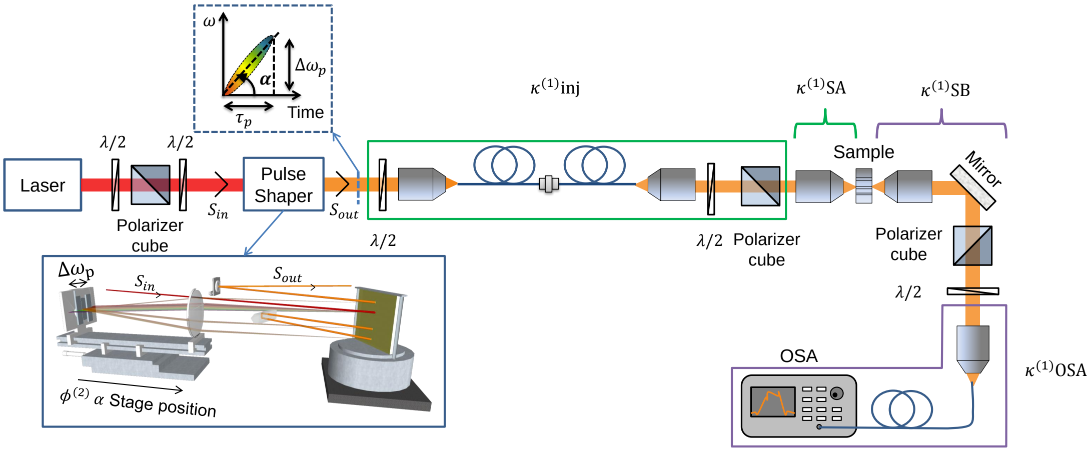

Figure 2.27: Experimental set-up injecting the light from 2 meters of polarization maintaining fibers and the input side the facet A. $\kappa_A^{(1)} = \kappa_{inj}^{(1)}\kappa_{SA}^{(1)}$ and $\kappa_B^{(1)} = \kappa_{OSA}^{(1)}\kappa_{SB}^{(1)}$.

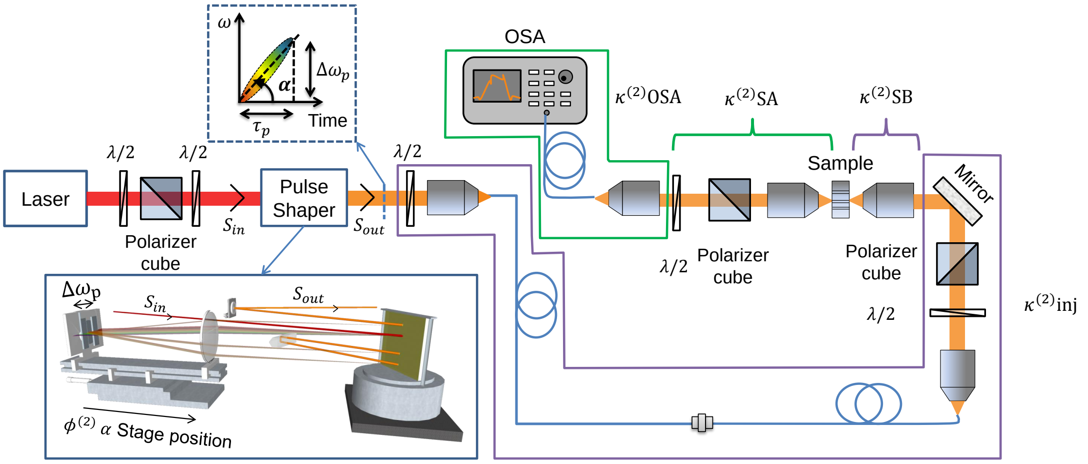

Figure 2.28: Experimental set-up injecting the light from 2 meters of polarization maintaining fibers and the input side the facet B. $\kappa_B^{(2)} = \kappa_{inj}^{(2)}\kappa_{SB}^{(2)}$ and $\kappa_A^{(2)} = \kappa_{OSA}^{(2)}\kappa_{SA}^{(2)}$.

2.5 Methods validation with a SOI strip waveguide

Hereby we present the first experimental measurements in integrated waveguides. We want to validate the proposed technique and set-up by using a squared-like Fourier limited pulse when traveling through a highly nonlinear lossy material. Silicon is a well-known material with large third order nonlinear properties.

To illustrate the two photon absorption process we have chosen monomode strip waveguide with typical geometrical values, 260 nm height, 450 nm wide. For the first test, we have removed the injection fiber to increase the available power. In Fig. 2.29, we have plotted the output spectra for input powers varying from 0.1 to 13 mW and the output power (measured after integration of the output spectra) as a function of the input power (measured with a powermeter). Our objective is to evaluate the energy of the injected pulses from the analysis of the nonlinear transmission.

From the curves in Fig. 2.29, we can appreciate the symmetric spectral broadening characteristic of a self-phase modulation induced by a pure optical Kerr effect. At this point it is clear that the sensitivity to measure new generated frequencies is higher with a rectangular like spectral shape (like in a double truncated spectrum) than in a gaussian shape. For powers larger than 10 mW, the spectra present an evident blue shift which is a characteristic of the refractive effect induced by the two-photon generated free carriers. On the transmission curve (right side graph in Fig. 2.29), we have added a red dashed line to show the expected linear behavior. The output power exhibits a saturation characteristic from a nonlinear absorption effect (losses that depend on the intensity). In the case of the chosen silicon waveguide, the maximum output power is around 4 μW. This unbreakable maximum power is a limit for the achievable nonlinear phase shift, so this curve is at the origin of the limitations of silicon for integrated nonlinear optics.

Now, we will use Eq. (2.8) to find two terms: the slope associated with the imaginary part of the third order susceptibility and a constant term depending on the coupling coefficients and linear propagation losses. In Fig. 2.30, we show the plot of P_{in}/P_{out} as a function of P_{in} with the respective linear fit and equation.

The linear fit of the experimental data gives the following parameters $a = 923.6$ and $b = 176.2$ mW^{-1} are estimated. Hereafter, our objective is also to get an estimation of the coupling efficiencies. To do so, the TPA coefficient is kept as a known parameter, equal to $\beta_{\text{TPA}} \approx 8 \times 10^{-12}$ m/W. In this process, the input coupling efficiency plays a

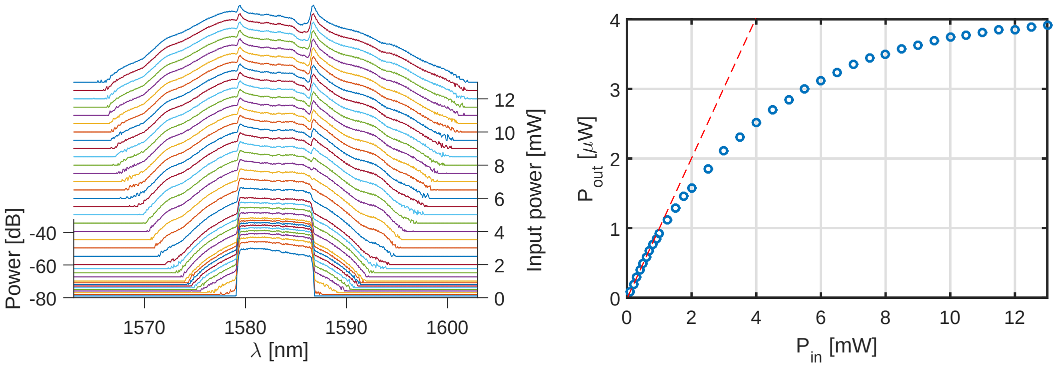

Figure 2.29: Left: Output spectra as a function of the input power for picosecond regime pulses. Right: Input vs. Output Power for a silicon strip monomode waveguide.

major role and could be easily found from the previous expressions (i.e. Eq. (2.9)):

$$\kappa_{\text{in}} = \frac{b}{a} \frac{A_{\text{NL}}}{S^2 \beta_{\text{TPA}} \eta L_{\text{eff}}} \tag{2.29}$$

Using the relation between the average power and the peak power, the power coupled inside the waveguide is calculated:

$$P_{\text{peak inj}} = \kappa_{\text{in}} \eta P_{\text{aver inj}} \tag{2.30}$$

Merging the previous two expressions gives the relation between the incident power (measured experimentally) and the injected power we need to assess:

$$P_{\text{peak inj}} = P_{\text{aver inj}} \frac{b}{a} \frac{A_{\text{NL}}}{S^2 \beta_{\text{TPA}} L_{\text{eff}}} \tag{2.31}$$

By taking the following parameters: $A_{\text{NL}} \approx 0.12\,\mu\text{m}^2$, $L_{\text{eff}} \approx 0.64\,\text{mm}$, $S \approx 1.46$ and $P_{\text{aver inj}} = 10\,\text{mW}$, we can estimate the injected peak power :

$$\boxed{P_{\text{peak inj}} \approx 20\,\text{W}} \tag{2.32}$$

In terms of coupling efficiencies, it corresponds to $\kappa_{in} \approx 10\%$. Similarly, the injected peak intensity $I(0)$ is connected to the input power $P_{in} = P_{\text{aver inj}}$ through the relation $I(0) = \kappa_{in} P_{in} \eta / A_{\text{NL}}$, so the typical intensity in the silicon strip waveguide is in the order

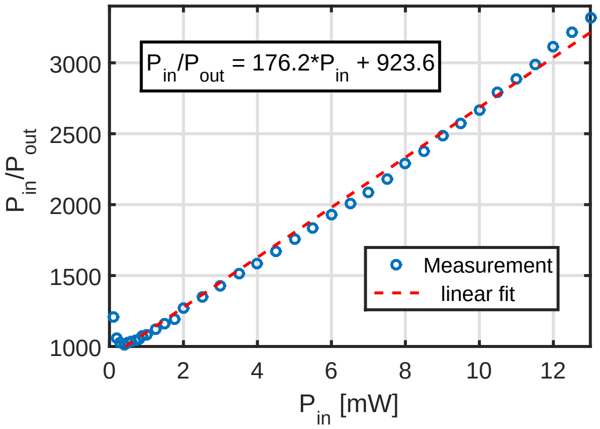

Figure 2.30: P_{in}/P_{out} as a function of P_{in} in a SOI strip waveguide, showing the linear fit in red and corresponding function.

of $I(0) \approx 165 * 10^{12}$ W/m$^2 = 16.5$ GW/cm^2, corresponding to an injected energy in the order of few pJ. The latest values strongly depend on the geometry, fabrication and material of the waveguides, but they give a hint of the small coupling and the importance of the accuracy in this measurement because only 1% difference in the injection could drastically modify the results.

The impossibility to experimentally determine all the parameters of the experiment (especially the TPA coefficient) under the present conditions, requires a specific procedure to determine the injected power (i.e. coupling efficiencies), so we will apply the technique proposed in section 2.2.

2.5.1 Silicon strip bi-directional nonlinear transmission

Here, we have chosen a standard SOI waveguide with no tapers (i.e. a constant cross section) with the geometrical parameters: height equals to 340 nm, width of 520 mn and geometrical length of 1 cm. It is a standard monomode strip waveguide and the transverse distribution of the fundamental TE mode is presented in Fig. 2.31.

First, we performed the experiment at zero dispersion injecting the pulse from a fiber as shown in the the set-up configurations depicted in Fig. 2.27 and Fig. 2.28. In Fig. 2.31, we use the superindices (1) and (2) to denote injection from facet A and facet B of the sample respectively. The evolution of the spectral broadening is presented, in the left, when injecting from side A and in the right from B. The spectral broadening induced by SPM is noticeable for input powers larger than 1.5 mW. The symmetry in all the spectra is characteristic from a SPM effect. From the recorded output spectra, it can be seen that the injection from the facet A is more efficient than that from the side B. This strong difference question the assumption of symmetric coupling (injection is the same from both sides) currently used in literature. The measured ratio P_{in}/P_{out} is plotted in terms of P_{in} for the two injection senses in order to find the linear parameters a and b from the linear trends. The experimental coefficients are $a^{(1)} = 17605 \pm 184$, $b^{(1)} = (1058.7 \pm 34.5)$ mW^{-1}, $a^{(2)} = 14967 \pm 162$ and $b^{(2)} = (314.3 \pm 30.4)$ mW^{-1}. Finally, the mode calculation allowed the estimation of an effective area of 0.107 μm^2 by using the vectorial expression in Eq. (1.72).

The relations to measure the coupling efficiencies, found for the bidirectional method (Eq. 2.12) can be easily adapted to our configuration, such that for the case (1): $\kappa_{\text{in}}^{(1)} = \kappa_{\text{inj}}^{(1)} \kappa_{\text{SA}}$ and $\kappa_{\text{out}}^{(1)} = \kappa_{\text{SB}} \kappa_{\text{OSA}}^{(1)}$[1], where κ_{SA} and κ_{SB} stand for the coupling efficiencies of the facet

---

[1] It is easy to demonstrate that the relation $\frac{a^{(1)}}{a^{(2)}} = \frac{\kappa_{inj}^{(2)} \kappa_{OSA}^{(2)}}{\kappa_{inj}^{(1)} \kappa_{OSA}^{(1)}} =$ constant, must be valid for all the cases.

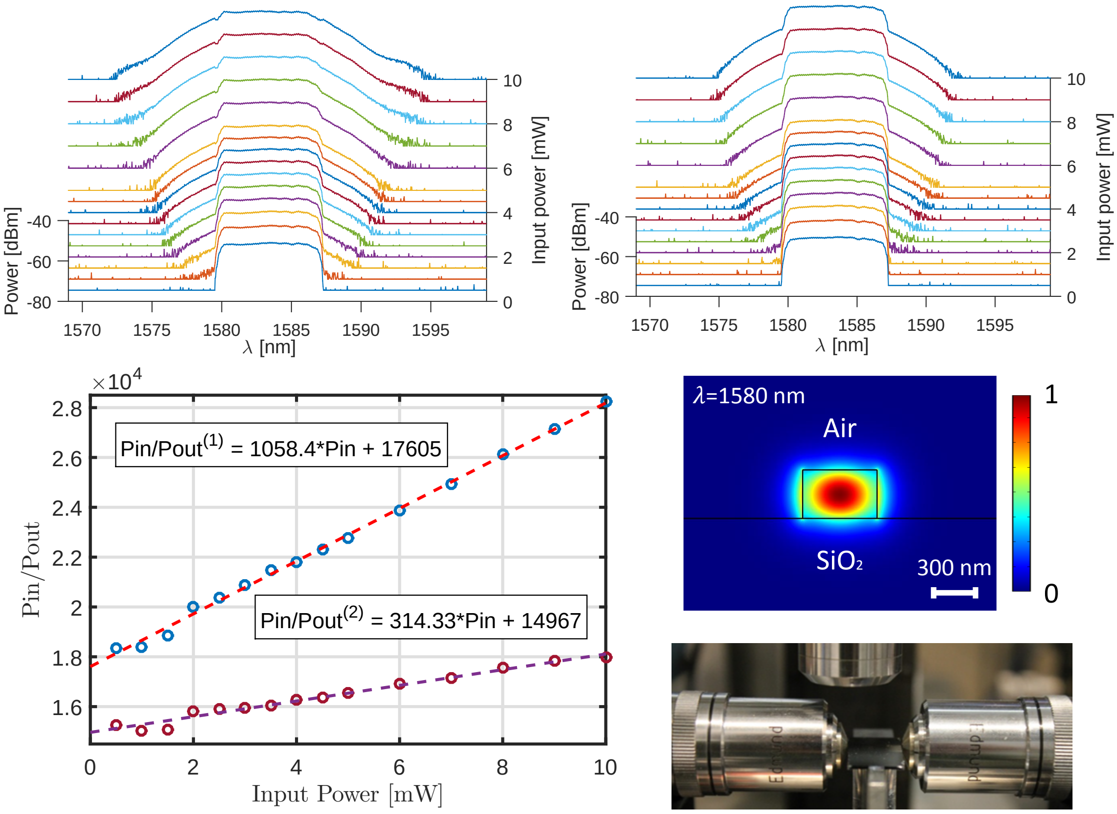

Figure 2.31: Spectra at zero dispersion for different powers when injecting by the facet A (Top-left) and B (Top-right). We display the linear tendencies and relations for P_{in}/P_{out} vs. P_{in} (Bottom-left) and the transverse distribution of the fundamental TE mode and a picture of the injection and collection microscope objectives with the sample (Bottom-right).

A and B. Analogously for the case (2).

$$\boxed{(\kappa_{\mathrm{SA}})^2 = \frac{b^{(1)}}{b^{(2)} a^{(1)} \kappa_{inj}^{(1)} \kappa_{OSA}^{(2)} \exp(-\alpha_l L)}} \boxed{(\kappa_{\mathrm{SB}})^2 = \frac{b^{(2)}}{b^{(1)} a^{(2)} \kappa_{inj}^{(2)} \kappa_{OSA}^{(1)} \exp(-\alpha_l L)}} \quad (2.33)$$

In this configuration the coupling efficiencies were verified and the linear losses and group index were estimated through the Fabry-Perot method, the values obtained are: $\kappa_{inj}^{(1)} = 27\%, \kappa_{OSA}^{(1)} = 22\%, \kappa_{inj}^{(2)} = 24\%, \kappa_{OSA}^{(2)} = 29\%, \alpha = 0.5\ \mathrm{cm}^{-1}, n_g = 3.8$. Finally, with the values of b and a in both experiences, coupling coefficients of $\kappa_{SA} = (6.4 \pm 0.4)\%$ and $\kappa_{SB} = (2.5 \pm 0.2)\%$, which are in the order of magnitude estimated in the previous section.

Now, we can measure the effective TPA parameter of the waveguide: $\gamma_{TPA}^{wg} = \beta_{TPA}^{bulk} S^2 / A_{\mathrm{NL}}$,

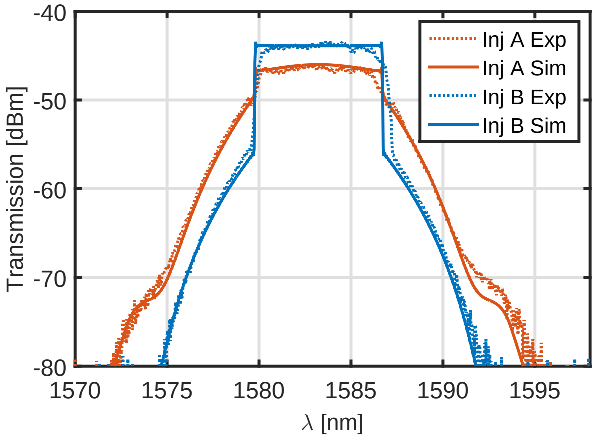

Figure 2.32: Comparison between the output spectra when injecting the same power from both facets in experiments and simulations.

with units of $(\mathrm{Wm})^{-1}$. Indeed, as we know the injection efficiencies and the parameters a and b from each injection case, we can use the expression (2.9) to measure the effective parameter in each configuration independently. Taking into account that the pulse duration is 1.20 ps (verified with simulations for the respective FT width), then $\eta \approx 16600$. We have an effective parameter for the strip waveguide of $\gamma_{TPA}^{1\mathrm{cm}(1)} \approx 26.8\ (\mathrm{Wm})^{-1}$, $\gamma_{TPA}^{1\mathrm{cm}(2)} \approx 26.9\ (\mathrm{Wm})^{-1}$, **with a calculated uncertainty of 9%,** $\gamma_{TPA}^{1\mathrm{cm}} \approx 27 \pm 2\ (\mathrm{Wm})^{-1}$. As expected, the measured value is independent of the injection side because it corresponds to a parameter linked to the waveguide.

To verify the results, we have simulated the broadening effect for the given injection efficiency with the same initial power and by considering $n_2 = 4 \times 10^{-18}\ \mathrm{m}^2/\mathrm{W}$, which is in the order of magnitude of the values given in the literature [98]. The two experimental spectra at 10 mW input power are shown in Fig. 2.32. It can be seen that the broadening is larger when side A is used as there is a broader spectrum generated by self-phase modulation and a lower global transmission, because the losses due to TPA are also larger. It is also important to notice that **the agreement of the simulations with the experimental spectra allows us to conclude that the method is reliable and is able to extract the effective TPA parameter of the waveguide**. We insist on the fact that the present sample has no designed couplers to improve the injection and that the simulated spectra in Fig. 2.32 do not result from a numerical fitting, as it is often times done in numerous publications.

To test the method accuracy, we have changed intentionally the coupling in one of the sides of the waveguide. In this case we have decreased the transmission of about half of the optimum in the linear regime by decreasing the coupling from the facet A (in this case by changing the height of the microscope objective). The spectra obtained are shown in 2.33. It is already evident that the broadening achieved with the injection from

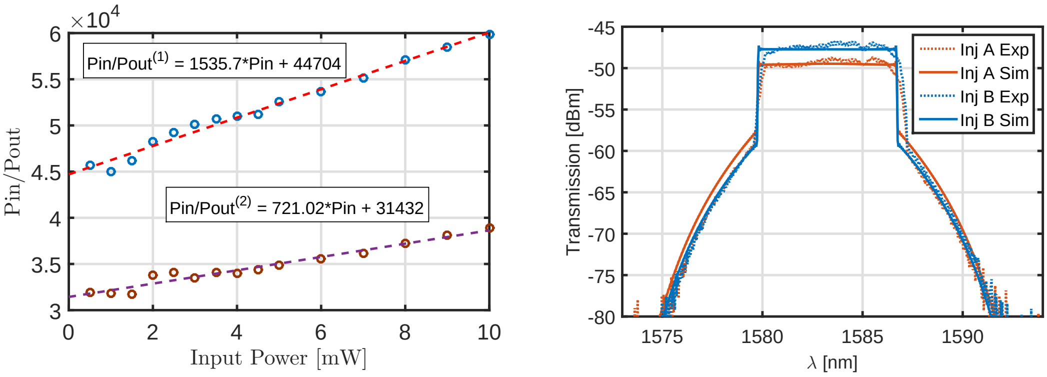

Figure 2.33: Left: P_{in}/P_{out} vs. P_{in} at zero dispersion when injecting by the two facets by decreasing the injection in the facet A. Right: Comparison between the output spectra when injecting the same power from both facets (experiments and simulations).

the facet A is smaller. We cannot directly compare the coefficients extracted from the linear plots $\mathrm{P_{in}/P_{out}}$ as the coupling efficiencies are involved in the expressions.

The re-calibrated set-up coupling coefficients are $\kappa_{inj}^{(1)} = 24\%, \kappa_{OSA}^{(1)} = 24\%, \kappa_{inj}^{(2)} = 27\%$, $\kappa_{OSA}^{(2)} = 15\%$. It could be noticed that even if the injection stages remain the same, the output were modified with respect to the previous experience. This change could be explained with the modification of the output beam, as one of the facets introduces a different collection/injection efficiency.

With those values and the information given by the double endfire coupling, we could estimate efficiencies of $\kappa_{SA} = 3.5\%$ and $\kappa_{SB} = 2.6\%$. This result is in perfect agreement with the expected values, as the facet B was not modified and the facet A was expected to decrease a half in the efficiency. Now, we have enough information to calculate the effective TPA parameter from both experiences: $\gamma_{TPA}^{1\mathrm{cm}_{changed-inj}(1)} \approx \gamma_{TPA}^{1\mathrm{cm}_{changed-inj}(2)} \approx 28.0\ (\mathrm{Wm})^{-1}$, again, this value should be the same regardless the injection and collection efficiencies, so it must be the same as in the previous bi-directional experience. In this case the same value was obtained with a difference of 4%.

From Fig. 2.33, a remarkable matching between the simulated and experimental spectra can be confirmed. In this particular experience, larger uncertainties are expected because the intentional misalignment could be slightly different in both cases.

After validating the method sensitivity, we proceed by measuring a geometrically identical strip waveguide located on the same sample in order to determine if the method is able to measure the same effective nonlinear parameter. Again the coupling coefficients of the set-up were re-measured: $\kappa_{inj}^{(1)} = 23\%, \kappa_{OSA}^{(1)} = 29\%, \kappa_{inj}^{(2)} = 28\%, \kappa_{OSA}^{(2)} = 21\%$.

With all the values, we could estimate injection coefficients of $\kappa_{SA} \approx 4.1\%$ and $\kappa_{SB} \approx 3.3\%$. Those values are consistent with the spectra depicted in Fig. 2.34 where the nonlinear

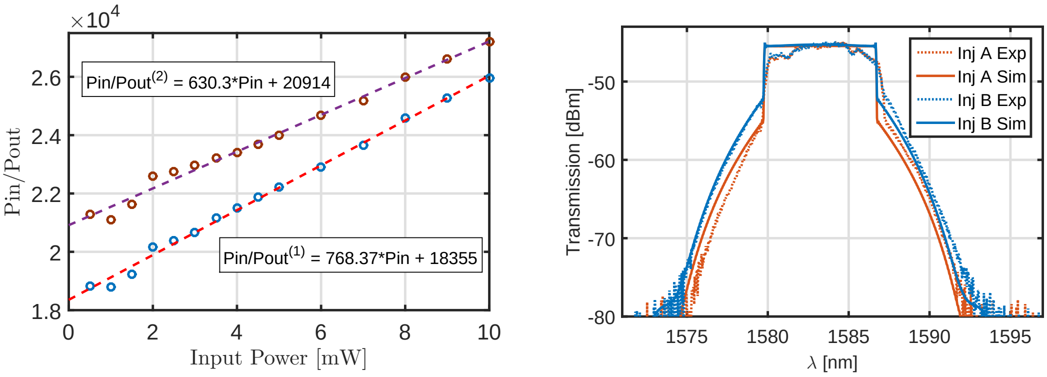

Figure 2.34: Left: P_{in}/P_{out} vs. P_{in} at zero dispersion when injecting by the two facets in a second strip waveguide with the same geometry. Right: Comparison between the output spectra when injecting the same power from both facets (experiments and simulations).

effects are stronger when injecting from the side B, opposite facet compared to the previous waveguide. It is also worth noticing that the κ_{OSA} value changes in all the experiences but remain within the same range, in the optimized conditions, between 20% and 30%. Finally, the estimation of the effective nonlinear parameter is: $\gamma_{TPA}^{1\text{cm}-II(1)} \approx 34.4\ (\text{Wm})^{-1}$ and $\gamma_{TPA}^{1\text{cm}-II(2)} \approx 34.5\ (\text{Wm})^{-1}$, where II denotes that a second waveguide was measured.

From these value, we can see that the order of magnitude of the effective susceptibility is of the same order of magnitude for both waveguides, nevertheless, the difference can be attributed to different propagation losses or a change in the effective area that could come from the variation in the wafer thickness or a different width.

2.5.2 Top-hat D-Scan applied to a SOI waveguide

The spectral output measurements are repeated with pulses under different dispersion $\phi^{(2)}$ varying from -3.5 to +3.5 ps^2 in the first waveguide characterized in the previous section. It is important to note that the injection was done from the facet A. Applying four different input powers P_{in}, the evolutions of the output power $P_{\text{out}}^{(1)}$ and the spectral r.m.s. width 2σ from the transmitted pulses are presented in Fig. 2.35 (Up) as a function of $\phi^{(2)}$. The 2σ curves present a dispersive shape similar to the transmission curves from Z-Scan (Fig. 1.26) and to the simulations performed in the D-Scan model section (Fig. 2.16). In agreement with the positive sign of n_2 for silicon, the maximum spectral broadening is expected for a positive value of $\phi^{(2)}$. Towards large dispersion values, the self-phase modulation becomes negligible due to the wide-spreading of the pulses and the spectral width tends to that of the input pulse as predicted from the D-Scan model. We have superimposed in dashed lines the output power, demonstrating the presence of TPA with an expected symmetric shape, in accordance with the simulations shown in Fig. 2.15.

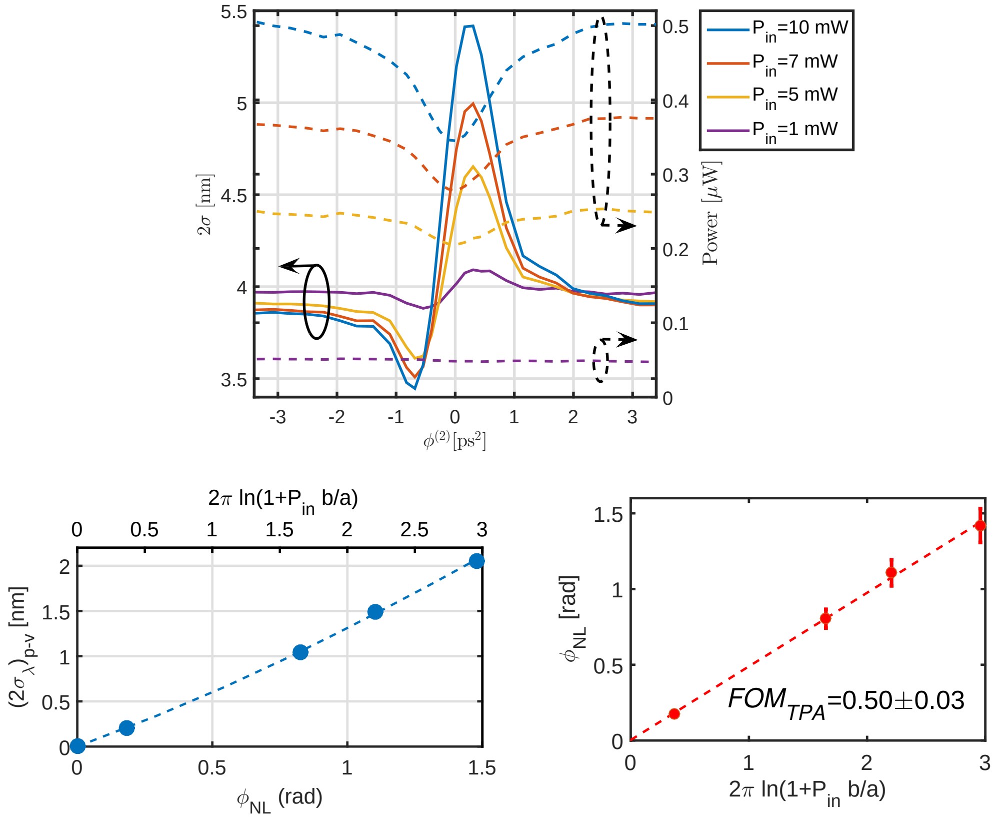

Figure 2.35: Up: Spectral r.m.s. width variation of the output transmitted pulses as a function of the applied dispersion $\phi^{(2)}$ on the input pulses and their respective output power. Down-Left: Experimental (dots) and simulated (dashed) peak to valley values as a function of the TPA and nonlinear phase shift respectively. Down-Right: Figure of merit measurement from the slope of the curve of $2\pi \ln(1 + P_{in}b/a)$ vs. the nonlinear phase.

From the r.m.s spectral linewidth plotted in Fig. 2.35-Top, we can measure directly the $(2\sigma)_{\mathrm{p-v}}$. We have plotted this quantity as a function of $2\pi \ln(1 + P_{in}b/a)$ (blue dots), as proposed to retrieve the FOM_{TPA} in section 2.3.2. We can overlap those points with the $(2\sigma)_{\mathrm{p-v}}$ as a function of the nonlinear shift ϕ_{NL} introduced by the waveguide from the D-Scan model (dashed line). We have plotted in Bottom-Right, the relation between ϕ_{NL} (semi-analytical) and $2\pi \ln(1 + P_{in}b/a)$ (experiments). The slope of the line gives directly the FOM_{TPA} value, in our case equals to 0.50 ± 0.03, in very good agreement with the reference values published for high resistivity silicon at telecom wavelengths. **The procedure applied to estimate the uncertainty is extensive to the other measurements in this manuscript and for the FOM_{TPA} is of 6%.**

After properly finding the figure of merit of the waveguiding structure, our objective is to separate the real and imaginary contributions. It is mandatory to measure the injection efficiencies from both facets of the waveguide, called A and B. This has been already done

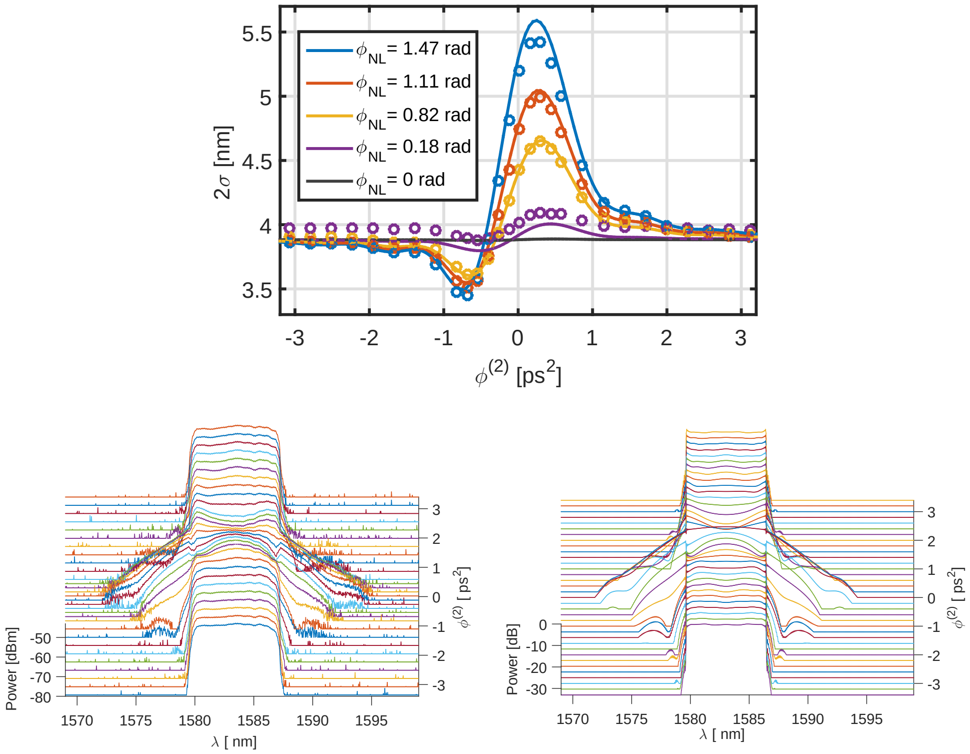

Figure 2.36: (a) Superposition of the spectral broadening from simulation (lines) and experiments (circles) with uncertainty bars for different calculated nonlinear phase shifts proportional to the variation in power. (b) Experimental spectra registered at $P_{in} = 10$mW and varying the second order dispersion. (c) Simulation results for a perfect temporal sinus cardinal pulse and a nonlinear phase shift of 1.47 rad corresponding to the same σ_{p-v} as (b) and the same dynamics.

by applying the double injection method giving the values 6.4 % and 2.5 %, respectively. We have deduced the values of the effective nonlinear parameters defined by $\gamma_{\text{TPA}} = b^{(1)}/(a^{(1)}\kappa_{inj}^{(1)}\kappa_{SA}\eta L_{\text{eff}}) = 27 \pm 2\ \text{W}^{-1}\text{m}^{-1}$ and $\gamma = 2\pi FOM_{\text{TPA}}\gamma_{\text{TPA}} = 85 \pm 9\ \text{W}^{-1}\text{m}^{-1}$, **which corresponds to an uncertainty of 10% for the real susceptibility**. Values that are in the same order of magnitude of those reported in the literature [99].

By simulating the modal field distribution in the waveguide, the effective nonlinear area A_{NL} could be calculated and the bulk nonlinear coefficients could be extracted. Values of $n_2 = 2.57 \times 10^{-18}\ \text{m}^2/\text{W}$ and $\beta_{\text{TPA}} = 3.26 \times 10^{-12}\ \text{m/W}$, are deduced, which are in good agreement with the standard coefficients used in silicon. It is important to recall that the high contrast in the peak-to-valley extraction is due to the rectangular pulse shape that allows the measurement of very fine nonlinear phase shifts.

We have simulated the trends through the semi-analytical simulation of the system as a temporal (Kerr) lens presenting TPA. In Fig. 2.36 we present the obtained curves from simulations taking into account the experimental coefficients. Using the susceptibilities found previously, we have calculated the r.m.s. spectral linewidth that we present in solid lines and the experimental values with their respective error bars. It is important to recall that **each point corresponds to one spectrum, so the model reproduces properly the features found in the experiments**. The apparent mismatch found with the maximum power is attributed to the small contribution of the fiber. Also a not evident increase in the experimental temporal width (larger sigma for the purple line) will be discussed in the next chapter. Nevertheless, it is not a critical point as the peak-to-valley difference is the same for simulation and experiment. We have finally added the output spectra recorded for the maximum power ($P_{in} = 10$ mW) that exhibits the maximum achieved nonlinearities. Next to it, we present the spectra obtained from the simulation, corresponding to a nonlinear phase shift of 1.47 rad. From the simulations, we reproduce features at the noise level (-30dB). Finally, we remark the fact that the power transmission at the central wavelength follow an inverse trend with respect to the dispersion than the standard deviation one. Indeed, the power is larger at 1584 nm for negative dispersion values, then decreases for the positive, this is expected from the NSPP as plotted in Fig. 2.15.

2.6 Nonlinear characterization of integrated photonic waveguides

In this section we will apply the bi-directional D-Scan technique to characterize different integrated materials. Some of the waveguides could be found in literature, so they will be useful to validate the methodology. Also, the third order susceptibility of novel hybrid structures and other semiconductor alloys will be presented. In particular some deeper analysis will be performed when interesting features will be found.

We have seen that the expression for γ depends on several factors, such as the effective area or the bulk material susceptibilities. We will indeed tune these parameters in order to test the method and find interesting structures for integrated nonlinear applications. For instance, we will explore in this chapter diverse materials such as Ge rich - Si-Ge alloys with different concentrations, chalcogenide and silicon nitride.

2.6.1 Ge rich - Si-Ge alloys

Germanium (Ge) is an interesting material for integrated proposes, nevertheless its electronic properties makes it an inconvenient material for the C-band telecom window optical nonlinearities. Instead, Ge have been largely used for photodetection. Another big interest of Ge in photonics is its transparency properties in the midIR window (between 3 and 14 μm), so this material shows potential for spectroscopic and nonlinear proposes in the midIR (lower frequencies). An alternative to pure germanium or to SOI waveguides also consists of waveguides having a $\mathrm{Si}_{1-x}\mathrm{Ge}_x$ core, opening the possibility of tuning the optical properties by changing the Ge concentration x. In particular, the nonlinearities of these compounds have not been thoroughly studied around $\lambda \sim$1550 nm and are expected to be very sensitive to any modification of the material energy bands.

As explained in section 1.4.2, there are two kind of gaps to be considered in SiGe alloys that affect the material electronic properties (in particular light-matter interactions are governed by this energetic landscape): the direct or indirect bandstructures, respectively (section 1.4.2). Meanwhile, it is not clear to which concentration x, the indirect gap model is applicable in order to estimate the nonlinear susceptibilities (section 1.2.1). Some numerical explorations have been performed recently showing a limit around x = 0.80, where the mismatch for the expected TPA from one model to the other varies by two orders of magnitude [100].

In this context, these approaches have been tested in the present manuscript with experimental data from pure Germanium and pure Silicon, so we will measure the nonlinearities to give further insights about the trends and the limits of the theoretical models used and evaluate the potentials of the SiGe alloys for nonlinear optics in the telecom waveband.

The samples used in this section have been fabricated in wafers with **three different Ge concentrations in the core of the waveguide, x = 0.70, 0.80, 0.90**, fabricated in the L-NESS laboratory (Politecnico di Milano) in the frame of the EU INSPIRE project coordinated by Dr. Delphine Morini. The concentration values were chosen due to the interest of distinguishing the general behavior of the compound with respect to the bandgap.

The fabricated waveguides consist of 1 μm etched in a 2 μm thick $Si_{1-x}Ge_x$ alloy (section 1.4.2). To compare similar effective areas, we have chosen a width of 1.6 μm. **In this configuration we have single mode waveguides at 1570nm for the three concentrations**.

To have an order of magnitude from the theoretical predictions given in the literature, we have provided some curves proposed in a review paper from Hon et al. [100]. In Fig. 2.37, we have selected the figures showing concentrations and wavelengths used in this manuscript. As it can be seen, the proposed trends of the real and imaginary parts of the third order susceptibility are the same as the ones presented in section 1.2.1 and section 1.2.2 respectively. The linear refractive index of $\mathrm{Si_{1-x}Ge_x}$ was calculated using the relation $n(\omega) = n_0 + n_1(\hbar\omega)$, where $n_0(x) = 4.01 - 0.81(1-x) + 0.22(1-x)^2$ and $n_1(x) = 0.216 - 0.211(1-x) + 0.089(1-x)^2$. The expressions used to calculate the indirect bandgap energy, plotted in Fig. 2.37(a), were[101]: $E_{\Gamma\Delta} = 1.11 - 0.34x + 0.227x^2$ and $E_{\Gamma L} = 2.01 - 1.46x + 0.227x^2$, where $E_{\Gamma\Delta}$ is the bandgap energy near the X valley [$E_{ig} = E_{\Gamma\Delta}(x)$ when $x = 0$ for Si], and $E_{\Gamma L}$ is the bandgap energy at the L valley. For the direct bandgap energy, a linear approximation was used taking into account the direct

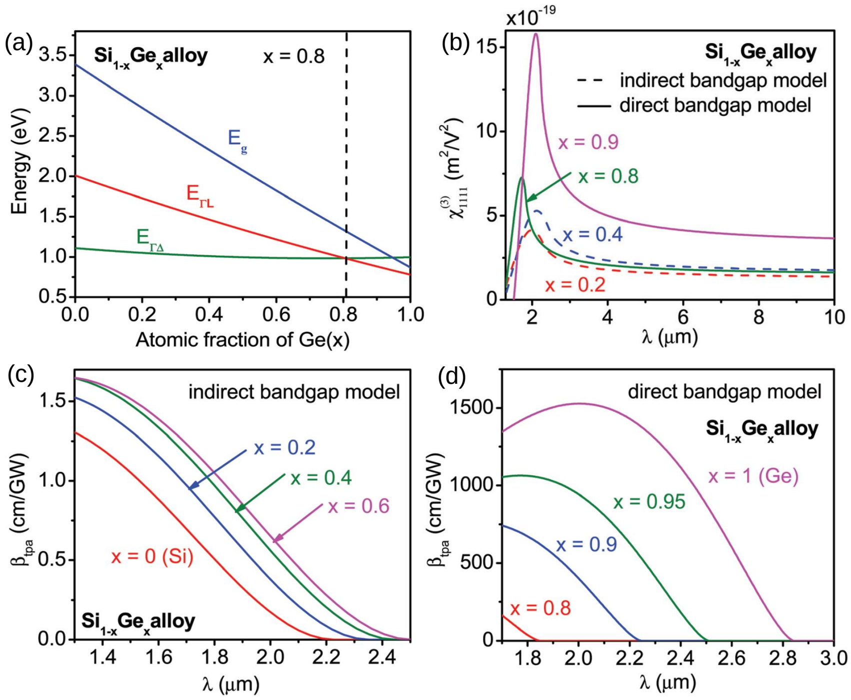

Figure 2.37: Theoretical predictions of $\mathrm{Si_{1-x}Ge_x}$ third order nonlinear properties from the chosen gap model. (a) Calculated bandgap energy of $E_{\Gamma\Delta}, E_{\Gamma L}$ and E_g with respect to the atomic fraction of Ge. (b) Theoretical $\chi^{(3)'}_{1111}$ (real part of the susceptibility) dispersion curves for different Ge concentration and applying the two models. (c) Theoretical β_{TPA} (imaginary part of the susceptibility) dispersion curves with x=0, 0.2, 0.4 and 0.6 using the indirect bandgap model. (d) x=0.8, 0.9, 0.95 and 1 using the direct bandgap model[100].

bandgaps of Si (3.30 eV) and of Ge (0.82 eV)[101, 100]: $E_g = 3.39 - 2.57x$. It is then clear that the alloy direct bandgap decreases when the concentration of Ge (x) increases.

From those two kinds of bandgaps, the dispersion curves for the real part of the susceptibility could be estimated by using the expression (1.21). As expected, the wavelengths close to the material gap experience stronger light-matter interactions. For lower $\hbar\omega$ values (midIR), the material n_2 tends to a constant value (Fig. 2.37(b)). The predicted values are different when using a direct model gap (x>80%) or an indirect one (x<80%).

In the case of the imaginary part (two photon absorption), the wavelength range is naturally restricted to the frequencies larger than the half of the cut-off (so lower wavelengths than 3 μm for all the cases). The shape of the TPA could be traced back by using Eq. (1.32). It could be noticed that for the TPA, the difference between the two models is of two orders of magnitude, making almost impossible to estimate the genuine nonlinear performance (figure of merit) with around 80% of Germanium. Furthermore, in the case of the indirect bandgap model (Fig. 2.37 (c)), the trends of the TPA saturate when increasing the Germanium concentration, making impossible an evident connection with the direct bandgap model. In the case of Fig. 2.37 (d), the trends were plotted from a wavelength of 1.7 μm, so the wavelength we will use (around 1.58 μm) is not represented but could be easily extrapolated.

In summary, there is a large interest in the characterization of SiGe waveguides in the nonlinear regime but there is a lack of experimental data that can confirm theoretical predictions in order to design devices for diverse wavelengths and proposes. The experimental set-up presented in section 2.4 and the bidirectional D-Scan technique will be used to investigate the effective waveguide third order susceptibilities and provide additional data about these alloys for nonlinear optics designers.

$\mathrm{Si}_{0.30}\mathrm{Ge}_{0.70}$ nonlinear characterization

The first concentration to be tested is the one with highest silicon concentration, so we expect a larger bandgap energy. The measured propagation losses were estimated to (10 ± 2) dB/cm by using the cut-back method. The calculated effective index for the fundamental TE mode is $n_{\mathrm{eff}} = 4.02$ and the effective area is $A_{\mathrm{eff}} = 5.38\ \mu\mathrm{m}^2$.

Differently from the case of silicon, we will present the spectral results in order to determine if different features are appreciable. We could apply the bi-directional method in order to estimate the coupling coefficients and the effective gamma parameter. In Fig. 2.38, we present the power spectra and the nonlinear transmission when injecting the light from both sides. As usual, we had to characterize the different coupling efficiency stages of the set-up. The measured values are: $\kappa_{inj}^{(1)} = 24\%$, $\kappa_{OSA}^{(1)} = 24\%$, $\kappa_{inj}^{(2)} = 28\%$ and $\kappa_{OSA}^{(2)} = 30\%$. The waveguide length is around $L = 6$ mm yielding to a $L_{\mathrm{eff}} = 3.3$ mm.

Applying the relations 2.33 with the coefficients found for both injections, we could extract: $\kappa_{SA} = 32\%$ and $\kappa_{SB} = 28\%$. A large coupling efficiency was expected due to

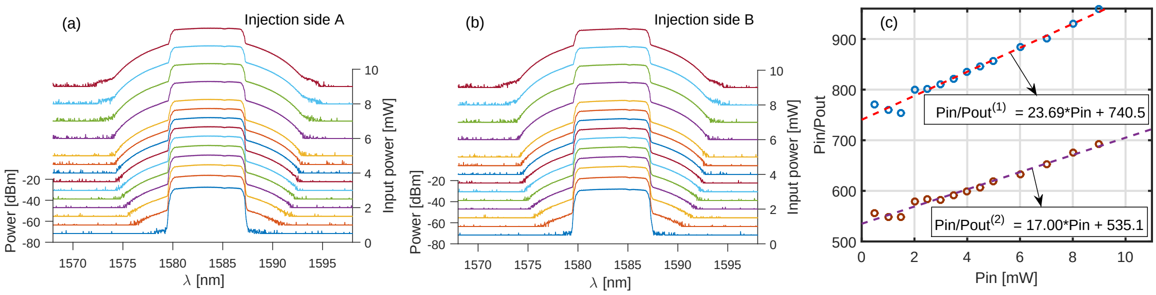

Figure 2.38: Bi-directional nonlinear transmission characterization of the 70% Ge concentration waveguide. (a) Output spectra as a function of the input power when injecting from the facet A. (b) Injection from facet B. (c) Input over output power showing the characteristic linear behavior.

the broad waveguide cross-section, more than one order of magnitude larger than a monomode silicon strip waveguide. It is also interesting to notice that in such kind of geometries, the approximation $\kappa_{SA} = \kappa_{SB}$ is reasonable.

From the relation found in Eq. 2.9, we could extract the effective TPA susceptibility with the independent coefficients of each side: $\gamma^{(1)}_{\mathrm{TPA}} = 7.66\ \mathrm{W^{-1}m^{-1}}$ and $\gamma^{(2)}_{\mathrm{TPA}} = 7.46\ \mathrm{W^{-1}m^{-1}}$. This value is smaller than the one found in the silicon waveguide, but it is important to recall the dependency with the nonlinear effective area which in this case is around 45 times larger.

To extract the β_{TPA} parameter from the material, we should take into account the slow light enhancement coefficient ($S = n_g/n_0 \approx 4.33/4.04 = 1.07$) and the nonlinear area (A_{NL}), such that: $\beta_{\mathrm{TPA}} = \gamma_{\mathrm{TPA}} A_{\mathrm{NL}}/S^2$. Finally an average TPA coefficient from the two experiences gives: $\beta^{Si_{0.3}Ge_{0.7}}_{\mathrm{TPA}} = 3.5 \pm 0.7$ cm/GW. This value is, as expected, larger than the case of silicon and from Fig. 2.37 (c) and (d), it is closer to the predicted indirect bandgap model but still 2.5 times larger.

Now that we had the coupling and the TPA coefficient values, we could proceed to the measurements with the D-Scan technique. As usual, we have varied the dispersion in the chirped pulse in order to plot the spectral broadening variation. In Fig. 2.39 we present the experimental broadening values (circles) and the corresponding simulation results (solid lines) for the equivalent input intensities. The D-Scan procedure gives a figure of merit $\mathrm{FOM_{TPA}} = 0.26$ which is lower than the values measured for silicon. We have seen that the TPA parameter (β_{TPA}) is much larger for this alloy.

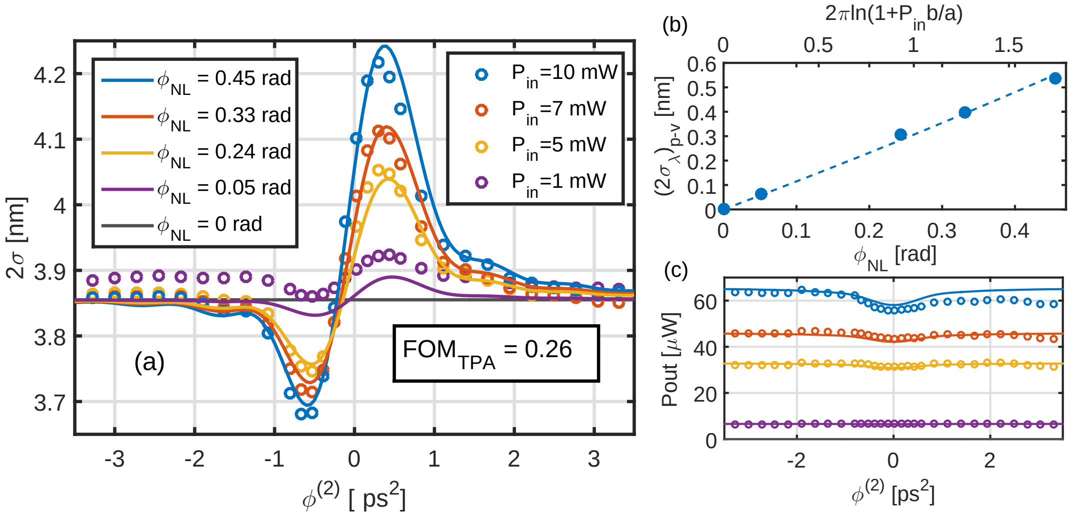

Figure 2.39: D-Scan applied to a 70% Ge concentration waveguide with 4 different power levels. The simulation corresponding to the total nonlinear phase shift is shown in solid lines with the corresponding input intensity difference.

With the values of γ^{wg}_{TPA} and FOM_{TPA}, γ^{wg} was easily found by means of Eq. (1.74). From the shape of the curves in Fig. 2.39, it is evident to conclude that the sign of n_2 is positive. So that:

$$\boxed{\gamma^{wg} = 2\pi\gamma^{wg}_{\text{TPA}}\text{FOM}_{\text{TPA}} = 12.3\ \text{W}^{-1}\text{m}^{-1}} \tag{2.34}$$

We could extract the nonlinear index from this value or equivalently by using the Eq. (1.75), such that:

$$\boxed{n_2 = \lambda_0\beta_{\text{TPA}}\text{FOM}_{\text{TPA}} = 13.9 \times 10^{-18}\ \frac{\text{m}^2}{\text{W}}} \tag{2.35}$$

From these values, we could extract an estimation of the real part of the third order optical susceptibility ($\mathbb{R}\mathbf{e}\{\chi^{(3)}_{\text{eff}}\}$) in order to compare the value predicted in Fig. 2.37 (b):

$$\boxed{\mathbb{R}\mathbf{e}\{\chi^{(3)}_{\text{eff}}(\omega_0)\} = \frac{4\varepsilon_0 c n_0^2}{3} n_2(\omega_0) = 8.0 \times 10^{-19}\ \frac{\text{m}^2}{\text{V}^2}} \tag{2.36}$$

This is in the same order of magnitude than the theoretical values proposed by Hon et al. ([100]), but as it can be seen, the wavelength region (around 1580 nm) where the measurement was performed is the most sensitive domain in term of third order susceptibilities. At the end of this section we will give some insights about the trends from this value.

$\text{Si}_{0.20}\text{Ge}_{0.80}$ nonlinear characterization

We have made an analogous procedure for another two concentrations by increasing steps of 10 % of additional Ge. We expected a lower gap with respect to the previous sample, so most likely a larger TPA probability. The measured propagation losses for a 1.6 μm waveguide width were estimated of 13 ± 3 dB/cm. In this case, after cleaving, the waveguide had a geometrical length of 7 mm, yielding to a $L_{\text{eff}} = 2.9$ mm, so, similar to the effective interaction length of the previous concentration. The effective index for the fundamental TE mode was estimated as $n_{\text{eff}} = 4.10$ and the effective area as $A_{\text{eff}} = 5.04\ \mu\text{m}^2$.

The measured values for the set-up were: $\kappa^{(1)}_{inj} = 24\%$, $\kappa^{(1)}_{OSA} = 32\%$, $\kappa^{(2)}_{inj} = 28\%$ and $\kappa^{(2)}_{OSA} = 23\%$. When applying the bi-directional method, we have found coefficients equal to $a^{(1)} = 528.4$, $b^{(1)} = 24.6\ \text{mW}^{-1}$, $a^{(2)} = 687.5$ and $b^{(2)} = 41.25\ \text{mW}^{-1}$. With this coefficients, we could trace the coupling efficiencies in the facets: $\kappa_{SA} = 31\%$ and $\kappa_{SB} = 36\%$. Next, in an analog procedure as the previous sample, we could extract two values for the effective TPA susceptibility: $\gamma^{(1)}_{\text{TPA}} = 12.3\ \text{W}^{-1}\text{m}^{-1}$ and

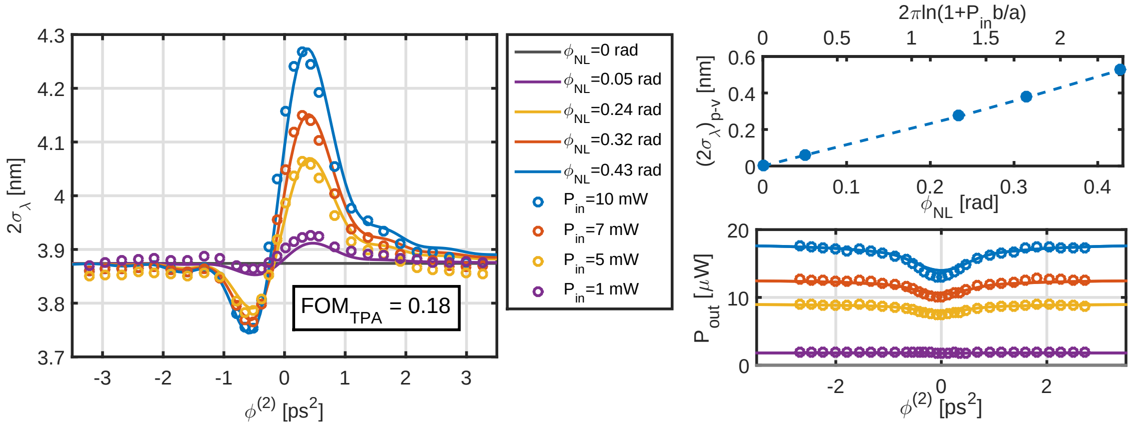

Figure 2.40: D-Scan applied to a 80% Ge concentration waveguide with 4 different power levels. The simulation corresponding to the total nonlinear phase shift is shown in solid lines with the corresponding input intensity difference.

$\gamma^{(2)}_{\text{TPA}} = 11.8\ \text{W}^{-1}\text{m}^{-1}$. These values are larger than for the doping of 70%, indeed, as predicted in Fig. 2.37, when the Ge concentration is increased, the TPA effect should also increase.

Now, to compare the bulk coefficients, we have again further taken into account the slow light enhancement coefficient ($S = n_g/n_0 \approx 4.44/4.12 = 1.08$) and the nonlinear area (A_{NL}), such that: $\beta^{Si_{0.2}Ge_{0.8}}_{\text{TPA}} = 5.3 \pm 1.0$ cm/GW.

Similarly, from γ^{wg}_{TPA} and FOM$_{\text{TPA}}$, γ^{wg} was found by means of Eq. (1.74). From the shape of the curves in Fig. 2.39, it is evident to conclude that the sign of n_2 is again positive. So that:

$$\boxed{\gamma^{wg} = 2\pi\gamma^{wg}_{\text{TPA}}\text{FOM}_{\text{TPA}} = 13.6\ \text{W}^{-1}\text{m}^{-1}} \tag{2.37}$$

We could also extract the nonlinear index from this value or equivalently by using the Eq. (1.75), such that:

$$\boxed{n_2 = \lambda_0\beta_{\text{TPA}}\text{FOM}_{\text{TPA}} = 15.1 \times 10^{-18}\ \frac{\text{m}^2}{\text{W}}} \tag{2.38}$$

Giving a $\mathbb{R}\mathbf{e}\{\chi^{(3)}_{\text{eff}}(\omega_0)\}$:

$$\boxed{\mathbb{R}\mathbf{e}\{\chi^{(3)}_{\text{eff}}(\omega_0)\} = \frac{4\varepsilon_0 c n_0^2}{3} n_2(\omega_0) = 9.1 \times 10^{-19}\ \frac{\text{m}^2}{\text{V}^2}} \tag{2.39}$$

$\mathrm{Si}_{0.10}\mathrm{Ge}_{0.90}$ nonlinear characterization

The final concentration to be tested was the one with highest germanium concentration. Following the trends of the previous two samples, we expected larger propagation losses, larger nonlinear losses and a smaller nonlinear figure of merit. Indeed, the measured propagation losses were 20 ± 4 dB/cm. The geometrical length was estimated as 6 mm, giving an effective interaction length of $L_{\mathrm{eff}} = 2.0$ mm. The effective index for the fundamental TE mode was estimated as $n_{\mathrm{eff}} = 4.18$ and the effective area as $A_{\mathrm{eff}} = 4.77\ \mu\mathrm{m}^2$.

The measured values for the set-up are: $\kappa_{inj}^{(1)} = 28\%$, $\kappa_{OSA}^{(1)} = 11\%$, $\kappa_{inj}^{(2)} = 23\%$ and $\kappa_{OSA}^{(2)} = 15\%$. When applying the bi-directional method, we find coefficients equal to $a^{(1)} = 6237$, $b^{(1)} = 511.9\ \mathrm{mW}^{-1}$, $a^{(2)} = 8071$ and $b^{(2)} = 320.9\ \mathrm{mW}^{-1}$. With this coefficients, we could trace the coupling efficiencies in the facets: $\kappa_{SA} = 36\%$ and $\kappa_{SB} = 19\%$. Next, in an analog procedure as for the previous sample, we could extract two values for the effective TPA susceptibility: $\gamma_{\mathrm{TPA}}^{(1)} = 29.0\ \mathrm{W}^{-1}\mathrm{m}^{-1}$ and $\gamma_{\mathrm{TPA}}^{(2)} = 29.4\ \mathrm{W}^{-1}\mathrm{m}^{-1}$. Finally, to compare the bulk coefficients, we have considered the slow light enhancement coefficient ($S = n_g/n_0 \approx 4.54/4.20 = 1.08$) and the nonlinear area (A_{NL}) such that: $\beta_{\mathrm{TPA}}^{Si_{0.1}Ge_{0.9}} = 11.9 \pm 1.9$ cm/GW.

These last results show a positive n_2 and:

$$\boxed{\gamma^{wg} = 2\pi\gamma_{\mathrm{TPA}}^{wg}\mathrm{FOM}_{\mathrm{TPA}} = 7.34\ \mathrm{W}^{-1}\mathrm{m}^{-1}} \tag{2.40}$$

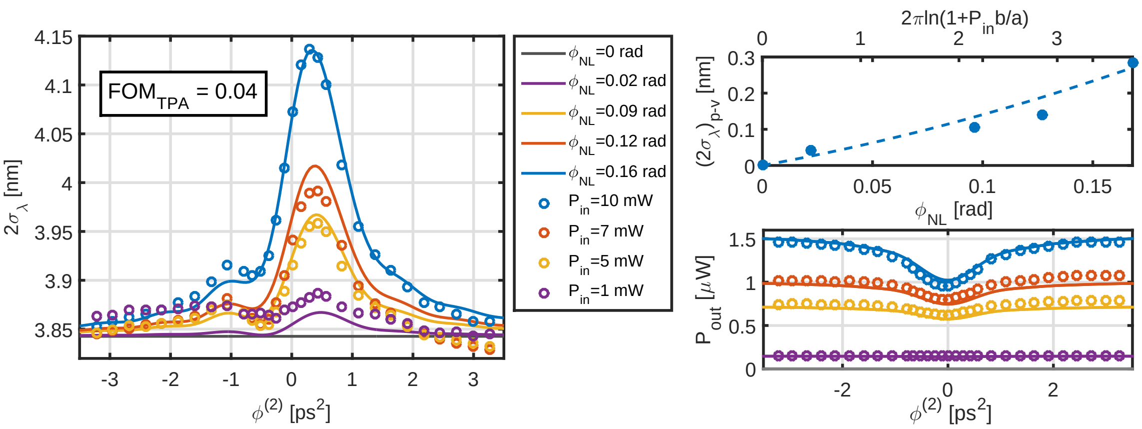

Figure 2.41: D-Scan applied to a 90% Ge concentration waveguide with 4 different power levels. The simulation corresponding to the total NL phase shift is shown in solid lines with the corresponding input intensity difference.

And:

$$\boxed{n_2 = \lambda_0 \beta_{\mathrm{TPA}} \mathrm{FOM}_{\mathrm{TPA}} = 7.54 \times 10^{-18}\ \frac{\mathrm{m}^2}{\mathrm{W}}} \tag{2.41}$$

Giving a $\mathbb{R}\mathbf{e}\{\chi^{(3)}_{\mathrm{eff}}(\omega_0)\}$:

$$\boxed{\mathbb{R}\mathbf{e}\{\chi^{(3)}_{\mathrm{eff}}(\omega_0)\} = \frac{4\varepsilon_0 c n_0^2}{3} n_2(\omega_0) = 4.7 \times 10^{-19}\ \frac{\mathrm{m}^2}{\mathrm{V}^2}} \tag{2.42}$$

Nonlinear optical properties of rich Ge - SiGe alloys in the telecom waveband: Discussion

From the photonic integration point of view, the combination of active devices with efficient and low loss waveguides is of major importance. Form the measured values, the first conclusion to be remarked is that we have not observed any negative Kerr coefficient, as it could be expected when operating with photons with energies close to the material gap.

Second, the extracted FOM_{TPA} decreases when the doping concentration of Germanium increases. This was expected from theoretical argumentation, but we found that this reduction of the figure of merit comes from an increase of the TPA effect.

In Fig. 2.42, we show the theoretical prediction of the Kerr coefficient by using the direct gap model. It can be noticed that the trends of n_2 are predicted. Nevertheless, the obtained values are not exactly the same. We should remark that the studied waveguides were grown in a graded buffer and part of each optical mode is confined in the underneath layer, so the effective nonlinearity needs to be considered as a whole. This feature is crucial for applications in the midIR because the mode size will increase, nevertheless, the $\mathrm{Si_{x-1}Ge_x}$ layer thickness can be increased in order to keep good confinement properties.

To summarize, we have reported to the best of our knowledge the first experimental values for instantaneous nonlinearities in Ge-rich SiGe alloy waveguides at a telecom wavelength (1.58 μm). The results are in agreement with the theoretical predictions made previously but clarifies that effectively none of the models (direct or indirect) is valid for Ge concentrations around 80%. We have experimentally demonstrated the possibility of using the SiGe alloys as a nonlinear material for third order nonlinearities. Furthermore, we demonstrate that the nonlinear properties of SiGe waveguides could be tuned through innovative band-gap engineering, while the use of such a graded buffer grants a high quality Ge-rich $\mathrm{Si}_{1-x}\mathrm{Ge}_x$ layer on Si. We have finally exploited the measurements to estimate the trends in the midIR region, giving a

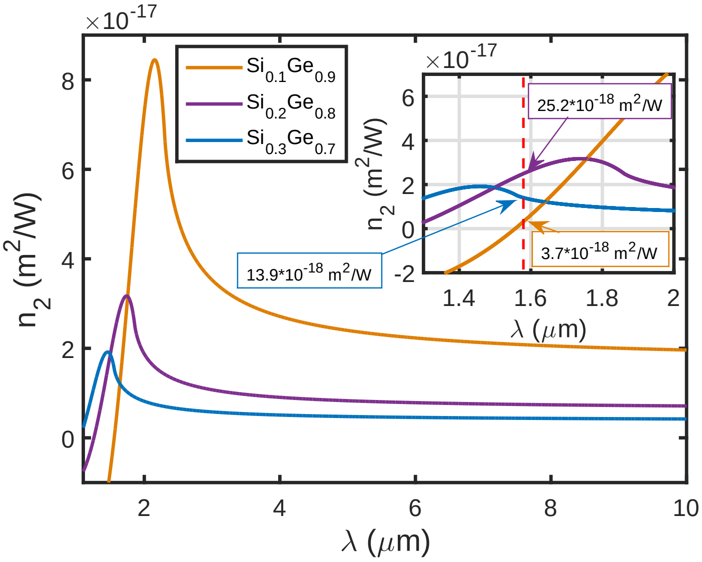

Figure 2.42: Theoretical trends of the Kerr coefficient as a function of the wavelength for various Ge fractions. Inset: Zoom around the C band marking the experiment operating central wavelength (∼ 1583 nm).

comprehensive picture for nonlinear photonics device designers in their efforts to explore Ge and SiGe for various applications.

2.6.2 Chalcogenide

The high material nonlinearity of chalcogenides, combined with the offered strong confinement makes them a good platform for ultrafast nonlinear optics and a key technology for future ultrahigh-bandwidth optical communications systems [53]. Nonlinear optical properties of As–S–Se glasses were measured by the Z-Scan technique at 1.6 μm, and values of n_2 up to 400 times the ones obtained for silica were observed [102]. Also, chalcogenide platforms have been explored in integrated photonic crystal configurations to exploit nonlinear effects [103]. In this section we will measure a chalcogenide GSS ($Ge_{23}Sb_7S_{70}$) waveguide in the nonlinear regime at $\lambda \sim$1550 nm. To our knowledge, there are no reported nonlinear values for this specific amorphous semiconductor.

From Fig. 2.43, we demonstrate that at the level powers used in the carried out experiment, no TPA effect was observed. So, we could apply a linear procedure to estimate the coupling efficiencies. We notice also from Fig. 2.43 (b) that the difference between the two slopes is not distinguishable, so in this case the assumption of $\kappa_{in} = \kappa_{out}$ is valid. On the other hand, we can notice that the spectral broadening induced by SPM is strong, so we can expect a large γ as expected.

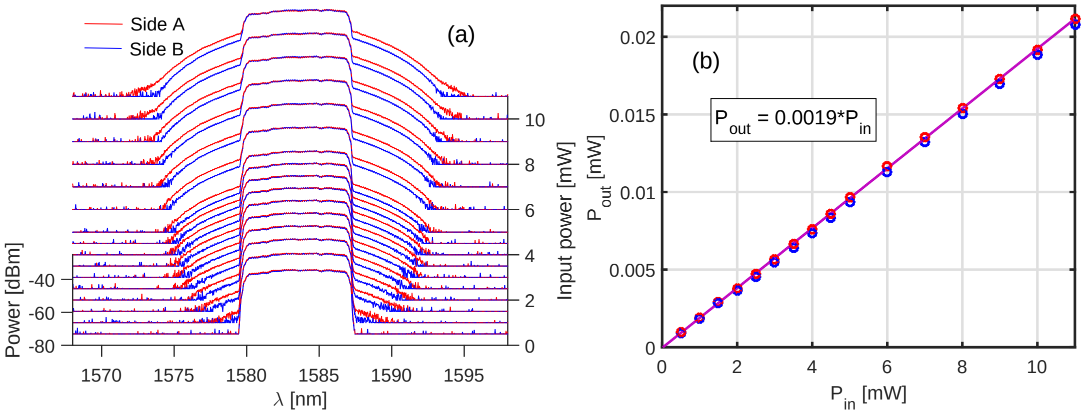

Figure 2.43: (a) Output spectra when injecting from both chalcogenide facets. (b) Output power as a function of the input power.

The measurement of the linear coefficients gave the following values: after estimating the $\kappa_{inj}^{(1)} = 25\%$, $\kappa_{OSA}^{(1)} = 26\%$:

$$\kappa_{SA} = \kappa_{SB} = \sqrt{\frac{0.0019}{\kappa_{inj}\kappa_{OSA}}} \approx 17\% \tag{2.43}$$

$$\phi_{NL} = \frac{S^2 k_0 n_2}{A_{NL}} P_p L_{eff} = \gamma^{wg} \kappa_{inj} \kappa_{SA} \eta P_{in} L_{eff} \tag{2.44}$$

With $L_{eff} = 4.7$ mm, for instance, taking the value of $P_{in} = 10$ mW, we could use the extracted value for the nonlinear phase shift after the D-Scan model. Finally, we measured a $\gamma^{wg} \approx 16.5$ W^{-1}m^{-1} which is in agreement with other integrated chalcogenide waveguides [104]. Nevertheless we should note that depending on the chalcogenide compound, the properties could differ substantially [53].

Finally, we used the relation (2.44) to estimate the Kerr coefficient in the chalcogenide waveguide. For this propose, we calculated the effective nonlinear area by using the mode depicted in Fig. 1.23 to obtain a $n_2 \approx 8.3 * 10^{-19}$ m^2/W.

These results validate the use of the D-Scan technique on samples that do not present TPA and highlight the interest of this kind of chalcogenide already applied on flexible chips to exploit nonlinear phenomena.

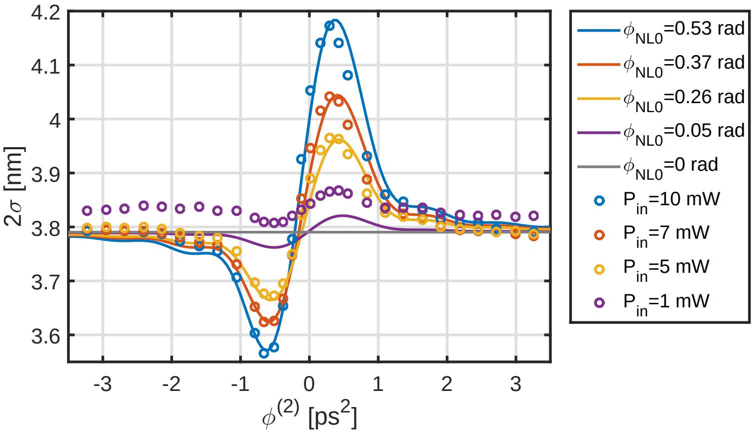

Figure 2.44: D-Scan applied to a monomode chalcogenide waveguide (420nm×800nm) in the absence of TPA.

2.6.3 Silicon Nitride

Silicon nitride has opened up many new capabilities such as on-chip optical frequency comb generation and ultrafast optical pulse generation and measurement [105]. Nevertheless the nonlinear effects are very small compared to Silicon and on the same order of silica. For this reason, we have injected the input beam directly from the stretcher, without crossing through the silica fiber. This has increased by an order of magnitude the resolution but has yet added difficulty for the estimation of the waveguide coupling efficiencies.

Fig. 2.45 displays the nonlinear properties of a nitride waveguide. Indeed the Kerr coefficient is around 20 times smaller than in silicon. Furthermore, due to its smaller refractive index, monomode waveguides have a larger effective area, requiring larger

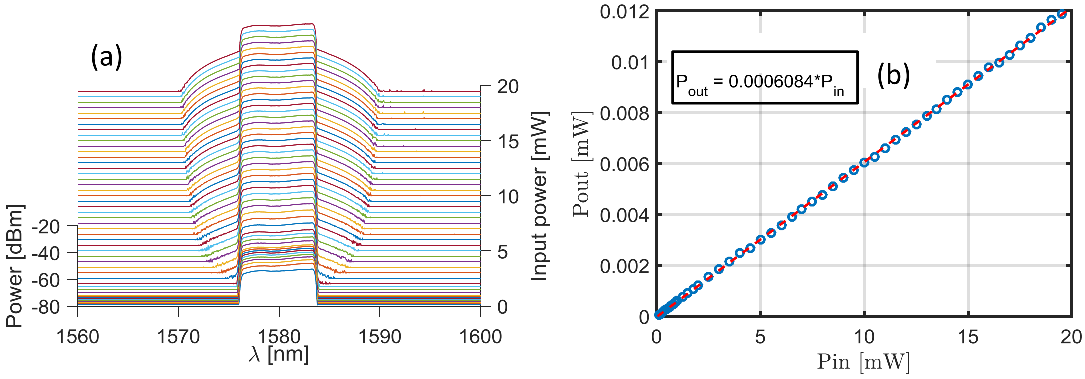

Figure 2.45: Nonlinear transmission of a silicon nitride strip waveguide. a) Spectra as a function of the average input power. b) Input power vs. output power showing no saturation.

powers to achieve the same intensities used in silicon waveguides.

The study of the nonlinear broadening was again performed by varying the second order dispersion. Also the semi-analytical model was used and allowed the estimation of the nonlinear phase shift generated by the studied waveguide.

In Fig. 2.46, we show the D-Scan trace for a stoichiometric Si_3N_4. In c), we have plotted the simulated trends by considering the $(2\sigma)_{\mathrm{p-v}}$. d) Shows the spectra for the largest optical intensity used. In this model, as for chalcogenide, no TPA was considered. Following the linear coupling estimation procedure. We estimated a coupling efficiency of $\sim 5\%$, and with an $L_{eff} \approx 0.8$ cm, we estimated a $\gamma^{wg} \approx 1.6\ \mathrm{W^{-1}m^{-1}}$, which corresponds to a $n_2 \approx 1.3 * 10^{-19}\ \mathrm{m^2/W}$.

This value is around 20 times lower than the value measured for n_2 of silicon in section 2.5.2. The same proportion has been measured with other methods [105]. This result shows that Si_3N_4 is a material ideal to make low loss waveguides, presenting a moderate

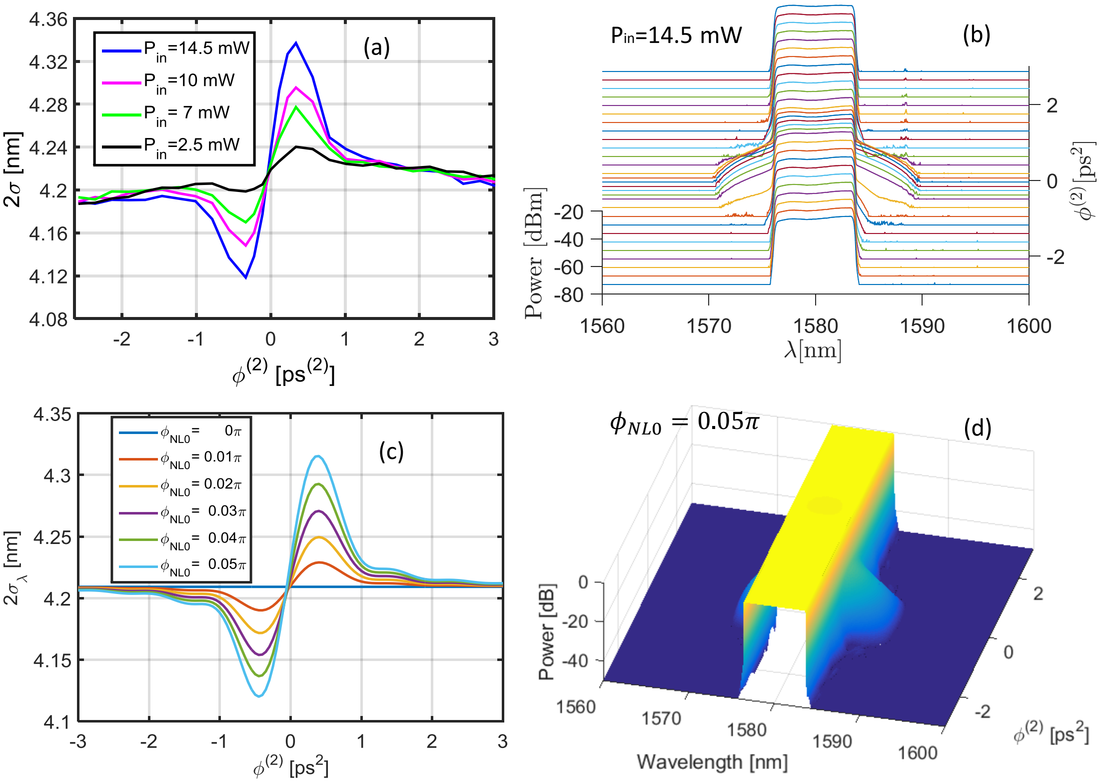

Figure 2.46: Measurements and simulations for silicon nitride. a) Experimental D-Scan. b) Spectra as a function of the second order dispersion for the maximum power (corresponding to the blue curve of a)). c) and d) are the simulated trends by considering the experimental conditions.

linear refractive index and a low Kerr coefficient (compared with silicon) but with no TPA. It thus opens the possibility to use large powers for nonlinear functionalities. Indeed, it is noticeable that the largest supercontinuum generation on-chip has been obtained in silicon nitride engineered waveguides [106].

2.7 Conclusion

In this chapter we have presented a novel method to characterize the instantaneous effective nonlinear susceptibilities from waveguiding structures, for instance fibers or integrated waveguides. We have introduced the model principles, a comparison between different excitation forms and the convenience of using Top-hat beams to increase the nonlinear phase shift sensitivity (from the r.m.s. spectral linewidth that quantifies the spectral broadening induced by SPM). The determination of the FOM_{TPA} was performed by means of a temporal analog of the top-hat Z-Scan. We have used a bidirectional injection procedure to discern the γ and the γ_{TPA}. The method allows the proper extraction of the coupling efficiencies, which are required to properly quantify the injected optical power in devices. The method could be used to compare the nonlinear performance of hybrid waveguides or photonic crystals in silicon photonics.

The proposed methods were tested by using an experimental set-up which enables to inject shaped pulses inside a waveguide with a well defined and characterized 2$^{\mathrm{nd}}$ order dispersion coefficient $\phi^{(2)}$ variable in the range of ± 3.5 ps^2, coinciding with the range required for a D-Scan study after the simulations of picosecond pulses. The input coupling efficiency was demonstrated to remain constant as we vary the value of $\phi^{(2)}$ over the full tuning range for $\phi^{(2)}$. Lastly, the nonlinear characterization of a monomode SOI waveguide was performed to validate the method proposed. The obtained values are in agreement with the standard quantities from the literature. The comparison between experimental and simulated spectra and their evolution as a function of the dispersion provided a remarkable correspondence. Regarding the uncertainties, the injection estimation is measured with an error of around 7%, the imaginary susceptibility with 9%, the FOM_{TPA} with 6% and the real susceptibility with 10%.

The method is finally applied to different kinds of integrated materials, showing a good agreement with experimental values in the literature and in the same order of magnitude as theoretical predictions for waveguides never characterized before in the nonlinear regime around $\lambda \sim 1580$ nm. Indeed, we have provided experimental values for SiGe waveguides in order to enrich the modeling of the nonlinear properties of these kinds of alloys towards applications in the midIR range. The presented results open perspectives towards the implementation of the D-Scan technique in other wavelength regions. Furthermore, we have measured some nonlinear properties of GSS ($\mathrm{Ge}_{23}\mathrm{Sb}_7\mathrm{S}_{70}$), used for flexible photonics structures. We have found values in the same order of magnitude of chalcogenides with similar compositions. As the refractive index of chalcogenides are moderate compare to the one of silicon, they could be used as a material for hybridization of silicon waveguides. Finally, the measurement of stoichiometric Si_3N_4 has allowed the validation of the method and demonstrated the material potentials for third order nonlinear applications due to its negligible TPA.

3 Nonlinear enhancement interaction in coherently excited cavities

One of the advantages of photonic crystal microcavities is to strengthen the interaction between an incident beam and the medium that makes up the cavity. On the other hand, the reinforcement of the nonlinear refractive index or loss/gain changes in the cavity limits the amount of energy that can be effectively coupled to the cavity mode. The frequency shift of the cavity resonance caused by the nonlinear refractive index variations precludes, in fact, the coincidence with the excitation signal frequency, thereby decreasing the coupling efficiency. In order to maintain the benefit of light localization throughout a pulsed excitation, we have experimentally and numerically studied the behavior of a silicon nanobeam micro-cavity excited by a tailored chirped pulse whose spectral phase relationship compensates for the nonlinear frequency drift of the cavity resonance. The **coherent control of microcavities** has been already theoretically proposed to enhance optical switching. In this work, we report both the experimental achievement and numerical investigation of a SOI nonlinear micro-cavity designed with two 1D Bragg mirrors (nanobeam) under coherent excitation, leading to an enhanced intra-cavity nonlinear interaction.

Contents

“Mas o que sonha o possível tem a possibilidade real da verdadeira desilusão. Não me pode pesar muito o ter deixado de ser imperador romano, mas pode doer-me o nunca ter sequer falado à costureira que, cerca das nove horas, volta sempre a esquina da direita”.

Fernando Pessoa, O Livro do Desassossego.

3.1 Introduction

The strong light confinement achieved in photonic crystal microcavities allows the enhancement of light-matter interactions, including nonlinear effects [107]. Recent developments of all-optical nonlinear functions, like optical switches [23], NAND gates [108] or all-optical random access memories [25], based on photonic crystal cavities rely on their very high ratio between the factor Q and the mode volume V. The consecutive strong enhancement of field intensity inside the cavity allows the realization of nonlinear functions with very-low control energy [23, 108, 25]. However, the field enhancement taking place inside high-Q microcavities necessarily restricts the signal bandwidth and the amount of energy that can be transferred between the control pulse and the intra-cavity material.

Among the **nonlinear functions**, low energy optical switches have been realized in nonlinear photonic crystal microcavities under the control of a resonant pulse in Silicon [24], InP [109] (containing quantum wells), GaAs [110], InGaAsP [23], and GaInP [111]. Although nonlinear refractive effects assist the switching operation, the imparted frequency shift dynamics of the cavity resonance tends to limit the coupling efficiency of the control pulse, inducing a modification of the cavity transmission for incoming optical signal. The induced refractive index changes in these materials are mainly driven by optical Kerr effect and by free carriers generated by either one-photon absorption or two-photon absorption. Although nonlinear refractive effects induce the switching operation, the imparted frequency shift dynamics of the cavity resonance, which is activated by the front edge of the control pulse, tends to limit the coupling efficiency of the rest of the pulse. As a result, the cavity enhancement effect is not maintained for the entire pulse duration, even if the latter is longer than the cavity photon lifetime, thereby limiting the energy transfer between the control pulse and the intracavity material. In addition, the mismatch between the drifting cavity resonance frequency and the frequency content of the control pulse leads to ringing behavior [112, 113], inducing temporal distortion on the signal pulse [114].

Ultrashort pulses are not the only requirement for optimally maximize nonlinear light-matter interactions, indeed Fourier limited pulses are less effective than pulses with a suitable design of the spectral phase [115]. In order to better control the pulse excitation of an optical resonance, the ideas of controlling either the coupling relationship into micro-resonators in relation with the pulse shape [116], or the pulse shape itself in

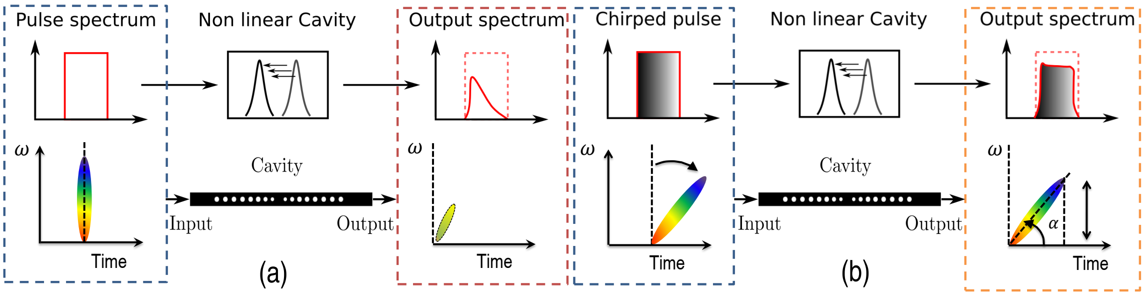

Figure 3.1: Scheme of a cavity under a pulse excitation in the nonlinear regime. (a) Fourier limited pulse and (b) chirped pulse [93].

relation with the temporal behavior of the intra-cavity amplitude field [117], have been theoretically investigated. The latter consists in transposing pulse shaping techniques that are routinely used to coherently excite atomic or molecular transitions in order to control light matter interactions [118, 119, 120]. In [117], the authors show with numerical simulations that a pulse with a controlled spectral phase relationship, compensating for the linear dispersion of the cavity resonance, can reduce the switching threshold power of a bistable Kerr microcavity. A controlled two-pulse excitation scheme of a pure-Kerr microcavity has also been theoretically investigated in [121]. And more recently, in [122], the researchers proposed a method enabling a broader transmitted bandwidth than the cavity resonance spectrum width by using a prechirped pulse and the optical Kerr effect. Their numerical analysis showed that a proper pulse could transmit about 11.8 times higher energy than an equivalent Fourier limited pulse. While these works deal with the behavior of cavities operating under pure Kerr effect, theoretical investigations of coherent excitation (tailored chirped pulse) of a semiconductor microcavity operating under optical Kerr, two-photon absorption (TPA), free carrier refraction (FCR) and free carrier absorption effects have been performed in [123]. In the case of silicon-based microcavities, the optical resonance mainly experiences a frequency blue-shift driven by the refractive index variation induced by free carriers generated by TPA. By delaying blue spectral components, corresponding to a positive linear chirp, it is shown that the benefit of light localization can be maintained throughout the pulsed excitation despite the cavity resonance dynamic frequency shift as illustrated in Fig. 3.1.

After the first experimental observation of a **coherent excitation of a nonlinear micro-cavity** performed by J. Oden in his PhD work [93], leading to an enhanced intra-cavity nonlinear interaction, our contribution resides on a detailed and systematic experimental study, along with numerical analysis of the coherent excitation. We investigate the nonlinear behavior of a **silicon-based microcavity** coherently excited with tailored positively chirped pulses with different spectral bandwidths and input energies. An increase of up to a factor 2.5 of the carrier density generated inside the cavity by TPA is demonstrated in comparison with Fourier transform limited pulses and negatively chirped counterpart. In addition, we show an enhanced nonlinear interaction allowing to induce a very large frequency blue-shift of the cavity resonance reaching 19 times the linear cavity linewidth. Such a blue-shift is achieved in a silicon microcavity with a Q factor close to 8 000, which is excited by a rectangular spectral shape pulse with a linewidth equal to 6.5 nm, or 30 times the bandwidth of the cold cavity. This result highlights the interest of such a coherent excitation to manipulate the optical bandwidth and the nonlinear dynamics of optical cavities, which could address future trends in the development of integrated resource-efficient ultra-high- speed optical communications systems [124].

We have used the same experimental pulse stretcher and laser source presented in section 2.4. The linear and nonlinear behaviors of the cavity are experimentally investigated and the transmission spectra are compared for different pulse excitations: Fourier limited, positive and negative tailored chirped pulses. Our results illustrate the **enhancement of the interaction between an incident pulse with a pre-chirp and a nonlinear optical resonator**. We finally discuss the interest of such coherent excitation to manipulate the optical bandwidth and the nonlinear dynamics of optical cavities and its dependence on the pulse properties such as the bandwidth, central wavelength and incident energy. All these procedures could address future trends in the development of integrated optical functions.

3.2 Designed microcavity

We chose to experimentally investigate the coherent excitation in a Fabry-Perot type microcavity engraved on a Silicon-On-Insulator (SOI) ridge waveguide, commonly known as photonic crystal nanobeam resonator. The cavity geometry is based on two-symmetric tapered Bragg mirrors [125] engraved on a 260×520 nm^2 SOI ridge waveguide, which offers small modal volume and quality factors Q of few thousands, compatible with few picoseconds pulse duration. The high-reflectivity mirrors were designed with Bloch-mode-engineering concepts [126]. They consist in a taper section with 4 holes and a periodic section made of 4 holes with a 200 nm diameter and a 370 nm periodicity constant. The parameters for the taper section have been optimized in order to achieve a quality factor close to 8000. The taper hole diameters are 130, 160, 190 and 200 nm with the center-to-center hole distances set to 320, 340, 360 and 370 nm (as shown in Fig. 3.2). For achieving this design, three-dimensional (3D) numerical calculations of the mirror reflectivity have been performed with the aperiodic Fourier modal method (a-FMM) [127]. The distance between the centers of the two-inner holes of the cavity is set to 590 nm in order to localize the cavity resonance nearby λ = 1580 nm. Using a 3D FDTD simulation, the calculated modal volume of the designed cavity is $V = 0.8(\lambda/n)^3$, with n = 3.48 the refractive index of silicon [93].

A SEM picture of the fabricated cavity is shown in the inset of Fig. 3.3. The SOI wafers have been processed with the fabrication steps described in section 1.4.1. TE-polarized

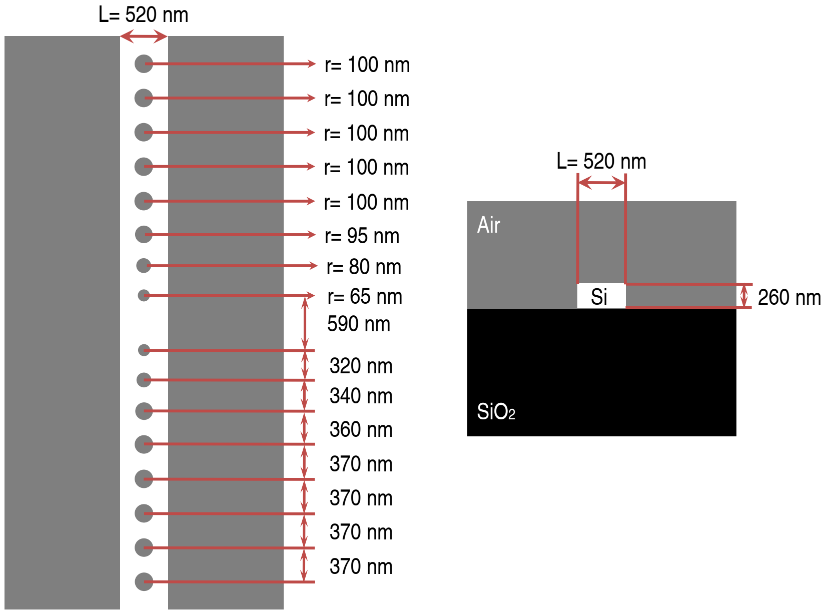

Figure 3.2: Geometrical parameters used to fabricate the cavity. The refractive indices used for the simulations were 1.44 for silica and 3.48 for silicon at a targeted resonance wavelength around 1580 nm.

light delivered by a tunable external cavity laser diode is injected into the access ridge waveguide by using a micro-lensed fiber connected to a polarization-maintaining single mode fibre. The transmitted light is collimated using a microscope objective followed by a TE polarizer, and sent to a sensitive power-meter. As expected from the simulations, the linear transmission measured by scanning the laser wavelength between 1530 and 1600 nm exhibits one peak shown in Fig. 3.3. The oscillations that are superimposed on the peak originate from the Fabry-Perot effects occurring between the cleaved facets of the device and the cavity mirrors. The 0.14 nm oscillation periodicity is in agreement with the Free-Spectral-Range for a 2.5 mm long cavity, considering that the cavity is situated at the middle of the 5 mm long waveguide. The microcavity peak transmission plotted in black line in Fig. 3.3 is obtained following low-pass filtering of the Fourier components of the recorded transmission. The Lorentzian fit, red line in Fig. 3.3, gives a cavity resonance located at 1578.8 nm with a full width at half maximum (FWHM) of $\Delta\lambda_0$ =0.217 nm. The quality factor of the microcavity is estimated to $Q = 7275$, close to the expected value, with a related photon lifetime $\tau_c = Q/\omega$ equal to 6 ps.

Because the experiment consists in evidencing different spectral transmission behaviors of the cavity as a function of input linear chirp of the excitation pulse, the dispersion of the access waveguides must be taken into account. If we consider a 0.1 μm^2 size SOI ridge waveguide, the second-order dispersion coefficient for a TE polarized mode is about $\beta_2 = 1$ ps^2/m [128]. For the shortest pulse duration $T_0 = 1$ ps that will be considered in the following, we verify that this dispersion effect can be neglected since the dispersion

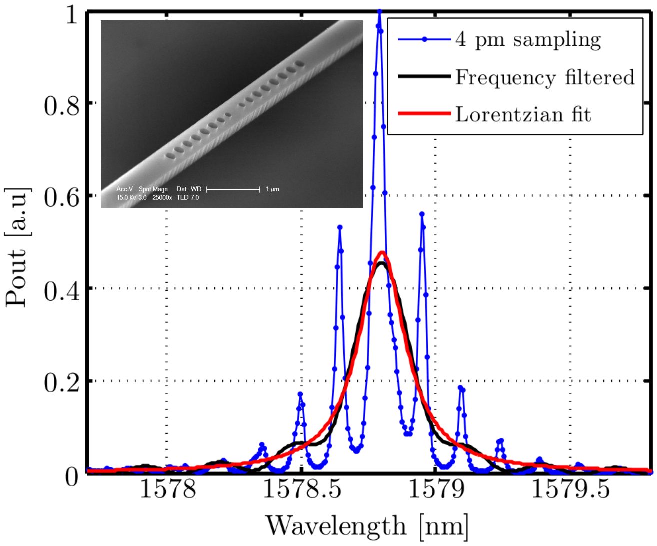

Figure 3.3: Linear transmission measurement of the Fabry-Perot type microcavity (blue solid line). The Lorentzian fit of the low-pass filtered linear transmission (black line) plotted in red solid line gives a quality factor $Q = 7275$. Inset: SEM picture of the Silicon microcavity made of two-symmetric Bragg mirrors engraved on a SOI ridge waveguide.

length $L_D = T_0^2/|\beta_2|$ equal to 0.5 m is much longer than the few millimeters waveguide length.

3.3 Analytical approach

Using the linear parameters of the microcavity, we are now able to proceed with the determination of the shaped pulse parameters that we need to generate in order to demonstrate the **coherent excitation of the microcavity under the nonlinear regime**. The experimental set-up scheme shown in Fig. 3.4 consists in controlling, by means of a pulse shaper, the spectral phase relationship and linewidth of pulses delivered by a laser prior to their injection inside the microcavity engraved on a nanowire. Under the nonlinear regime, the injected pulses induce a refractive index variation $\Delta n(t)$ of the intra-cavity material, which dynamically modifies the cavity resonance through the relation $\Delta\omega(t)/\omega_0 = -\Delta n(t)/n$. By controlling the spectral phase relationship of the pulse, we seek the instantaneous pulse frequency to follow the cavity resonance drift and to maintain a resonant excitation of the cavity. In such a condition, the cavity is expected to experience a larger frequency shift, which would demonstrate the coherent excitation of a nonlinear cavity and its ability to control its nonlinear behavior.

For a silicon microcavity excited with a few ps pulse duration and at a low repetition time around 20 ns, the nonlinear refractive index variation is predominately governed

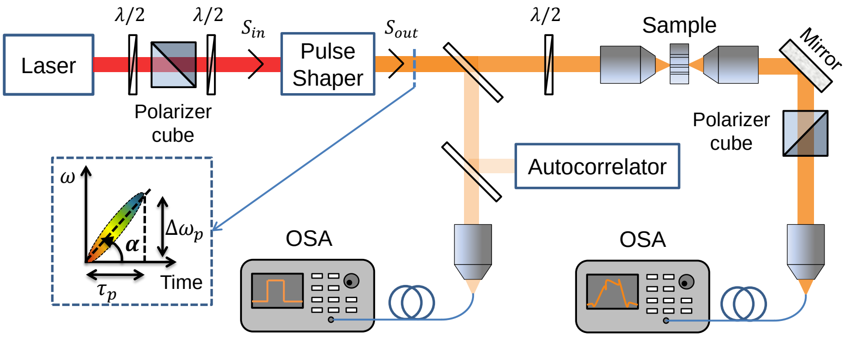

Figure 3.4: Experimental set-up used to excite the cavity. We recall the use of a femtosecond source consisting on an Er-doped amplifier fiber laser. The beam is sent into a grating-based pulse shaper prior to their injection into the sample by means of a microscope objective.

by the free-carrier density $N(t)$ generated by two-photon absorption (TPA) [123]. Anticipating that the carrier lifetime is much longer than the cavity photon lifetime, the cavity frequency shift follows the time integral relation $\Delta\omega(t)/\omega_0 = -\sigma_r N(t)/n = -\frac{\sigma_r}{n}\int_{-\infty}^{t}\frac{\beta_{TPA}}{2\hbar\omega_0}\left(\frac{c|u(\tau)|^2}{nV}\right)^2 d\tau$, which depends on the intra-cavity pulse energy $|u(t)|^2$, the effective volume of the free-carriers σ_r and the TPA coefficient β_{TPA}. This relation shows that the cavity resonance exhibits, for a square temporal pulse shape, a linear blue shift with time and $\Delta\omega(t) \simeq \alpha t$, with α the chirp parameter of the nonlinear cavity resonance. The chirp is represented as the slope of the pulse in the time vs. frequency plot in Fig. 3.1 (b) and Fig. 3.4. As shown in section 2.4, the generation of an excited pulse with a linear frequency chirp can be achieved through the propagation of a transform limited pulse inside a second order dispersive medium, with a dispersion coefficient $\phi^{(2)} \simeq 1/\alpha$.

We now assess pulse parameters that are optimal to coherently excite a cavity exhibiting this resonance frequency shift, under the square temporal shape approximation. An order of magnitude for the optimal amount of second-order phase and energy can be simply calculated by setting a target value for the cavity frequency shift $\Delta\omega_p$ covered during the pulse duration τ_p. The target we seek in this work would be to reach a nonlinear shift equal to 30 times the linear cavity linewidth, meaning that $\Delta\omega_p = 30\ \omega/Q$. Under a pulse duration equal to the cavity photon lifetime $\tau_p = \tau_c = Q/\omega$, the dispersion coefficient value is estimated, through $\phi^{(2)} = \tau_p/\Delta\omega_p = Q^2/(30\ \omega^2)$, to a value of $+1.3$ ps^2. This required chirp value is achievable with the pulse shaper introduced in section 2.4 and used for the D-Scan tests. Finally, we must estimate the amount of energy required to reach such a blue shift range, or equivalently the amount of free-carrier density to be generated inside the cavity. An order of magnitude of the energy is given by considering a squared pulse shape in the time integral relation for $N(t)$, which gives $|u|^2 = -\frac{nV}{c}\sqrt{\frac{n^2\hbar\Delta\omega_p}{\sigma_r\beta_{TPA}\tau_p}}$ [129], corresponding to a reasonable energy value of 0.4 pJ. With the attained peak powers from the laser source introduced in section 2.4 ($\sim$ 160 W) and the estimation of coupling coefficients on tapered silicon chips ($\sim$ 10%) and in the ps regime, on-chip pulse energies up to $\sim$16 pJ are possible to achieve, making the set-up suitable to attain the required free carriers generation from silicon.

For all forthcoming estimations, we have used the following nonlinear parameters for silicon $\beta_{TPA} = 0.8$ cm/GW [98] and $\sigma_r = -1.35\ 10^{-27}$ m^3 [10].

3.4 Nonlinear behavior of a coherently excited microcavity

We next seek to study the nonlinear behavior of the previously characterized SOI microcavity under a coherent excitation in order to demonstrate that a proper control on the spectral shape of the excited pulse enables to control the intracavity nonlinear interaction. This experimental study is performed by measuring the evolution of the transmission spectra for different dispersion coefficients $\phi^{(2)}$ at a fixed incident energy and for two spectral shapes.

In addition to the dependence of the nonlinear behavior of the cavity under the spectral phase relationship of the pulse, we would like to give an illustration of the spectral power distribution effect. Because our pulse shaper in the present configuration cannot offer a sufficient flexibility in that regards, we could only play with the injection current of the two laser diode pumps of the fiber laser module. By doing so, we could slightly modify the spectral power distribution of the incident pump. In Fig. 3.5, we display the cavity spectra evolution by using two pulse excitations set at the same input power of 6.8 mW and spectral bandwidth (we will refer to them as red-i, shown in (a) and purple-ii in (b)). We recorded the transmission spectra varying the dispersion coefficients from -3.5 to +3 ps^2 and we display the linear cavity in gray (× 5) as a guide to estimate the blue-shift. Despite the small change in the spectral power distribution of the incident pulse, the comparison between the two sets of transmission spectra in Fig. 3.5(a) and (b) underlines the influence of both the spectral phase and power relationships.

The grating of the pulse shaper is slightly rotated in order to deliver pulses centered around 1578 nm. The incident pump optical spectrum is plotted on the top of Fig. 3.5 with a red and purple dotted lines. At very low input power, the transmission spectra plotted in gray line (×20) coincide with the linear transmission of the microcavity previously depicted in Fig. 3.3. While the spectrum of the incident pulse is 30 times larger than the linear cavity resonance, with a spectral linewidth set to 6.5 nm, only the spectral components that coincide with the cavity resonance are transmitted.

For an incident power set to a fixed value of 6.8 mW, the transmission spectra recorded for dispersion coefficients varying between -3.5 to +3 ps^2 are plotted in Figure 3.5 for two different excitation spectrum (i-red and ii-purple). We highlight that the input power, spectral width and initial induced chirp are the same for both experiences, only

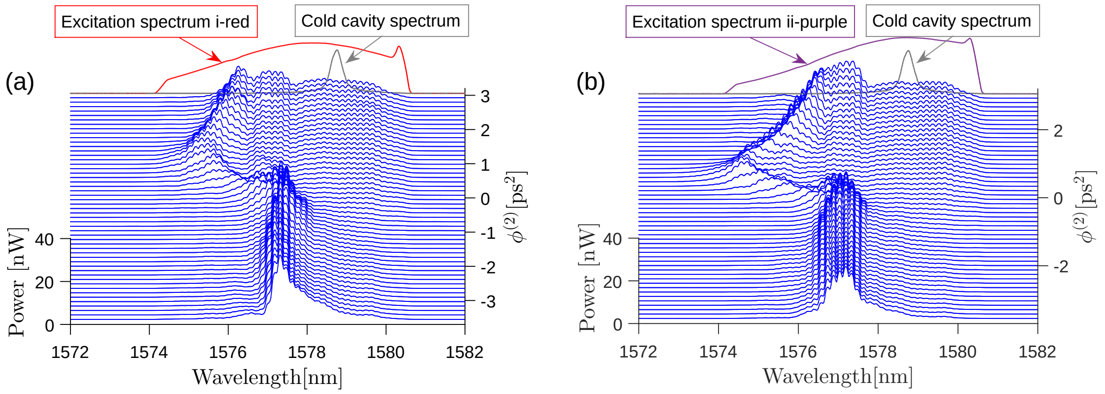

Figure 3.5: Evolution of the transmission spectra of the cavity measured with varying the chirped pulse excitation from $\phi^{(2)} = -3.5$ up to $+3.5$ ps^2 for two different excitation spectra (a) and (b). The spectral linewidth of the two excitation pulses are plotted in red-i (a) and purple-ii (b) and the cold cavity transmission in gray ($\times$ 5).

the spectral content distribution (shape) is different. One can first notice that all the transmission spectra are blue-shifted respect to the linear cavity resonance. Considering a Fabry-Perot type microcavity, a frequency shift in the transmission spectra coincides to that of the the cavity resonance, which in our case is driven by the refractive index change induced by the free carriers generated by TPA. This nonlinear effect has been already employed to realize all-optical switches on SOI micro cavities [130, 24]. Whereas the transmission spectra under both excitations remain almost unchanged for negative chirps, they clearly exhibit an increasing blue-shift content for positive values of $\phi^{(2)}$ varying from 0 to around +1.6 ps^2. Beyond the optimum control (ideal spectral delay), the blue shift slightly decreases. Even though the cavity evolution under the two excitation pulses follow the same trends. It can be seen in Fig. 3.5 that the optimum required chirp is slightly different for both excitation spectra. In the case of excitation i-red, the largest transmitted bandwidth is obtained when a pre-chirp of $\phi^{(2)} = +1.6$ ps^2 is applied [131, 132]. In the case of excitation ii-purple, the optimum pre-chirp is obtained at $\phi^{(2)} = +1.2$ ps^2 [133]. This change can be understood as a more adequate wavelength distribution to excite free carriers and also to charge the cavity within the new frequency after the blue-shift. The result presented in this section demonstrate the possible optimization of the coherent excitation not only with a linear chirp but also with the spectral shape used to excite the cavity.

To give physical insights in the nonlinear cavity behavior, we compare in Fig. 3.6(a) the transmission spectra achieved under the excitation i-red with $\phi^{(2)} = 0$ and with two opposite chirps + and -1.6 ps^2. Analogously, in Fig. 3.6(b), the three spectra are plotted for the excitation ii-purple for chirps at + and -1.2 ps^2. The cold cavity is plotted ($\times$ 5) in gray to compare with the transmission under 5 pJ incident energy. The nonlinear output under a Fourier limited pulse excitation is plotted in blue. It is interesting to

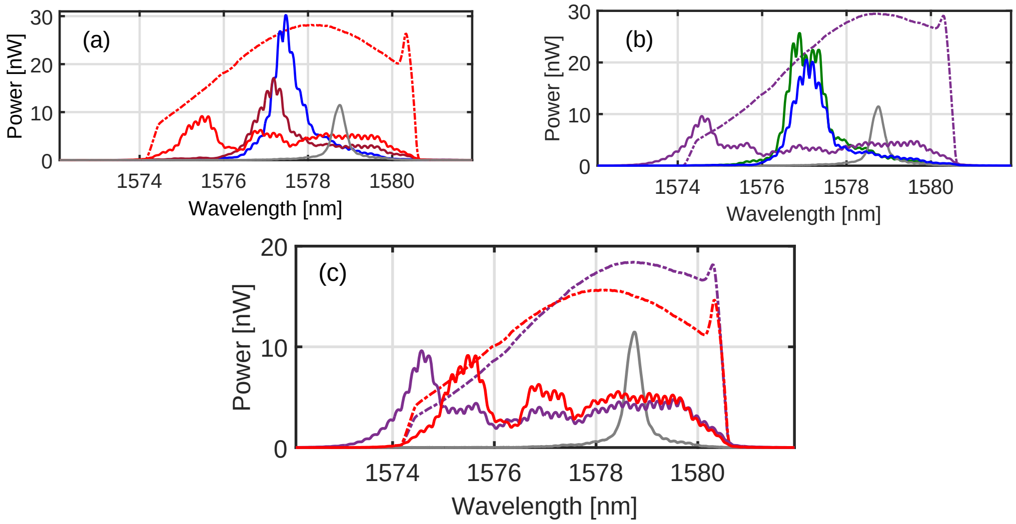

Figure 3.6: Measured incident (dashed line) and transmission spectra, plotted in linear scale at low energy (gray line, ×5 in linear scale) and at 5pJ incident energy for various chirped pulse excitations: Fourier-Transform limited pulses (blue line), negative dispersion (brown-(a) and green-(b) curves) corresponding to the optimum positive excitation $\phi^{(2)} = +1.6\text{ps}^2$ (red-(a) curve) and $\phi^{(2)} = +1.2\text{ps}^2$ (purple-(b) curve). (c) Comparison between the optimum chirp for both spectra.

notice that even though the shift is very similar, in the case of the purple excitation (Fig. 3.6 (b)), the spectral content around 1578 nm is larger than in the red case (Fig. 3.6 (a)), generating more free-carriers, exhibiting a larger blue-shift and a lower transmission. In quantitative terms, under the red-i input excitation, the cavity exhibits 1.4 nm blue-shift and under the purple-ii case is of 1.6 nm. In the time domain, the pulse duration, which is about 1.1 ps, is shorter than the cavity photon lifetime and the cavity resonance is excited in a slightly transient regime. In contrast, the two opposite chirped pulses exhibit an autocorrelation pulse duration of around 8 ps, giving a pulse duration (5.7 ps) close to the cavity photon lifetime.

Compared with the negative excitation chirps: in brown (Fig. 3.6 (a)) the output spectrum at $\phi^{(2)} = -1.6$ ps^2 and in green (Fig. 3.6 (b)) at $\phi^{(2)} = -1.2$ ps^2, the transmission spectra for $\phi^{(2)} = +1.6$ ps^2 (red-(a)) and $\phi^{(2)} = +1.2$ ps^2 (purple-(b)) lead to a larger blue-shift and a remarkably broader transmission spectrum, which closely matches the input pulse bandwidth. It can be seen that the resonant shift for negative chirps remains similar than the one obtained with no pre-chirp. Whereas the two signed pulse excitations for each of the two spectral shapes give the same pulse duration, they differ in the sign of their spectral phase relation. Under the positive chirp case, the cavity is first excited by the red components of the pulse. Although the red side of the pulse spectrum is detuned from the centered wavelength of the cavity resonance, the transmission around 1580 nm is not null, meaning that the cavity resonance starts to store some energy and to shift

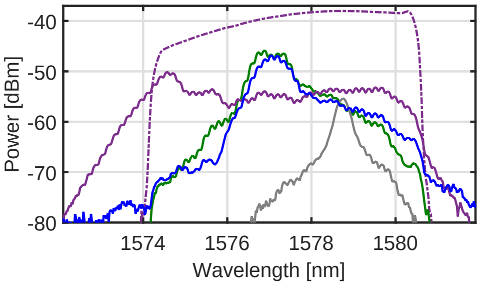

Figure 3.7: Measured incident (dashed line) and transmission spectra, plotted in dBm scale at low energy (gray line, ×5 in linear scale) and at 5pJ incident energy for various chirped pulse excitations: Fourier-Transform limited pulses (blue line), $\phi^{(2)} = -1.2\text{ps}^2$ (green curve), $\phi^{(2)} = +1.2\text{ps}^2$ (purple curve).

towards the blue. Owing to the linear time-frequency relation of the pulse, the coupling efficiency to the drifted resonance can be maintained, increasing further the blue-shift extension compared with the negative chirped pulse.

The unambiguous differences between the transmission spectra for the two chirped pulses signify that the nonlinear behavior taking place inside the microcavity clearly depends on the delay between the spectral components of the excited pulse. We claim that the $+1.6$ ps^2 chirped pulse excitation coincides with the situation where the delay between the spectral components of the pulse matches the instantaneous cavity frequency drift, which, with a good approximation, follows a linear time variation [123]. Aiming a comparison between the transmitted bandwidth for both optimal excitations, we have added an additional plot (Fig. 3.6 (c)) where the difference between the attained transmissions is clearer.

In Fig. 3.7, we present the three spectra in dBm scale for the purple excitation in order to appreciate the optimization of frequency generation and the covering of all the input frequencies, meaning that all of them were at resonance.

The broader transmission spectrum, and equivalently the larger spectral blue-shift experienced by the cavity resonance achieved with the positively chirped pulse, proves that a larger amount of free-carriers have been generated inside the microcavity thanks to a better energy transfer between the incident pulse and the intracavity material. The larger spectral broadening achieved with the positively chirped pulse is necessarily assisted by a higher carrier density generation and proves an enhanced nonlinear interaction between the pulse and the intracavity material, equivalently a better energy transfer between the incident pulse and the cavity resonance. In Fig. 3.8, the measured spectra are evaluated under different figures of merit. In (a) we have plotted the r.m.s. spectral linewidth (2σ) versus the introduced chirp. Taking into account that the 2σ of the input pulse was 3.2 nm, we can see that the 2σ ratio between output and input spectra increases from 50% at the baseline up to 125% for the optimum excitation. This ratio

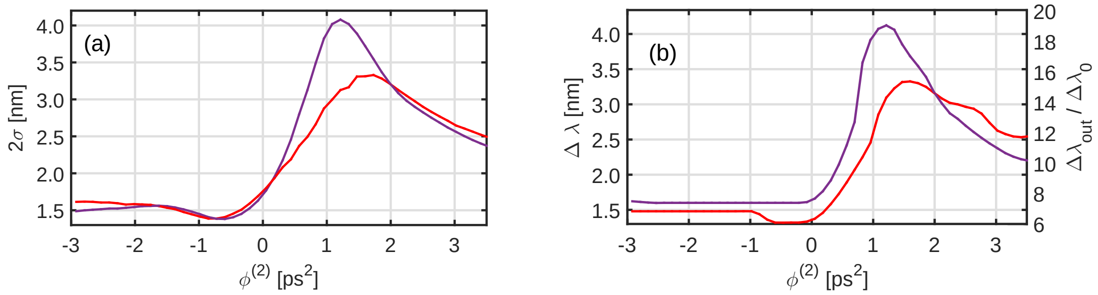

Figure 3.8: (a) Measured r.m.s. spectral linewidth for the chirp coefficients $\phi^{(2)}$ reported in Fig. 3.5 under two different excitation pulses. (b) Measured cavity blue-shift in wavelength with respect to the linear cavity resonance. In the right axis: number of times that an equivalent bandwidth to the FWHM of the cold cavity is transmitted.

determines the quantity of spectral content transmitted through the cavity. Indeed it is larger than 100%, because other generated new frequencies, absent in the input pulse are effectively measured in the output spectrum (Purple spectra in Fig. 3.7). In (b), there are two axes, one representing the wavelength shift (towards the blue) with respect to the linear cavity resonance and the right-axis consists in a comparison between the output bandwidth ($\Delta\lambda_{\mathrm{out}}$) and the bandwidth of the cold cavity ($\Delta\lambda_0$). As previously said, the cavity blue-shift is maintained at a fixed value $\Delta\lambda_{\mathrm{out}} \approx 1.6$ nm for negative dispersion coefficients, which tends to signify that the amount of energy transferred from the incident pulse to the microcavity remains unchanged. On the other hand, the cavity blue-shift behavior towards $\phi^{(2)} > 0$ shows an increase by a factor 2.5 between 0 and $+1.2\mathrm{ps}^2$ for the purple case, meaning that TPA generated carrier density is 2.5 times higher. For higher dispersion coefficients, the blue-shift experienced by the cavity resonance decreases. A better transfer of energy between the incident pulse and the intra-cavity material is achieved under the $\phi^{(2)} = +1.2\mathrm{ps}^2$ excitation pulse, leading to an enhanced nonlinear interaction.

To compare with the preliminary values we targeted in section 3.3, we can use the values of the right axis from Fig. 3.7 (b). While the cavity blue-shift is constantly equal to $\Delta\lambda_{\mathrm{out}} = 7 \times \Delta\lambda_0$ for $\phi^{(2)}{<}0$, it reaches $\Delta\lambda_{\mathrm{out}} = 15 \times \Delta\lambda_0$ for the red excitation at $\phi^{(2)} = +1.6\mathrm{ps}^2$ and $19 \times \Delta\lambda_0$ for the purple excitation at $\phi^{(2)} = +1.2\mathrm{ps}^2$, values that are close to the dispersion coefficient previously anticipated to reach a cavity blue-shift of $30 \times \Delta\lambda_0$. Note that, experimentally for both excitation spectra, the red side of the pulse spectrum is red detuned from the linear cavity resonance by 2 nm, or equivalently by $10 \times \Delta\lambda_0$, which is not counted in the evaluation of $\Delta\lambda_{\mathrm{out}}$ in Fig. 3.8.

Finally, we can estimate the amount of absorbed energy achieved for $\phi^{(2)}$ =+1.2 ps^2 (purple excitation) by substituting the frequency blue shift $\Delta\lambda_{\mathrm{out}} = 4.1$ nm into the relation given at the end of section 3.3, which gives an estimated energy of 0.3 pJ for a refractive index variation $\Delta n/n = \Delta\lambda_{\mathrm{out}}/\lambda = 2.5\ \times 10^{-3}$. This variation is about one order of magnitude higher than the values reported in [134] in a SOI ring cavity with a quality factor of 3 000, or in [135] in a SOI photonic crystal cavity with $Q = 7\ 000$.

3.4.1 Central excitation wavelength dependence

In previous experiences the excitation pulse was optimized in terms of its spectral position respectively to the cold cavity resonance (shifted towards the blue with respect to the resonance). So, the intra-cavity field could interfere constructively with the blue components of the pulse. So the impact of the central wavelength position is crucial for a proper excitation.

Experimentally, the tilt on the diffraction grating allows the change of the central wavelength without modifying the characterized dispersion. Nevertheless, as the laser gain-spectrum is not homogeneous, we obtain a different spectral shape (changing the temporal pulse duration), but the general trends will be useful to understand the central wavelength dependency. We will only study the most interesting case, meaning the optimum dispersion to properly excite the cavity ($\phi^{(2)}>0$), for insights in the negative and the Fourier limited regimes, the reader is invited to see Ref. [93].

In Fig. 3.9, we present the output spectra for different central wavelength excitations at a fixed dispersion. We have used the purple excitation from the previous section and chosen the optimum value: $\phi^{(2)}= 1.2\ \text{ps}^2$. In (a), the pulse is totally shifted towards the blue and do not cover the resonant frequency of the cold cavity. The output wavelength content is

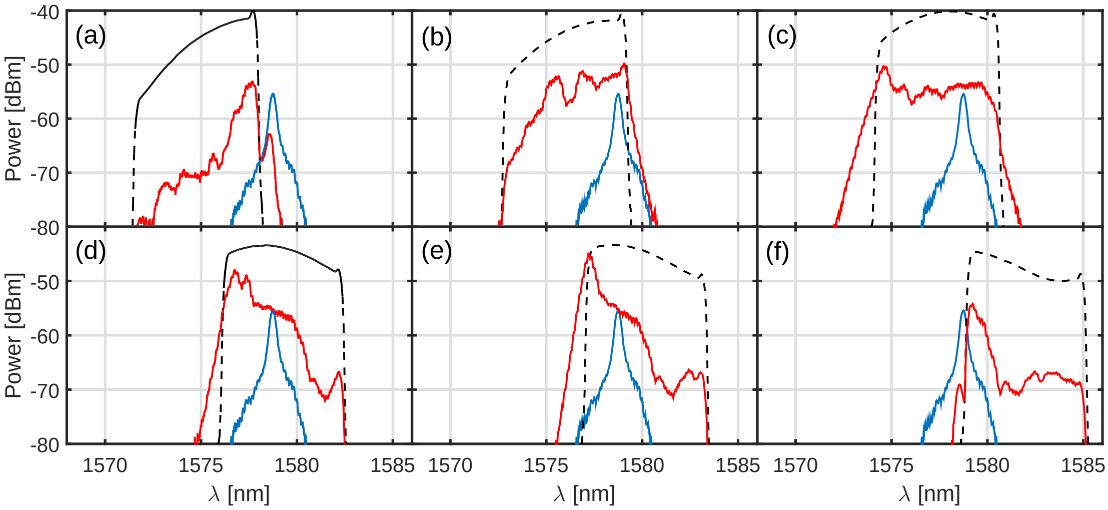

Figure 3.9: Transmitted spectra in dBm as a function of the central excitation wavelength for a $\phi^{(2)}= 1.2\ \text{ps}^2$. The spectral width and injected power are kept the same for all the experiences. In dashed black the input spectrum, in blue the linear cavity to locate the resonance and in red the recorded transmission.

poor but interestingly, there is a small tail (10 dBm lower than the maximum transmission) that matches with the resonant frequency. We attribute these new wavelengths to the ones generated via SPM in the access waveguide. We can expect that for the Fourier limited case, the spectral components at the resonant wavelength are larger as the pulse peak intensity increases. After the cavity resonance wavelength is included in the pulse bandwidth (b), the control is evident, yet not optimum. In this case as well as for (c) and (d), the wavelengths shift towards the blue in a larger amount than the expected Fourier limited case (usual blue shift), meaning a light-matter enhanced interaction due to more generated free carriers. Finally for the cases (e) and (f), the coherent excitation gets truncated as there is no bluer components available. In (e) the accumulation of photons at the blue-side of the input spectrum indicates the possibility to inject lower frequencies in the resonator.

3.4.2 Input energy dependence on the nonlinear interaction

Up to this point, we have experimentally demonstrated the enhanced nonlinear interaction in a silicon microcavity by controlling the pulse frequency drift and we have seen the effect of different linear chirps for two distinct input spectral shapes. Now, we would like to dedicate this section to a more systematic study on the way to control the cavity nonlinear transmission as a function of the input pulse energy and dispersion $\phi^{(2)}$.

These experiences were performed in another nanobeam cavity. It could be noticed that the excitation is not centered around ~1578 nm but approximately to 1584 nm. The only difference with respect to the previous cavity is the increase by 10 nm of the distance between the center of the two-inner holes (600 nm in Fig. 3.2). The hole tapers and the reflectivity mirrors are identical, so the measured quality factor and figures of merit are of the same order of magnitude. The cavity linewidth is around $\delta\lambda \approx 0.20$ nm, giving a quality factor around 8000 as for the previous cavity. This change was performed to obtain more gain from the Er-doped laser and to demonstrate the coherent excitation in a different structure.

First, we started using an excitation width of 7 nm, so slightly larger than the one used in the previous demonstrations. The wavelength distribution was more homogeneous, so we could expect a less optimum control than in the case of stronger lower frequency components. In Fig. 3.10, we show the evolution as a function of the introduced dispersion. We have plotted all the spectra from 1 mW (linear regime) until 13 mW in steps of 4 mW. The pulse energy for the Fourier limited case inside the cavity is of few pJ.

Fig. 3.10 (a) shows the linear case, when the nonlinear effects are negligible. As expected, the transmission is equivalent to the cavity linewidth regardless the induced pre-chirp, translating in an almost flat line of the r.m.s spectral linewidth (light blue - Fig. 3.10

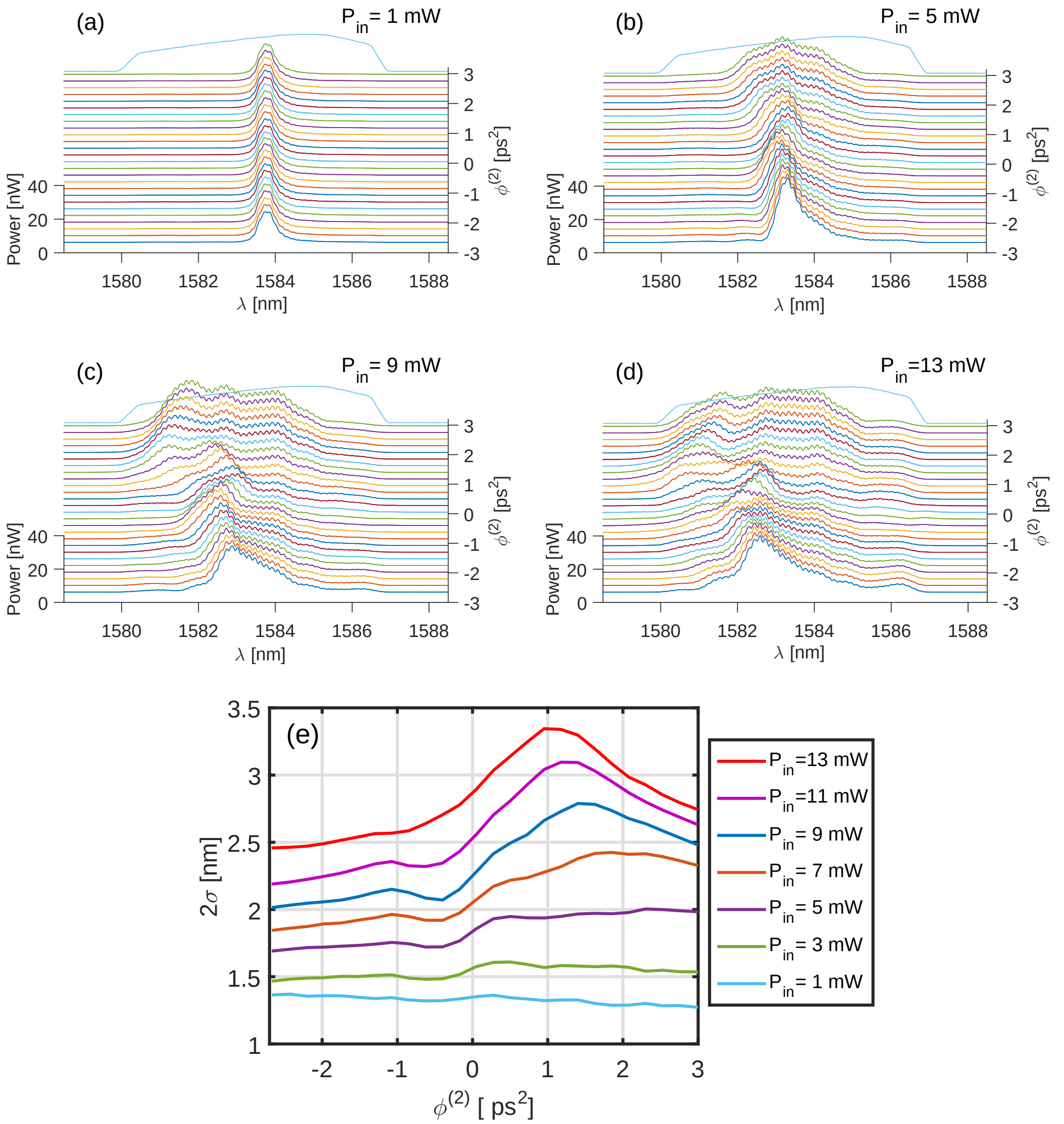

Figure 3.10: Energy dependence of the coherent control for a 7 nm pulse width. (a-d) Output spectra for different injection powers: (a) 1 mW, (b) 5 mW, (c) 9 mW and (d) 13 mW. (e) Standard deviation as a function of the induced dispersion for different input powers.

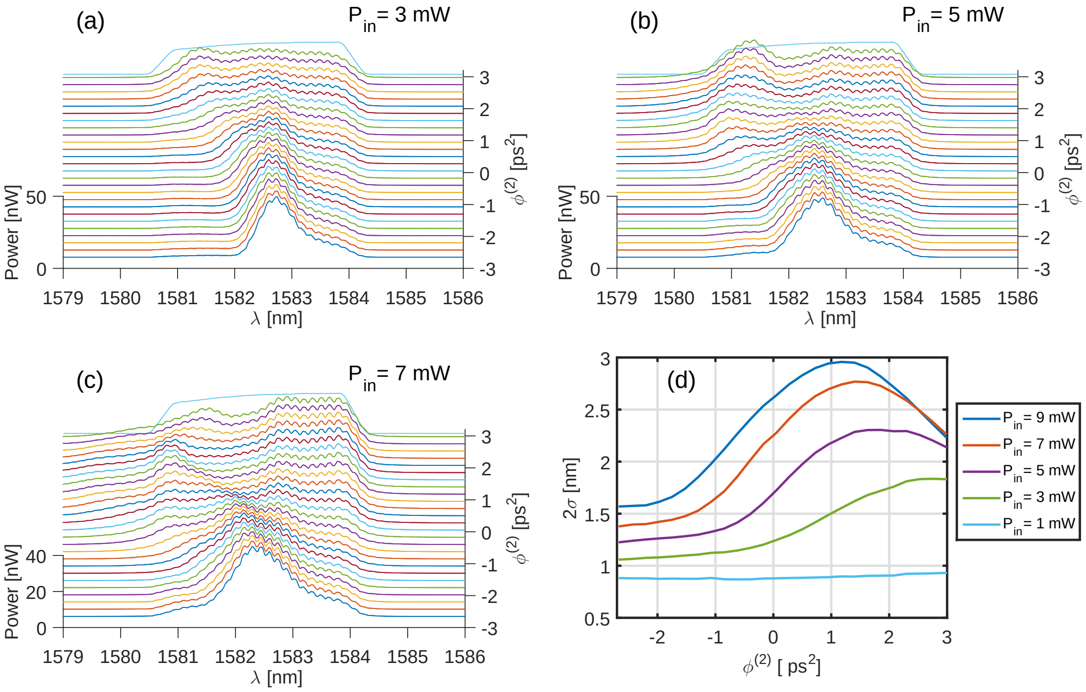

Figure 3.11: Energy dependence of the coherent control for a 3.5 nm pulse width. (a-c) Output spectra for different injection powers: (a) 3 mW, (b) 5 mW, (c) 7 mW. (d) Standard deviation as a function of the induced dispersion for different input powers.

(e)). When the power is increased 5 times (Fig. 3.10 (b)), an asymmetric behavior with respect to the sign of dispersion is noticed. Indeed, for positive chirps (red components before the blue), a broader transmission is obtained. In the r.m.s spectral linewidth curve (purple - 3.10 (e)) an increase is noticed, but the optimum point seems not to be reached until 3 ps^2. When the power is further increased up to 9 mW (Fig. 3.10 (c)), the expected blue shift is faster, so the optimum drift is reached at lower dispersion, in this case around 1.4 ps^2, so of the same order of magnitude as the one used in the previous cavity. We should recall that the input power in that experience was around 7 mW.

Finally, we present the highest attainable power (13 mW) and strong nonlinearities that could be observed in the spectral evolution at different dispersions. When approaching to the Fourier limited case, the spectral peak presents a fast red shift prior a fast optimization, obtained at around 1 ps^2.

We have performed a last study by using the same cavity but decreasing the bandwidth of the excitation pulse (from 6.5 nm to 3.5 nm), meaning a Fourier limited case, increasing the temporal width by a factor of ∼2. So, a pulse width of ∼2 ps was applied. Assuming that the coupling efficiency was the same, we obtained pulse energies twice larger for the same previous case input power. We have thus recalibrated the correspondence between the stage position and the introduced dispersion, as shown in section 2.4.

In Fig. 3.11, we present the spectra for three incident powers. With an input power of 3 mW (a), it can be observed that even though the control is present, the optimum value is not reached for dispersion values lower than 3 ps^2. Then a case where the average input power is ∼5 mW allows an optimum control at around 1.7 ps^2. It can be noticed that the output spectral shape for the optimum case is remarkably flat, covering all the wavelengths of the exciting pulse. Finally, we studied a case under input power equals to 7 mW (Fig. 3.11 (c)). As could be anticipated from the previous experiences, the best spectral content is found at lower dispersion values (∼1.2 ps^2), but the output is not as flat as in the previous case.

These trends demonstrate the existence of an optimum dispersion value for each pulse energy that allows the broadest possible output transmission. As expected, when more energy is present, the cavity frequency shift is faster, requiring a stronger frequency drift applied to the chirped pulse. It means that for higher energies, lower dispersion (strong drift) optimizes the transmission.

3.5 Simulations

After the presentation on the transient operation of a microcavity under a coherent excitation, we have demonstrated that through appropriate shaping of the incident signal, the coupling efficiency and the enhancement of the non-linearities are shown to be increased. Nevertheless it would be crucial to develop a tool that predicts the optimum values for nonlinear light-cavity interactions. For instance: the pulse position with respect to the cold cavity, the required pre-chirp for a given injected energy or even more, the possibility of using other integrated materials or hybrid waveguides.

In this context, we conducted preliminary simulations of the nonlinear behavior of our cavity by using the coupled mode theory which accurately emulates the limitation of the energy that can be coupled inside a nonlinear resonator whose refractive index is changing with time [123, 129].

The intracavity field dynamics can be described by two coupled ordinary differential equations [129], where the dynamical variables are the intracavity field $u(t)$ and the free carrier density $N(t)$:

$$\begin{aligned}\frac{du(t)}{dt} &= i\omega_0\left(1-\frac{n_2 c}{n^2 V_K}\left|u(t)\right|^2-\frac{\sigma_r}{n}N(t)\right)u(t)\\ &\quad-\left(\frac{\omega_0}{2Q}+\frac{\beta_{TPA}c^2}{2n^2V_{TPA}}\left|u(t)\right|^2+\frac{\sigma_a c}{2n}N(t)\right)u(t)+\sqrt{\frac{\omega_0}{Q_e}}s_{in}(t)\end{aligned} \tag{3.1}$$

$$\frac{dN(t)}{dt} = -\frac{1}{\tau_c}N(t)+\frac{\beta_{TPA}}{2\hbar\omega_0}\frac{c^2}{n^2V_{FC}^2}\left|u(t)\right|^4 \tag{3.2}$$

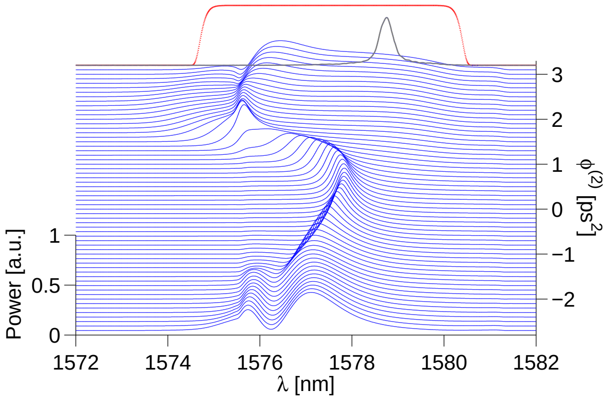

Figure 3.12: Simulated transmission spectra of the cavity under chirped pulse excitations varying from $\phi^{(2)} = -3$ to $+3.5$ ps^2. The spectral linewidth of the incident pulse is plotted in red line. The transmission spectrum calculated at low incident power is shown in gray line.

where $s_{in}(t)$ is the temporal shape of the input pulse field defined as $|s_{in}(t)|^2 = P_{in}(t)$, with $P_{in}(t)$ the incident pulse peak power, ω_0 the angular frequency of the linear cavity, c the speed of light in vacuum, $\hbar$ the reduced Planck's constant, V_K and V_{TPA} the Kerr and two-photon absorption (TPA) nonlinear volumes (assumed equal) calculated by means of FDTD simulations, giving $V_K = V_{TPA} = \frac{\left(\int_V \varepsilon(\vec{r})\left|\vec{E}(\vec{r})\right|^2 d^3r\right)^2}{\int_V \varepsilon^2(\vec{r})\left|\vec{E}(\vec{r})\right|^4 d^3r} = 2.3(\lambda/n)^3$ and V_{FC}, the volume related to free carrier effects $V_{FC} = \sqrt{\frac{\left(\int_V \varepsilon(\vec{r})\left|\vec{E}(\vec{r})\right|^2 d^3r\right)^3}{\int_V \varepsilon^3(\vec{r})\left|\vec{E}(\vec{r})\right|^6 d^3r}} = 1.7(\lambda/n)^3$. The linear parameters of the cavity were determined by the simulations initially performed in section 3.2 and set to $Q = 7\ 900$ and $Q_e = 8\ 500$ (coupling between the incident field and the cavity). To complete the model, the nonlinear parameters of silicon were used, for instance, the Kerr index n_2, the TPA coefficient β_{TPA}, the free carrier refraction effective volume σ_r and the free carrier absorption effective area σ_a . The carrier lifetime was set to $\tau_c = 0.4$ ns [125]. For the modeling, a 32$^{\text{nd}}$ order supergasussian was used in order to simulate the input spectral shape. As shown in previous works [123], we have neglected nonlinear contribution from thermal effects.

For the sake of simplicity, the free carrier nonlinear effects occurring in the access waveguide were not included in the present model. This assumption has been verified through numerical simulations and nonlinear transmission measurements through an equivalent strip waveguide with no cavity. On the contrary, the accumulated nonlinear phase and power depletion due to the Kerr and TPA effects in the access waveguide are included.

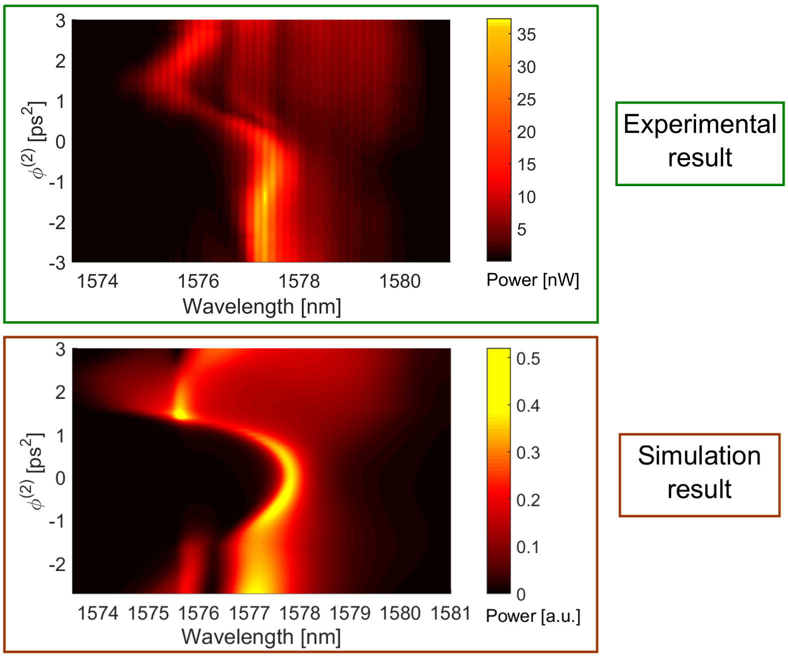

Figure 3.13: Top: Extrapolated transmission map as a function of the wavelength (horizontal axis) and the introduced dispersion (vertical axis). Colormap in nW. Bottom: Correspondent simulated transmission. Colormap in a.u.

Keeping $\varphi^{(2)} = 0$ ps^2, 5 pJ Fourier-limited injected pulses induce a 1.4 to 1.6 nm blue-shift of the cavity resonance (Fig. 3.8). The frequency blue-shift is governed by the time varying refractive index of silicon induced by the free carriers being generated by TPA during the pulse excitation. The larger spectral broadening achieved with the positive chirped pulse is assisted by a higher carrier density generation and proves an enhanced nonlinear interaction between the pulse and the intracavity silicon material. In Fig. 3.5, the red spectra correspond to the optimum control of the cavity, so the largest coupled energy is obtained for the experimental (left) and the simulated (right) cases. On the contrary, the green line curves show the spectra under the same chirp but with an opposite sign, demonstrating that the enhancing effect is only obtained with positive chirps. It can be seen that despite the periodic modulations in the experimental data, the simulated spectra reproduce the trends of the coherent control that are observed experimentally.

In Fig. 3.13, we present the comparison in a colormap between the numerical results and the experimental measurements for the red excitation (as it the input pulse is closer to the simulated one). It is interesting to remark the output asymmetry given by the model following a broader transmission for positive dispersion values (coherent excitation). The model also predicts the red shift present around the Fourier limited case. Also, the optimum value obtained in the simulations is very close to the one extracted from the experimental spectra at around $\phi^{(2)} = +1.6$ps^2. These preliminary results shows that

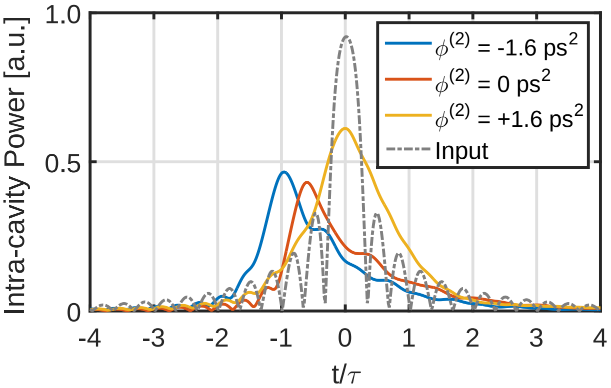

Figure 3.14: Intracavity field temporal evolution under different pulse excitations.

the adopted model can be used to anticipate the required compensation for particular resonators with different materials and diverse quality factors.

Finally, we have simulated the intra-cavity energy in order to demonstrate that at the proper excitation the temporal drift is compensated. Fig. 3.14 displays the calculated intracavity fields for a frequency square-like pulse. The Fourier limited pulse (orange) and the negative dispersion (blue) cases present a temporal drift and a decrease of the coupled power that are compensated in the case of the positive dispersion (yellow). In the latter, the simulated shape is very close to the envelope of the original sinus-cardinal function used as input and the curve is almost symmetric.

3.6 Conclusion

We have experimentally demonstrated and thoroughly studied the coherent excitation of a nonlinear SOI microcavity. By controlling the linear chirp of the excitation pulse, an enhanced nonlinear interaction between the pulse and the intra-cavity silicon material is experimentally verified. Compared with a Fourier-transform limited pulse of equal energy, positively chirped pulse excitation enables to increase the free carrier density generated by TPA by up to a factor of 2.5. It is accompanied by a large frequency blue-shift of the cavity resonance reaching 19 times the linear cavity linewidth, corresponding to a refractive index variation $\Delta n/n = 2.6 \times 10^{-3}$. These experimental results have been verified using a coupled mode theory model that includes silicon nonlinearities.

The spectral pulse linewidth used to excite the silicon microcavity, with a Q factor close to 8 000, is 30 times larger than the bandwidth of the cold cavity. Although our experimental results do not include temporal measurements, one has to remind that the variations in the transmission spectra are necessarily accompanied by differences in the intra-cavity field dynamics, as illustrated in [123] for gaussian shape pulse excitations, underlying the interest of coherent excitation in the purpose of controlling the nonlinear dynamics of optical cavities or optical devices.

Thanks to a physical analysis of the nonlinear behavior of the microcavity, we were able to predetermine the pulse shape, in particular the spectral phase relationship approximated to a positively linear chirp. Such an approach refers to an open-loop coherent control scheme [118] that does not require any experimental feedback. In contrary, close-loop scheme could be envisaged to excite optical resonators, as it is routinely achieved for atomic and molecular resonances [136], which could be an interesting method to characterize nonlinear dynamics of optical resonators and nonlinear parameters of intra-cavity materials.

Finally, our study demonstrates the capability to manipulate the optical bandwidth and the nonlinear dynamics of a cavity by means of a coherent excitation. The same could be applied to more complex structures like coupled cavities or optimized with more elaborated pulse shaping schemes. This coherent control of on-chip resonators may open new routes for low-power optical switches [23] and all-optical memories [137].

4 Dispersion engineered PhC for hybrid and nonlinear integration

In this chapter we will explore the properties of slot photonic crystal waveguides (SPhCW). We start with the design and simulation of the dispersion engineered structures, then we introduce some fabrication improvements to obtain low loss waveguides. The linear properties, in particular the dispersion curves are characterized under two different methods for diverse covering refractive indices. Finally, we give insights in the optimization of hybrid waveguides for nonlinear applications followed by some preliminary results on the enhancement of light-matter interactions in the slow-light regime.

Contents

“Man könnte den ganzen Sinn des Buches etwa in die Worte fassen: Was sich überhaupt sagen lässt, lässt sich klar sagen; und wovon man nicht reden kann, darüber muss man schweigen”.

Wittgenstein, Tractatus Logico-Philosophicus (1922).

4.1 Introduction

In the first chapter, we have introduced the basic concepts of waveguiding in PhC and the effects of introducing a slot for applications via hybrid integration (see section 1.3.4). In this chapter we will relate these physical principles to silicon based structures. Indeed, the maturity of the Silicon on Insulator (SOI) platform allows the fabrication of submicrometer patterns required to make holes and slotted defects with low propagation losses while benefiting from a natural compatibility with the CMOS technology [138]. The two objectives of small footprint optical components and the shrinkage of energy consumption for the information treatment require the enhancement of the light matter interactions in small volumes. In this purpose, photonic crystal waveguides (PhCW) rise as candidates due to their confinement and versatile dispersion properties including slow light and possible control of group velocity dispersion (GVD) effects [16].

Besides, nonlinear phenomena in photonic integrated circuits [139, 18] have been considered as a promising route to ensure important functionalities like modulation or commutation at higher rates than their electronic counterparts, especially by using third-order nonlinear optical effects in silicon [140, 141]. Additionally, in slow light structures, there is a scaling of the light matter interaction that depends on the group index (n_g). This behavior is quantified by the enhancement slow down factor defined as $S = n_g/n$, with n the material refractive index [142]. Third order nonlinear effects -such as Kerr self phase modulation- scale with S^2, which means proportionally to the square of the group index [107, 87]. Consequently, slow light structures are of great interest due to their improvement of the nonlinear device performance. However, their bandwidth becomes narrower as the average group index ($\langle n_g \rangle$) increases and with no careful design (i.e. engineering) of the waveguide, the wavefront is severely distorted by GVD [143].

Moreover, light propagation losses increase in the slow light domain due to back and out-of-plane scattering [144], so there is a practical upper limit for the group index, typically around 50. For W1 waveguides, where the fabrication errors are minor compared to the slot case, the dramatic increase of extrinsic optical losses for large group indices have shown that even for waveguide lengths of the order of 100-200a and $n_g \approx 50$, the modeling of the system departs from perfect Bloch-modes [145], so careful attention should be addressed to the propagation losses.

An additional trade-off needs to be targeted: bandwidth-group index. A simple figure of merit to estimate the buffering capacity of a slow light structure comparing different lengths or operating frequencies is the Normalized Delay Bandwidth Product (NDBP), defined as $NDBP \approx \langle n_g \rangle \Delta\omega/\omega$, where $\langle n_g \rangle$ is calculated within 10% variation with respect to the mean group index value [146, 147]. We will use this parameter to characterize the designed waveguides.

At telecommunication wavelengths, the strong two photon absorption (TPA) in silicon and its associated effects related to the presence of a free carrier plasma (e.g. Free carriers absorption and dispersion), indeed spoil the benefits of Kerr-induced nonlinear phase shifts [141]. Even in the range of moderate propagation losses for n_g<40, the optimistic picture of enhanced optical nonlinearities by slow light phenomena is thus severely counterbalanced by free carrier effects in silicon.

Furthermore, it has been shown that the expected nonlinear dependencies predicted by analytical relations hold as long as both realistic losses and the dependency of the mode shape with respect to the group index are taken into account [148], as well as considering the multiphoton absorption and linear scattering effects [149]. To circumvent these limitations, other materials with better nonlinear figures of merit than silicon, such as GaInP, have been explored [150]. Nevertheless the costs of integrability make solutions based on silicon still of prior interest. In this sense, hybrid silicon waveguides based on a hollow core slot geometry have been proposed and demonstrated, first in a classical picture [14] and later within a PhCW scheme [17]. In the versatile toolbox of PhCW, these slotted (SPhCW) configuration have brought the possibility to add up slow light and GVD-nearly-on-demand properties of PhCW with a hollow core waveguide geometry. Indeed, in this chapter we will explore these structures and demonstrate for the first time the fabrication of dispersion engineered (DE) SPhCW.

4.2 Design

Currently, combination of photonic crystals and photonic nanowires is considered as a viable alternative for densely integrated, highly functional circuits, so we need to deal with coupling stages that will have a non-negligible influence in the dispersion, losses and nonlinear properties of the circuit. We will increase the complexity in the waveguide design of the silicon samples by adding stages to couple the fundamental mode in several geometries.

4.2.1 Coupling stages

Up to this point, we have considered in the experiments only slot and strip waveguides in different materials, but we have not discussed the problem of injection efficiencies when varying the waveguide geometry. The proper coupling between strip and PhC slow

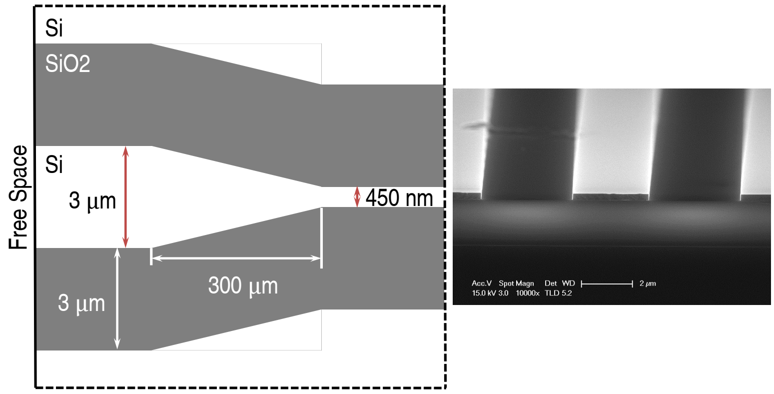

Figure 4.1: Left: First two coupling stages between a free space beam and a monomode waveguide. The silicon height is typically 220 nm or 260 nm. Scheme not in scale. Right: SEM image of the cleaved region.

light modes is crucial due to the difference of the transverse mode profile and the energy density mismatch [151]. The problem becomes critical if a slot is added. So, in this subsection we will give a brief summary of the design and fabrication efforts to optimize each step. We will have mainly five transitions: (1) free space to multimode access waveguide, (2) multimode to a monomode strip waveguide, (3) strip to slot waveguide, (4) slot to fast light SPhCW and (5) fast to slow light SPhCW. Even though we have worked with gratings to couple light in silicon waveguides [28], the used structures in this manuscript are excited via butt-coupling. The first two stages are the same for all the waveguides and are negligible for our purposes. Indeed a multimode input waveguide of 3 μm width is set and a transition of 300 μm long is defined to end in a monomode waveguide of around 450 nm width as shown in Fig. 4.1-Left. On the right of the image, we present a SEM figure of the multimode access waveguide with the 3 μm isolation. The 2 μm silica box underneath is appreciable.

The stage (3) is more complex as the mode shapes in strip and slot waveguides are remarkably different. Indeed in recent years, several studies have been performed to optimize this transition. Proposals as symmetric and asymmetric strip-loaded to slot converters [152, 153], Y-like couplers [154] and side coupling converters [155, 41] have been numerically and experimentally demonstrated by using electronic and optical lithography. The latter two have been chosen in our studies, even though the side coupling will be preferred (we will specify when the Y-like coupler will be used).

In Fig. 4.2 (a) and (b), we depict the SEM images of the two used coupler designs. The typical length for the Y-like adapter is 15 μm and for the side-coupled 20 μm. We present in (c) and (d) the normalized strip and slot fundamental TE modes at 1580 nm for waveguides covered with a refractive index material of n =1.46. The reader could notice that the two mode profiles are very dissimilar. Yet, we obtain losses lower than 1 dB for Y-like couplers and 0.2 dB for side couplers.

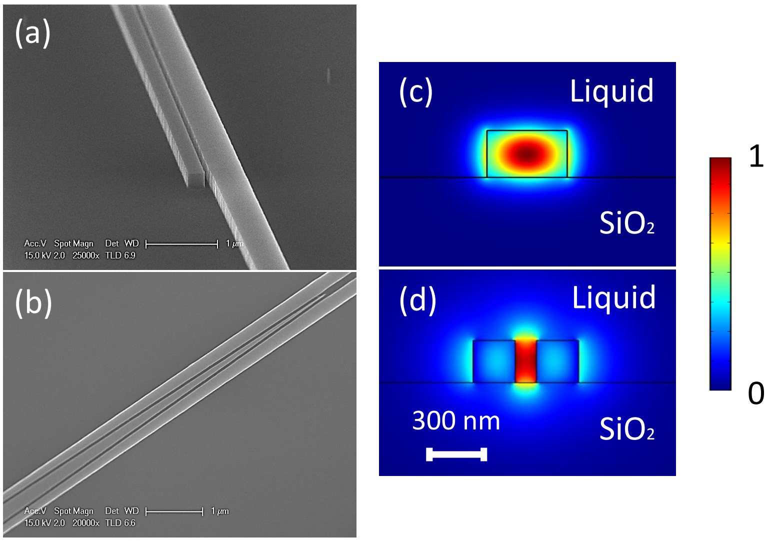

Figure 4.2: (a) and (b) SEM images of strip to slot converters by Side coupling and Y-like, respectively. (c) and (d) are the normalized fundamental modes for a strip and a slot waveguides.

Next, the light propagates in the slot waveguide before arriving to the photonic crystal. At this point, the energy density difference becomes the predominant problem to be addressed. Indeed, apart from the modal spatial distribution, if the mode enters in a slow light photonic crystal, the mode gets spatially compressed and the peak intensity increases with the slow down factor $S = n_g/n_0$ [142]. In Fig. 4.3, we depict the effect of that strong slow light mismatch in a W1 waveguide that was experimentally measured via SNOM by Volkov et al. [156]. So, an additional coupling stage is required to optimize the light injection in the slow light PhCW.

Even though some works have proposed to cancel the large fields associated with the slow mode at the interface with the contribution of evanescent fields in abrupt interfaces[157], we have chosen the transition steps proposed by Hugonin et al. [158] and experimentally realized in W1 waveguides by Li et al. [147], where the mode transits from a propagation invariant mode towards a fast light engineered PhC, prior the slow light waveguide. This is obtained by tuning among the propagation direction the lattice period of the crystal. The general principle is: the longer the distance between holes the larger the cut-off wavelength (this is not a linear relation).

In our design, as shown in Fig. 4.4, the lattice constant variation is set to 10 nm and the number of periods for each coupler lattice constant is set to 5. We show also with a horizontal black line in (a) when the mode that enters in a fast light PhC crosses to a slower guide and finally arrives to a structure operating near the bandgap. In this example, the central waveguide period is 400 nm. It should be noticed that this parameter will vary for other structures, particularly when the dispersion is tunned. The

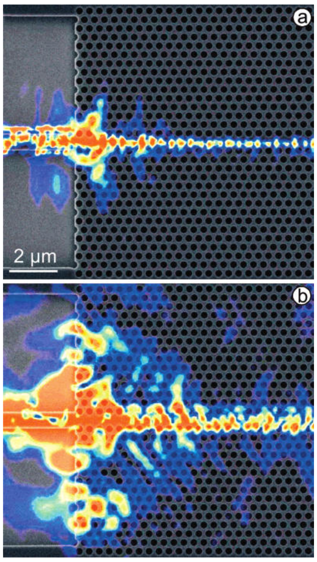

Figure 4.3: Pseudo-color near-field optical images recorded in the (a) linear (at $\lambda = 1430$ nm) and (b) slow-light (at $\lambda = 1545$ nm) regimes and directly superimposed on the corresponding SEM images by making use of the corresponding SNOM topographical images taken simultaneously with the ones. Figure from [156].

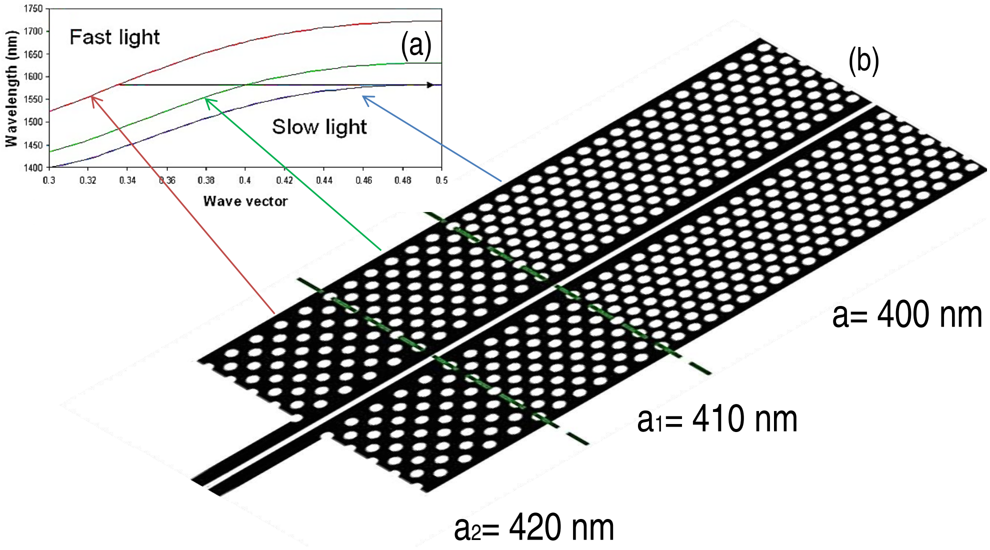

Figure 4.4: Fast to slow light converter in a SPhCW. (a) Band diagram for the three different periods depicted in (b). The figure is not in scale and was adapted from [159].

objective is to have a slow light regime close to the optimum wavelength operation of Er-doped fiber lasers (~ 1580 nm).

4.2.2 Tuning the dispersion

One of the biggest interests in PhC is the possibility to exploit the slow light behavior manifest close to the structure forbidden gap (limit of the Brillouin zone). In this subsection we will briefly describe the methods that we have numerically and experimentally applied to control the dispersion curves of guided modes.

In Fig. 1.12, we have shown a dispersion diagram of a non-DE SPhCW. By using the expression to estimate the group velocity for Bloch waves $v_g = d\omega/dk$, we have plotted the theoretical group index map as a function of the k vector. We attribute this slow light behavior to a constructive interference of the subsequent transmitted and reflected waves in a strongly dispersive medium. The component phase mismatch generates an envelope that propagates slowly compared to the speed of light imparted by the non-structured material. These phenomena have been used for applications in telecom such as delay lines and buffers [160], modulators [140, 161] or the particular interest of this work, enhancement of nonlinear effects like Third-Harmonic Generation (THG) [139], SPM [89] and FWM [72]. But there is a compromise between two crucial parameters for signal applications: the delay and the bandwidth. Indeed, we will see throughout this chapter that for higher targeted group index, the obtained bandwidth with the same delay is smaller. This requirement could be qualitatively explained by the fact that if different spectral components experience dissimilar delays, the output signal will be chirped, so to say, a chromatic dispersion due to the different group velocities will be introduced in the pulse distorting the temporal information, critical in high speed schemes. To quantify this effect the GVD expression is used:

$$GVD = -\frac{1}{\lambda^2}\left(\frac{d\omega}{dk}\right)^{-1} \tag{4.1}$$

To avoid the spreading problem, a method to optimize the dispersion diagram by modifying the hole net of the crystal has been proposed. This procedure is called dispersion engineering (DE). By this mean, we can perturb the coupling between the index guided mode and the gap mode. As the guided light in the photonic crystal remains highly confined in the defect, the tunning variables will be focused on the first three rows of holes. Many approaches have been proposed and experimentally demonstrated in W1 waveguides such as the variation of the hole radius [146, 162], the shift of the row of holes [147], the lattice shift of particular rows [163] or a combination of those techniques [164].

In Fig. 4.5 we present the case of tuning the row of holes (the fabrication tolerance is larger) in order to illustrate the dispersion engineering procedure and the bandwidth-delay

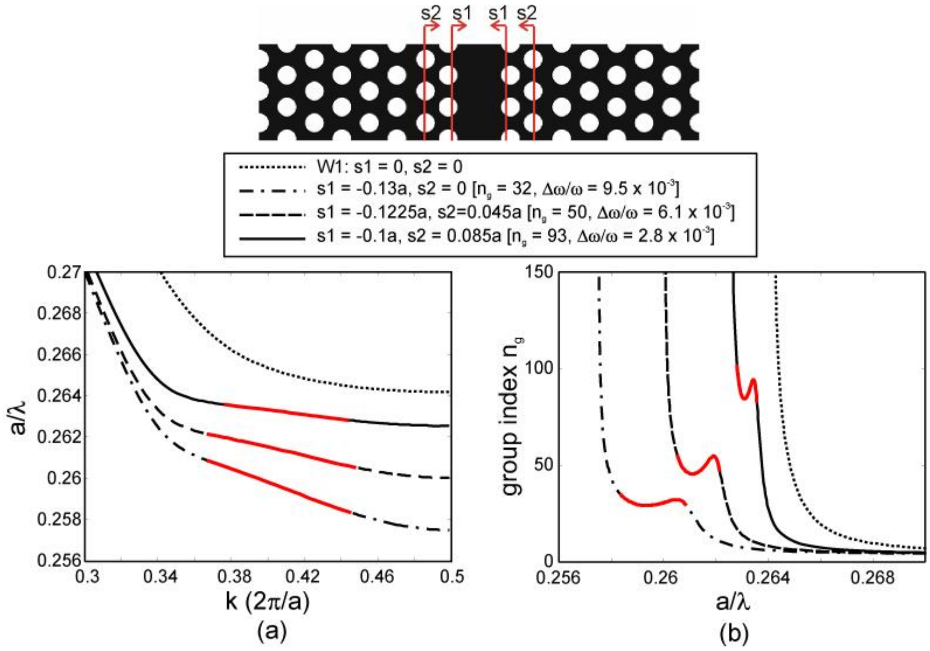

Figure 4.5: Geometry effect of modified W1 PhC waveguides: the first and second rows of holes are displaced symmetrically about the waveguide axis. (a) Calculated dispersion curves and (b) group indices, for the fundamental mode of the modified W1 PhC waveguides with given s1 and s2 values. The thick solid red line represents the flat band slow light region [147].

trade-off. In the diagram shown in Fig. 4.5 (a), it could be noticed that for lower slopes, the smaller the covered frequencies (y-axis). The derivative of this slope is the group velocity, so for higher constant group velocities (shown with the red line), smaller the bandwidth. Rather to discuss about group velocities it is more common to describe the group index; as shown in Fig. 4.5 (b), for higher group indices (smaller group velocities) the transmitted frequencies with the same group velocity (in red) are fewer.

To quantify this compromise, we use the normalized delay bandwidth ($NDBP$) product [87] as figure of merit defined as:

$$NDBP \approx \frac{\langle n_g \rangle \Delta\omega}{\omega} \tag{4.2}$$

where $\langle n_g \rangle$ is calculated within 10% variation with respect to the mean group index value as proposed in [146, 147]. Typically in W1 waveguides on SOI with air holes, the maximum $NDBP$ values are on the order of 0.30. This corresponds roughly to a bandwidth of 36 nm for a group index of 12 [164]. Later we will clarify the interest on moderate slow light regimes (n_g<50). This optimum figure will be even smaller for SPhCW, as the light line will restrict the available bandwidth due to the covering material (index contrast reduced).

At the present time, the dispersion properties of SPhCW have been explored numerically with interesting results [165, 166] mainly in a free-standing configuration. Yet, they remain essentially unexplored experimentally. The reasons stem first, from the sensitivity of SPhCW dispersion properties on the fabricated geometrical parameters. For instance, some of the theoretical proposals rely in exotic shapes or asymmetries that are difficult to control in lithographic processes [166, 167], and second on the difficulty to directly evidence the slow light and GVD waveguide features. Though, the control of slow-light and GVD in SPhCW is essential in order to fully benefit from the hybrid integration of soft matter (and low index) material on silicon (eg polymers). Furthermore, compared to their standard plain counter-part, hybrid slotted structures are of greater interest due to their even smaller effective areas [168].

In the next sections we will use the concepts of DE to simulate, fabricate and then characterize for the first time slotted PhC devices.

4.3 Simulations

The initial geometry consists in a 260 nm silicon thin film SOI wafer with lattice constant a = 420 nm, and hole radius r = 125 nm (0.30a) to ensure a wide TE bandgap. In order to pre-tune the dispersion curve, the first and second rows of holes are shifted towards and outwards the slot by 0.20a and 0.35a, respectively [169]. This first approach was elected because the position of the holes is easier to control during fabrication than their size and shape. Under these premises, the radius of the second row of holes is kept fixed to 125 nm and the radius of the first row (r_1) is swept between 95 nm (0.23a) and 125 nm (0.3a) in order to quantify firstly the experimental effects deriving from the modification of only one parameter [170] covering different group indices. Fig. 4.6 presents a schematics of the geometrical parameters obtained after optimization.

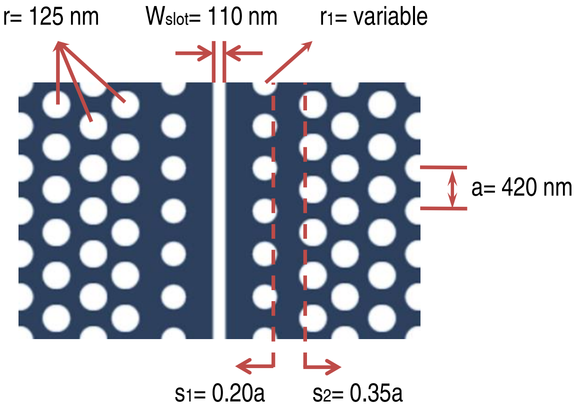

Figure 4.6: Geometrical characteristics of the design structure.

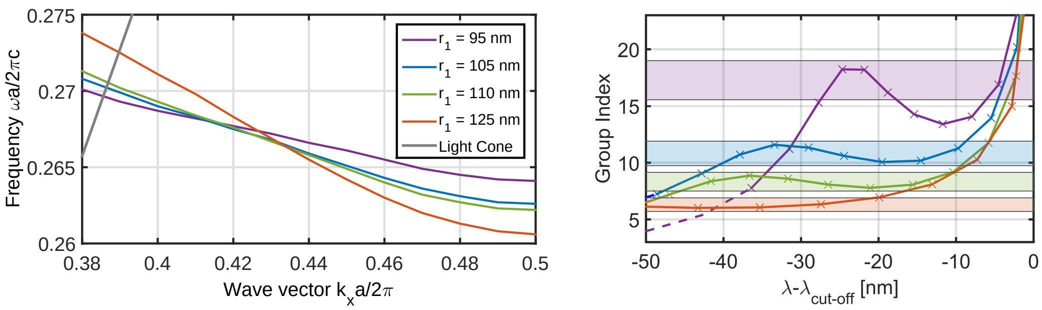

Figure 4.7: Left: Dispersion of the engineered modes as a function of the first radii. Right: extracted group indices highlighting a 10 % variation of $\langle n_g \rangle$. The dashed line corresponds to frequencies above the light line.

Frequency band engineering of the proposed structure is studied first numerically by the plane wave expansion method using the MPB software [171] for a quasi-TE polarization. Eigenmodes have been calculated in a unit cell reproducing the geometrical parameters described in the fabrication. A mesh resolution a/20= 21 nm and subpixel smoothing were used. The cladding has been assumed to have a refractive index of 1.45, close to the one of Silica and other interesting materials for hybrid integration.

The related results are shown in Fig. 4.7. From the depicted dispersion curves, there is a clear increase of the $\omega(k)$ slope when the first row hole radius increases, which means that a lower group index is achieved. Fig. 4.7-Right shows the group index as a function of the cut-off wavelength difference for each geometry. The dashed lines represent the leaky wavelengths above the light line and the color boxes have been used to calculate the figures of merit of the structures summarized in table 4.1. Those quantities will be confronted with experimental values.

In particular, the smallest radius structure will be intentionally over-engineered in order to test the characterization methods. In general, bandwidths larger than 30 nm and NDBP of the order of 0.20 are achieved. Note that these relatively modest group indices would yet actually correspond to slow light enhancement of S= 10–14 in the cladding.

In Fig. 4.8, we display the different $|E|^2$ profiles for the designed structures in the slow light regime (at $k = 0.46 * 2\pi/\text{a}$). It could be appreciated that a large part of

$\mathbf{r_1}$ **[nm]**	$\langle \mathbf{n_g} \rangle$ **(±10%)**	$\mathbf{\Delta\lambda}$ **[nm]**	**NDBP**
95	17.3 (±1.7)	9.8	0.108
105	10.8 (±1.1)	32.1	0.221
110	8.32 (±0.83)	35.1	0.186
125	6.30 (±0.63)	49.9	0.200

Table 4.1: Parameters calculated from simulations shown in Fig. 4.7 [170].

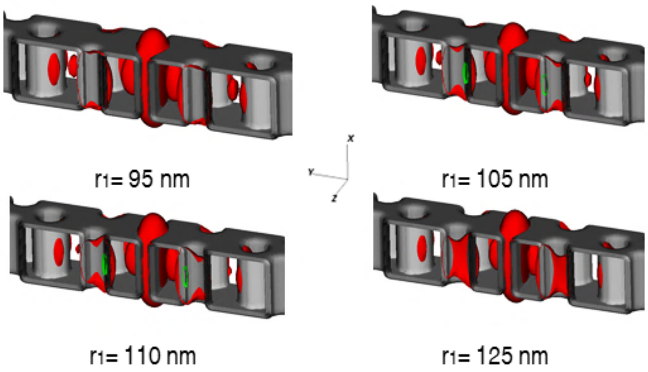

Figure 4.8: $|E|^2$ 3D profile of the DE SPhCW modes for different radii at $k = 0.46 * 2\pi/a$ [170].

the dielectric energy interacts with the filling material, for instance highly nonlinear compounds.

4.4 Fabrication

To confirm experimentally the simulation trends, the C2N/CTU-Minerve clean room facilities were used to fabricate the structures by following the steps described in section 1.4.1. A careful calibration of the current and the knowledge of the relation between the number of points to describe one motif and the mismatch between the drawn holes and structures with respect to the real value was carefully effectuated with the help of Ing. Xavier Le Roux. It is out of the scope of this chapter to describe each step and test performed but in this section we will comment on an improvement in the fabrication of the slot, as it is the main source of losses in the studied waveguides.

In Fig. 4.9, we display a schematic design of the different approaches followed in the mask design. For this propose, we have assigned to the slot a different layer with respect to the holes, so the dose used in the lithographic step could be, in principle, optimized independently. All the approaches are a combination of two ideas: i) slicing the slot to induce a preference electronic writing direction, as the machine will do it along the smaller dimension, so the borders (rugosity) will be better defined an ii) the overlapping of motifs to overdose the center of the slot. The optimized hole dose value for 2 nm step lithography was found to be at 2.8 C/m^2.

Under the electronic microscope none of the previous approaches show a significant difference (same statistical deviation), but the optical transmission measurements performed in the next section will help to understand the effects in the signal. In Fig. 4.10, we show an optical image with different SPhCW lengths and their respective reference waveguide containing a monomode strip with the same length as the SPhCW. It should

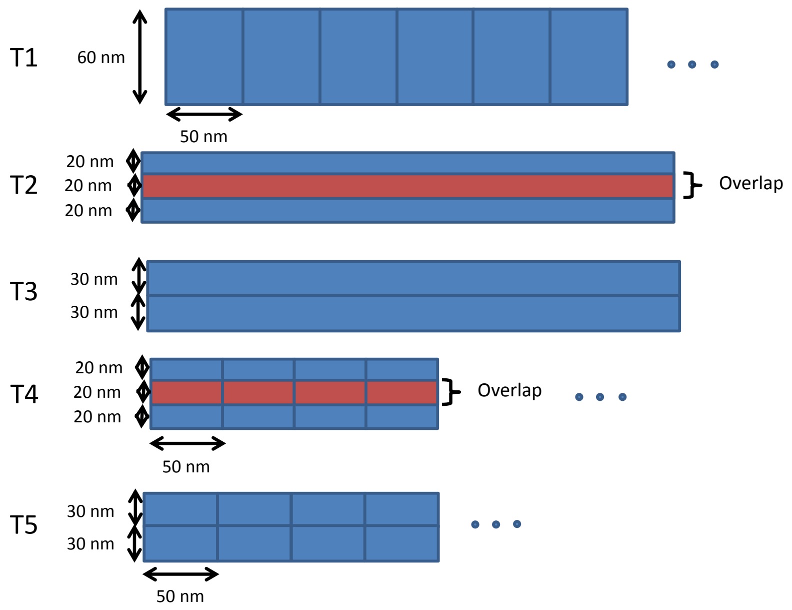

Figure 4.9: Different writing geometries for the slot in the lithographic process.

be noticed that the beginning of each photonic crystal is vertically the same. Indeed, the position of this critical part with respect to the main lithographic fields+sub-fields and the propagation prior the crystal should be equivalent to guarantee a fair comparison. In the same figure, the simple slot sections prior and after the PhC (couplers) are appreciable with a different tone of blue. In Fig. 4.10 Left, a zoom of a 50 μm long waveguide (Fig. 4.10-Right bottom) is presented with its respective reference waveguide, the different size in the hole radii is perceptible as well as the markers for the fast light to slow light couplers.

Finally, a closer inspection with an electronic microscope (SEM) (Fig. 4.11) allows us to differentiate the shift in the row of holes for the DE waveguide. Furthermore, a

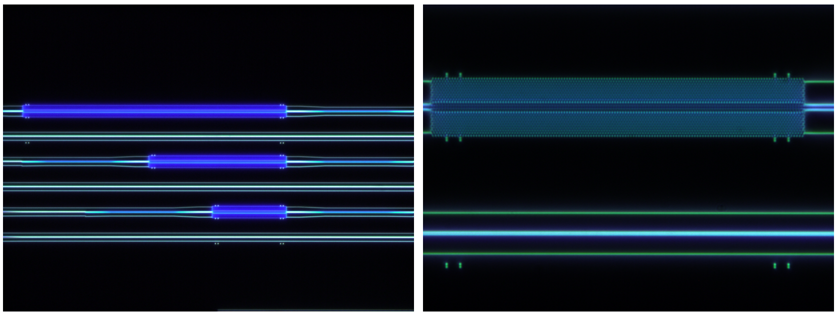

Figure 4.10: Dark field optical microscope images. Left: Different SPhCW lengths with a corresponding reference waveguide. Right: Zoomed image of the 50 μm long waveguide.

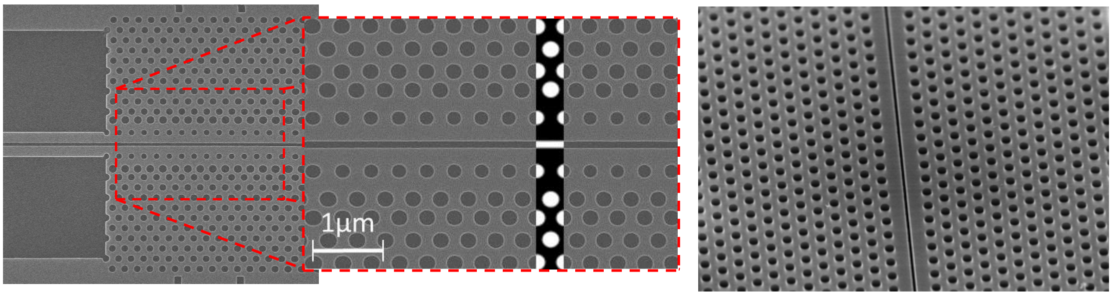

Figure 4.11: SEM figures of SPhCW. Right: Dispersion engineered (DE) waveguide with small first radius and hole shift of the second row with an inset of the simulated unit cell. Left: Non-DE waveguide.

superposition of the permittivity supercell used in the simulation with the fabricated structure gives a very good accordance. This geometrical insights will be verified and discussed in the optical measurements. Fig. 4.11-Right presents a non-DE SPhCW that will be used for comparative proposes in the last section.

4.5 Properties of fabricated structures

The designed and fabricated structures are then explored in the linear optical regime, particularly the study of the propagation dispersion is critical prior any nonlinear consideration, for instance, the phase matching required for some of them is dominated by the engineered crystal dispersion. In order to reproduce the simulated conditions, we mechanically cleaved the samples and drop casted a Cargille liquid with refractive index of 1.45 at 1550 nm.

4.5.1 Optical Transmission

Optical characterization was performed using two tunable lasers from Yenista to cover a broad band from 1370 nm until 1640 nm in the set-up described in section 1.4.2. In Fig. 4.12, we display the transmission measurements for different SPhCW. In (a) to (c), we show the transmission of 700 μm long PhC. The names T1 until T5 correspond to the different design approaches explained in Fig. 4.9 with diverse slot doses: (a) 2.7 C/m^2, (b) 3.0 C/m^2, (c) 3.4 C/m^2, it should be reminded that the hole dose is set to 2.8 C/m^2. All the plots are given in dBm and the transmission of a strip waveguide is plotted as reference.

It can be noticed that the transmission of the approach T1 presents a bandgap at larger wavelengths, which is characteristic of smaller slot sizes. On the other hand, T2 and T4 present the higher frequency gaps, which could be easily explained from the overdose expected from the overlapping approaches. More importantly, the best defined and

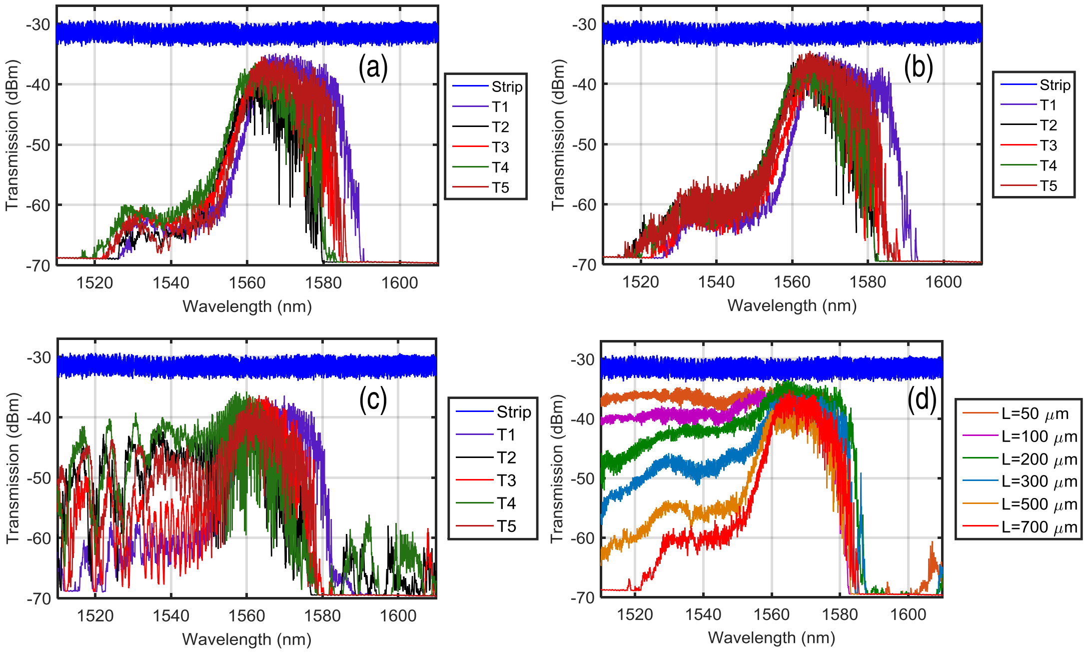

Figure 4.12: (a) to (c) Transmission measurements of 700 μm long SPhCW by using the test approaches numbered in Fig. 4.9 for (a) 2.7 C/m^2, (b) 3.0 C/m^2, (c) 3.4 C/m^2 slot dose. (d) Transmission spectra for different lengths after the approach T1 for a slot dose of 3.0 C/m^2.

sharper band-edge is given after the approach T1. Regarding the doses, we have only displayed the extrema and the optimum value (3.0 C/m^2), but other values were tested. The strong variation in the behavior after small changes reveals the importance of the slot in the losses.

Fig. 4.12 (d) shows the transmission for different SPhCW lengths at a slot dose of 3.0 C/m^2 for the approach T1. It could be appreciated that at short wavelengths, the decrease of the transmission is related to the crossing of the light-line, region where out-of-plane scattering becomes important. At longer wavelengths, light group velocity decreases and backscattering reduces the transmission. Strong variations of the transmission are typical of multiple scattering, as well known in PhCW. Even though, we have tapered the passage between fast and slow light, with long structures the decrease of transmission is appreciable in the slow light regime. In fact, we can conclude that the dose is the prior variable to be optimized followed by the slot design.

Propagation Losses

Photonic crystals are theoretically lossless, but in the telecom wavelengths, the control of size and position of motifs are limited by the fabrication technology. Furthermore, we are dealing with planar structures, so there is no forbidden gap to confine light in the vertical direction, instead, the index contrast allows the guidance through total internal reflection (TIR). So the guided modes decay within the crystal because of the bandgap and within the cladding because they are index-guided. In the PhC, above the light line, the wavevector does not satisfy the conditions for TIR, meaning that 2D PhCs exhibit intrinsic losses.

Another kind of losses coming from the imperfections in the fabrication process are refereed as extrinsic. Particularly, the limitations from the lithographic and etching processes generate a disorder in the crystalline structure that is not exactly reproducible. For instance, we should study it as an statistical experimental variable. In this frame, disorder has been described by a correlation length that will define the coherent propagation of a pulse or the loss of its coherence.

The losses problem is a very important affair for photonics. The use of PhC is interesting if the respective propagation losses are permissible. For this matter, we can distinguish different propagation regimes that are experimentally evident for SPhCW, as shown in Fig. 4.13. In the first regime, marked in blue, the frequencies are above the light cone (for our case short wavelengths), hence with a small wave vector, where the frequencies are not well confined and the mode experiences important propagation loss. This effect become more evident as the PhC length is increased.

As a criterion to assess the effect of disorder we choose the ratio of the SPhC length L_{SPhC} and the so-called mean free path l, which gives the scale of exponential decay of the propagating wave due to disorder [151, 172, 173]. In the dispersive regime, that we associate with the fast light and moderate slow light (n_g<30) regimes, $L_{SPhC}/l \ll 1$, the attenuation length is much larger than the one of the PhC. In this region, light propagation can be considered as ballistic, so rare scattering events are present. In Fig. 4.13 this regime is evident between 1561 nm and 1580 nm, where the transmission of all the SPhCW is roughly the same. This spectral region is the one interesting for coherent applications. In the strong slow light regime, known also as diffusive, $L_{SPhC}/l \approx 1$: constructive and destructive interference mechanisms are then responsible for the complex transmission spectrum. Several models have been proposed to account either for the brutal variations or for the general drop [174, 175, 144] of the transmission. In this regime, many scattering events occur and dominate over ballistic propagation. In such a regime neither the dispersion curve, nor the group velocity can be defined [151]. Here a partially coherent wave still transports energy but is not very useful for telecommunication proposes requiring coherent propagation [176]. In the experimental transmission, this regime is characterized by strong oscillations in the spectral response that could be appreciated around 1581 nm.

Finally as we locate the pulse in the bandgap, we enter in a regime of arbitrary localized states, here the attenuation length is shorter than the PhC length (L_{SPhC}/l>1). In [177]

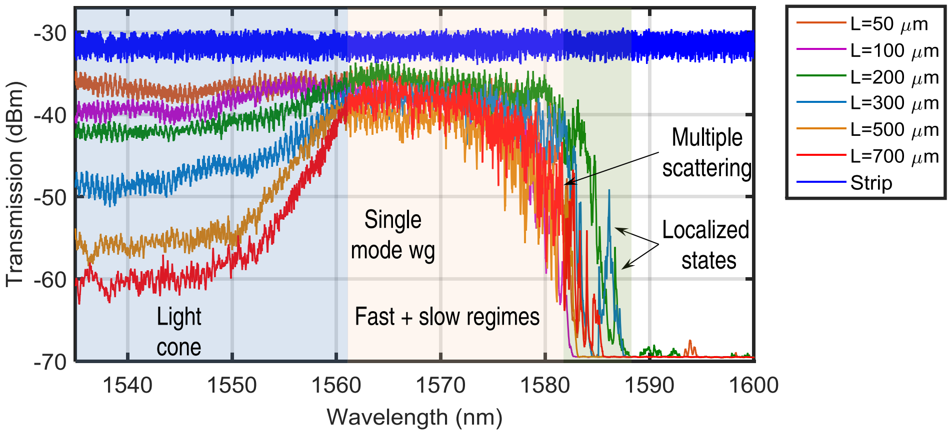

Figure 4.13: Different propagation regimes characteristic of PhC waveguides.

researchers have demonstrated experimentally that structural perturbations imposed on highly-dispersive photonic crystal-based waveguides give rise to spectral features that bear signatures of Anderson localization. Sharp resonances with the effective Qs of over 30,000 are found in scattering spectra of disordered waveguides.

For the interesting regime, where the ballistic propagation is valid, the study of the losses has been of common interest in order to exploit the slow light feature [173, 178, 144, 179, 180, 181, 174, 182]. As it was studied by O'Faolin et al [183], in a W1 waveguide, the assumption of the entire hole as a scattering source fitted adequately the experimental results. This mechanism plays an important role in the explanation of the backscattering effect, because as n_g increases, the latter becomes the dominant process, making the mode exit the dispersive regime (also called ballistic) where the perturbative solution approach is valid and entering in a diffusive regime where the dispersion curve and the concept of group velocity are no longer valid and where we should rather speak about partially coherent energy transport. Engelen et al.[143] have demonstrated the existence of those regimes, after their measurements in W1 waveguides. For group velocities beyond $n_g = 30$, the losses scale proportionally to n_g^2, meanwhile, bellow this value, the detected intensity increases sublinearly.

4.5.2 Time of Flight measurements

An interferometric optical coherent tomography (OCT) technique was implemented, allowing to measure the time-frequency transmittance using a partially coherent source that allowed to extract quantities such as the complex frequency-dependence reflectance or the group velocity from fringes analysis [168, 184, 174, 185]. A simplified scheme of the set-up is presented in Fig. 4.14 that have been mounted with the valuable help of Dr. Pierre Colman. It consists in placing the PhC waveguide in one arm of a Mach-Zehnder interferometer (MZI). At the output, two counter-balanced photodiodes

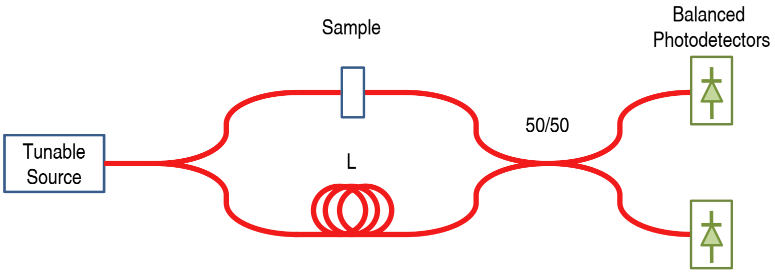

Figure 4.14: Interferometric set-up to measure the transmittance maps.

record the interferometric pattern. Additionally to the group index, it gives access the arrival time distribution of the energy, useful to study disorder [184]. Here we used a slightly different setup which does not require the use of a low coherent optical source. Considering that light accumulates a phase shift $\phi(\lambda) = K(\lambda) * L$ sample, the signal recorded at the output is proportional to $S(\lambda) \propto |E_0|^2 * T_0(\lambda) * \cos(\phi(\lambda))$. Here it is assumed the output of the waveguide is simply $E_{out} = E_0 * \sqrt{T_0} * e^{i\phi}$. The dispersion could then be retrieved using the relationship $\Delta\lambda_{fringes} = \lambda^2/(L * n_g)$ [186].

The spectrograms of 700μm-long DE SPhCW are shown in Fig. 4.15. The delay was calibrated using a reference sample without SPhCW. The contributions from the access waveguides were taken into account in the final measurement. So, to extract only the photonic crystal information, the group index of the access was conservatively assumed equal to 4 (in accordance with numerical simulations). The group index of the device under test was then obtained by the deduction of the delay introduced by the access as

$$n_{\mathrm{gPhC}} = \frac{ct_T}{L_{\mathrm{PhC}}} - \frac{L_A n_{gA}}{L_{\mathrm{PhC}}} \tag{4.3}$$

where the sub-indices PhC and A stand for Photonic Crystal and accesses, respectively, and t_T is the total delay measured with the spectrogram.

The transmission level for long structures demonstrates the good fabrication quality; and several of the investigated structures clearly exhibit a *plateau* in the group index trend (i.e. same delay), demonstrating the potential of such waveguides for applications requiring low GVD. Note that two lines can be seen on the spectrogram: the one at lower group index that decreases continuously corresponds to the TM mode intentionally coupled in. The dispersion of this mode is very close to the expected behavior of an index-guided waveguide [184], meaning that it is not affected (i.e. not guided) by the PhC design, and thus it serves as an internal reference to determine more precisely the actual group index. No specific post-processing regarding the polarization of light was thus performed. Regarding the thickness of the dispersion curve due to experimental uncertainties, a criterion corresponding to a decay of 10 dB in the transmission for a given

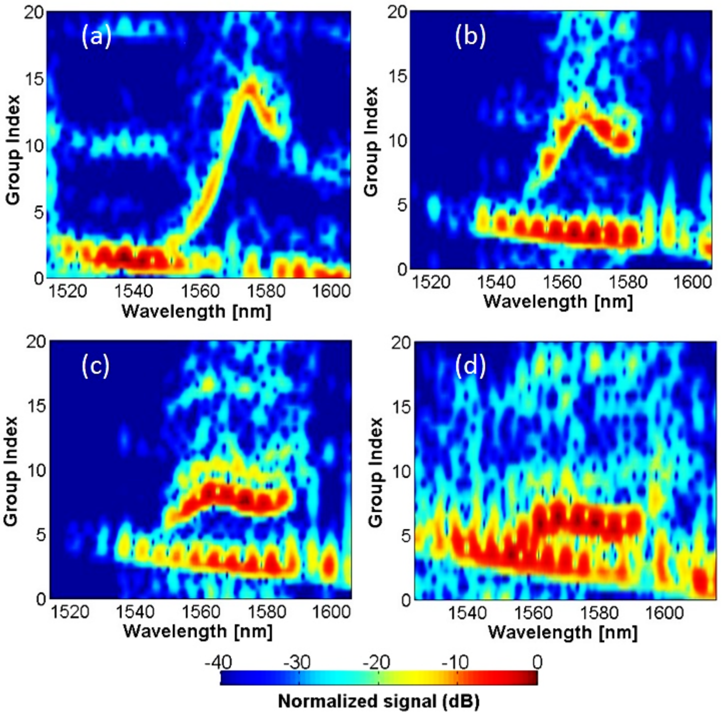

Figure 4.15: Spectrograms of different SPhCW: (a) r_1= 95 nm, (b) r_1= 105 nm, (c) r_1= 110 nm and (d) r_1= 125 nm.

wavelength was chosen, corresponding to an estimation of n_g with an average accuracy of ±0.6 [170]. Let note that Fig. 4.16 gives also interesting qualitative features about the propagation losses. Indeed dispersion engineering does not only modify the dispersion properties of slow light modes, but also impacts their propagation losses [183, 187].

In Fig. 4.16, we display the extracted group index curves for different structures where the points are experimental values and the solid lines are the corresponding fits. We have plotted additional squares within a 10% variation in the average group index, marked explicitly in the left axis. All of these values are used to estimate the $NDBP$ (see Eq. 4.2). In particular, we can zoom the largest curve to notice the over-engineering predicted from the simulations. Indeed, the group index variation is larger than 10% after 1583.2 nm wavelength, giving a NDBP of 0.136. A summary with the extracted values is presented in table 4.2, were a maximum $NDBP$ value of around 0.16 is obtained.

In order to estimate the field enhancement in the photonic crystal, assuming a structure with n_g=15, the third order nonlinear properties of silicon is increased by a factor $S_{Si}^2 = (n_g/n_{0-Si})^2$ of around 18.6. In the same time, a material filling the slot with the same refractive index used in these experiments encounters a $S_{Fill}^2 = (n_g/n_{0-Fill})^2 \approx 107.0$ enhancement. So, **even with modest group indices corresponding to acceptable losses through long propagation lengths for practical applications (700 μm, here), the enhancement experienced by the slot material in ultra-small effec-**

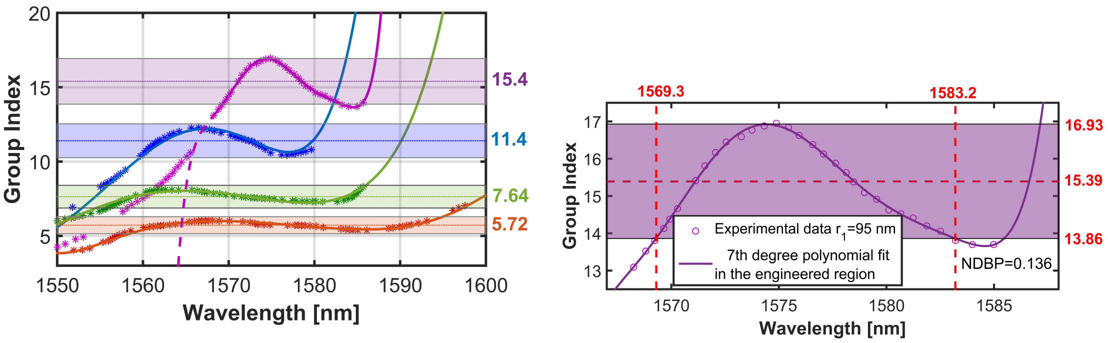

Figure 4.16: Left: Extracted Group Index for the different spectrograms withing 10 dB (marked with color bars) and a 7th order polynomial fit. The average group index is marked in the left axis. Purple: 95 nm, blue: 105 nm, green: 110 nm, orange: 125 nm. Right: Zoom for the 95 nm radius case to describe an over-engineered waveguide.

tive areas is very promising regarding highly nonlinear liquids and polymers with low refractive indices at $\lambda = 1550$ nm exhibiting ultra-fast response [188, 189, 190]. For instance, in the lower n_g obtained experimentally ($n_g \approx 5.72$), representing the best waveguide in terms of transmission, the expected slowdown enhancement would be of $S^2_{Fill} = (n_g/n_{0-Fill})^2 \approx 15$.

The resulting total effective nonlinearity experienced by the light is then a result of the slow light enhancement S^2 combined with the light confinement (i.e. the effective area). Sometimes, large slow light enhancements are mitigated by larger effective area; this is not the case here. To give out some numbers, if we consider the polymer PSTF66 ($n_{2I} = 2.8 * 10^{-18}$ m^2/W) [191] which has modest Kerr nonlinearity, then the waveguides presented in this article, particularly for the case r_1= 105 nm , would exhibit a Kerr nonlinearity up to 1259/W/m: 165/W/m comes from the cladding itself while the surrounding silicon PhC structure participates to 1094/W/m. But if other material with better nonlinear properties, but still at the same refractive index, such as nanocomposites ($n_{2I} \approx 1 * 10^{-16}$m^2/W) [192], the Kerr nonlinearity would then be 6992/W/m with (as expected) exactly the same contribution from silicon (1259/W/m) and 5898/W/m from the cladding. These estimations highlight the importance of the cladding material.

$\mathbf{r_1}$ **[nm]**	$\langle \mathbf{n_g} \rangle$ **(±10%)**	$\mathbf{\Delta\lambda}$ **[nm]**	**NDBP**
95	15.4 (±1.5)	13.9 ± 1.0	0.136 ± 0.014
105	11.4 (±1.1)	21.5 ± 1.5	0.156 ± 0.018
110	7.64 (±0.76)	31.4 ± 1.8	0.153 ± 0.010
125	5.72 (±0.57)	36.6 ± 2.1	0.133 ± 0.014

Table 4.2: Parameters from the measured curves.

4.5.3 Integrated MZI for slow light extraction

In order to confirm the light group index measured in the previous section, another complementary method was implemented. We used integrated Mach-Zehnder interferometers (MZI) containing one arm with a 200 μm long SPhCW and the other arm with a strip waveguide as a reference. The coupling approach for the interferometer was analogous to the one described in Ref. [193]. In Fig. 4.17, we display an optical microscope image of the integrated structures. Different testing and reference devices were added, but in this chapter the interesting structure will be the second from top to bottom.

The dispersion curves were extracted by means of the interference analysis, following the relation [140]:

$$n_g = \frac{\lambda_{max}\lambda_{min}}{2L(\lambda_{max} - \lambda_{min})} + n_g^{ref} \tag{4.4}$$

where λ_{max} and λ_{min} are the two wavelength extrema of a fringe, L the length of the SPhCW and n_g^{ref} the group index of the reference arm. In the integrated MZI, the reference arm was assumed to have a constant group index (n_g^{ref}) equal to 3.8 (calculated at λ=1.55 μm). In Fig. 4.18 we show an example of n_g extraction for $r_1 = 105$ nm. In red, we mark the wavelength position of the maximum transmission and in green the minimum. High contrast fringes decrease the uncertainty, so good quality fabrication is required to ease the extraction. No filtering was performed, making difficult the group index estimation close to the bandgap. Even though it is possible to extract higher indices, we indeed prefer to assume a conservative approach in order not to deal with diffusive features or localized/defect artifacts.

A clear remarkable flat band can be observed over several nanometers ($\sim$ 20 nm), meaning nearly-zero GVD. We remind that relatively modest group indices ($\sim$ 15) were considered to ensure a good trade-off between light-matter enhancement induced by slow light effect and low propagation losses which have been demonstrated to increase quadratically with the group index square after a given n_g-threshold [183]. In the following, we will use this method to study the effect of the covering material.

Figure 4.17: Optical image of a chip section. From bottom to up: i) strip reference waveguide (RW), ii) 200 μm long SPhCW, iii) RW, iv) power division test device, v) MZI - 200 μm SPhCW and strip, vi) MZI - 200 μm SPhCW and 100 μm SPhCW.

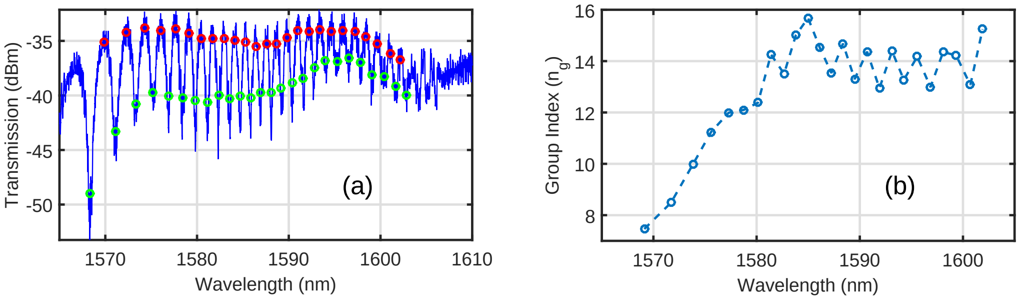

Figure 4.18: Illustration of the group index (n_g) extraction from the interference fringes of an integrated MZI. (a) Transmission spectra with an overlap with the automatic tracking of wavelength at maxima (red) and minima (green) values. (b) Group index values after applying Eq. 4.4.

4.5.4 Second order dispersion curves (GVD)

Using the direct time of flight measurements (external MZI), a seventh order polynomial fit was done following the higher transmission points for the TE mode in order to retrieve the group index as a function of light wavelength. Now, from these curves, the group velocity dispersion β_2 coefficient[96] could be estimated through the first derivative of the fit:

$$\beta_2(\lambda) = -\frac{\lambda^2}{2\pi c} D = -\frac{\lambda^2}{2\pi c^2}\frac{dn_g(\lambda)}{d\lambda} \tag{4.5}$$

where D is the standard optical fiber dispersion parameter, yet usually reported in ps/(nm-mm) for integrated waveguides. Note that under normal dispersion ($\beta_2 > 0$), optical pulse broadens along light propagation. However, in the anomalous case ($\beta_2 < 0$), an optical soliton can be formed and the pulse hence propagates without further distortions[96]. To properly exploit the benefits of slow light, the dispersive compensation condition needs to be achieved over a large spectral bandwidth. For instance, engineered chalcogenide planar waveguides have been exploited for supercontinuum generation [104].

From Fig. 4.19, it is seen that the structures exhibit very interesting dispersion features, especially in the large group index regions. Both normal (positive) and anomalous (negative) GVD can be obtained and some SPhCWs exhibit an almost flat n_g plateau over more than 20 nm bandwidth. This is encouraging because state of the art nonlinear effects in integrated optics have been demonstrated in the anomalous dispersion regime and for relatively modest NDBP products [148, 194, 195, 196], demonstrating the important role played by the optical losses (both linear and nonlinear) that must be meticulously treated. As **the proposed structures offer wavelength windows in the anomalous regime with moderate losses**, they are convenient for nonlinear applications.

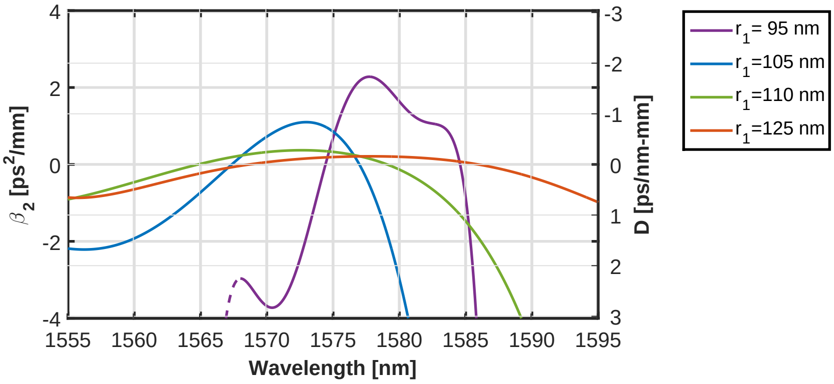

Figure 4.19: Second order dispersion extracted after the delay measurement.

As the radius increases, the dispersion becomes flatter and tends to zero over larger intervals at the price of lower group indices. The flat behavior is explained by the change of n_g over short wavelength ranges, that is smoother for larger radii. The results summarized in table 4.2 are confronted with the trends of Fig. 4.19: a decreasing bandwidth ($\Delta\lambda$) as a function of the average group index increasing is related. We obtained devices with experimental NDBP values ranging between 0.133 and 0.156, i.e. extremely large for slotted waveguides limited by a silica and top cladding light lines. By comparing with the simulated values shown in table 4.1, we see that the fabrication errors (exact hole positions, sidewall roughness, etc.) tend to decrease the actual PhC performances: designs with the best features (in theory) have often (in practice) very low fabrication tolerance. Therefore it is also important to assess the robustness of the PhC design –namely the sensitivity of the PhC's features to small variations of the design parameters-, and not to rely only on its theoretical performances. The designs with r_1= 95 nm and r_1= 105 nm appear to exhibit the best compromise regarding fabrication errors.

4.5.5 Covering material refractive index effect in the dispersive properties

During this thesis we have exploited the properties of PhC under different covering linear materials which has allowed the demonstration of versatile cavity structures with potential applications in biological sensing (the reader may consult Ref. [26, 27] as this particular topic is out of the scope of this manuscript). Under the same spirit, we have studied first numerically and then experimentally the robustness of the dispersion engineered properties in SPhCW under different covering materials. This is of dramatic importance due to the intrinsic index sensitivity of hollow core waveguides. It is then expected that the properties of the hybrid waveguide will vary with the linear and nonlinear characteristics of the covering material.

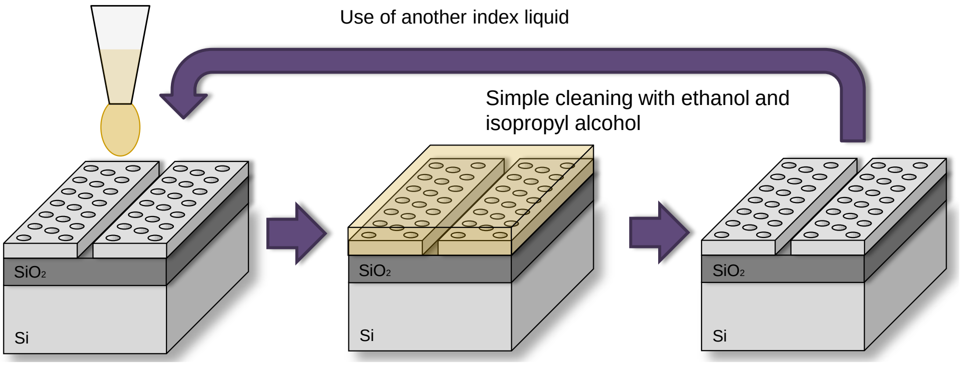

Figure 4.20: Procedure scheme used to change the cladding optical material.

Up to this point we have assumed a covering refractive index of the structures close to the one of silica ($n_{Clad} \approx 1.45$). Our structures allowed a very simple procedure (Fig 4.20) to change the covering refractive index, so we could study different claddings in the range of interesting polymers and thin films already reported in literature.

First, for the evaluation of the dispersion engineered structures, simulations were performed using the MPB software [171] considering quasi-TE light polarization. The cell parameters were $n_{Si} = 3.48$, $n_{SiO_2} = 1.44$ and $n_{Clad} = 1.40, 1.45$ and 1.50. The structures under test were the same as the ones used in previous sections. In this study, the radius of the first row was swept to achieve different group indices. We considered for that three different values: r_1= 95 nm, r_1= 105 nm and r_1= 110 nm [165]. We have ignored the case of r_1= 125 nm as the obtained group indices are then very small. It can be noticed that the consideration of the buried oxide layer and top cladding indices of the same order considerably shrinks the available bandwidth below the light line, as it can be noticed in Fig. 4.21.

In Fig 4.22, the transmission spectra of 50 μm long SPhCW for the three geometries are displayed. The filling of the SPhCW was performed by drop-casting different commercial Cargille liquids that were cleaned with Acetone and Ethanol between two successive experiments with different liquids, as depicted in Fig. 4.20. A translation of the bandgap as a function of the cladding index is observed, simultaneously with a slight reduction of the average ng when the cladding index increases. Finally, the bandwidth for a constant group index remains similar for different top cladding indices keeping preserved the waveguide flat band slow light properties. We would like to remark that the finding associated with the design presented remain valid for filling material whose index is lower than ~1.8. Above, the contrast between the slotted PhC and its surrounding is too weak to allow propagation and proper confinement of light.

From Fig. 4.22, we can state that the fabrication limits are a critical parameter when engineering SPhCW. Even though the photonic bandgap is clear for all the structures,

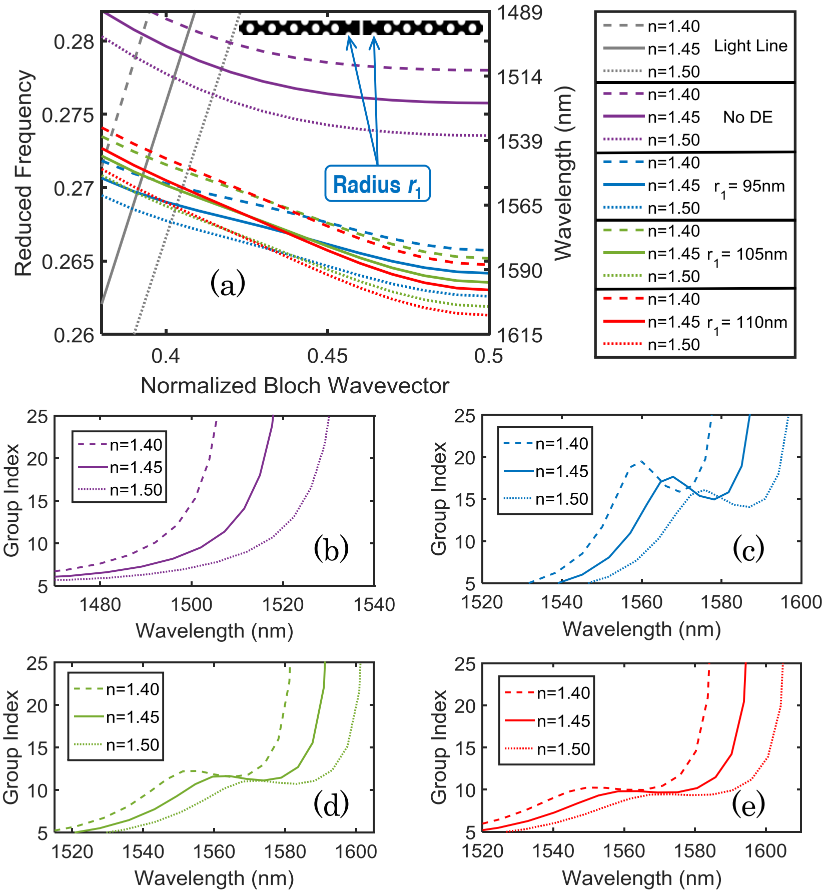

Figure 4.21: MIT Photonic Band simulations for different conditions (a) Band diagram of the different structures under the effect of changing the refractive index, No DE refers to a structure with the same radius (r=125 nm) and no hole shift. The blue, green and red curves correspond to Dispersion Engineered (DE) structures changing the position of the first two row of holes and varying the radii for r_1=95 nm, r_1=105 nm and r_1=110 nm, respectively. Inset: fundamental cell of a DE waveguide with r_1=95 nm, (b-e) Effect of the refractive index change on the dispersion of the structures [197].

smaller holes give rise to a reduction in the transmission close to the bandgap (case a). This could be explained by the increased difficulty to fabricate smaller holes which induces larger wall roughness, that are even more critical close to the bandgap (slow light). On the contrary, hole radius of 110 nm (only 30 nm difference in diameter) provides a net decay of 30 dB in a couple of nm. Also, as increasing the hole size, a waveguide band-edge sensitivity increase is expected because the interaction between the mode and the cladding material is higher.

The sensitivity of the bandgap position was estimated with a 20 dB transmission decay basis and is in average of around 250 nm/RIU. This means that, for our case, a change of 0.10 RIU gives a shift on the order of 25 nm. Beyond this known effect [198, 199], we

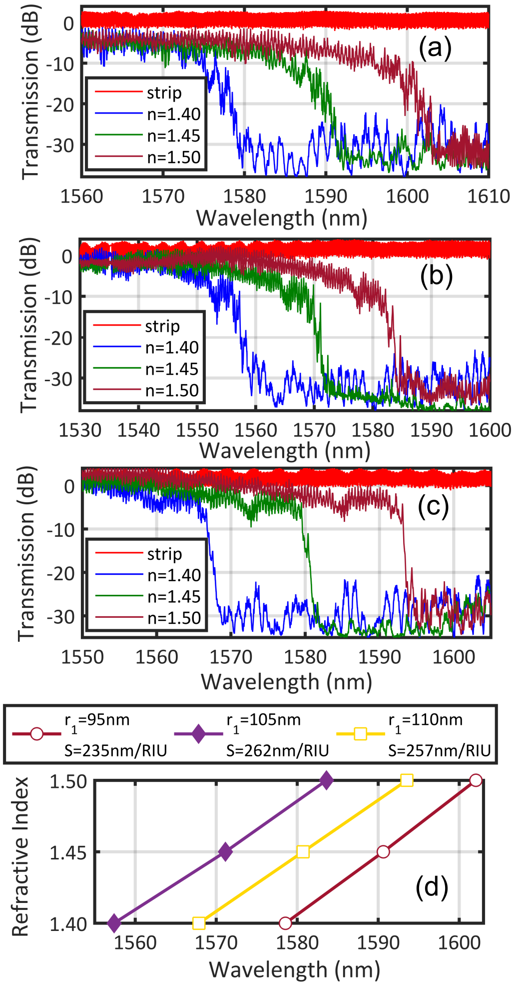

Figure 4.22: Transmission spectra and sensitivity (parameter S) of different waveguides as a function of the cladding index with the transmission (red) of a strip waveguide as a reference. (a) r_1=95 nm, (b) r_1=105 nm, (c) r_1=110 nm and (d) bandgap refractive index sensitivity [197].

put hereafter the focus on investigating the effect of changing the cladding properties on the slow light mode dispersion of the investigated hollow core waveguides.

In Fig. 4.23 (a), (c), (e), the transmission of the integrated MZI are shown for three geometries, considering a n=1.50 top cladding material. The interference fringes contrast and the clear cut-off wavelength (marked with a dashed blue line) reveal the high quality of the fabricated structures.

It is interesting to notice that the contrast of the fringes follows the group index, as the larger the introduced delay, the lower the contrast, so the MZI gets unbalanced due to larger losses. Additionally, we assumed a conservative approach, considering that in the

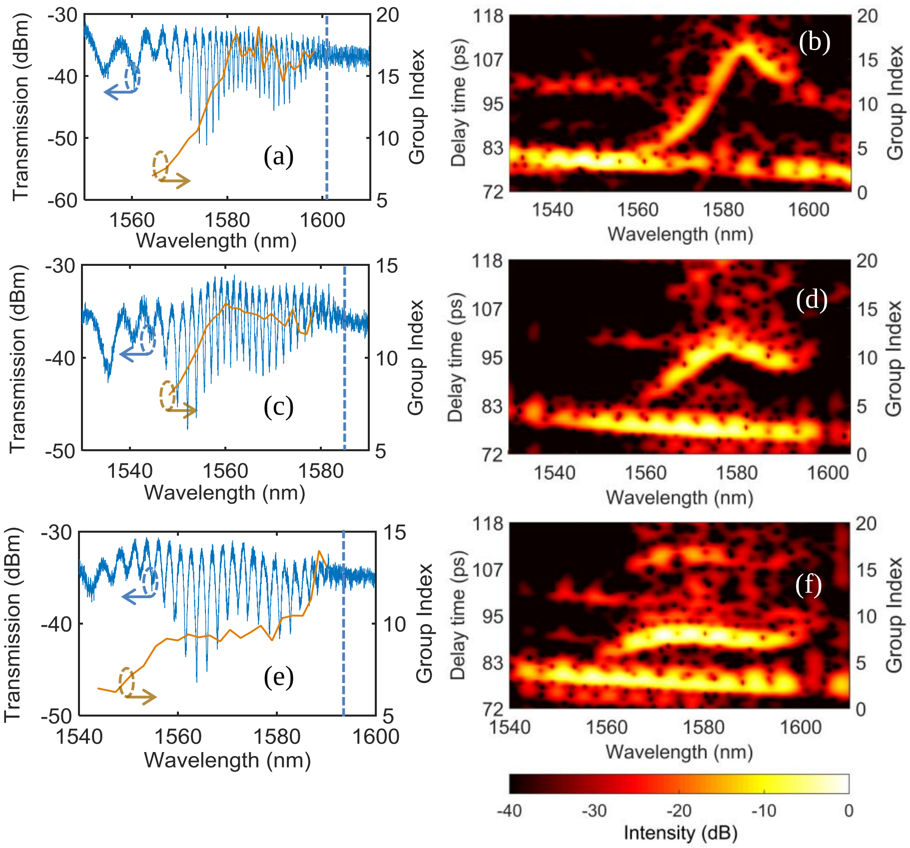

Figure 4.23: Dispersion curves extraction with 2 different approaches, on the left an integrated MZI with a 200 μm SPhCW in one arm and on the right the reflectance maps for 700 μm long crystals. (a)-(b) correspond to r_1=95nm, (c)-(d) to r_1=105nm and (e)-(f) to r_1=110nm for a fixed filling refractive index of n=1.50. Adapted from [197].

butt-coupling configuration, the strong FP resonances from the sample facets and the features from the difussive and localized regimes hinder the measurement of large group indices, requiring a post-filtering processing. The results observed in the simulations are here confirmed. For instance, the larger the radii of the first row of holes, the smaller the group index in the flat band region, but at the same time the larger the slow light bandwidth.

We have also used the ToF set-up to confirm the findings. We show the transmittance maps in Fig. 4.23, corresponding to the same geometry as for the integrated devices. The main difference is the propagation length, indeed for the cases (a), (c) and (e), the SPhCW is 200 μm long, while for (b), (d) and (f) is 700 μm.

Next, we have performed a similar analysis as for the case of $n_{clad} = 1.45$ to extract the group index curves and the second order dispersion evolution. We present the results in Fig. 4.24, as visible from the comparison with Fig. 4.21, the close agreement with

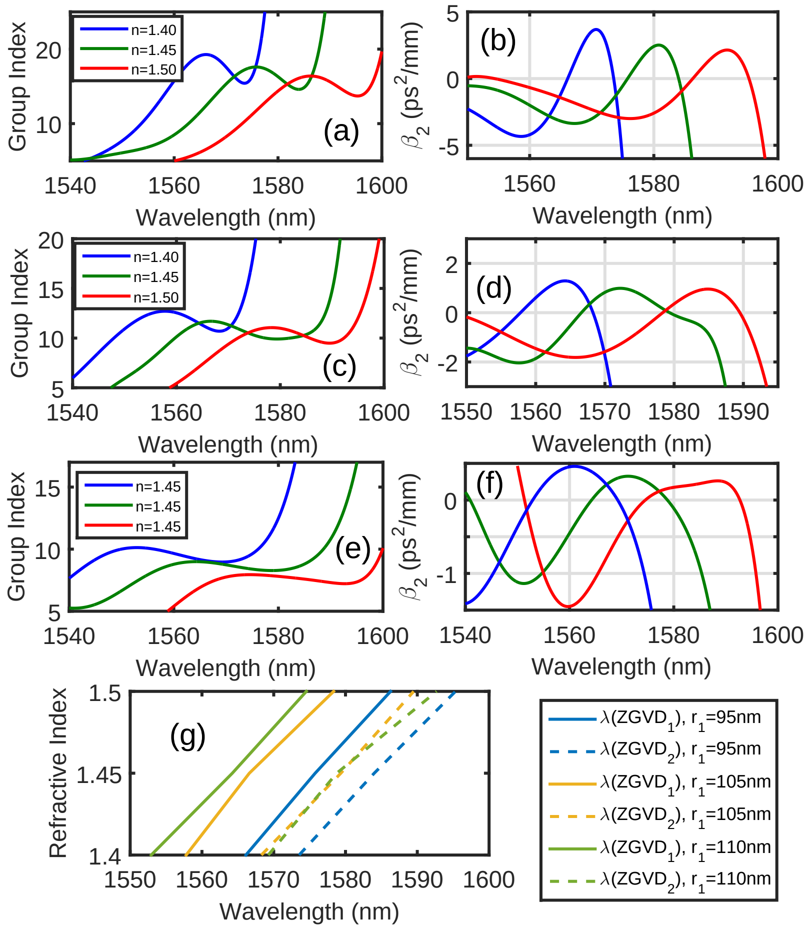

Figure 4.24: Experimental group index and derived second order dispersion curves for the 3 geometries considered: r_1=95 nm (a)-(b), r_1=105 nm (c)-(d) and r_1=110 nm (e)-(f). Each one for three different filling indices. (g) Sensitivity of the two ZGVD-wavelengths as a function of the index for different geometries [197].

the simulation is remarkable. From simulations, the effective area in the slot region[168] is estimated to be around 0.03 μm^2. The fraction of dielectric energy confined within the slot[200] is around 27% at k= 0.46 * 2π/a for all the structures, and about 52% of the energy is contained in the cladding region (including the holes and the field above silicon).

Again, the dispersion parameter of the waveguides (b), (d) and (f) exhibits interesting anomalous and normal zones, including two zero group velocity dispersion points. The sensitivity of the dispersion curves is noteworthy considering that the hole radius changes only by 5 nm in the first row and that the shape of the second order dispersion curve remains almost unaltered. For this reason, we have plotted a curve showing the variation of the ZGVD points as a function of the cladding index. From the trends, we can see that this interesting region could be tuned very precisely as a function of the index,

$\mathbf{r_1}$ **[nm]**	**Method**	$\langle \mathbf{n_g} \rangle$ **(±10%)**	$\boldsymbol{\Delta\lambda}$ **[nm]**	**NDBP**
95	Integrated MZI	16.3 (± 1.6)	18 ± 2	0.18 ± 0.03
	Time of Flight	15.1 (±1.5)	20 ± 2	0.19 ± 0.03
105	Integrated MZI	12.1 (±1.2)	21 ± 2	0.16 ± 0.01
	Time of Flight	10.3 (±1.0)	24 ± 2	0.15 ± 0.01
110	Integrated MZI	9.03 (±0.90)	25 ± 3	0.14 ± 0.03
	Time of Flight	7.58 (±0.76)	32 ± 3	0.15 ± 0.03

Table 4.3: Figures of merit for DE SPhCW filled with a n=1.50 liquid following two different experimental procedures.

being promising for materials with narrow band properties or for using high power lasers at specific wavelengths. It is also observed that the dispersion (positive and negative) slightly decreases for larger refractive indices (as well as the group index), so, the slow light dispersion curve becomes flatter.

Again, from the reflectance maps, one clear transmission line is strong at around 80 ps delay. This corresponds to a TM mode that is insensitive to the delay induced by the SPhCW. This group delay time agrees with the length of the considered sample. Also, as expected, the TE-transmission drops quickly when approaching the bandgap (i.e. increasing the group index), validating our experiences from the integrated MZI devices.

This result highlights the discussed fabrication sensitivity of the waveguides, similar geometries giving rise to very similar dispersion properties but still subject to some possible frequency shift. It is stressed that both employed experimental methods are based on a reference arm calibration. For the integrated MZI, it depends on the accuracy of the considered reference group index, and for the second method in the delay calibration of the external reference arm.

From measured curves, we have extracted important parameters and figures of merit for the devices, such as the bandwidth and the NDBP. It can be seen the agreement of the properties for both independent methods, even though the group index values for measurements achieved with the integrated MZI scheme are slightly larger. Also, the calculated NDBP values are large taking into account the theoretical limit of around 0.3 for our configuration. Fig. 4.24 and table 4.3 condensate the methodology and results for only one refractive index case (n=1.50). Analogous experiences were performed for the other two refractive indices using the same kind of devices. The reported values take into account the uncertainty sources from the fabrication process until the data analysis. There is a whole consistency between two independent devices measured in two different set-ups and the 3D plane wave expansion (MPB) simulations.

The zero dispersion points are obtained in maxima and minima of the n_g curve, and the maxima and mimina of D correspond to a concavity change of the group index (zero group

	$\mathbf{r_1 = 95}$ **nm**	$\mathbf{r_1 = 105}$ **nm**	$\mathbf{r_1 = 110}$ **nm**	**Average**
Cut-off [nm/RIU]	235 ± 12	262 ± 13	257 ± 13	251 ± 21
1st **ZGVD [nm/RIU]**	202 ± 10	206 ± 10	216 ± 11	208 ± 12
2nd **ZGVD [nm/RIU]**	218 ± 11	212 ± 11	235 ± 12	222 ± 15
Max $\mathbf{n_g}$**/RIU**	-29 ± 1	-16 ± 1	-22 ± 1	–
Max β_2 **[ps**^{2}**/mm/RIU]**	-15.4 ± 0.8	-3.3 ± 0.2	-2.0 ± 0.1	–
NDBP for $n_{Clad} =$ **[1.40 1.45 1.50]**	[0.14 0.14 0.19] ± 16%	[0.17 0.16 0.15] ± 7%	[0.20 0.15 0.15] ± 20%	–

Table 4.4: Figures of merit variations as function of the filling refractive index material for the diverse DE SPhCW.

velocity dispersion point), so, there is a particular interest on the influence of the index in those singular wavelengths. Finally, we like to point out that from a practical point of view, independently of the exact variations of the group index (∼ -20/RIU) and ZGVD position (∼ 210nm/RIU), the concern lies in the knowledge of the trends (i.e. increasing the filling index results in a red shift for cut-off and ZGVD points and a decrease of the group index) and in the demonstration of dispersion engineered waveguides with good performances trough the variation of the NDBP. This figure of merit evolution depends on the sensitivity of the group index and the frequencies suffering from the same delay. The available bandwidth is roughly set by the frequency spacing between the two ZGVD and the mean group index can be taken as the average of the group index values at the ZGVD positions. Normally the general trend is an increase of the performance (i.e. larger NDBP) for lower refractive indices. Indeed, it is noteworthy the fact that the over-engineered waveguide by getting flatter with smaller group indices, increases its NDBP from 0.14 to 0.19. So effectively in SPhCW, the cladding index is another important parameter in the engineering process.

4.6 Towards hybrid nonlinear integration

In the continuity of the efforts described in previous sections, we will now develop a numerical procedure to **engineer nonlinear hybrid silicon based waveguides**. The idea is to use the potentials for silicon as waveguide and cover it with low-index ($n \sim 1.6$) high performance third order nonlinear optical polymer and doped materials. The main goal is to **reduce the waveguide effective TPA susceptibility, or in other terms, to maximize the** FOM_{TPA}. After fixing the covering material, we will study different geometries with realistic physical values (possible to fabricate). **Two types**

of waveguides will be analyzed. First, silicon **simple slot** guides by tuning the rail and slot widths in order to find the maximum nonlinear figure of merit. In a second subsection, the interest will be focused on **SPhCW** in the slow light regime. Interesting insights about the mode evolution as a function of the group index and a comparison with other kind of photonic crystals will be given. The last part of this section will be devoted to exploit the experimental procedure of top-hat D-Scan to perform some preliminary measurements in the nonlinear regime for slow light silicon photonic structures.

4.6.1 Nonlinear optimization of hybrid waveguides

The $\chi^{(3)}$ nonlinear properties of slotted crystalline silicon photonic waveguides filled with third-order nonlinear materials (NM) are studied here by calculating the effective nonlinear susceptibilities associated to the silicon and cladding material, respectively. The adopted approach circumvents the assumptions that the introduced NM dominates the nonlinear behavior of the slotted waveguide and that strong light confinement due to the slot or the slow light effects allow neglecting the two-photon absorption (TPA) process in the silicon host [201].

Slot waveguides

Geometrical optimization of silicon-slotted waveguides is performed on the basis of the nonlinear figure of merit (FOM_{TPA}) of the guided mode, which is related to the balance between the Kerr and the TPA effects. The obtained results reveal the importance of properly choosing the waveguide width of the silicon rails in order to minimize the TPA effect even by tolerating a reduced overall nonlinearity. The COMSOL software was used to calculate the full-vectorial optical mode profiles required for this optimization and two typical modes with different geometries are depicted in Fig. 4.25.

The covering material presents the following linear and nonlinear properties: refractive index $n_0 = 1.80$, Kerr index $n_2 = 2.0 \times 10^{-17}$ m^2/W and $FOM_{TPA} = 5.0$ at $\lambda = 1.55$ μm, similar to materials used in other research [202, 203]. These parameters can be easily tuned in the model.

As the propagating mode remains invariant, we will use an expression from Ref. [99] (analogous to the one deduced in Eq. 1.73):

$$\gamma_{wg} = \frac{i3\omega\Gamma}{4\varepsilon_0 A_0 v_g^2} \tag{4.6}$$

with

$$\Gamma = \frac{A_0 \int_{A_{NL}} e^*(r_\perp,\omega)\chi^{(3)}(r_\perp,-\omega,\omega,-\omega,\omega)\vdots e(r_\perp,\omega)e^*(r_\perp,\omega)e(r_\perp,\omega)dA}{\left|\int_{A_\infty} n^2(r_\perp)\left|e(r_\perp)\right|^2 dA\right|^2} \tag{4.7}$$

where v_g represents the modal group velocity, and A_0 an arbitrary confined mode area that cancels out when calculating the nonlinear waveguide parameter (γ_{wg}). The Γ parameter corresponds to the effective waveguide nonlinear susceptibility as the weighted integral of the tensor susceptibility over the slot waveguide mode described by its transverse electric field distribution $e(r_\perp)$. This integral is calculated over A_{NL}, the surface of the waveguide cross-section corresponding to nonlinear materials (here, the NP and Si regions).

These expressions take into account the contributions, for all the materials in the hybrid structure, of the susceptibilities real and imaginary parts with respect to the mode field distribution in the full waveguide cross-section. Additionally, this formulation of the nonlinear waveguide coefficient allows a natural evaluation of the nonlinear contributions of the different waveguide materials by estimating γ_{Si} and γ_{CC} over the host material (Si) and the cover cladding (CC). The advantage of this formalism is the additivity of the two susceptibilities to estimate the complete nonlinear figures of the hybrid waveguide, so to say, $\gamma_{wg} = \gamma_{CC} + \gamma_{Si}$, implying that $\mathbb{R}\mathrm{e}(\gamma_{wg}) = \mathbb{R}\mathrm{e}(\gamma_{CC}) + \mathbb{R}\mathrm{e}(\gamma_{Si})$ and $\mathbb{I}\mathrm{m}(\gamma_{wg}) = \mathbb{I}\mathrm{m}(\gamma_{CC}) + \mathbb{I}\mathrm{m}(\gamma_{Si})$.

In the first approach, the optimization of the nonlinear waveguide properties has been conducted in a 220 nm thick silicon waveguide by sweeping the silicon rail (W_{rail}) and slot (W_{slot}) widths in the ranges of 170 nm-to-240 nm and 50 nm-to-200 nm, respectively as they are realistic values with respect to fabrication constrains. The lower rail width was set to 170 nm in order to limit an excessive mode spreading by maintaining the effective index(n_{eff}) of the TE-mode reasonably above the cladding index (set to 1.8). The waveguide nonlinear parameter (γ_{wg}) and light power confinement in both materials (P_{CC} and P_{Si}) have been calculated as a function of W_{rail} and for a fixed slot width value of 100 nm are shown in Fig. 4.26.

As expected, the contribution from the silicon rails is not negligible, so the engineering of these rails is necessary. The overall trend of the FOM_{TPA} is to decrease as the rail width is larger. A closer inspection to Fig. 4.26 (a) and (b) allows us to understand this

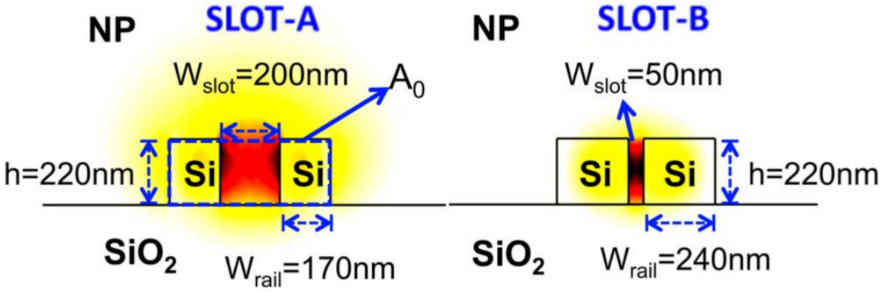

Figure 4.25: Mode distribution for two different slot waveguides covered with a nonlinear polymer (NP) for TE polarization at $\lambda = 1550$nm [201].

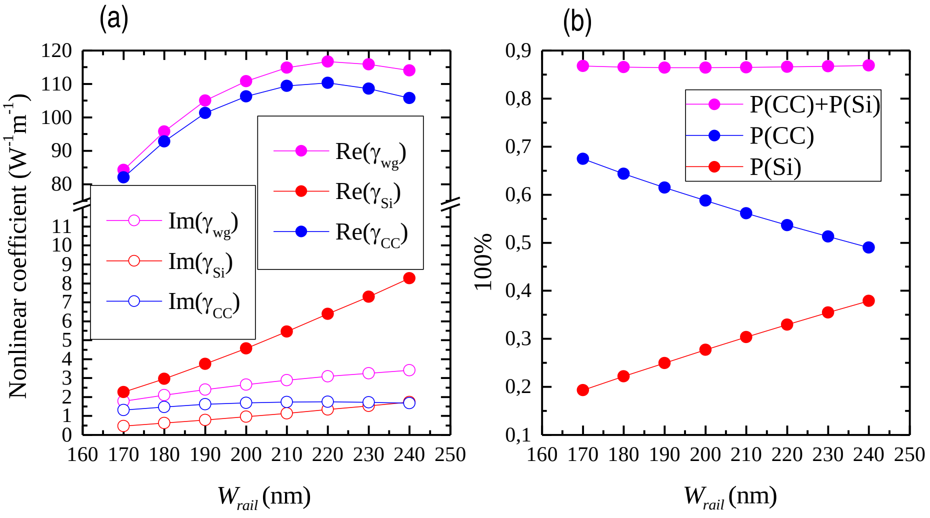

Figure 4.26: Influence of the silicon rails width on the slot waveguide nonlinear properties (W_{slot}=100 nm): (a) nonlinear parameter γ of the silicon rails, cover cladding material, and full waveguide, respectively. The real parts are associated with the Kerr effect while the imaginary ones are related to the TPA process. (b) Power confinement in the two regions, respectively [201].

trend. As it could have been anticipated, it can be first observed that larger silicon rails lead to an increase of the Kerr effect of silicon [$\mathbb{R}\mathrm{e}\left(\gamma_{Si}\right)$]. Yet, this trend is accompanied by a simultaneous rise of the TPA process in silicon [$\mathbb{I}\mathrm{m}\left(\gamma_{Si}\right)$] due a nearly 37% of power confinement in Si for W_{rail} approaching 240 nm [Fig. 4.26 (b)]. On the contrary, reducing W_{rail} down to 170 nm is responsible for a strong decrease of the optical power confined in Si [down to 20% according to Fig. 4.26 (b)], which allows an efficient decrease of $\mathbb{I}\mathrm{m}\left(\gamma_{Si}\right)$ and thus of the imaginary part of the overall waveguide susceptibility [see Fig. 4.26 (a)].

Starting from these first results, the slot width influence was further investigated. Fig. 4.27 shows how individual nonlinear contributions change when W_{slot} increases from 40 to 200 nm. As mentioned in previous works, it is evident that the overall nonlinear coefficient [$\mathbb{R}\mathrm{e}\left(\gamma_{wg}\right)$] increases by reducing the slot width [204, 205]. It can be also seen that the silicon rails contribution to $\mathbb{R}\mathrm{e}\left(\gamma_{wg}\right)$ is almost negligible in the full slot width range. The interesting point of the discussion is yet not related to the real part of the nonlinear parameter but to its imaginary component: reducing the slot width is responsible for a stronger confinement of light in the silicon rails [see Fig. 4.27 (b)], explaining the increase of the TPA contribution in silicon [see Fig. 4.27 (a)], and in turn an increase of $\mathbb{I}\mathrm{m}\left(\gamma_{wg}\right)$. On the contrary, enlarging the slot is responsible for a $\mathbb{R}\mathrm{e}\left(\gamma_{wg}\right)$ decrease, which is intrinsically not desired, but at the same time allows a significant reduction of the TPA in silicon and thus a strong decrease of $\mathbb{I}\mathrm{m}\left(\gamma_{wg}\right)$. The balance between the two effects is summarized by the FOM_{TPA} evolution, showing an increase from FOM_{TPA}=3.5 to 3.95 for slot widths ranging from 50 to 200 nm.

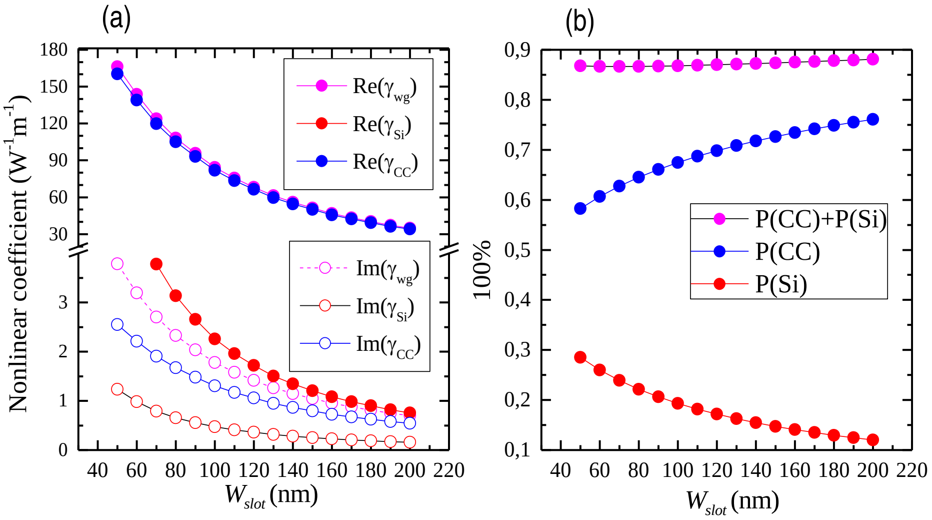

Figure 4.27: Influence of the silicon slot width on the nonlinear properties for (W_{rail}=170 nm): (a) nonlinear parameter γ of the silicon rails, cover cladding material, and full waveguide, respectively. The real parts are associated with the Kerr effect while the imaginary ones are related to the TPA process. (b) Power confinement in the two regions, respectively [201].

In order to get a more complete picture of the possible slot waveguide geometry optimization regarding the third-order optical nonlinearities, the calculated FOM_{TPA} for various W_{slot} and W_{rail} values is plotted in Fig. 4.28. It gives an overview of the necessary compromise between mode spreading (related to the effective index n_{eff} plotted with dotted lines) and the desired FOM_{TPA}. The maximum FOM_{TPA} value of 4.25 is achieved for

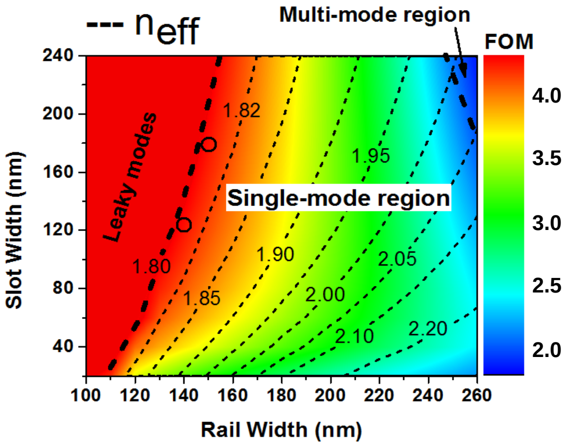

Figure 4.28: 2D-color map of slot waveguide FOM_{TPA} in terms of the rail and slot widths. Effective index values of the fundamental TE-mode are plotted with dotted lines, while the single-mode region is highlighted. The two open circles show the two sets of (W_{rail}, W_{slot}) leading to the maximum FOM_{TPA} values [201].

(W_{rail}, W_{slot}) equals to (140 nm, 120 nm) and (150 nm, 180 nm), indicated by the two open circles in Fig. 4.28. In practice, the applied slot waveguide dimensions would have to be chosen by considering both the linear and nonlinear optical propagation losses that directly influence the waveguide effective nonlinear length. About linear losses, recent results have shown that losses of SOI slot waveguide can be minimized down to around 2 dB/cm [40, 28] with rail widths of 220 nm, while this level could still be reduced by oxidation surface treatments.

Slot Photonic Crystal Waveguides: SPhCW

We have also explored the FOM_{TPA} optimization of propagating invariant waveguides and we have shown that a minimization of the TPA effect (i.e. maximization of FOM_{TPA}) could be obtained for given values of rails and slot widths. The problem of nonlinear pulse propagation has been studied since the beginning of the century [206] and has given keys to study new physical phenomena. In this section, we consider the core structures of this chapter: SPhCW. For these waveguides, another crucial feature should be addressed: the effect of the slow light, both in the local field enhancement and in the mode distribution. This additional degree of complexity is accompanied by a more complicated geometry and the necessity of treating the 3D periodic Bloch mode.

Indeed, relying on slow light effects [207, 208, 193], we can enhance one step further the interaction between light and the cladding nonlinear material. Although, as shown in the previous section, the use of slotted waveguides brings improvement to the aforementioned free carrier issue, it does not solve entirely the free carrier penalty as only a part of the propagating optical mode dielectric energy is confined in the low index soft-material filling the slot. As a consequence, TPA in silicon, which directly depends on the optical mode spreading outside the slot, cannot be entirely removed. So, one fundamental question arises, how does FOM_{TPA} evolves as a function of n_g?. In other words, is it interesting to slow down the light to improve the performance of third order nonlinear hybrid waveguides?.

Previous results dedicated to standard slow light W1 waveguides have shown that the gap-guided mode field profile tends to spread in silicon when approaching the bandgap, thus by increasing the slow down factors [142, 88]. As we have seen, the expected enhancement of the third order effective nonlinear susceptibility ($\chi^{(3)}$) scales with n_g^2 [71]. Considering reasonable slow down factors typically corresponding to n_g=20-40, this approach can lead to spectacular effective nonlinear parameter in Silicon γ values of a few 1000 $W^{-1}m^{-1}$ in silicon PhCW [13], so at least one order of magnitude larger than an already optimized simple slot waveguide covered with a highly nonlinear material (see Fig. 4.26 and 4.27). But this improved picture is dismantled when the nonlinear losses scaling (in the same ratio) spoils the slow light enhancement in the silicon structure.

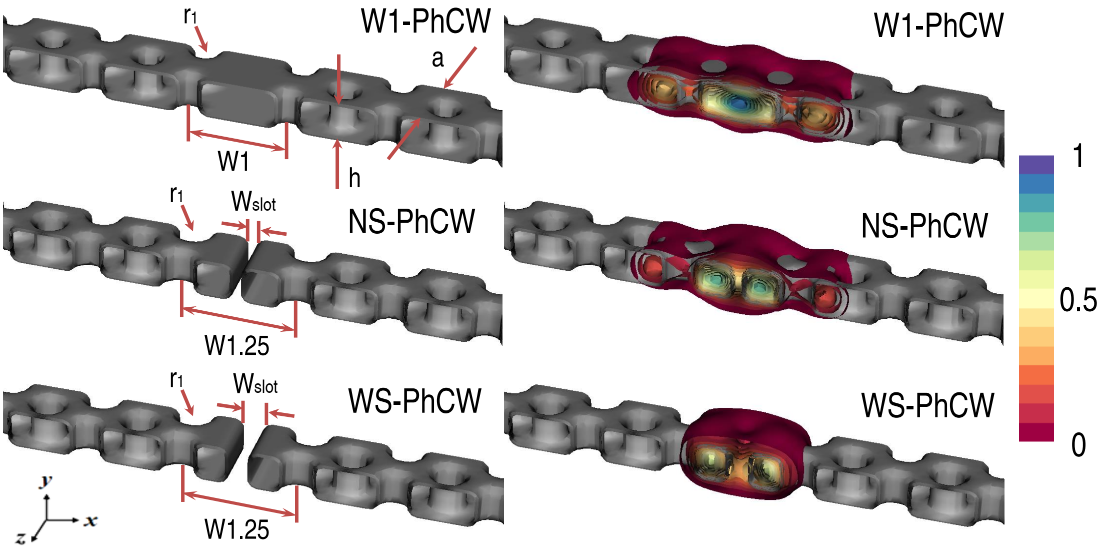

Figure 4.29: Schematic views of the investigated photonic crystal waveguide geometries (W1-PhCW, NS-PhCW and WS-PhCW) and the corresponding normalized $|E|^2$ of the studied modes at $k = 0.48 * 2\pi/\text{a}$. a= 400 nm, h= 260 nm.

In order to investigate this question, we consider here several PhC geometries, including non-slotted and slotted waveguides. We calculate for each their dispersion and nonlinear properties as a function of the light group index. Typical silicon photonic waveguide parameters are considered, so that results obtained can be estimated as general trends for this photonic platform. A lattice constant a= 400 nm and a silicon thin film of 260 nm height on a buried box of 2 μm have been first adopted. Standard linear refraction index values of 3.48 and 1.44 at λ=1.55μm are set for Si and SiO$_2$.

The present study is driven in regard with doped *PMMA* nonlinear polymers (NP), whose base refractive index is very close to 1.50, as some of them having interesting nonlinear optical properties at telecommunication wavelengths [192, 191]. A top cladding material with a linear index of 1.5, a Kerr index $n_2 = 2 \times 10^{-17}\text{m}^2/\text{W}$, and a TPA coefficient $\beta_{TPA} = 2.6 \times 10^{-12}$ m/W (i.e. $FOM_{TPA}^{NP} \approx 5.0$) at λ=1.55μm are considered as a typical situation of a strongly nonlinear soft-material filling the slot and holes of the SPhCW [188].

The three investigated geometries are made of a W1 photonic crystal waveguide (W1-PhCW), a narrow slot SPhCW (NS-PhCW) and wide slot photonic crystal waveguide (WS-PhCW), respectively, as shown in Fig. 4.29. Choosing different values for the slot width of the NS-PhCW (W_{slot}=100nm) and the WS-PhCW (W_{slot}=175nm), leads to the possibility of exploiting the so-called “W1-like mode” and “true-slot mode” of slotted photonic crystal waveguides, respectively, while ensuring large enough slots to avoid fabrication issues and guarantee proper filling.

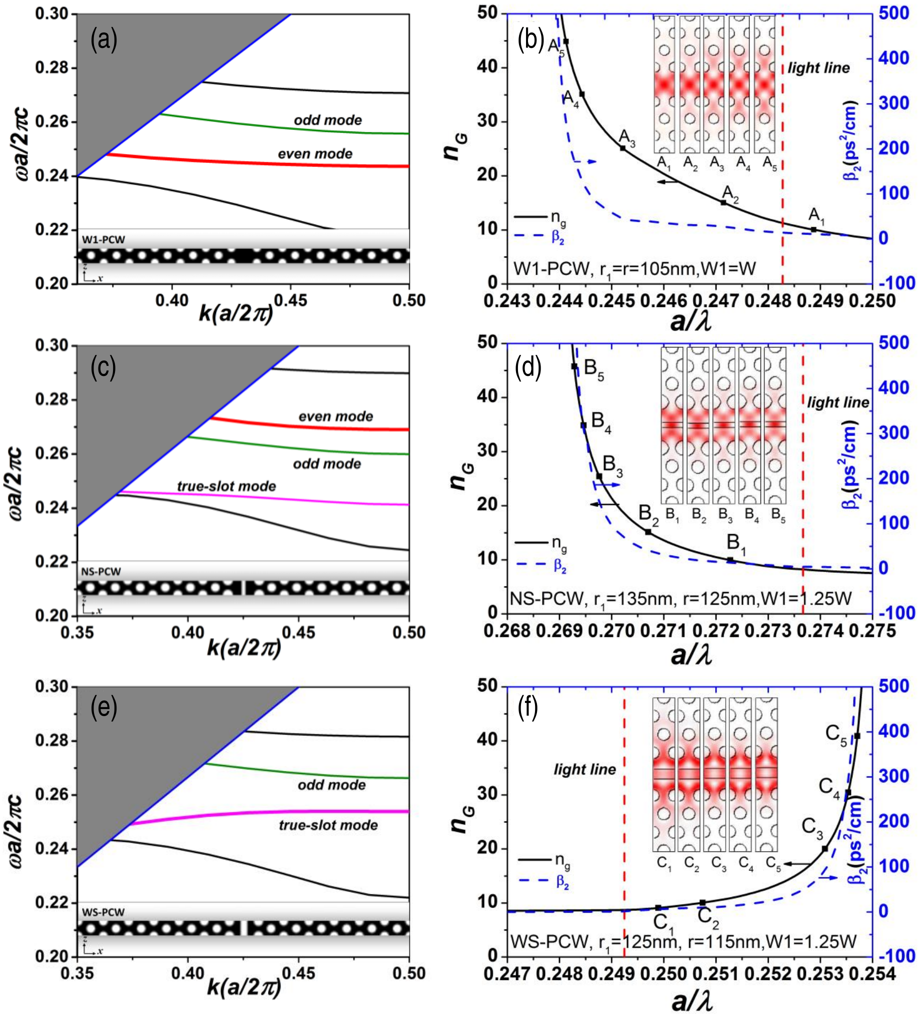

Figure 4.30: Dispersion curves of the three photonic crystal waveguides with the respective group index of the interesting particular mode: a) W1-PhCW - b) W1-even mode, c) NS-PhCW - d) W1-like-even mode, e) WS-PhCW - f) True-slot mode. As an inset the mode profile for different slow light values [209].

With respect to the standard situation of the W1-PhCW made of identical holes of 105 nm radius and width of $\sqrt{3}$a, the width of the NS-PhCW and WS-PhCW is enlarged to 1.25$\sqrt{3}$a, following previous guidelines [208, 193]. The diameter of the lattice holes of the slotted waveguides are also adjusted to r_1= 135 nm and r= 120 nm for the NS-PhCW and r_1= 125 nm and r= 115 nm for the WS-PhCW in order to prepare single-mode propagation and nearly mid-gap conditions for each investigated E_y-even mode. The band structure for the considered geometries and the group index and second order dispersion of the specific mode under study are depicted in Fig. 4.30.

Similar approaches as those conducted in [99] and [210, 211] for silicon wire and W1 waveguides, respectively, have been considered. As stated in these works, mode field spreading in the silicon region can be responsible for the generation of carriers by the TPA process, which in turn are responsible for the free-carrier dispersion and absorption effects. These different mechanisms should be introduced in the nonlinear Schrödinger equation (NLSE) that can be solved, for instance, by the split-step method [99].

Yet, in order to investigate the amount of free-carriers, estimation of only one parameter is necessary as all terms of the NLSE depending on free carriers scale with it [210], the overlapping factor κ. The $\langle\kappa(z)\rangle$ coefficient characterizes in fact the overlap between the optical mode and the silicon region. This parameter (0< $\langle\kappa(z)\rangle$ <1) is of direct interest for the quantitative estimation of the free carrier effects depending on the slow down factor and giving the information about the amount of energy in silicon. The expression of $\langle\kappa(z)\rangle$ is given by:

$$\kappa(z) = \frac{\mathrm{a} n_{Si}^2 \int_{S_{Si}} |\mathbf{e}(\mathbf{r})|^2 dS}{\int_{V_{Cell}} \frac{\partial}{\partial\omega}(\omega n_c^2) |\mathbf{e}(\mathbf{r})|^2 dV} \tag{4.8}$$

$$\langle\kappa(z)\rangle = \frac{1}{\mathrm{a}} \int_0^{\mathrm{a}} \kappa(\xi) d\xi \tag{4.9}$$

where V_{Cell} is the volume of the fundamental cell, n_c is the cladding refractive index, S_{Si} is the effective area in the cross-section (xy-plane) [99, 210, 74, 211].

We also recall another important metrics, the effective waveguide third-order susceptibility at one specific z point over the waveguide lattice period [210, 211]:

$$\Gamma(z) = \frac{\mathrm{a}^4 \int_{S_{NL}} e^*(\mathbf{r}) \chi^{(3)}(\mathbf{r}) \vdots e(\mathbf{r}) e^*(\mathbf{r}) e(\mathbf{r}) dS}{\left| \int_{V_{Cell}} \frac{\partial}{\partial\omega}(\omega n_c^2) |\mathbf{e}(\mathbf{r})|^2 dV \right|^2} \tag{4.10}$$

$$\langle\Gamma\rangle = \frac{1}{\mathrm{a}} \int_0^{\mathrm{a}} \Gamma(\xi) d\xi \tag{4.11}$$

where S_{NL} corresponds to the optical nonlinear region. Similarly, averaging this quantity over one lattice period leads to $\langle\Gamma(z)\rangle$, i.e. to the effective waveguide nonlinear susceptibility. These two parameters have been calculated in the three waveguide configurations described above, i.e. by considering the W1 and two slotted hybrid silicon photonic crystal waveguides. This relation is identical to the one deduced in Ref. [212], nevertheless, as we are working with a singular wavelength, we assume that the geometrical dispersion dominates over the material dispersion which is considered negligible. **In the three cases, nonlinearity comes from both silicon and the nonlinear material filling the holes and the slot**. For each material, estimation of $\chi^{(3)\prime}$ and $\chi^{(3)\prime\prime}$ has been done from the n_2 and β_{TPA} parameters, as follows [99]:

$$\frac{\omega}{c}n_2 + \frac{i}{2}\beta_{TPA} = \frac{3\omega}{4\varepsilon_0 c^2 n^2}\chi_{eff}^{(3)} \tag{4.12}$$

The integrations over space in Eq. (4.8) and (4.10) were done over the full photonic crystal lattice cell, i.e. by considering the complex nonlinear susceptibilities of both materials: Si and NP. The calculated $\langle\Gamma\rangle$ was finally used to estimate the effective $\langle\gamma_{wg}\rangle$ in order to compare with the measurements and the calculations performed up to this point. The expression for the effective waveguide susceptibility is given by:

$$\langle\gamma_{wg}\rangle = \frac{3\omega n_g^2}{4\varepsilon_0 \mathrm{a}^2}\langle\Gamma\rangle \tag{4.13}$$

The related results for the overlapping $\langle\kappa(z)\rangle$ calculations are shown in Fig. 4.31 (a). They have been obtained after the master internship work of Junfei Xia under my co-supervision. It can be appreciated that the mode field/silicon overlap in the W1 waveguide is extremely large (>95%) and is nearly constant (although a very small decrease is appreciable). On the other hand, for increasing slow down factors in slotted PhC waveguides, $\langle\kappa(z)\rangle$ decreases, meaning stronger interaction with the covering material. This overlap drops further (by around 20%) for the wide SPhCW that exploits the so-called even true slot mode (see Fig. 4.30 (e-f)).

To further analyze the waveguide properties, we plot in Fig. 4.31 (b) $\mathbb{R}\mathrm{e}(\gamma_{wg})$ and $\mathbb{I}\mathrm{m}(\gamma_{wg})$ as a function of n_g (with a double y-axis to manage two different scales). We observe that group index values around 15-20 are sufficient to lead to $\mathbb{R}\mathrm{e}(\gamma_{wg})$ values of 5000-20000 $\mathrm{W}^{-1}\mathrm{m}^{-1}$ in hybrid slotted silicon photonic crystal waveguides, i.e. at least 50 times larger than those obtained for typical silicon slot waveguides [201].

The final firm information regarding the effect of slow waves on the Kerr/TPA balance in the investigated standard and slotted PhCW is depicted in Fig. 4.31 (c). We plot here FOM_{TPA} of the three waveguides as a function of n_g. FOM_{TPA} is nearly constant for the W1-PhCW, with a value slightly above the silicon material FOM_{TPA} of 0.38. This result is consistent with the fact that the overlap between the mode field and the nonlinear material filling the holes is very weak. On the contrary, we clearly observe an increase of FOM_{TPA} for the two slow light slotted waveguide geometries, with a saturation for group indices larger than 40 (n_g>40), which is an encouraging result regarding propagation losses and the measured flat bands in dispersion engineered SPhCW discussed in previous sections.

To conclude, we show that properly filled silicon slotted photonic crystal waveguides have not the same behavior as standard W1 ones with respect to the influence of slow light on

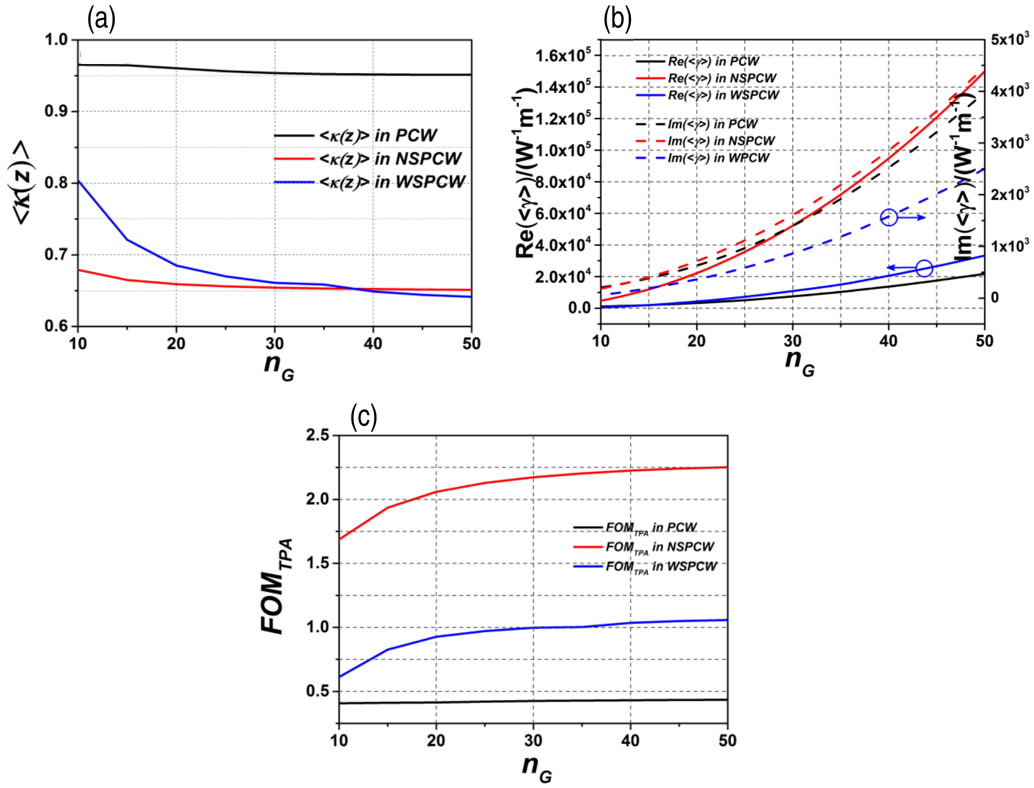

Figure 4.31: Nonlinear properties parameters vs. group indices; (a) Mode field/silicon overlap factor; (b) Nonlinear waveguide parameter (real and imaginary parts); (c) FOM_{TPA} in the three investigated structures. Black, red and blue curves represent the parameters in W1-PhCW, NS-PhCW and WS-PhCW, respectively [209].

the TPA process at telecommunication wavelengths. Both narrow and wide slot PhCW, operating on the two slot PhCW modes (W1-like and true-slot modes, respectively), are characterized by a mode field concentration in the slot for increasing slow down factors. These results show that the hybrid platform made of non-membrane slow light slotted silicon waveguides filled with nonlinear low-index materials can efficiently rely on slow light effects for on-chip data processing. The relative free-carrier penalty indeed tends to decrease with increasing slow light factors.

4.6.2 Preliminary nonlinear measurements

In the final section of this manuscript we would like to give some insights about initial measurements on the designed photonic crystal structures under the D-Scan set-up. We have started the integration of the engineered waveguides with other materials but the linear characterization is still under progress. Nevertheless, we have performed some measurements by using the refractive index liquids explored in previous sections. In PhCW, the model and interpretation are more complex than in standard waveguides and

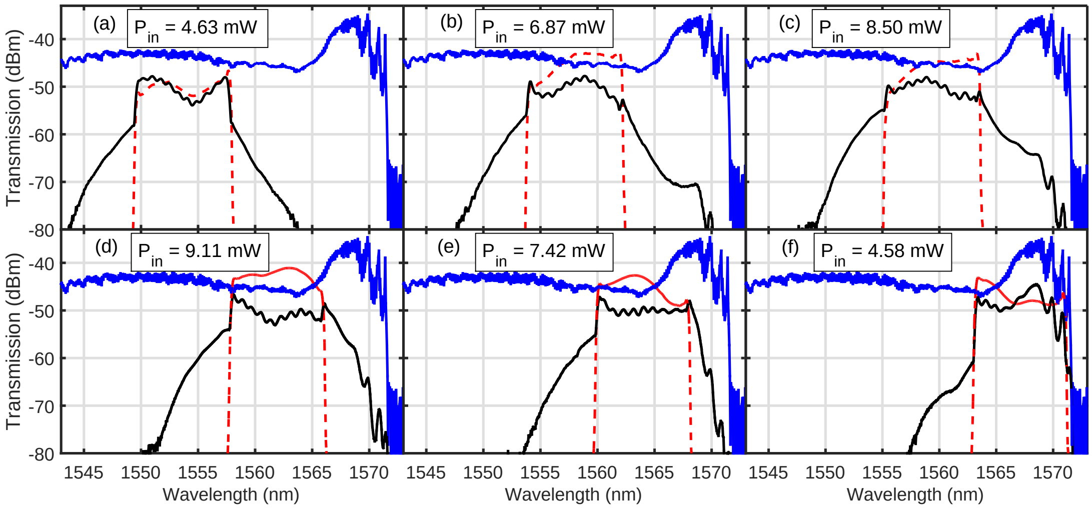

Figure 4.32: Spectral broadening at zero dispersion for different regimes in a 50 μm long W1 waveguide. PhC transmission in blue, input pulse in red and output transmission in black. The average input power is specifically marked.

many of the features remain to be deeper explored. In particular, the losses (propagation, coupling efficiencies, localized modes, etc.) and the intrinsic high dispersion in the slow light regime change the response with respect to strip waveguides. Nevertheless, the retrieved FOM_{TPA} should be close to that of silicon neglecting the 3^{rd} order NL response of the liquid.

Nonlinear W1 PhCW

In Fig. 4.32, we have plotted the output transmission spectra of a **50 μm long W1 PhCW**. The linear transmission of the waveguide is marked in blue for guideline. The input Fourier limited pulses are plotted in red and the output spectra is shown in black.

Different responses can be appreciated as function of the central frequency position. First, in (a), the pulse is intentionally located in the fast light regime. A characteristic and typical symmetric broadening is observed. As the input pulse spectrum is closer to the bandgap, the symmetric broadening is broken (b) and the red spectral components are enhanced. We attribute this feature to the improved light-silicon interaction expected in the slow light regime. Closer to the bandgap and with larger power, the asymmetry is more evident, marking the entrance of the diffusive regime characterized with some peaks. In (d), we are so close to the gap that the broadening gets truncated by the forbidden frequencies, even if the input pulse has lower energetic content in the red, the output pulse shows an enhancement in the original pulse edge. When some of the input frequencies of the pulse enters the slow light regime, the generation of new frequencies is noticeable by comparing the input and output spectra. Indeed, the output is flat while

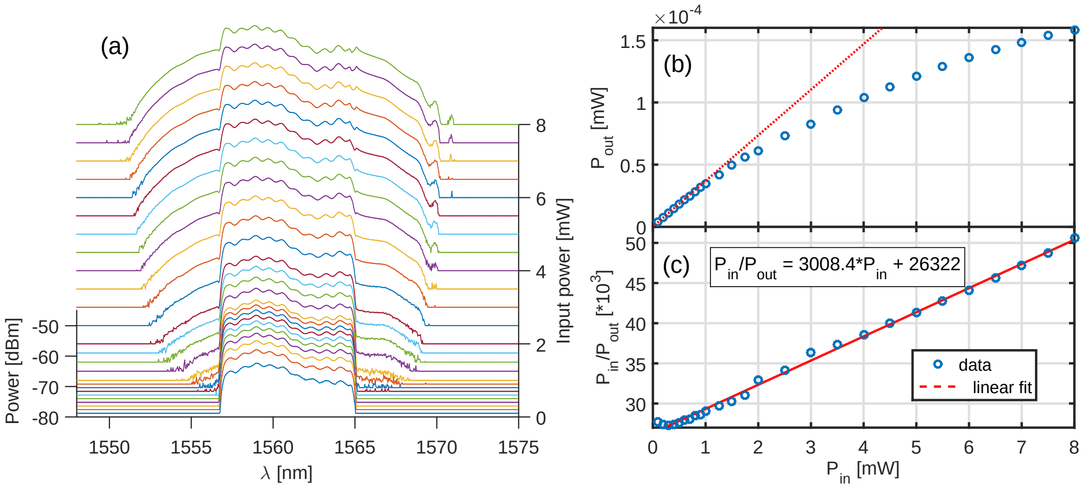

Figure 4.33: (a) Transmission of a 50 μm long W1 PhCW as a function of the power. (b) P_{in} vs. P_{out} with a linear expected tendency in red to highlight the nonlinear saturation. (c) P_{in}/P_{out} as a function of P_{in} with the respective linear fit.

the spectral content in the excitation pulse exhibits several dBm lower powers for lower frequencies. Finally, in a last experience, the red part of the excitation pulse is located at the border edge of the bandgap. As expected, there is no broadening in lower frequencies, meaning that the exit strip waveguides do not generate any appreciable nonlinear effect.

A qualitative enhancement close to the photonic bandgap is then confirmed in W1 waveguides as have been already demonstrated and exploited in previous publications. Next, we have placed the input spectrum in a interesting region, between the cases (c) and (d). We show the output spectra as a function of the input power in Fig. 4.33 (a). In (b) and (c) we perform a similar analysis as the one with previous waveguides (section 2.6).

Nonlinear SPhCW: importance of dispersion management

Coming back to our main interest, we now present preliminary results related to the nonlinear properties of SPhCW. First, we analyze a **1 mm long non-DE SPhCW**. In Fig. 4.34, we present the measurements at zero dispersion pre-chirp for different powers. As it can be appreciated in (b), the excitation pulse is located close to the bandgap. Furthermore, it could be noticed in (a) that for large enough powers, there is a presence of an asymmetric broadening. Part of the pulse spectrum is located in the diffusive regime.

Next, in (c) we plot the usual linear curve of P_{in}/P_{out} vs. P_{in}. The large value obtained for the parameter a (from the linear fit $P_{in}/P_{out}=b*P_{in}+a$), equals to 12068, is a indicator for low coupling efficiencies or large linear propagation losses, two expected contributions

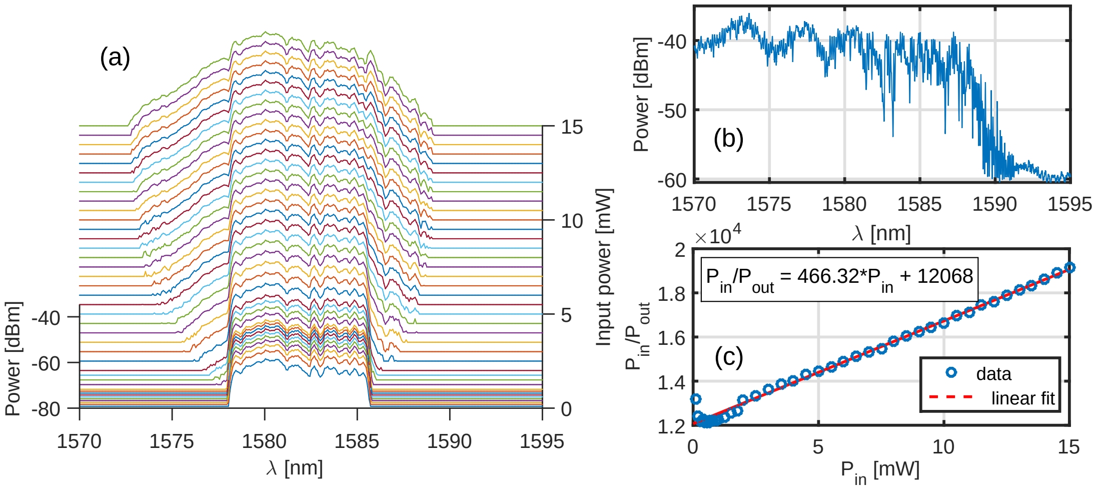

Figure 4.34: (a) Output spectra of a 1 mm long SPhCW as a function of the input power. (b) Linear transmission. (c) P_{in}/P_{out} vs. P_{in} with the linear fit and the corresponding equation.

in long SPhCW. The first one from the additional couplers and the second due to the out-of-plane and backscattering enhanced in the slow light regime. We would like to remark that even though the spectra is not symmetric and we expect several phenomena to occur, the linear trend is still present in (c).

Then, we have used this structure to test the D-Scan technique. As usual, we have varied the input power and the injected pre-chirp ($\phi^{(2)}$). The trace of the standard deviation (2σ) is depicted in Fig. 4.35. The first noticeable feature is the positive sign of the nonlinearity, as expected the main contribution is attributed to silicon. Second, the unusual shape of the 2σ curves that cannot be reproduced directly with our model. We attribute this behavior to the strong GVD introduced by the waveguide in the regime close to the bandgap. In such a non DE waveguide, β_2 (and consequently the $\phi^{(2)} = \beta_2 z$) is large, about tens of ps^2/mm. We present in Fig. 4.35 (b) the spectra for the highest available power ($P_{\text{in}} = 15$ mW) as a function of the introduced dispersion. It could be noticed that, as expected, close to the zero dispersion point, the maximum (asymmetric) broadening is present. In the dBm scale no particular features are observed.

In a second step, we want to work in a condition where the waveguide dispersive effect can be neglected. We have used the **DE-SPhCW** with $r_1 = 105$ nm studied in section 4.5. This geometry offers the best compromise of achieved n_g, available bandwidth and losses. The **DE SPhCW length is 200 μm** and the transmission overlapped with the n_g curve are depicted in Fig. 4.36. We have also plotted the pulse transmitted through the SPhCW at low power ($P_{in} = 0.1$ mW) to illustrate the central frequency and bandwidth of the excitation pulse. From the image, it can be appreciated that we are in the ballistic regime of the waveguide and that the average group index is $n_g \approx 10$.

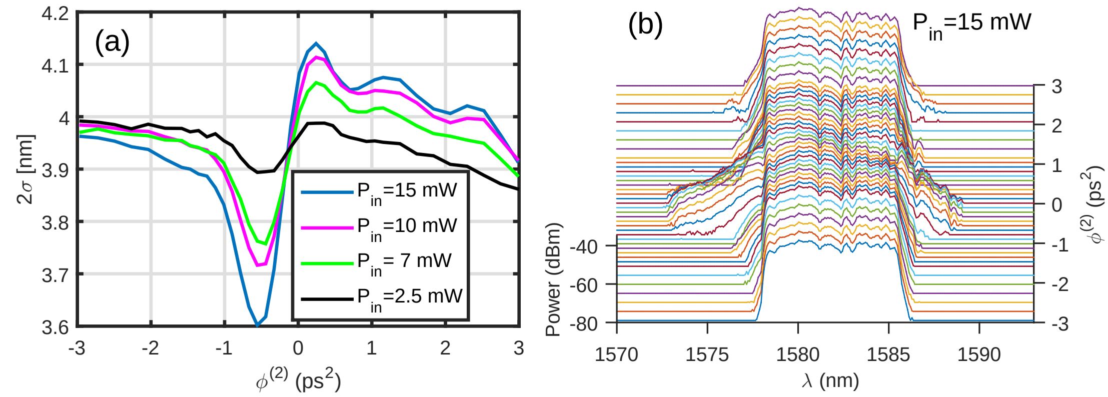

Figure 4.35: (a) D-Scan applied to a 1 mm long non-DE SPhCW covered with a refractive index liquid. (b) Spectra measured for the largest input power as a function of the introduced chirp ($\phi^{(2)}$).

We can estimate the dispersion length by considering the variation of the group index as a function of frequency. To have an order of magnitude, we may refer to Fig. 4.24, where we have calculated the dispersion expected for this geometry. It can be seen that

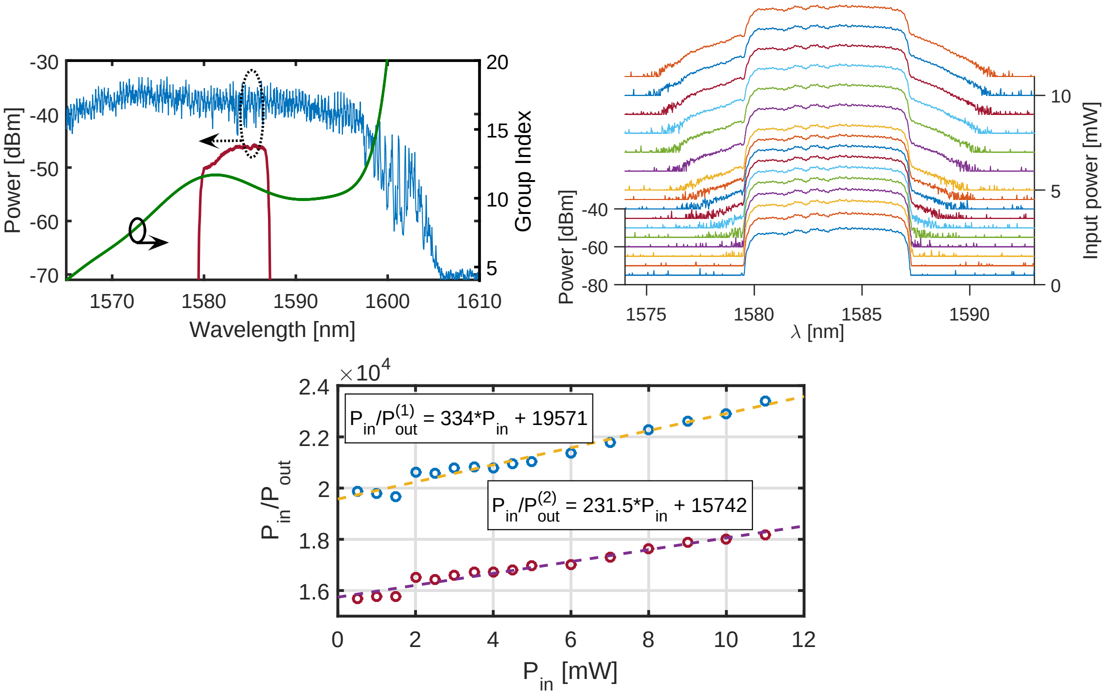

Figure 4.36: Up-left: SPhCW transmission with the extracted group index. The excitation pulse shape is shown in red. Up-right: Spectra as a function of the input power at zero dispersion. Down: Bidirectional curves for measuring the TPA effect.

in our case $\max(\beta_2) \approx 1$ ps^2/mm. After the Fourier limited pulse, we estimated a pulse duration of $\tau_0 \approx 1.2$ ps. We can easily calculate the dispersion length as:

$$L_D = \frac{\tau_0^2}{\max(\beta_2)} = 1.4 \text{ mm} \tag{4.14}$$

that compared to the dispersive waveguide length ($L = 0.2$ mm) gives $L/L_D = 0.14 < 1$. In a first approach, the dispersive effects can be neglected.

The bi-directional method is applied and the obtained slopes with the two side injection shown with the spectra when injected from side (1). Conversely to the experience with non DE SPhCW, we highlight the symmetry of the broadening exhibiting a compensated transmission and n_g over the exploited frequencies. The values measured in the set-up are: $\kappa_{\text{inj}}^{(1)} = 24\%$, $\kappa_{\text{OSA}}^{(1)} = 25\%$, $\kappa_{\text{inj}}^{(2)} = 27\%$ and $\kappa_{\text{inj}}^{(2)} = 30\%$, the losses are estimated to be around 20 dB/cm. After using the coupling estimation equations, we have obtained $\kappa_{\text{SA}} = 5.1\%$ and $\kappa_{\text{SB}} = 4.0\%$. For a reminder of the notations and procedure please refer to section 2.5.1.

Using these values the waveguide effective TPA nonlinear susceptibility is estimated to: $\gamma_{TPA} \approx 63.3$ (Wm)$^{-1}$, which is already twice the value found for the strip waveguide. In SPhCW a part of the mode is not in silicon but within the slot, so the estimated gamma should be weighted with the effective mode area in silicon. After the calculation of the 3D modes, an estimated $A_{NL} \approx 0.36$ μm^2 was obtained [170]. We performed a D-Scan to complement the measurements and properly define the enhancement. We show in Fig. 4.37, the standard deviation and the output power by overlapping the measurements and the simulation for a $FOM_{TPA} = 0.39$ which is very close to the value measured in the silicon used to fabricate the PhC, demonstrating the negligible effect of the liquid.

As expected, the model reproduces properly the trends, demonstrating a compensation of the GVD and its importance when dealing with nonlinear effects. It has not been the case for the previous PhC, where the maximum achievable broadening ($\max(2\sigma)$) gets depleted. Now, we can easily estimate the γ for the waveguide: $\gamma = 2\pi * FOM_{TPA} \times \gamma_{TPA} \approx 155.1$ (Wm)$^{-1}$. Reminding that $\gamma = S^2 n_2 k_0 / A_{NL}$, and assuming the n_2 measured in previous experiences, we can estimate a $S^2 \approx 5.3$ that corresponds (in silicon) to a $n_g \approx 8$. This is a bit smaller than the value expected but we attribute this difference to the contribution of the input access.

To sum up, we have experimentally demonstrated the enhancement of the nonlinear effects in SPhCW which were properly engineered to avoid second order dispersion issues. This represents a first milestone in the way to apply the technique and platform to potential nonlinear materials that could cover the slot. Developing further the presented preliminary results and upcoming samples covered with highly nonlinear interesting materials is among the perspectives of this thesis.

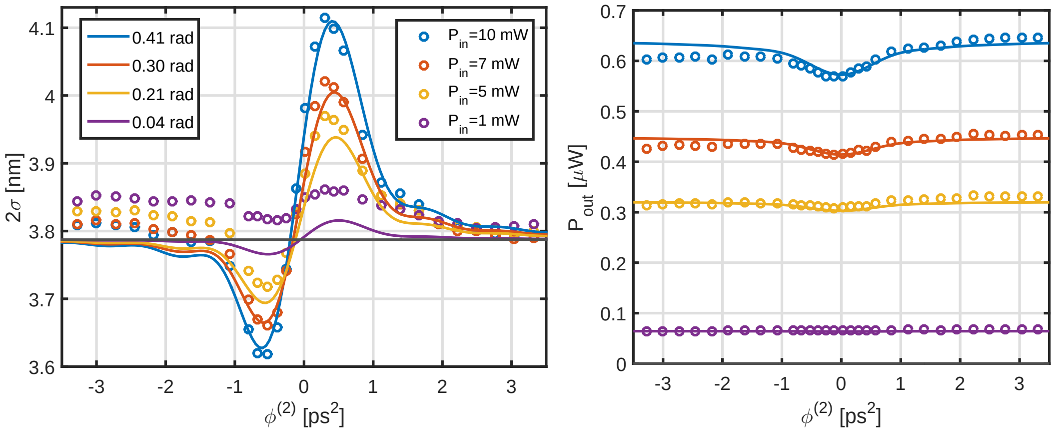

Figure 4.37: Left: Simulated and measured standard deviation is a 200 μm long DE-SPhCW for different input powers with the corresponding nonlinear phase shift. Right: Output power.

4.7 Conclusion

In this chapter, we have briefly explained the coupling design, fabrication issues and strategies, simulation tools and characterization of SPhCW. We have reported experimental results demonstrating the possible control of light group index, GVD sign and bandwidth in long ShPCW (700 μm) through a proper design of the waveguide geometrical parameters. These results are in agreement with 3D numerical calculations. We stress that all experiences are carried out in SPhCW on SOI (i.e. non-free-standing air membranes) where the holes [213] and the slot have been filled with different index liquids. Hence it mimics the integration of soft matter materials such as polymers or doped compounds [191, 192] in hybrid waveguides in the purpose of relying on a mechanically robust and viable integration PhC-on-silicon scheme.

Experimental evidence for flat-band dispersion engineered behavior is provided for the first time in SPhCW, meaning a compensation over a given bandwidth of the large group velocity dispersion in the slow light regime. An Optical Coherent Tomography (OCT) based method was used [184] in order to directly measure the optical delay and to estimate the group index as a function of wavelength. We also demonstrate that the advantages of slow light structures, optimized for low propagation losses and with careful dispersion engineering, can thus be obtained in such hybrid structures filled by various materials. This fact opens broad perspectives in view of the richness of materials that can be drop-casted, spin-coat, or grown on top of silicon wafers including nonlinear and active materials.

Slow light propagation with normalized delay-bandwidth product (NDBP) up to 0.20 with a transmission level only 5 dB lower than the one of reference SOI strip waveguides open the concrete possibility to use DE SPhCW for all optical processes. In particular, they can be used for enhancing third order nonlinear optical effects through slow-light boost while preserving the phase matching condition (flat band) for broadband four wave mixing [214] and other nonlinear phenomena. We have finished the chapter with simulations demonstrating the potential of the fabricated structures for nonlinear optics and we gave first experimental insights on the light-matter enhancement in the slow light regime for dispersion compensated waveguides.

Summary and Perspectives

In this manuscript, we present our contribution to the analytical, numerical, and experimental investigation of integrated devices for on-chip nonlinear all-optical functionalities at telecommunication wavelengths. We have studied analytically and semi-analytically a model that treats a waveguiding structure (regardless of its composition) as a Kerr lens and in analogy with the Z- Scan technique for thin-film samples, and allows the measurement of optical output spectra variations to determine the effective complex nonlinear susceptibilities of optical waveguides. Furthermore, a simple bidirectional useful technique to precisely determine coupling efficiencies from free space to chip has been proposed and experimentally demonstrated. As this stage does not require pre-shaping of optical pulses, it can be used to accurately estimate light injection efficiencies for any integrated device. The method provides not only the magnitude of the effective nonlinearity but also its sign. Interestingly, the measurement principles and the numerical tools are easily scalable in wavelengths and size, making it suitable, for fibers or as a tool to measure material nonlinear coefficients, for example in the midIR.

We have validated the method with known materials such as silicon or silicon nitride waveguides at telecommunication wavelengths and we have explored Ge-rich $\mathrm{Ge}_x\mathrm{Si}_{1-x}$ alloys filling literature data gaps in their direct-gap/indirect-gap band-structure region (i.e., from x=0.7 to x=0.9) where purely theoretical estimation of the expected nonlinearities is difficult. We have also characterized chalcogenide waveguides under collaboration with MIT. These materials, which are usually used for flexible photonics exhibit susceptibilities comparable to silicon strip waveguides but with no two-photon absorption (TPA) around λ=1.55 λm, thus opening room to the realization of a flexible nonlinear integrated optical platform.

Next, we have explored configurations to further enhance light-matter nonlinear interactions relying on enhanced electromagnetic field dielectric structures. In this purpose, we have first designed and fabricated 1D silicon photonic crystal (Bragg) cavities with moderate Q factors around 8 000. Then, by estimating the nonlinear blue shift generated by free carrier refraction, we have used a set-up to optimize the output transmission by changing input optical pulse spectral wavelength position in time. Furthermore, we have explored parameters such as the central pulse wavelength, bandwidth and incident energy in order to understand the optimal conditions for an improved transmission, demonstrating the resonance of large part of the input spectral content into the cavity.

We have shown that it is possible to enhance the intra-cavity field by phase shaping of the input pulse, which opened the possibility to optimize the optical bandwidth and the nonlinear dynamics for all-optical integrated functions. We have finally explored a numerical tool to simulate the intracavity interactions that could be used to engineer optimum pulses and cavities.

To fabricate our samples, we have used the clean room facilities in C2N/CTU. Furthermore, we have explored novel methods to decrease the wall roughness responsible for the major source of losses. We have done codes and simulations to optimize the dispersion properties of SPhCW. After their fabrication, we could demonstrate for the first time that flat band slow light transmission can be obtained in long (700 μm) waveguides over a large bandwidth ($\sim$ 25 nm) with robust dispersion features as function of the cladding index. These results have opened perspectives for applications requiring enhanced light-matter interactions and very small footprints with CMOS compatible hosts. Finally, we have demonstrated with preliminary results that the light-matter interactions in these structures are enhanced due to the slowing down of light, illustrating the potentials of hybrid silicon photonics made of properly designed hollow core waveguides made of slots properly filled with highly nonlinear materials. The latest shows the need for a continued exploration of hybrid platforms to profit from the good waveguiding properties and potential massive production of Silicon with the nonlinear performances of novel materials such as polymers, doped-solids or liquids.

There are a lot of future research perspectives that this work has opened. We will draw here the short term ones following the thesis results. Regarding the D-Scan technique (chapter 2), we have made the first steps in measuring the silicon nitride waveguides that we have fabricated, covered with semiconductor single wall carbon nanotubes (s-SWCNT). The first results under the D-Scan show a negative Kerr coefficient, which is very interesting for integrated applications. Further studies remain to be done by controlling the CNT concentration and alignment. Another material that we have tested is the strain silicon by a layer of silicon nitride under a pressure of (1000 ± 25) MPa in order to achieve maximum stress. First results have shown an improvement of the nonlinear figure of merit (from 0.38 of the original silicon waveguide to 0.48 in the silicon strained), showing that this material can be used not only for $\chi^{(2)}$ proposes [215] but also to improve third order nonlinear characteristics of bulk Si. In these waveguides, we have observed the presence of an additional absorption contribution at intermediate power levels (average powers between 0.3 and 1 mW) that we attribute to the presence of surface generated carriers. These kinds of physical phenomena have been recently studied [216] and proposed for sensing applications. Under the same logic, we expect to apply our method in novel functionalized oxides-strained waveguides under development in our group.

Improvements in the D-Scan technique could be done by following analogies with the Z-Scan explorations, particularly variations as the two color Z-Scan [64], eclipsing Z-Scan [65] or time-resolved Z-Scan[217], allowing measurements sensitive to diverse wavelengths, polarization or time, respectively. Furthermore, the study of the orientation of molecules is envisaged for hybridization for instance CNT or DDMEBT polymers. Considering nonlinear temporal dynamics of waveguides, time resolved excite-probe techniques[218] could be implemented for instance by using the zeroth order beam from the diffraction grating of the set-up not exploited up-to-now.

Regarding the coherent excitation of nonlinear microcavities, we can increase the complexity on the system by pumping photonic crystal coupled cavity waveguides (CCWs). Furthermore, a better control in the amplitude and phase of the injection pulse could be done to compensate the nonlinear shift of a given silicon cavity. In the same order of ideas, integrated materials with different free carrier generation via two photon absorption could be used to study their coherent control. Also, after the development of integrated optics an on-chip pulse stretcher could be designed in order to optimize the pulse prior the cavity, reducing the footprint by several orders of magnitude (from m to mm). In this sense, we have also seen in this work that strongly dispersive structures such as dispersion engineered photonic crystal waveguides reach second order dispersion coefficients in the order of ps^2/mm (Fig. 4.23), so we can target ϕ^2 values in the order of the optimum required for the tested nanobeam cavity ($\sim$1.2 ps^2) with a usable bandwidth and realistic waveguide lengths.

The study of coupled cavities could give also interesting results regarding both coherent excitations and slow light features. This could be envisaged for new frequency generation or switching.

Considering fabrication disorder in SPhCW, we note that its study has been used only as a mean to interpret experimental results, rather than being by itself a central point of discussion. Nevertheless, some open problems that could be explored are worth noting, for instance, when adding a slot, new questions about the losses rise, such as the definition of the coherence length or the evolution of the losses as a function of the group index. Precise knowledge of physics of energy dissipation in the slow-light regime may help to identify the photonic designs truly suitable for practical slow light applications [151].

The set-up of time of flight measurements could be modified in order to measure the nonlinear properties of integrated structures. We could extract the information of phase changes indirectly via the interferometric method and track directly the nonlinear effects for given dispersive properties.

Silicon dispersion engineered photonic crystals have also been demonstrated as promising structures to generate entangled photons [219], but still the nonlinear losses are a big constraint to improve the performance. So, it is of direct interest for quantum optics on chip [220] to use hybrid platforms.

To conclude, the presented characterization procedure, coherent excitation technique and novel hybrid host reported in this thesis represent a fraction of recent achievements in silicon integrated photonics, suggesting that microfabricated optical structures are becoming a mature technology for nonlinear classical and/or quantum on-chip applications with reduced footprints and required low powers.

A Acronym Glossary

CMOS = Complementary metal-oxide semiconductor
CW = Continuous wave
FCA = Free carrier absorption
FCR = Free carrier refraction
FOM = Figure of merit
FWHM = Full width at half maximum
FWM = Four wave mixing
FT = Fourier transform
GVD = Group-velocity dispersion
ICP = Inductively coupled plasma
LEPECVD = Low energy plasma enhanced chemical vapor deposition
MZI = Mach-Zehnder interferometer
NDBP = Normalized delay bandwidth product
NSPP = Normalized spectral peak power
OSA = Optical spectrum analyzer
PECVD = Plasma enhanced chemical vapor deposition
PhC = Photonic crystal
PhCW = Photonic crystal waveguide
PMMA = Polymethylmethacrylate $(C_5O_2H_8)_n$
RIE = Reactive ion etching
SEM = Scanning electron microscope
SHG = Second harmonic generation
SOI = Silicon on insulator
SPhCW = Slot photonic crystal waveguide
SPM = Self-phase modulation
TE = Transverse electric
THG = Third harmonic generation
TIR = Total Internal Reflection
TM = Transverse magnetic
TPA = Two photon absorption
wg = Waveguide
ZGVD = Zero group-velocity dispersion

B Symbol and Physical Units Glossary

Symbol	**Physical parameter**	**Expression**	**Units**
α	Propagation losses	$\alpha\left[\frac{\mathrm{dB}}{\mathrm{cm}}\right] = 10\log_{10}(e)\alpha\,[\mathrm{cm}^{-1}] \approx 4.34\alpha\,[\mathrm{cm}^{-1}]$	dB/cm
β	Mode propagation constant		m^{-1}
β_1	First-order dispersion coefficient		
β_2	Second-order dispersion coefficient	$\beta_2 = -\frac{\lambda^2}{2\pi c}D = -\frac{\lambda^2}{2\pi c^2}\frac{dn_g(\lambda)}{d\lambda}$	$\mathrm{ps}^2/\mathrm{mm}$
β_{TPA}	Two-photon absorption coefficient	$\beta_{TPA} = \frac{3\omega}{2\epsilon_0 c^2 n_0^2}\ \mathbb{I}\mathbf{m}\{\chi^{(3)}\}$	m/W
$\chi^{(2)}$	Second-order optical susceptibility		
$\chi^{(3)}$	Third-order optical susceptibility	$\chi^{(3)}\ (\mathrm{SI}) = \frac{4\pi}{3^2}\times 10^{-8}\ \chi^{(3)}\ (\mathrm{cgs})$	$\mathrm{m}^2/\mathrm{V}^2$
ε	Dielectric constant		
ε_0	Vacuum permittivity	8.854×10^{-12}	$\mathrm{Fm}^{-1} = \mathrm{CV}^{-1}\mathrm{m}^{-1}$
γ	Third order real nonlinear coefficient	$\gamma = k_0 S^2 n_2/A_{\mathrm{NL}}$	$(\mathrm{mW})^{-1}$
γ_{TPA}	Third order imaginary nonlinear coefficient	$\gamma_{TPA} = S^2\beta_{\mathrm{TPA}}/A_{\mathrm{NL}}$	$(\mathrm{mW})^{-1}$
L_{eff}	Effective length	$L_{\mathrm{eff}} = (1-e^{-\alpha L})/\alpha$	m
λ	Wavelength		m
n	Refractive index		
n_2	Nonlinear refractive index, Kerr coefficient	$n_2 = \frac{3}{4\epsilon_0 c n_0^2}\ \mathbb{R}\mathbf{e}\{\chi^{(3)}\};\ n_2\left[\frac{m^2}{W}\right] = \frac{40\pi}{cn}n_2\,[\mathrm{esu}] = \frac{4.19\cdot 10^{-7}}{n}n_2\,[\mathrm{esu}]$	m^2/W

C Analytical D-Scan model

We want to establish a mathematical relation between the second order dispersion term ($\phi^{(2)}$) and two important quantities: the spectral peak intensity and the spectral broadening. The latest is quantified by the standard deviation of the spectra.

$$\sigma_\lambda = \sqrt{\frac{\int \lambda^2 P(\lambda) d\lambda}{\int P(\lambda) d\lambda} - \left(\frac{\int \lambda P(\lambda) d\lambda}{\int P(\lambda) d\lambda}\right)^2} \tag{C.1}$$

where $P(\lambda)$ corresponds to the power as a function of the wavelength (experimentally given by an Optical Spectrum Analizer (OSA)). To simplify the analytical calculation we will assume a gaussian pulse in the paraxial approximation regime which at $z = 0$ has a temporal profile given by:

$$U(0,t) = U_0 e^{-\frac{t^2}{2T_0^2}} \tag{C.2}$$

In the Fourier domain, we could propagate the wave in the space by a distance z:

$$\widetilde{U}(z,\nu) = \widetilde{U}(0,\nu) e^{\frac{i\beta_2 (2\pi\nu)^2 z}{2}} = \widetilde{U}(0,\nu) e^{\frac{i\phi^{(2)} (2\pi\nu)^2}{2}} = U_0 \sqrt{2\pi} T_0 e^{-\frac{(2\pi\nu)^2}{2}(T_0^2 - i\phi^{(2)})} \tag{C.3}$$

where $\widetilde{U}$ is the Fourier transform of U, $e^{\frac{i\phi^{(2)}(2\pi\nu)^2}{2}}$ is a transfer function and $\phi^{(2)} = \beta_2 z$ is the second order dispersion term in units of time squared. We could write the previous expression in the temporal domain as:

$$U(z,t) = \frac{U_0}{\sqrt{1-\frac{i\phi^{(2)}}{T_0^2}}} e^{-\frac{t^2\left(T_0^2+i\phi^{(2)}\right)}{2\left(T_0^4+\left(\phi^{(2)}\right)^2\right)}} = |U(z,t)|e^{i\phi(z,t)} \tag{C.4}$$

where the wave amplitude and phase are given at any z point as:

$$|U(z,t)| = \frac{U_0}{\sqrt[4]{1+\left(\frac{\phi^{(2)}}{T_0^2}\right)^2}} e^{-\frac{t^2}{2T^2(z)}} \tag{C.5}$$

$$\phi(z,t) = -t^2 \frac{\operatorname{sign}(\phi^{(2)})\left(\frac{|\phi^{(2)}|}{T_0^2}\right)}{2T_0^2\left[1+\left(\frac{\phi^{(2)}}{T_0^2}\right)^2\right]} \tag{C.6}$$

$$T^2(z) = T_0^2 + \frac{\left(\phi^{(2)}\right)^2}{T_0^2} = T_0^2\left[1+\left(\frac{\phi^{(2)}}{T_0^2}\right)^2\right] \tag{C.7}$$

Now, we can propagate the field from $z=0$ until just before the Kerr lens ($z=z_1$) as follows:

$$U(z_1,t) = \frac{\sqrt{I_0}}{\sqrt[4]{1+\left(\frac{\phi^{(2)}}{T_0^2}\right)^2}} e^{-\frac{t^2}{2T^2}} e^{-i\frac{\zeta}{2}t^2} \tag{C.8}$$

with

$$\zeta = \frac{\phi^{(2)}}{T_0^4\left[1+\left(\frac{\phi^{(2)}}{T_0^2}\right)^2\right]} \tag{C.9}$$

After the nonlinear element (Kerr lens), in the temporal domain, only the field phase is affected such that:

$$U(z_2,t) = U(z_1,t)e^{i\phi_{NL}(t)} \tag{C.10}$$

where $\phi_{NL}(t)$ contains the nonlinear phase introduced by the waveguide. In order to find an exact solution, we will first consider only the real part of the nonlinear susceptibility, so the TPA effect will be considered negligible. To simplify the notation, we will also consider the enhancement factor included in the Kerr coefficient. So, the nonlinear phase shift in the temporal domain is written as:

$$\phi_{NL}(t) = \frac{k_0 n_2 I_0 L_{eff}}{\sqrt{1+\left(\frac{\phi^{(2)}}{T_0^2}\right)^2}} e^{-\frac{t^2}{T^2}} = k_0 n_2 L_{eff} \left|U(z_1,t)\right|^2 \tag{C.11}$$

For the next we define the nonlinear phase shift at $t=0$, without nonlinear losses nor dispersion ($\phi^{(2)}=0$) as $\phi_{NL0}=\phi_{NL}(0)=k_0 n_2 I_0 L_{eff}$. This is the maximum attainable phase shift as it corresponds to the highest peak power. The nonlinear phase has a gaussian temporal shape, so to simplify the expression, we will assume the paraxial approximation, which remains valid close to $t=0$ as schematically shown in Fig. C.1.

$$e^{-\frac{t^2}{T^2}} \approx 1 - \frac{t^2}{T^2} \tag{C.12}$$

So the expression (C.10) will take the form

$$U(z_2,t) \approx U(z_1,t) e^{-i\frac{\phi_{NL0}}{\sqrt{1+\left(\frac{\phi^{(2)}}{T_0^2}\right)^2}}\frac{t^2}{T^2}} = U(z_1,t) e^{-i\frac{\eta}{2}t^2} \tag{C.13}$$

with

$$\eta = \frac{2\phi_{NL0}}{\sqrt{1+\left(\frac{\phi^{(2)}}{T_0^2}\right)^2}} \frac{1}{T^2} \tag{C.14}$$

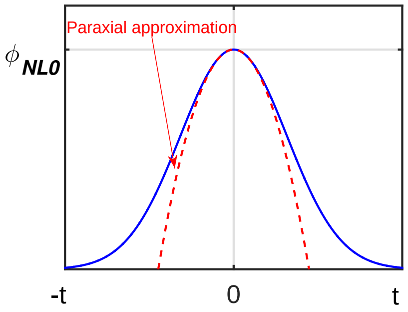

Figure C.1: Paraxial approximation of the temporal nonlinear phase profile.

Finally, with the equations (C.8) and (C.13), we could find the field in z_2 in terms of the initial intensity:

$$U(z_2,t) \approx \frac{\sqrt{I_0}}{\sqrt[4]{1+\left(\frac{\phi^{(2)}}{T_0^2}\right)^2}} e^{-\frac{t^2}{2T^2}} e^{-i\frac{\zeta}{2}t^2} e^{-i\frac{\eta}{2}t^2} = \frac{\sqrt{I_0}}{\sqrt[4]{1+\xi^2}} e^{-\frac{t^2}{2}\left[\frac{1}{T^2}+i(\zeta+\eta)\right]} \tag{C.15}$$

where we have introduced the normalized parametric dispersion term $\xi = \frac{\phi^{(2)}}{T_0^2}$. The last expression is integrable under a Fourier transform (FT), so we are able to find a mathematical relation for the spectrum after the pure-Kerr nonlinear medium:

$$\boxed{\widetilde{U}(z_2,\nu) = FT\left[U(z_2,t)\right] = FT\left[\frac{\sqrt{I_0}}{\sqrt[4]{1+\xi^2}} e^{-\frac{\pi t^2}{a^2}}\right] = \frac{a\sqrt{I_0}}{\sqrt[4]{1+\xi^2}} e^{-\pi\nu^2 a^2}} \tag{C.16}$$

with

$$a^2 = \frac{2\pi T^2}{1+iT^2(\zeta^2+\eta^2)} = \frac{2\pi T_0^2(1+\xi^2)}{1+i\left[\xi+\frac{2\phi_{NL0}}{\sqrt{1+\xi^2}}\right]} \tag{C.17}$$

Now, with this expression, we can calculate the two quantities analog to Z-scan techniques. First: the spectral peak power as a function of $\phi^{(2)}$.

$$P(\nu=0) = \left|\widetilde{U}(z_2,\nu=0)\right|^2 = \frac{2\pi T_0^2\sqrt{1+\xi^2}}{\sqrt{1+\left[\xi+\frac{2\phi_{NL0}}{\sqrt{1+\xi^2}}\right]^2}} P_0 \tag{C.18}$$

If there is only linear effects, i.e. $\phi_{NL0}=0$, then $P(\nu=0,\phi_{NL0}=0)=2\pi T_0^2 P_0$, so the spectral peak power gets independent of the second order dispersion term and proportional to T_0^2. Now, at zero dispersion, $P(\nu=0,\phi^{(2)}=0) = \frac{2\pi T_0^2}{\sqrt{1+4\phi_{NL0}^2}} P_0 \approx 2\pi T_0^2 P_0(1-2\phi_{NL0}^2)$ with the approximation valid for $\phi_{NL0} \ll \frac{1}{2}$, or, in terms of π: $\phi_{NL0} \ll 0.16\pi$. In Fig. C.3 we show the expected shape of the Normalized Spectral Peak Power (NSPP) for the case of pure-Kerr materials exhibiting positive and negative Kerr coefficients. It is important to remark that at $\phi^{(2)}=0$ ps^2 (inset), it is not possible to define the sign of the real susceptibility.

Now to determine the spectral standard deviation (σ) we will make use of the general rules for gaussian distributions, indeed we can express them as: $e^{-\frac{u^2}{2\sigma^2}}$, where the standard deviation is implicit. In our case, we can express the intensity at the waveguide output as $|\widetilde{U}|^2 \propto e^{-\pi\nu^2[a^2+(a^*)^2]}$. Where $a^2+(a^*)^2 = \frac{4\pi T_0^2(1+\xi^2)}{1+\left[\xi+\frac{2\phi_{NL0}}{\sqrt{1+\xi^2}}\right]^2}$.

So the expression for the standard deviation in the frequency domain is:

$$\sigma_\nu^2 = \frac{1}{2\pi\left[a^2+(a^*)^2\right]} \tag{C.19}$$

$$2\sigma_\nu = \frac{1}{\pi\sqrt{2}T_0}\sqrt{\frac{1+\left[\xi+\frac{2\phi_{NL0}}{\sqrt{1+\xi^2}}\right]^2}{1+\xi^2}} \tag{C.20}$$

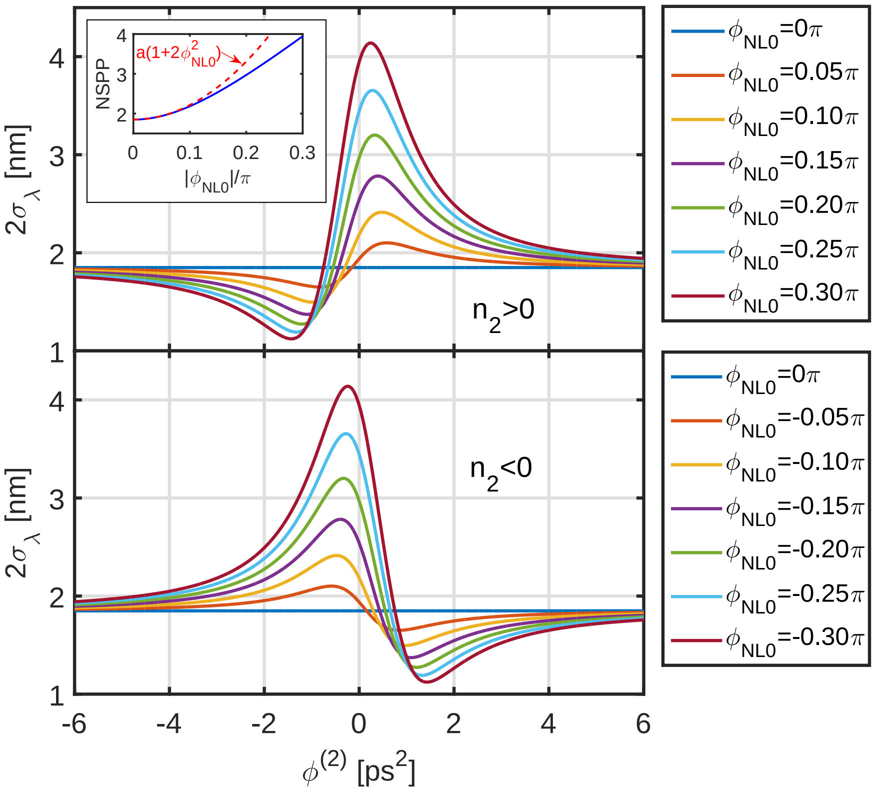

Figure C.2: Total standard deviation as a function of the second order dispersion parameter for different ϕ_{NL0} with $T_0 = 1$ ps and $\lambda = 1570$ nm. Inset: NSPP as a function of ϕ_{NL0} for $\phi^{(2)} = 0$ ps^2, where a=$\frac{\lambda^2}{\sqrt{2}\pi c T_0}$.

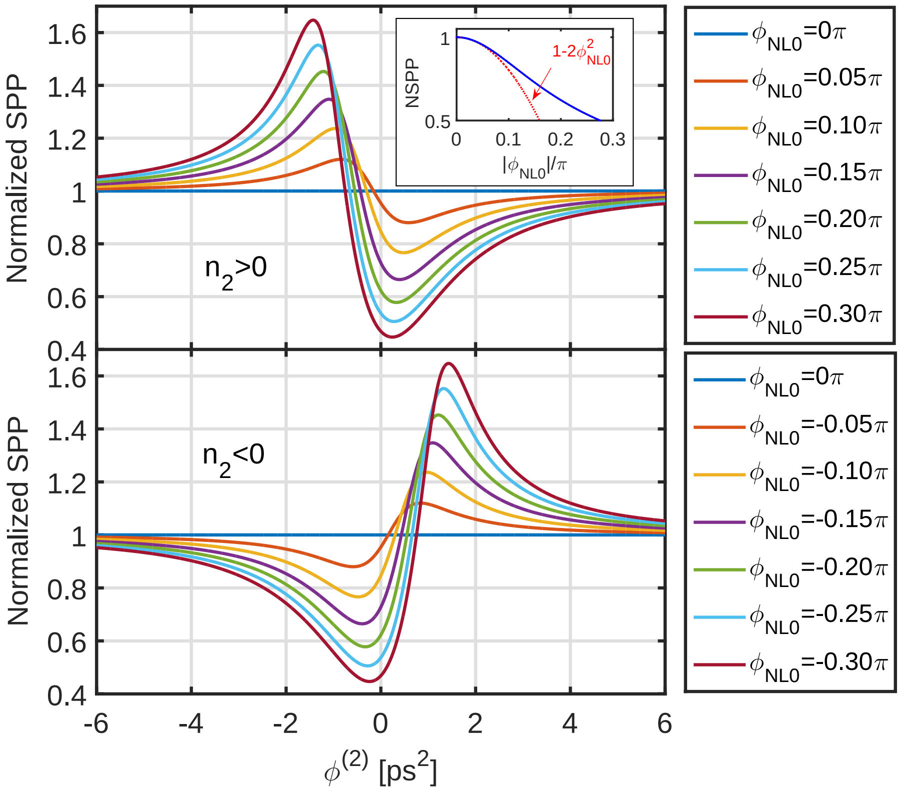

Figure C.3: Normalized Spectral Peak Power (NSPP) as a function of the second order dispersion for different nonlinear phase shifts. Inset: NSPP as a function of ϕ_{NL0} for $\phi^{(2)} = 0$ ps^2.

The change into a wavelength standard deviation is straightforward:

$$\boxed{2\sigma_\lambda = \frac{\lambda^2}{c} 2\sigma_\nu = \frac{\lambda^2}{\pi c\sqrt{2T_0}} \sqrt{\frac{1 + \left[\xi + \frac{2\phi_{NL0}}{\sqrt{1+\xi^2}}\right]^2}{1+\xi^2}}} \tag{C.21}$$

The tendencies of this analytical expression can be studied. For $2\sigma_\lambda(\phi_{NL0} = 0) = \frac{\lambda^2}{\pi c\sqrt{2T_0}}$, so inversely proportional to T_0 and independent of the second order dispersion term as found for the spectral peak power. If $\phi^{(2)} = 0$, then $2\sigma_\lambda = \frac{\lambda^2}{\pi c\sqrt{2T_0}} \sqrt{1 + 4\phi_{NL0}^2}$ which becomes $2\sigma_\lambda \approx \frac{\lambda^2}{\pi c\sqrt{2T_0}}(1 + 2\phi_{NL0}^2)$ if $\phi_{NL0} \ll \frac{1}{2}$ and $2\sigma_\lambda \approx \frac{\lambda^2\sqrt{2}}{\pi c T_0}\phi_{NL0}$ if $\phi_{NL0} \gg \frac{1}{2}$, so quadratic and linear behavior respectively as function of ϕ_{NL0}.

Finally, an evaluation of the curves displayed in Fig. C.2 will allow us to calculate the peak to valley difference $(2\sigma_\lambda)_{p-v}$. From Fig. C.4, the linear tendency is clearer for higher nonlinear phases, but the question about the validity of the paraxial approximation

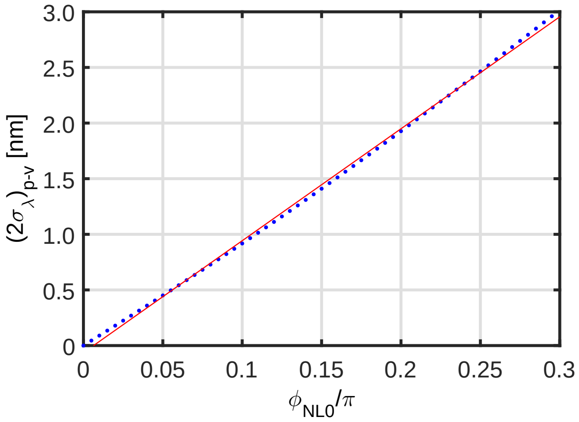

Figure C.4: Peak to valley values for different ϕ_{NL0} with a linear fit in red until $\phi_{NL0} = 0.3\pi$.

range raises. This is the reason why we have also performed more rigorous numerical simulations throughout this manuscript.

D Basic codes

D.1 dispersion.m

For this code, a FWHM routine coded by Ebo Ewusi-Annan from University of Florida was used at the end of the code.

```matlab
% Calculation code to numerically measure the FWHM of an intensity
% autocorrelated spectrum affected by dispersion.
% Samuel F. Serna O. IEF-LCF
% 06/03/2014

clear all
close all
tic,

%% Definition of the variables
N = 1025;                           % Number of steps; Default 1025
lambda0=1580e-9;                    % Central spectrum wavelength; Default 1580e-9 [m]
Window=200e-9;                      % Size of the wavelength window; Default 200 [m]
width=5.72e-9;                       % Size of the transmitted spectrum: 3.7e-9 to 7.3e-9 [m] 5.8e-9 3.5e-9
Nphi2=1001;                           % Number of phi2 points where the FWHM will be measured
phim=4e-24;                       % Maximum phi2, the calculation will be symmetrical, i.e. phim=3e-24=>phi2=[-3e-24:dphi2:3e-24] [s]

c = 3e8;                            % Speed of light in vacuum [m/s]

lambdai=lambda0-Window/2;           % Initial wavelength [m]
lambdaf=lambda0+Window/2;           % Final wavelength [m]
lambdav=linspace(lambdai,lambdaf,N);% Lambda vector

nu0=c/lambda0;                      % Central frequency [1/s]
nuv=fliplr(c./lambdav);             % Frequency vector; Inverse relation so flip the output
Trans = exp(-((lambdav-lambda0)/width*2).^32);  % Supergaussian 32nd order to simulate the spectrum
plot(nuv,Trans)                     % Plot of the square (super gaussian) spectrum
xlabel ('Frequency \nu (s^{-1})'), ylabel ('Intensity [a.u.]')

```

```
dNu=nuv(2)-nuv(1);                  % Frequency differential [1/s]
Nu = nuv(end)-nuv(1) + dNu;         % Inverted normalization parameter [1/s]
t = 1/Nu * (-(N-1)/2 : (N-1)/2);    % Calculation of the Fourier transformed vector - time [s]

FWT=ones(1,Nphi2);                  % Preallocation for speed
FWA=ones(1,Nphi2);
Deltanu=nuv-nu0.*ones(size(nuv));   % Taylor expansion term [1/s]
%% Calculation loop
for i=1:Nphi2
    disp=exp(1i*(-phim+(2*i-1)*phim/Nphi2)*2*pi*pi.*Deltanu.*Deltanu);  % Dispersion term

    Sin = fftshift(width*fft(Trans.*disp)); % Fourier transform of the spectrum times the dispersion phase
    as=Sin.*conj(Sin);              % Intensity of the pulse in temporal domain
    dataT(:,2)=as;                  % Creation of a matrix to use the FWHM function
    dataT(:,1)=t;
    FWT(i)=fwhm(dataT);             % FWHM of the pulse in intensity

    asw=xcorr(as,as);               % Calculation of the Intensity autocorrelation
    tasw=linspace(-2*max(t),2*max(t),2*N-1);% Size is twice the temporal vector
    data(:,2)=asw;                  % Creation of a matrix to use the FWHM function
    data(:,1)=tasw;
    FWA(i)=fwhm(data);              % FWHM of the Intensity autocorrelation
end
%% Plot settings
FWAps=FWA*1e12;                     % Change to ps
phi2=linspace(-phim,phim,Nphi2);    % phi2 vector
phi2ps=phi2*1e24;                   % Change to ps^{2}

figure;
plot(phi2ps,FWAps)
grid on
xlabel ('\phi^{(2)} (ps^{2})'), ylabel ('FWHM autocorrelation [ps]')
toc
```

E Synthèse en français

La photonique sur silicium est arrivée à un niveau de maturité élevé et propose aujourd'hui un large panel de fonctions optiques (filtrage, distribution de lumière, etc) et optoélectroniques (modulation et photodétection rapides) permettant l'intégration de liens optiques complexes (liaisons rapides et multiplexés en longueur d'onde, récepteurs à formats de modulation avancés : DQSK, etc) et une co-intégration sur le même substrat de circuits photoniques avec des circuits CMOS. Simultanément, le silicium, en tant que matériau, présente en lui-même un certain nombre de limitations physiques pour l'optoélectronique dans la bande télécom, en particulier sa structure de bandes indirecte et un niveau d'absorption à deux photons élevé, très gênant pour l'exploitation des effets optiques nonlinéaires d'ordre 3.

Cette thèse est une contribution à l'étude des propriétés optiques non-linéaires d'ordre 3 de structures hybrides sur silicium, mettant l'accent sur l'utilisation de matériaux actifs en rupture (chalcogénures, GeSi) et de structures de guidage ou de résonateurs à exaltation du champ électromagnétique.

1. Mesure des nonlinéarités effectives du 3ème ordre d'un guide optique par une technique D-Scan bi-directionnelle

La technique Z-scan est couramment utilisée pour mesurer les susceptibilités nonlinéaires d'ordre 3 d'un matériau [1]. En revanche, elle ne s'applique pas au cas des milieux guidés. Cette technique a néanmoins été transposée dans le domaine temporel afin de caractériser les indices nonlinéaires de fibres optiques [2, 3]. La technique D-Scan, pour Dispersive Scan, consiste à faire varier le coefficient de dispersion $\varphi^{(2)}$ appliqué aux impulsions et à mesurer l'évolution de leur largeur spectrale en sortie, modifiée par les effets d'automodulation de phase.

Nous présentons à la suite la première caractérisation nonlinéaire complète effectuée grâce à l'utilisation d'une technique D-Scan modifiée dans un nano-guide présentant à la fois un effet Kerr optique et de l'absorption à deux-photons (TPA). Contrairement au cas des fibres optiques, la difficulté réside ici dans l'évaluation de la puissance réellement injectée dans le mode du nano-guide. Dans un premier temps, et indépendamment des pertes d'injection en entrée et en sortie du guide, nous faisons la démonstration de la possible mesure du facteur de mérite non-linéaire $FOM_{TPA} = \gamma/2\pi\gamma_{TPA}$, avec $\gamma = k_0 S^2 n_2/A_{\mathrm{NL}}$ et $\gamma_{TPA} = S^2\beta_{TPA}/A_{\mathrm{NL}}$ les nonlinéarités effectives Kerr et TPA du guide s'exprimant en fonction de n_2 et β_{TPA}, l'indice de réfraction nonlinéaire et le coefficient TPA du matériau, et de l'aire effective nonlinéaire du mode guidé A_{NL}. Ces expressions tiennent également compte du renforcement des nonlinéarités par le rapport entre les indices de groupe du mode guidé et du matériau massif, soit : $S = n_g^{wg}/n_g$. Par une mesure de transmission nonlinéaire bi-directionnelle, les valeurs des coefficients de couplage sur chaque facette du guide ainsi que le paramètre γ_{TPA} sont ensuite évalués expérimentalement. A partir de la mesure de FOM_{TPA}, on accède ainsi au coefficient Kerr γ du guide. Dans le souci de disposer d'une méthode très sensible, nous présentons le premier montage de type top-hat D-scan, qui utilise des impulsions de forme spectrale quasi-rectangulaire, l'équivalent dans le domaine spatial au montage top-hat Z-scan [4, 5].

a. Montage Top-hat D-Scan bi-directionnel

Le banc expérimental, décrit sur la figure 1.1, utilise un laser à fibre dopée Erbium fonctionnant en régime de verrouillage de modes qui délivre des impulsions de 150 fs de durée, avec un taux de répétition F = 50 MHz. Ces impulsions sont envoyées dans un étireur à réseau qui fixe le spectre des impulsions suivant une forme quasi-rectangulaire de largeur 7,3 nm et introduit un coefficient de dispersion $\varphi^{(2)}$ ajustable. Pour $\varphi^{(2)}$= 0, la durée d'autocorrélation des impulsions est égale à T_0 = 2 ps, c'est-à-dire proche de la limite de Fourier. Le faisceau polarisé issu de l'étireur est alors injecté dans une fibre monomode à maintien de polarisation (PM). Grâce un objectif de microscope (×65), le faisceau issu d'une fibre PM est injecté dans un nano-guide de type ridge fabriqué sur SOI (Silicon On Insulator) d'aire effective A_{eff} = 0,1 µm^2 et de longueur L = 5 mm. L'analyse des franges de Fabry-Perot du spectre de transmission linéaire donne accès aux pertes linéiques évaluées à 1 dB/cm et à la mesure de S = 1,41. Deux cubes séparateurs de polarisation (PBS) sont disposés de part et d'autre du montage d'injection afin de contrôler l'état de polarisation du faisceau injecté et transmis, selon la direction TE. Les lames demi-ondes (λ/2) servent à aligner les états de polarisation des cubes PBS avec les directions propres des fibres PM disposées en amont et en aval du montage. L'injection dans le guide peut se faire selon les deux directions opposées (1) et (2) (figure 1.1).

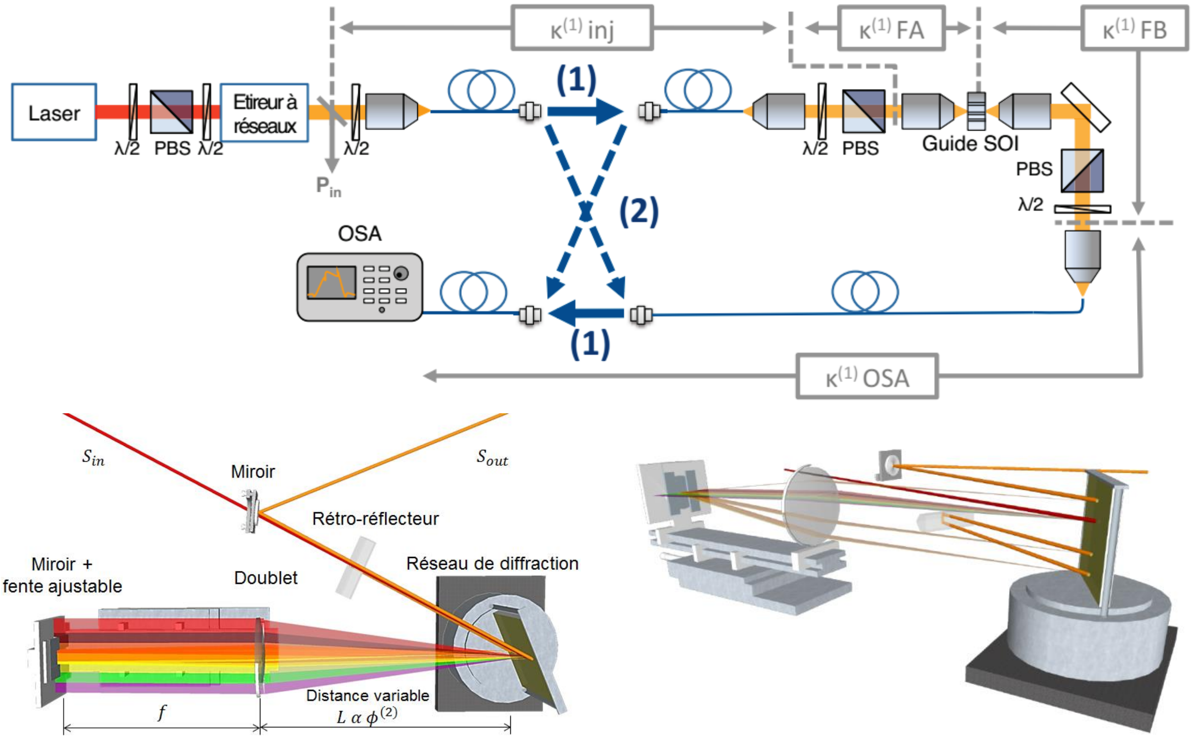

Figure 1.1. Montage top-hat D-scan pour la caractérisation nonlinéaire bi-directionnelle d'un nano-guide.
En bas : Vue en détail de l'étireur à réseaux.

En fixant $\varphi^{(2)}$= 0 et une transmission dans la direction (1), et pour des puissances moyennes incidentes P_{in} variant de 0,5 à 10 mW, les spectres des impulsions transmises sont tracés sur la figure 1.2(a). Ils présentent un élargissement spectral symétrique dû à l'automodulation de phase induite par effet Kerr et qui augmente avec P_{in}. A partir des spectres, la puissance moyenne de sortie P_{out} (1) est calculée et le rapport $P_{\mathrm{in}}/P_{\mathrm{out}}$ (1) est tracé sur la figure 1.2(b) en fonction de P_{in}. En présence de TPA, l'évolution attendue est donnée par $P_{\mathrm{in}}/P_{\mathrm{out}} = \mathrm{a} + bP_{\mathrm{in}}$, avec $\mathrm{a} = 1/(\kappa_{\mathrm{in}}\kappa_{\mathrm{out}}\exp(-\alpha\mathrm{L})$, $b = \gamma_{TPA}T_0FL_{\mathrm{eff}}/(\kappa_{\mathrm{out}}\exp(-\alpha L))$. Les coefficients a et b dépendent des efficacités de couplage en entrée κ_{in} et en sortie κ_{out} du guide, de ses pertes linéiques α et de sa longueur effective L_{eff}. Les valeurs a$^{(1)}$ et $b^{(1)}$ indiquées sur la figure 1.2(b) pour la direction d'injection (1) sont déduites de l'ajustement linéaire des points expérimentaux.

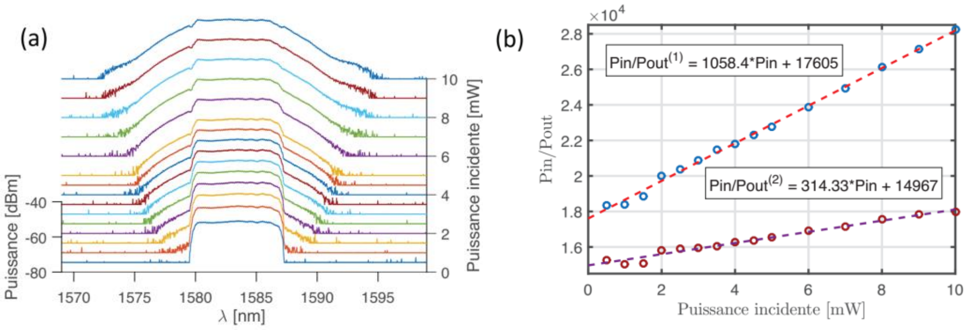

Figure 1.2. (a) Spectres des impulsions transmises pour $\varphi^{(2)} = 0$ ps^2 et des puissances incidentes variant de 0,5 à 10 mW. (b) Courbes P_{in}/P_{out} en fonction de Pin mesurées suivant les deux sens d'injection (1) et (2).

b. Mesure du FOM_{TPA} d'un nano-guide indépendamment des pertes d'injection

La mesure des spectres en sortie est alors répétée avec des impulsions dont la dispersion $\varphi^{(2)}$ varie de -3 à +3 ps^2. Pour différentes puissances incidentes P_{in}, les évolutions de $P_{\text{out}}^{(1)}$ et de la largeur spectrale r.m.s 2σ des impulsions transmises sont représentées sur la figure 1.3(a) en fonction de $\varphi^{(2)}$. Les courbes 2σ présentent une allure dispersive identique aux courbes Z-scan. En accord avec le signe positif de n_2 pour le silicium, l'élargissement spectral maximal est atteint autour d'une valeur positive de $\varphi^{(2)}$.

Afin d'analyser nos résultats, nous simulons la propagation nonlinéaire de nos impulsions et suivant les approches pratiquées en Z-scan, on trace sur la figure 1.3(b) (traits pointillés) l'évolution calculée de l'écart $(2\sigma)_{P-V}$ entre le maximum et le minimum de la courbe 2σ en fonction du déphasage nonlinéaire φ_{NL} introduit par le guide. En présence de TPA, on montre que $\varphi_{NL} = 2\pi FOM_{TPA}\ln\left(1 + \beta_{TPA} I_0 L_{eff}\right)$ avec I_0 l'intensité injectée dans le guide. Sachant que $\beta_{TPA} I_0 L_{eff} = P_{\text{in}} b^{(1)}/\text{a}^{(1)}$, l'écart $(2\sigma)_{P-V}$ mesuré expérimentalement en fonction de $2\pi\ln\left(1 + P_{\text{in}} b^{(1)}/\text{a}^{(1)}\right)$ est alors ajouté sur le graphe de la figure 1.3(b) (points). Ainsi, pour chaque valeur de $(2\sigma)_{P-V}$, le paramètre expérimental $2\pi\ln\left(1 + P_{\text{in}} b^{(1)}/\text{a}^{(1)}\right)$ peut être relié à une valeur φ_{NL} comme le montre la courbe de la figure 1.3(c). Les points s'alignent remarquablement sur une droite dont la pente donne directement la valeur du FOM_{TPA} mesuré égal à 0,5 en accord avec les données de la littérature sur le silicium.

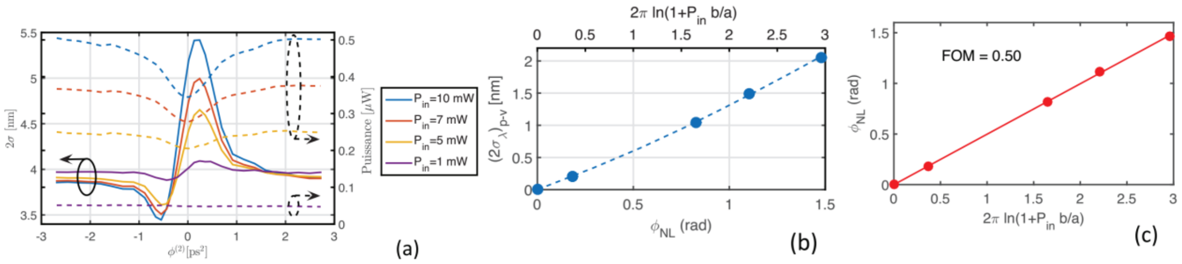

Figure 1.3. (a) Pour différentes puissances incidentes, variation de la largeur spectrale r.m.s. 2σ et de la puissance des impulsions transmises en fonction de la dispersion $\varphi^{(2)}$. (b) Ecart calculé (reps. mesuré) entre les valeurs Min et Max de la largeur 2σ en fonction du déphasage nonlinéaire φ_{NL} (reps. du paramètre mesuré $2\pi\ln\left(1 + P_{in} b^{(1)}/\text{a}^{(1)}\right)$). (c) Déphasage nonlinéaire en fonction du paramètre mesuré $2\pi\ln\left(1 + P_{in} b^{(1)}/\text{a}^{(1)}\right)$.

c. Mesure des nonlinéarités effectives Kerr et TPA d'un guide SOI

Notre objectif est de mesurer les nonlinéarités effectives du guide. Il est alors nécessaire de déterminer les pertes d'injection au niveau de chacune des deux facettes du guide, repérées comme A et B. Les paramètres $\mathrm{a}^{(1)}$ et $b^{(1)}$ mesurés dans la direction d'injection (1) sont reliés aux pertes globales en entrée et en sortie $\kappa_{in}^{(1)} = \kappa_{inj}^{(1)}\,\kappa_{FA}$ et $\kappa_{out}^{(1)} = \kappa_{FB}\kappa_{OSA}^{(1)}$, où κ_{FA} et κ_{FB} désignent les pertes de couplage au niveau des facettes A et B. Les pertes $\kappa_{inj}^{(1)}$ et $\kappa_{OSA}^{(1)}$, identifiées sur la figure 1.1, sont mesurées sur le banc optique. Le sens d'injection dans le guide est ensuite inversé et les coefficients $\kappa_{inj}^{(2)}$ et $\kappa_{OSA}^{(2)}$ sont mesurés. La courbe $P_{in}/P_{out}^{(2)}$ en fonction de P_{in} est tracée sur la figure 1.2(b) et les coefficients $\mathrm{a}^{(2)}$ et $b^{(2)}$ sont évalués par ajustement linéaire.

En supposant les pertes sur les facettes identiques pour les deux directions, leurs valeurs se déduisent des relations $(\kappa_{FA})^2 = \mathrm{b}^{(1)}/\left(\mathrm{b}^{(2)}\mathrm{a}^{(1)}\kappa_{\mathrm{in}}^{(1)}\kappa_{\mathrm{OSA}}^{(2)}\exp(-\alpha\mathrm{L})\right)$ et $(\kappa_{FB})^2 = \mathrm{b}^{(2)}/\left(\mathrm{b}^{(1)}\mathrm{a}^{(2)}\kappa_{\mathrm{in}}^{(2)}\kappa_{\mathrm{OSA}}^{(1)}\exp(-\alpha\mathrm{L})\right)$, et valent respectivement 6,4 % et 2,5 %. Connaissant les efficacités de couplage, nous en déduisons les valeurs des nonlinéarités effectives définies par $\gamma_{TPA} = b^{(1)}T_0F/\left(\mathrm{a}^{(1)}\kappa_{\mathrm{in}}^{(1)}\kappa_{FA}L_{\mathrm{eff}}\right) = 0{,}22\ \mathrm{W}^{-1}\mathrm{cm}^{-1}$ et $\gamma = 2\pi FOM_{TPA}\gamma_{TPA} = 0{,}69\ \mathrm{W}^{-1}\mathrm{cm}^{-1}$. En simulant la distribution de champ dans le guide, A_{NL} est calculée et les coefficients nonlinéaires du matériau déduits de nos mesures, $n_2 = 2{,}57 \times 10^{-18}\ \mathrm{m}^2/\mathrm{W}$ et $\beta_{TPA} = 3{,}26 \times 10^{-12}\ \mathrm{m/W}$, sont en parfait accord avec les données de la littérature.

2. Renforcement des interactions nonlinéaires par excitation cohérente d'une micro-cavité

La réalisation de micro-cavités à cristal photonique permet de fortement augmenter les effets de localisation du champ et donc les interactions entre la lumière et le milieu intra-cavité, comme les interactions nonlinéaires. En revanche, le renforcement des nonlinéarités, qui induit des variations sur les propriétés du milieu, modifie les conditions de résonance de la micro-cavité au cours de son excitation et conduit à une diminution des effets de localisation. A la suite, nous traitons l'effet d'une nonlinéarité réfractive qui induit un décalage en fréquence de la résonance au cours de l'excitation et conduit à un désaccord entre les composantes spectrales de l'impulsion et celles de la résonance. Le bénéfice du renforcement du champ dans la cavité n'est plus alors maintenu, même si la durée de l'excitation excède la durée de vie des photons dans la cavité.

Afin de préserver les effets de localisation, nous avons étudié expérimentalement le comportement nonlinéaire d'une micro-cavité de type Fabry-Pérot excitée par des impulsions á dérive de fréquence linéaire. La micro-cavité, fabriquée en silicium, est principalement soumise à la variation d'indice induite par l'augmentation de la densité de porteurs générés par absorption á deux photons (TPA), et qui produit un décalage vers le bleu de la résonance de la cavité. En appliquant une phase spectrale contrôlée à l'impulsion, on s'assure qu'à chaque instant une de ses composantes spectrales coïncide avec la fréquence de résonance de la cavité qui se décale vers le bleu. Bien que cette technique d'excitation cohérente soit couramment utilisée pour le contrôle des interactions lumière-matière dans des systèmes atomiques ou moléculaires [6], sa transposition aux résonateurs optiques n'avait fait l'objet jusqu'à présent que de travaux théoriques [7,8,9]. Nos résultats représentent la première démonstration du renforcement de l'interaction nonlinéaire dans une micro-cavité excitée de manière cohérente [10].

Nous avons conçu et fabriqué une microcavité Fabry-Pérot constituée de deux miroirs de Bragg gravés sur un guide ridge en Silicium sur Isolant (SOI) et dont le volume modal vaut $0{,}8(\lambda/n)^3$. Une photo de la cavité prise au microscope électronique à balayage (MEB) est présentée sur la figure 2.1. La mesure du spectre de transmission linéaire de la cavité montre un pic de transmission centrée autour de 1578,8 nm, avec une largeur de raie égale à 0,22 nm, coïncidant avec une résonance dont le facteur de qualité vaut Q = 7275, équivalent á une durée de vie des photons de 6 ps.

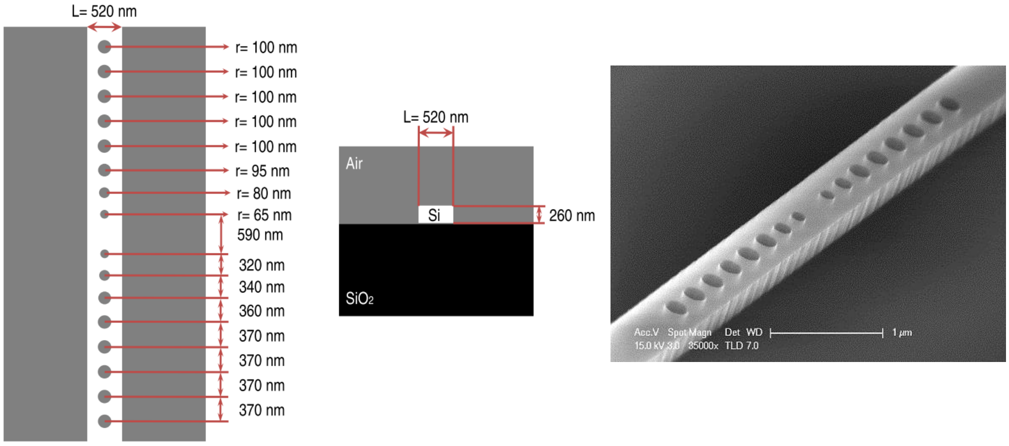

Figure 2.1. Dimensions pour la microcavité Fabry-Pérot en SOI plus une photo MEB de la structure fabriquée.

Au cours de l'excitation en régime nonlinéaire, la génération des porteurs libres par TPA modifie de manière dynamique l'indice de réfraction du milieu. Le décalage vers le bleu de la résonance de la cavité est traité, en première approximation, comme une dérive de fréquence linéaire dans le temps [9]. Nous allons comparer la transmission de la cavité excitée de manière non-cohérente, avec des impulsions dont les composantes spectrales sont en phase ($\varphi^{(2)}= 0$), et de manière cohérente, avec des impulsions de même énergie mais à dérive de fréquence linéaire ($\varphi^{(2)} \neq 0$).

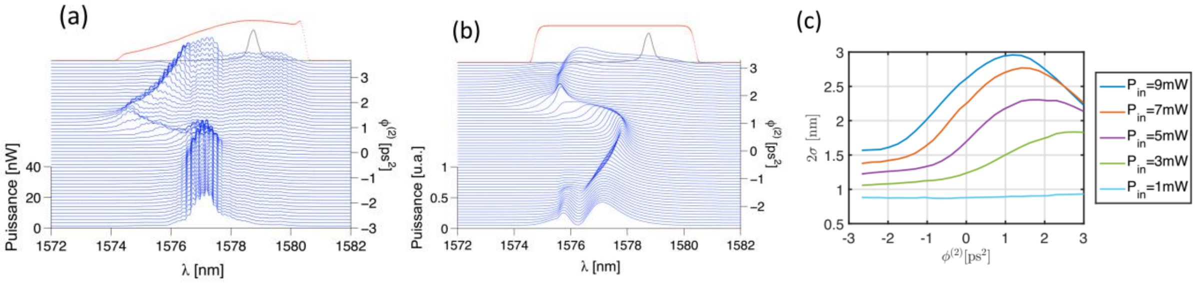

Figure 2.2. Évolution des spectres de transmission pour une énergie incidente de 3 pJ, mesurés (a) et simulés (b) pour des dispersions $\varphi^{(2)}$ variant de -3 à +3 ps^2. Spectres des impulsions incidentes (en rouge) et de la résonance linéaire de la cavité (en gris). (c) Pour des impulsions de largeur spectrale 3 nm, largeurs spectrales r.m.s. des spectres transmis mesures en fonction de la dispersion $\varphi^{(2)}$ pour différentes puissances incidentes.

La largeur spectrale des impulsions est fixée à 7,3 nm, qui excède celle de la résonance linéaire de la cavité (spectres indiqués sur la figure 2.2). Pour $\varphi^{(2)}= 0$, la durée d'autocorrélation des impulsions est mesurée égale à T_0 = 2 ps, proche de la limite de Fourier. Pour une énergie injectée dans le guide de 3 pJ, l'évolution des spectres transmis á travers la cavité pour des dispersions $\varphi^{(2)}$ variant de -3 à +3 ps^2 est tracée sur la figure 2.2(a). L'ensemble des spectres présente un décalage de la résonance de cavité vers le bleu, comme attendu. Pour des dispersions négatives, où les composantes bleues de l'impulsion sont en avance sur les composantes rouges, le décalage de la résonance ne varie pratiquement pas. En revanche, il s'accentue très nettement pour $\varphi^{(2)}$ compris entre 0 à +1,2 ps^2 et diminue a nouveau pour $\varphi^{(2)} > 1.2$ ps^2. Les valeurs positives de $\varphi^{(2)}$ coïncident avec la situation schématisée sur la figure 1 où la cavité est excitée en premier lieu avec les composantes rouges de l'impulsion. Alors que la résonance se décale vers le bleu, la dérive de fréquence appliquée sur l'impulsion maintient un couplage efficace et accentue le décalage. Le bénéfice de l'excitation cohérente est démontré en comparant les spectres obtenus pour deux impulsions de durée identique, supérieure à la durée de vie des photons dans la cavité, mais dont les dispersions diffèrent en signe. En particulier, les spectres obtenus pour les dispersions +1,2 et -1,2 ps^2, qui correspondent à une durée d'impulsion de 5,7 ps, montrent que le décalage vers le bleu de la résonance est nettement plus important pour $\varphi^{(2)} = +1.2\ \text{ps}^2$. Par ailleurs, on note que la largeur spectrale transmise coïncide pratiquement avec celle de l'impulsion incidente. A partir du décalage en fréquence, on montre que la densité de porteurs générée entre ces deux excitations est augmentée d'un facteur 2,5 et démontre le renforcement de l'interaction nonlinéaire entre une impulsion mise en forme et la micro-cavité.

Nous avons confronté nos résultats expérimentaux à des simulations numériques qui s'appuient sur la théorie des modes couplés. Les spectres simulés sont reportés sur la figure 2.2(b) et sont en très bon accord avec les spectres expérimentaux.

Enfin, nous avons conduit une étude plus systématique sur la manière de contrôler la transmission nonlinéaire de la cavité en fonction de l'énergie des impulsions et de leur dispersion $\varphi^{(2)}$. Les évolutions, pour différentes puissances incidentes, de la largeur spectrale r.m.s. des spectres transmis en fonction de la dispersion $\varphi^{(2)}$ sont tracées sur la figure 2.2(c). Ces expériences ont été conduites avec des impulsions de largeur spectrale égale à 3 nm. Ces courbes démontrent qu'il existe, pour chaque énergie d'impulsion, une valeur de $\varphi^{(2)}$ qui optimise la largeur spectrale transmise. Plus l'énergie des impulsions incidentes augmente et plus le décalage en fréquence est rapide, nécessitant d'appliquer sur les impulsions une plus forte dérive de fréquence (correspondant à une faible valeur de dispersion).

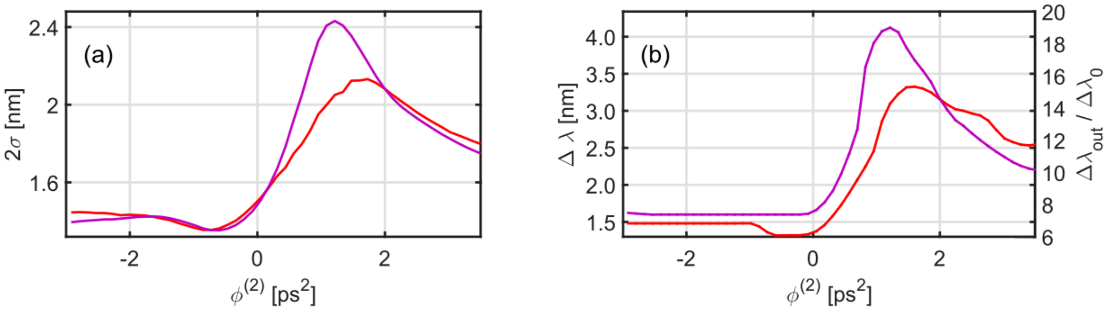

Figure 2.3. (a) mesure de l'écart type pour les coefficients de chirp avec deux excitations. (b) Changement de longueur d'onde par rapport à la résonance de la cavité linéaire. Dans l'axe de droite: le nombre de fois qu'une bande passante équivalente à la valeur FWHM de la cavité froide est transmis.

L'excitation cohérente d'un résonateur optique en régime nonlinéaire est démontrée expérimentalement pour la première fois. L'application d'une dérive de fréquence contrôlée sur des impulsions permet de renforcer leur interaction nonlinéaire avec une micro-cavité en silicium. À énergie constante, l'excitation cohérente augmente d'un facteur 2,5 la densité de porteurs générés dans la cavité, ce qui induit une variation d'indice $\Delta n/n = \Delta\lambda/\lambda = 2{,}5 \times 10^{-3}$, directement reliée à celle du décalage en longueur d'onde $\Delta\lambda$ de la résonance. Ce résultat illustre également la capacité à manipuler le spectre de transmission d'une cavité par le contrôle de son excitation, puisque les impulsions utilisées dans cette expérience ont une largeur spectrale 20 fois plus grande que celle de la résonance linéaire de la cavité (Figure 2.3).

3. Ingénierie et fabrication des cristaux photoniques à fente: vers une plateforme nonlinéaire hybride

Dans une dernière partie, notre travail s'inscrit dans une perspective d'intégration hybride de matériaux actifs sur silicium, en particulier de polymères nonlinéaires, permettant de conserver la maturité des processus technologiques de la filière silicium et les caractéristiques de guidage de la lumière qui en découlent et, simultanément, d'étendre l'amplitude des effets physiques par le biais des matériaux rapportés. Afin de maximiser l'amplitude des interactions matériaux/champ électromagnétique, notre approche s’est focalisée sur des guides à cœur creux et à modes lents (guides cristaux photoniques à fente) [11].

Nous présentons tout d’abord les méthodes d’ingénierie de dispersion étudiées en simulation, notamment celle basée sur une ingénierie des trous à proximité de la fente, et exposons les résultats obtenus par la méthode des ondes planes 3D. On veut obtenir une dispersion de la vitesse de groupe (GVD) nulle sur plusieurs nanomètres de bande passante optique. La figure 3.1 montre la structure de base utilisée pour simuler les cristaux photoniques à fabriquer. Sont également présentes les courbes d’indice de groupe attendus et la distribution de champ dans les trois dimensions pour $k = 0.46 * 2\pi/a$ (régime lent).

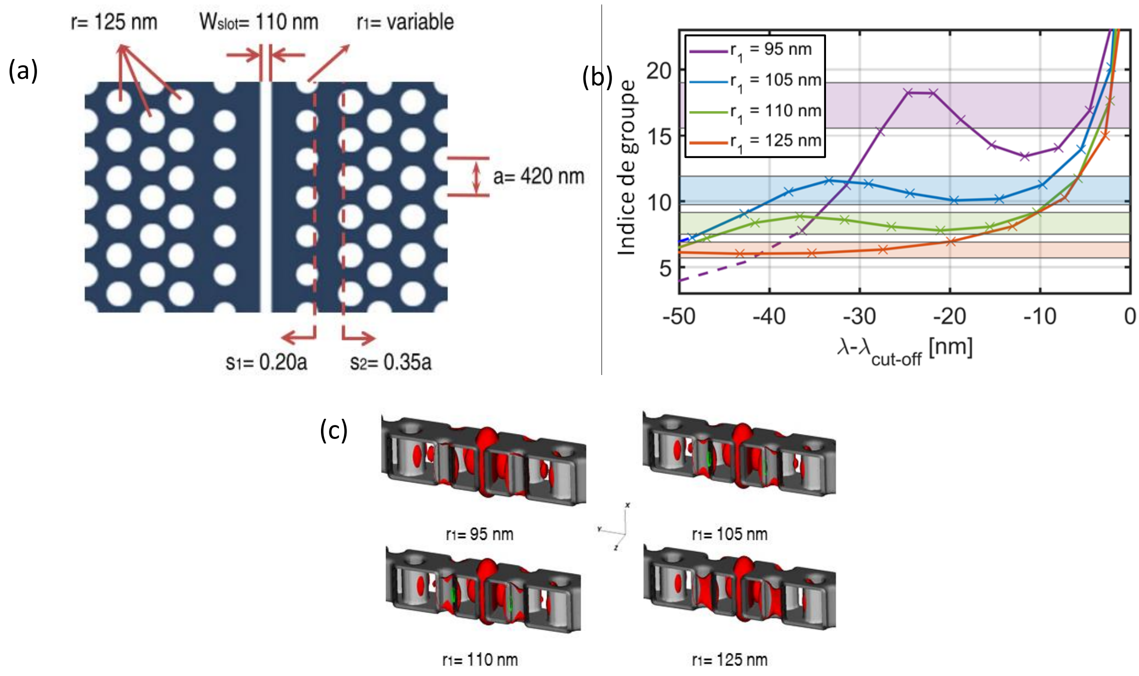

Figure 3.1. (a) Schéma illustrant la géométrie des cristaux photoniques simulés. (b) Extraction des courbes des indices de groupe pour chaque géométrie. (c) profils du mode guidés $(|\vec{E}|^2)$ pour $k = 0.46 * 2\pi/a$ (régime lent) [12].

Les améliorations apportées à la conception des masques et à la fabrication ont permis d’accroître notablement la transmission des guides. Dans un premier temps, nous présentons les résultats de caractérisation linéaire obtenus sur une géométrie particulière présenté en Figure 3.2. On remarque les différents régimes de propagation déjà largement étudiés dans la littérature pour les cristaux photoniques sans fente (W1). On note notamment le fait que la transmission au-dessus du cône de lumière (bleu) chute, la présence de la région de propagation balistique , et enfin celle située près de la bande interdite où de multiples interférences apparaissent (régime diffusif). Nous avons ensuite effectué la caractérisation en transmission des échantillons fabriqués après leur remplissage par des liquides d’indice dans la gamme n_{liq}=1,40 à n_{liq}=1,50, par injection d’une source laser accordable au moyen d’une fibre lentillée puis collection du faisceau de sortie et analyse de son spectre. Dans un deuxième temps, des mesures d’ondes lentes ont été effectuées de manière complémentaires basées une méthode de temps de vol exploitant un interféromètre Mach-Zehnder externe, puis également par analyse de franges d’interférences obtenues à l’aide d’interféromètres intégrés. Nous avons étudié l’impact des variations des trous et du liquide de remplissage sur la dispersion des guides à modes lents. En Figure 3.3, nous montrons une photo MEB d’un cristal photonique fabriqué avec les mesures de temps du vol (b)-(d) liées, puis issues des MZI intégrés (c)-(e) pour, respectivement, un premier rayon de trou de r_1=95 nm et r_1=110 nm.

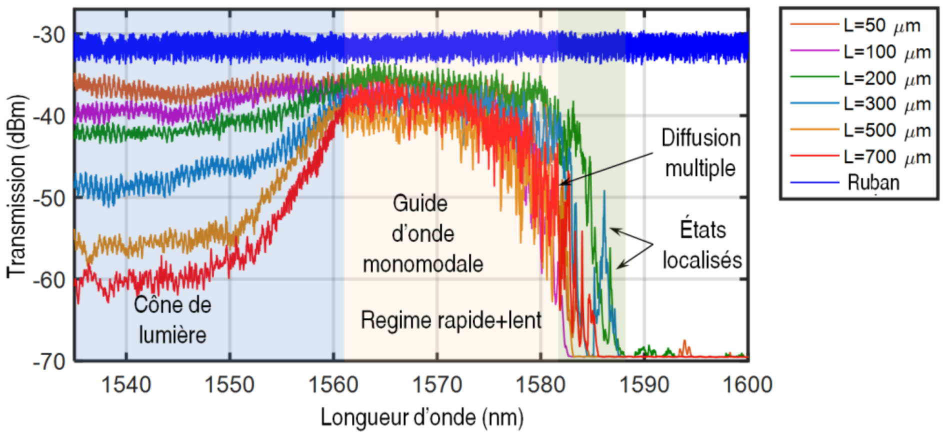

Figure 3.2. Différents régimes de propagation caractéristique de guides d'ondes à cristal photonique.

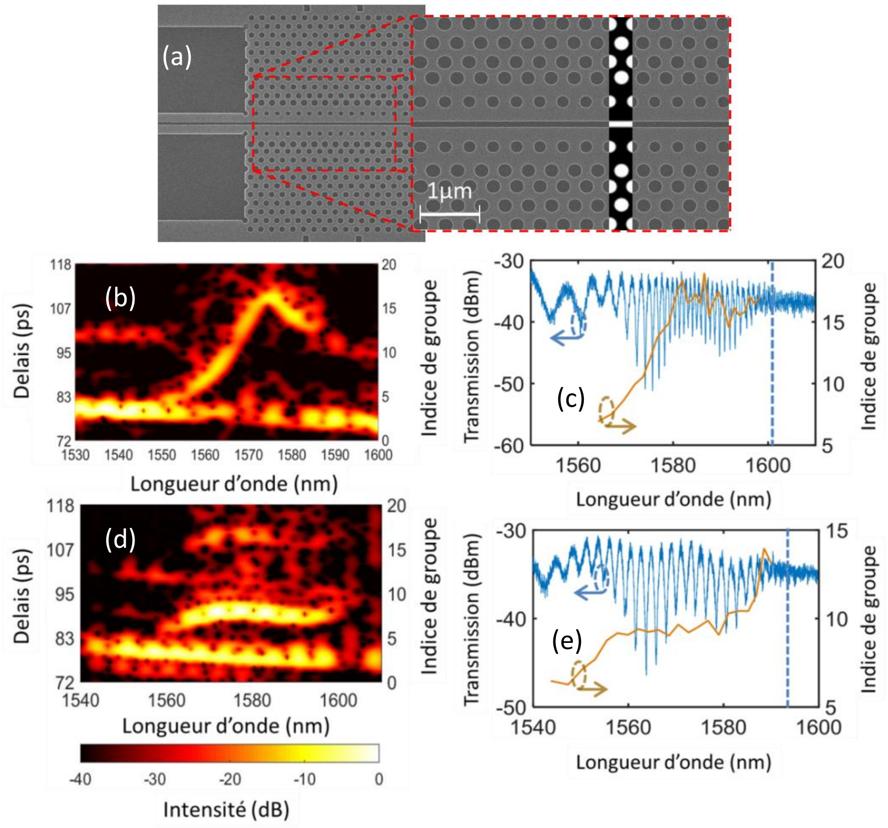

Figure 3.3. (a) Photo MEB du cristal photonique à fente à ingénierie de dispersion. Détail de la période exploitée lors des simulations PWE (MPB). (b) Mesure de temps de vol du cristal à fente de 700 μm de longueur pour r_1=95 nm. (c) Mesure de transmission d'un interféromètre intégré présentant un bras de cristal à fente de 200 μm de longueur pour r_1=95 nm. (d) et (f) : conditions identiques à (b) et (c) pour r_1=110 nm [13].

Table 3.1. Paramètres extraits en fonction du matériau de remplissage, pour différents indices de réfraction et diverses géométries**.**

	r_1 = 95 nm	**r_1 = 105 nm**	**r_1 = 110 nm**	**Moyenne**
Coupure [nm/UIR]	235 ± 12	262 ± 13	257 ± 13	251 ± 21
1^{st} ZGVD [nm/IUR]	202 ± 10	206 ± 10	216 ± 11	208 ± 12
2^{nd} ZGVD [nm/UIR]	218 ± 11	212 ± 11	235 ± 12	222 ± 15
Max n_g/UIR	-29 ± 1	-16 ± 1	-22 ± 1	–
Max β_2 [ps^2/mm/UIR]	-15.4 ± 0.8	-3.3 ± 0.2	-2.0 ± 0.1	–
NDBP pour n_{Rempl} = [1.40 1.45 1.50]	[0.14 0.14 0.19] ± 16%	[0.17 0.16 0.15] ± 7%	[0.20 0.15 0.15] ± 20%	–

La table 3.1 présente finalement un bilan des mesures effectuées. Les variations les plus importantes des paramètres y sont examinées afin d'estimer la performance des structures photoniques à lumière lente La sensibilité des bandes interdites en fonction de l'indice de remplissage en nanomètres par Unités d'Indice de Réfraction (nm/UIR) peut y être observée et l'on observe un décalage moyen de 250 nm/indice de réfraction. Ceci démontre l'intérêt de ces structures pour des applications en régime de capteur d'indice.

Conclusion

Les nonlinéarités effectives Kerr et absorption à deux-photons (TPA), ainsi que les pertes par couplage, d'un nano-guide ont été mesurées pour la première fois par une technique D-scan (transposée du Z-scan dans le domaine temporel), bi-directionnelle et utilisant des impulsions de forme spectrale quasi-rectangulaire pour une sensibilité accrue.

Le renforcement des interactions nonlinéaires dans une micro-cavité en silicium grâce à une excitation cohérente est démontré pour la première fois. En contrôlant la dérive de fréquence sur les impulsions, nous assurons à chaque instant que la fréquence d'excitation coïncide avec la fréquence de résonance de la cavité qui se décale vers le bleu au cours du temps sous l'effet des porteurs générés par absorption à deux photons.

Les cristaux photoniques à fente offrent des perspectives intéressantes pour l'optique non linéaire en raison de la possibilité de confiner très fortement le champ électrique dans le cœur creux du guide et de le remplir par des matériaux à très fortes nonlinéarités optiques. Dans ce contexte, cette thèse présente aussi la réalisation de structures tout-diélectriques, à cœur creux (remplissables), sur substrat sur silicium sur isolant présentant une compensation de la dispersion dans une plage de longueur d'onde d'environ 20 nm dans le spectre des télécoms (λ~1.55µm). Cette étape prépare l'intégration de matériaux actifs non-linéaires sur SOI pour la réalisation de fonctions tout-optiques sur puce à haut débit.

Références

[1] M. Sheik-bahae, A. A. Said, and E. W. V. Stryland, “High-sensitivity, single-beam *n*2 measurements,” *Opt. Lett.*, vol. 14, no. 17, pp. 955–957, 1989.

[2] F. Louradour, E. Lopez-Lago, V. Couderc, V. Messager, and A. Barthelemy, “Dispersive-scan measurement of the fast component of the third-order nonlinearity of bulk materials and waveguides,” *Opt. Lett.*, vol. 24, no. 19, pp. 1361–1363, 1999.

[3] Fonseca, E. J.S., Gouveia, E. A., and Hickmann, J. M., “Time analogue of the z-scan technique suitable to waveguides,” *Eur. Phys. J. D*, vol. 17, no. 1, pp. 75–78, 2001.

[4] W. Zhao and P. Palffy-Muhoray, “Z-scan technique using top-hat beams.” *Appl. Phys. Lett.*, vol. 63, no. 12, p. 1613, 1993.

[5] S. Cherukulappurath, G. Boudebs, and A. Monteil, “4f coherent imager system and its application to nonlinear optical measurements,” *J. Opt. Soc. Am. B*, vol. 21, no. 2, pp. 273–279, 2004.

[6] A. Weiner, “Femtosecond pulse shaping using spatial light modulators,” *Rev. Sci. Instrum.*, vol. 71, p. 1929, 2000.

[7] S. Sandhu, M. L. Povinelli, and S. Fan, “Enhancing optical switching with coherent control,” *Appl. Phys. Lett.*, vol. 96, no. 23, p. 231108, 2010.

[8] P. Trøst Kristensen, M. Heuck, and J. Mørk, “Optimal switching using coherent control,” *Appl. Phys. Lett.*, vol. 102, no. 4, p. 041107, 2013.

[9] J. Oden, S. Trebaol, P. Delaye, and N. Dubreuil, “Coherent excitation of a nonlinear microcavity,” *J. Eur. Opt. Soc.-Rapid*, vol. 8, p. 13046, 2013.

[10] S. Serna, J. Oden, M. Hanna, C. Caer, X. L. Roux, C. Sauvan, P. Delaye, E. Cassan, and N. Dubreuil, “Enhanced nonlinear interaction in a microcavity under coherent excitation,” *Opt. Express*, vol. 23, no. 23, pp. 29 964–29 977, Nov 2015.

[11] J. Leuthold, C. Koos, and W. Freude, “Nonlinear silicon photonics”. *Nat. Photonics* vol. 4, pp. 535–544, 2010.

[12] S. Serna, P. Colman, W. Zhang, X. Le Roux, C. Caer, L. Vivien, and E. Cassan, ”Experimental GVD engineering in slow light slot photonic crystal waveguides”. *Scientific reports*, vol. 6, pp. 26956, 2016.

[13] S. Serna-Otalvaro, W. Zhang, P. Colman, X. Le roux, J.-R. Coudevylle, L. Vivien, E. Cassan: Experimental investigation of top cladding on properties of silicon slotted photonic crystal waveguides. *IEEE Journal of Selected Topics in Quantum Electronics*, 2016. (in press). DOI:10.1109/JSTQE.2016.2612198.

F Publications

- **Samuel Serna**, Weiwei Zhang, Pierre Colman, Xavier Le Roux, Jean-Rene Coudevylle, Laurent Vivien and Eric Cassan. "Experimental investigation of top cladding on properties of silicon slotted photonic crystal waveguides". *IEEE Journal of Selected Topics in Quantum Electronics*, 22(6)(2016). DOI:10.1109/JSTQE.2016.2612198

- Junfei Xia, **Samuel Serna**, Weiwei Zhang, Laurent Vivien and Eric Cassan. "Hybrid silicon slotted photonic crystal waveguides: how does third order nonlinear performance scale with slow light?". *Photonics Research*, 4(6)(2016).

- **Samuel Serna**, Pierre Colman, Weiwei Zhang, Xavier Le Roux, Charles Caer, Laurent Vivien and Eric Cassan. "Experimental GVD engineering in slow light slot photonic crystal waveguides". *Scientific Reports*, 6(2016). DOI:10.1038/srep26956

- Elena Duran Valdeiglesias, Weiwei Zhang, Adrien Noury, Carlos Alonso Ramos, Thi-Hong Cam Hoang, **Samuel Serna**, Xavier Le Roux, Eric Cassan, Nicolas Izard, Francesco Sarti, Ughetta Torrini, Francesco Biccari, Anna Vinattieri, Matteo Balestrieri, Al-Saleh Keita, Hongliu Yang, Viktor Bezugly, Gianaurelio Cuniberti, Arianna Filoramo, Massimo Gurioli and Laurent Vivien. "Integration of Carbon Nanotubes in Silicon Strip and Slot Waveguide Microring Resonators". *IEEE Transactions on Nanotechnology*, 15(4)(2016). DOI:10.1109/TNANO.2016.2556225

- Weiwei Zhang, **Samuel Serna**, Xavier Le Roux, Laurent Vivien and Eric Cassan. "Highly sensitive refractive index sensing by fast detuning the critical coupling condition of slot waveguide ring resonators". *Optics Letters*, 41(3)(2016). DOI:10.1364/OL.41.000532

- Weiwei Zhang, **Samuel Serna**, Xavier Le Roux, Carlos Alonso-Ramos, Laurent Vivien and Eric Cassan. "Analysis of silicon-on-insulator slot waveguide ring resonators targeting high Q factors". *Optics Letters*, 40(23)(2015). DOI:10.1364/OL.40.005566

- **Samuel Serna**, Jérèmy Oden, Marc Hanna, Charles Caer, Xavier Le Roux, Christophe Sauvan, Philippe Delaye, Eric Cassan and Nicolas Dubreuil. "Enhanced nonlinear interaction in a microcavity under coherent excitation". *Optics Express*, 23(23)(2015). DOI:10.1364/OE.23.029964

- Thi-Hong Hoang, Weiwei Zhang, **Samuel F. Serna-Otalvaro**, Charles Caer, Xavier Le Roux, Laurent Vivien and Eric Cassan. "SOI Slotted Photonic Crystal Cavities Spanning From 1.3 to With Factors Above 800 000". *IEEE Photonics Technology Letters*, 27(20)(2015). DOI:10.1109/LPT.2015.2454335
- Weiwei Zhang, **Samuel Serna**, Nicolas Dubreuil and Eric Cassan. "Nonlinear optimization of slot Si waveguides: TPA minimization with FOMTPA up to 4.25". *Optics Letters* , 40(7)(2015). DOI:10.1364/OL.40.001212
- Charles Caer, **Samuel F. Serna-Otalvaro**, Weiwei Zhang, Xavier Le Roux and Eric Cassan. "Liquid sensor based on high-Q slot photonic crystal cavity in silicon-on-insulator configuration". *Optics Letters*, 39(20)(2014). DOI:10.1364/OL.39.005792
- **Samuel Serna**, Weiwei Zhang, Xavier Leroux, Dingshan Gao, Daming Zhang, Laurent Vivien and Eric Cassan. "Potential for large optical gain improvement of erbium-doped slot waveguide amplifiers in silicon photonics". *Journal of the Optical Society of America B*, 31(9)(2014). DOI:10.1364/JOSAB.31.002021
- Charles Caer, Xavier Le Roux, **Samuel Serna**, Weiwei Zhang, Laurent Vivien and Eric Cassan. "Large group-index bandwidth product empty core slow light photonic crystal waveguides for hybrid silicon photonics". *Frontiers of Optoelectronics*, 7(3):376-384(2014). DOI:10.1007/s12200-013-0384-0

Book Chapter

- D. Christodoulides, **S. Serna-Otalvaro**, and S. Wittek. Chapter: "Symmetries in optics". Book: *Frontiers in Modern Optics*, 190(123) (2016). IOS, Amsterdam; SIF, Bologna. DOI:10.3254/978-1-61499-647-7-123

List of Figures

List of Tables

Bibliography

[1] EW Van Stryland, M Sheik-Bahae, AA Said, and DJ Hagan. Characterization of nonlinear optical absorption and refraction. *Progress in crystal growth and characterization of materials*, 27(3):279–311, 1993.

[2] TK Liang and HK Tsang. Role of free carriers from two-photon absorption in raman amplification in silicon-on-insulator waveguides. *Applied physics letters*, 84(15):2745–2747, 2004.

[3] Xiaoping Liu, Richard M Osgood, Yurii A Vlasov, and William MJ Green. Mid-infrared optical parametric amplifier using silicon nanophotonic waveguides. *Nature Photonics*, 4(8):557–560, 2010.

[4] Richard Espinola, Jerry Dadap, Richard Osgood Jr, Sharee McNab, and Yurii Vlasov. Raman amplification in ultrasmall silicon-on-insulator wire waveguides. *Optics Express*, 12(16):3713–3718, 2004.

[5] T.H. Maiman. Stimulated optical radiation in ruby. *Nature*, 187:493 – 494, 1960.

[6] PA Franken, Alan E Hill, CW Peters, and G Weinreich. Generation of optical harmonics. *Physical Review Letters*, 7(4):118, 1961.

[7] Allan W Snyder and John Love. *Optical waveguide theory*. Springer Science & Business Media, 2012.

[8] R.W. Boyd. *Nonlinear optics*. Academic Pr, 2003.

[9] M. Sheik-Bahae, D.C. Hutchings, D.J. Hagan, and E.W. Van Stryland. Dispersion of bound electron nonlinear refraction in solids. *Quantum Electronics, IEEE Journal of*, 27(6):1296 –1309, jun 1991.

[10] Lianghong Yin and Govind P Agrawal. Impact of two-photon absorption on self-phase modulation in silicon waveguides. *Optics letters*, 32(14):2031–2033, 2007.

[11] A. Baron. *Optique non-linéaire dans les structures semi-conductrices à fort confinement du champ*. PhD thesis, Université PARIS XI, UFR Scientifique D'Orsay, 2010.

[12] Robert W Boyd. Material slow light and structural slow light: similarities and differences for nonlinear optics [invited]. *JOSA B*, 28(12):A38–A44, 2011.

[13] Christelle Monat, Bill Corcoran, Dominik Pudo, Majid Ebnali-Heidari, Christian Grillet, Mark D Pelusi, David J Moss, Benjamin J Eggleton, Thomas P White, Liam O'Faolain, et al. Slow light enhanced nonlinear optics in silicon photonic crystal waveguides. *Selected Topics in Quantum Electronics, IEEE Journal of*, 16(1):344–356, 2010.

[14] Vilson R Almeida, Qianfan Xu, Carlos A Barrios, and Michal Lipson. Guiding and confining light in void nanostructure. *Optics letters*, 29(11):1209–1211, 2004.

[15] Qianfan Xu, Vilson R Almeida, Roberto R Panepucci, and Michal Lipson. Experimental demonstration of guiding and confining light in nanometer-size low-refractive-index material. *Optics letters*, 29(14):1626–1628, 2004.

[16] J.D. Joannopoulos. *Photonic Crystals: Molding The Flow Of Light*. Princeton University Press, 2008.

[17] A Di Falco, L O'Faolain, and TF Krauss. Dispersion control and slow light in slotted photonic crystal waveguides. *Applied Physics Letters*, 92(8):083501, 2008.

[18] J Leuthold, C Koos, and W Freude. Nonlinear silicon photonics. *Nature Photonics*, 4(8), 2010.

[19] Jana Jágerská, Hua Zhang, Zhaolu Diao, Nicolas Le Thomas, and Romuald Houdré. Refractive index sensing with an air-slot photonic crystal nanocavity. *Optics letters*, 35(15):2523–2525, 2010.

[20] Jie Gao, James F McMillan, Ming-Chung Wu, Jiangjun Zheng, Solomon Assefa, et al. Demonstration of an air-slot mode-gap confined photonic crystal slab nanocavity with ultrasmall mode volumes. *APPLIED PHYSICS LETTERS*, 96:051123, 2010.

[21] Kerry J Vahala. Optical microcavities. *Nature*, 424(6950):839–846, 2003.

[22] Momchil Minkov and Vincenzo Savona. Automated optimization of photonic crystal slab cavities. *Scientific reports*, 4, 2014.

[23] K. Nozaki, T. Tanabe, A. Shinya, S. Matsuo, T. Sato, H. Taniyama, and M. Notomi. Sub-femtojoule all-optical switching using a photonic-crystal nanocavity. *Nature Photonics*, 4(7):477–483, 2010.

[24] Takasumi Tanabe, Masaya Notomi, Satoshi Mitsugi, Akihiko Shinya, and Eiichi Kuramochi. All-optical switches on a silicon chip realized using photonic crystal nanocavities. *Applied Physics Letters*, 87(15):151112, 2005.

[25] K. Nozaki, A. Shinya, S. Matsuo, Y. Suzaki, T. Segawa, T. Sato, Y. Kawaguchi, R. Takahashi, and M. Notomi. Ultralow-power all-optical ram based on nanocavities. *Nature Photonics*, 6:248–252, 2012.

[26] Charles Caër, Samuel F Serna-Otálvaro, Weiwei Zhang, Xavier Le Roux, and Eric Cassan. Liquid sensor based on high-q slot photonic crystal cavity in silicon-on-insulator configuration. *Optics letters*, 39(20):5792–5794, 2014.

[27] Thi Hong Cam Hoang, Weiwei Zhang, Samuel F Serna-Otalvaro, Charles Caer, Xavier Le Roux, Laurent Vivien, and Eric Cassan. Soi slotted photonic crystal cavities spanning from 1.3 to 1.6 μm with factors above 800 000. *Photonics Technology Letters, IEEE*, 27(20):2138–2141, 2015.

[28] Weiwei Zhang, Samuel Serna, Xavier Le Roux, Carlos Alonso-Ramos, Laurent Vivien, and Eric Cassan. Analysis of silicon-on-insulator slot waveguide ring resonators targeting high q-factors. *Optics letters*, 40(23):5566–5569, 2015.

[29] Weiwei Zhang, Samuel Serna, Xavier Le Roux, Laurent Vivien, and Eric Cassan. Highly sensitive refractive index sensing by fast detuning the critical coupling condition of slot waveguide ring resonators. *Optics letters*, 41(3):532–535, 2016.

[30] Jacob T Robinson, Christina Manolatou, Long Chen, and Michal Lipson. Ultra-small mode volumes in dielectric optical microcavities. *Physical review letters*, 95(14):143901, 2005.

[31] Hatice Altug, Dirk Englund, and Jelena Vučković. Ultrafast photonic crystal nanocavity laser. *Nature Physics*, 2(7):484–488, 2006.

[32] Shigeru Makino, Yuhei Ishizaka, Kunimasa Saitoh, and Masanori Koshiba. Slow-light-enhanced nonlinear characteristics in slot waveguides composed of photonic crystal nanobeam cavities. *Photonics Journal, IEEE*, 5(2):2700309–2700309, 2013.

[33] Janik Wolters. *Integrated Quantum Hybrid Systems.* CRC Press, 2015.

[34] JS Foresi, Pierre R Villeneuve, J Ferrera, ER Thoen, G Steinmeyer, S Fan, JD Joannopoulos, LC Kimerling, Henry I Smith, and EP Ippen. Photonic-bandgap microcavities in optical waveguides. *nature*, 390(6656):143–145, 1997.

[35] Matt Eichenfield, Ryan Camacho, Jasper Chan, Kerry J Vahala, and Oskar Painter. A picogram-and nanometre-scale photonic-crystal optomechanical cavity. *Nature*, 459(7246):550–555, 2009.

[36] Yiyang Gong and Jelena Vuckovic. Photonic crystal cavities in silicon dioxide. *Applied Physics Letters*, 96(3):1107, 2010.

[37] Hermann A Haus. Waves and fields in optoelectronics (prentice-hall series in solid state physical electronics). 1984.

[38] Stéphane Trebaol. *Études expérimentales des propriétés dispersives de structures photoniques à base de microrésonateurs pour la réalisation de fonctions optiques*. PhD thesis, Université de Rennes 1, 2010.

[39] DR Lide and HPR Frederikse. *Handbook of Chemistry and Physics*.

[40] Samuel Serna, Weiwei Zhang, Xavier Leroux, Dingshan Gao, Daming Zhang, Laurent Vivien, and Eric Cassan. Potential for large optical gain improvement of erbium-doped slot waveguide amplifiers in silicon photonics. *JOSA B*, 31(9):2021–2028, 2014.

[41] A Säynätjoki, L Karvonen, T Alasaarela, X Tu, TY Liow, M Hiltunen, A Tervonen, GQ Lo, and S Honkanen. Low-loss silicon slot waveguides and couplers fabricated with optical lithography and atomic layer deposition. *Optics express*, 19(27):26275–26282, 2011.

[42] Roman Koerner, Michael Oehme, Martin Gollhofer, Marc Schmid, Konrad Kostecki, Stefan Bechler, Daniel Widmann, Erich Kasper, and Joerg Schulze. Electrically pumped lasing from ge fabry-perot resonators on si. *Optics express*, 23(11):14815–14822, 2015.

[43] Rodolfo E Camacho-Aguilera, Yan Cai, Neil Patel, Jonathan T Bessette, Marco Romagnoli, Lionel C Kimerling, and Jurgen Michel. An electrically pumped germanium laser. *Optics express*, 20(10):11316–11320, 2012.

[44] AV Krishnamoorthy, X Zheng, D Feng, J Lexau, JF Buckwalter, HD Thacker, F Liu, Y Luo, E Chang, P Amberg, et al. A low-power, high-speed, 9-channel germanium-silicon electro-absorption modulator array integrated with digital cmos driver and wavelength multiplexer. *Optics express*, 22(10):12289–12295, 2014.

[45] Jifeng Liu, Mark Beals, Andrew Pomerene, Sarah Bernardis, Rong Sun, Jing Cheng, Lionel C Kimerling, and Jurgen Michel. Waveguide-integrated, ultralow-energy gesi electro-absorption modulators. *Nature Photonics*, 2(7):433–437, 2008.

[46] Léopold Virot, Paul Crozat, Jean-Marc Fédéli, Jean-Michel Hartmann, Delphine Marris-Morini, Eric Cassan, Frédéric Boeuf, and Laurent Vivien. Germanium avalanche receiver for low power interconnects. *Nature communications*, 5, 2014.

[47] Hong Tao Chen, Peter Verheyen, Peter De Heyn, Guy Lepage, Jeroen De Coster, Philippe Absil, Gunther Roelkens, and Joris Van Campenhout. High-responsivity low-voltage 28-gb/s ge pin photodetector with silicon contacts. *Journal of Lightwave Technology*, 33(4):820–824, 2015.

[48] Papichaya Chaisakul, Delphine Marris-Morini, Jacopo Frigerio, Daniel Chrastina, Mohamed-Said Rouifed, Stefano Cecchi, Paul Crozat, Giovanni Isella, and Laurent Vivien. Integrated germanium optical interconnects on silicon substrates. *Nature Photonics*, 8(6):482–488, 2014.

[49] Erich Kasper. *Properties of strained and relaxed silicon germanium.* INSPEC, Institution of electrical engineers London, 1995.

[50] J Weber and MI Alonso. Near-band-gap photoluminescence of si-ge alloys. *Physical Review B*, 40(8):5683, 1989.

[51] Rubin Braunstein, Arnold R Moore, and Frank Herman. Intrinsic optical absorption in germanium-silicon alloys. *Physical Review*, 109(3):695, 1958.

[52] Vladyslav Vakarin, Papichaya Chaisakul, Jacopo Frigerio, Andrea Ballabio, Xavier Le Roux, Jean-René Coudevylle, David Bouville, Diego Perez-Galacho, Laurent Vivien, Giovanni Isella, et al. Sharp bends and mach-zehnder interferometer based on ge-rich-sige waveguides on sige graded buffer. *Optics express*, 23(24):30821–30826, 2015.

[53] Benjamin J Eggleton, Barry Luther-Davies, and Kathleen Richardson. Chalcogenide photonics. *Nature photonics*, 5(3):141–148, 2011.

[54] Lan Li, Hongtao Lin, Shutao Qiao, Yi Zou, Sylvain Danto, Kathleen Richardson, J David Musgraves, Nanshu Lu, and Juejun Hu. Integrated flexible chalcogenide glass photonic devices. *Nature Photonics*, 8(8):643–649, 2014.

[55] Hongtao Lin. *Chalcogenide glass mid-infrared on-chip sensor for chemical sensing.* PhD thesis, University of Delaware, 2015.

[56] J Bauer. Optical properties, band gap, and surface roughness of si3n4. *physica status solidi (a)*, 39(2):411–418, 1977.

[57] Carlos Ríos, Matthias Stegmaier, Peiman Hosseini, Di Wang, Torsten Scherer, C David Wright, Harish Bhaskaran, and Wolfram HP Pernice. Integrated all-photonic non-volatile multi-level memory. *Nature Photonics*, 9(11):725–732, 2015.

[58] M Kolesik and JV Moloney. Nonlinear optical pulse propagation simulation: From maxwell's to unidirectional equations. *Physical Review E*, 70(3):036604, 2004.

[59] Moloney Kolesik, JV Moloney, and M Mlejnek. Unidirectional optical pulse propagation equation. *Physical review letters*, 89(28):283902, 2002.

[60] Victor Mizrahi, MA Saifi, MJ Andrejco, KW DeLong, and GI Stegeman. Two-photon absorption as a limitation to all-optical switching. *Optics letters*, 14(20):1140–1142, 1989.

[61] Cid B de Araújo, Anderson SL Gomes, and Georges Boudebs. Techniques for nonlinear optical characterization of materials: a review. *Reports on Progress in Physics*, 79(3):036401, 2016.

[62] Mansoor Sheik-Bahae, Ali A Said, and Eric W Van Stryland. High-sensitivity, single-beam n 2 measurements. *Optics letters*, 14(17):955–957, 1989.

[63] W Zhao and P Palffy-Muhoray. Z-scan technique using top-hat beams. *Applied physics letters*, 63(12):1613–1615, 1993.

[64] M Sheik-Bahae, J Wang, R DeSalvo, DJ Hagan, and EW Van Stryland. Measurement of nondegenerate nonlinearities using a two-color z scan. *Optics letters*, 17(4):258–260, 1992.

[65] T Xia, DJ Hagan, M Sheik-Bahae, and EW Van Stryland. Eclipsing z-scan measurement of $\lambda/10$ 4 wave-front distortion. *Optics letters*, 19(5):317–319, 1994.

[66] W Zhao and P Palffy-Muhoray. Z-scan measurement of χ (3) using top-hat beams. *Applied physics letters*, 65(6):673–675, 1994.

[67] Richard L Sutherland. *Handbook of nonlinear optics*. CRC press, 2003.

[68] GC Cho, W Kütt, and H Kurz. Subpicosecond time-resolved coherent-phonon oscillations in gaas. *Physical review letters*, 65(6):764, 1990.

[69] Richard S Lepkowicz, Jie Fu, Claudiu M Cirloganu, Olga V Przhonska, David J Hagan, Eric W Van Stryland, Mike V Bondar, and Yuriy L Slominsky. Femtosecond to nanosecond characterization of the excited-state properties of polymethine molecules. In *Nonlinear Optics: Materials, Fundamentals and Applications*, page FB8. Optical Society of America, 2004.

[70] FP Strohkendl, LR Dalton, RW Hellwarth, HW Sarkas, and ZH Kafafi. Phase-mismatched degenerate four-wave mixing: complex third-order susceptibility tensor elements of c 60 at 768 nm. *JOSA B*, 14(1):92–98, 1997.

[71] James F McMillan, Mingbin Yu, Dim-Lee Kwong, and Chee Wei Wong. Observation of four-wave mixing in slow-light silicon photonic crystal waveguides. *Optics Express*, 18(15):15484–15497, 2010.

[72] Christelle Monat, Majid Ebnali-Heidari, Christian Grillet, B Corcoran, BJ Eggleton, TP White, Liam O'Faolain, Juntao Li, and TF Krauss. Four-wave mixing in slow light engineered silicon photonic crystal waveguides. *Optics express*, 18(22):22915–22927, 2010.

[73] Juntao Li, Liam O'Faolain, and Thomas F Krauss. Four-wave mixing in slow light photonic crystal waveguides with very high group index. *Optics express*, 20(16):17474–17479, 2012.

[74] Spyros Lavdas and Nicolae C Panoiu. Comparative analysis of four-wave mixing of optical pulses in slow-and fast-light regimes of a silicon photonic crystal waveguide. *Optics letters*, 40(18):4233–4236, 2015.

[75] Panagiotis Kanakis, Thomas Kamalakis, and Thomas Sphicopoulos. Designing photonic crystal waveguides for broadband four-wave mixing applications. *Optics letters*, 40(6):1041–1044, 2015.

[76] Michael J Moran, Chiao-Yao She, and Robert L Carman. Interferometric measurements of the nonlinear refractive-index coefficient relative to cs 2 in laser-system-related materials. *Quantum Electronics, IEEE Journal of*, 11(6):259–263, 1975.

[77] Nguyen Phu Xuan, Jean-Louis Ferrier, José Gazengel, and Geneviève Rivoire. Picosecond measurements of the third order susceptibility tensor in liquids. *Optics communications*, 51(6):433–437, 1984.

[78] SM Saltiel, B Van Wonterghem, and PM Rentzepis. Measurement of χ (3) and phase shift of nonlinear media by means of a phase-conjugate interferometer. *Optics letters*, 14(3):183–185, 1989.

[79] N Tang and JP Partanen. Four-wave-mixing interferometer. *Optics letters*, 21(15):1108–1110, 1996.

[80] GR Meredith, B Buchalter, and C Hanzlik. Third-order optical susceptibility determination by third harmonic generation. i. *The Journal of Chemical Physics*, 78(3):1533–1542, 1983.

[81] Christelle Monat, Christian Grillet, Bill Corcoran, David J Moss, Benjamin J Eggleton, Thomas P White, and Thomas F Krauss. Investigation of phase matching for third-harmonic generation in silicon slow light photonic crystal waveguides using fourier optics. *Optics express*, 18(7):6831–6840, 2010.

[82] Christelle Monat, Marcel Spurny, Christian Grillet, Liam O'Faolain, Thomas F Krauss, Benjamin J Eggleton, Douglas Bulla, Steve Madden, and Barry Luther-Davies. Third-harmonic generation in slow-light chalcogenide glass photonic crystal waveguides. *Optics letters*, 36(15):2818–2820, 2011.

[83] Christelle Monat, Christian Grillet, Matthew Collins, Alex Clark, Jochen Schroeder, Chunle Xiong, Juntao Li, Liam O'Faolain, Thomas F Krauss, Benjamin J Eggleton, et al. Integrated optical auto-correlator based on third-harmonic generation in a silicon photonic crystal waveguide. *Nature communications*, 5, 2014.

[84] F Louradour, E Lopez-Lago, V Couderc, V Messager, and A Barthelemy. Dispersive-scan measurement of the fast component of the third-order nonlinearity of bulk materials and waveguides. *Optics letters*, 24(19):1361–1363, 1999.

[85] EJS Fonseca, EA Gouveia, and JM Hickmann. Time analogue of the z-scan technique suitable to waveguides. *The European Physical Journal D-Atomic, Molecular, Optical and Plasma Physics*, 17(1):75–78, 2001.

[86] Sudhir Cherukulappurath, Georges Boudebs, and André Monteil. 4f coherent imager system and its application to nonlinear optical measurements. *JOSA B*, 21(2):273–279, 2004.

[87] Toshihiko Baba. Slow light in photonic crystals. *Nature photonics*, 2(8):465–473, 2008.

[88] A. Baron, A. Ryasnyanskiy, N. Dubreuil, P. Delaye, Q. Vy Tran, S. Combrié, A. de Rossi, R. Frey, and G. Roosen. Light localization induced enhancement of third order nonlinearities in a gaas photonic crystal waveguide. *Optics Express*, 17(2):552–557, 2009.

[89] Christelle Monat, Bill Corcoran, Majid Ebnali-Heidari, Christian Grillet, Benjamin J Eggleton, Thomas P White, Liam O'Faolain, and Thomas F Krauss. Slow light enhancement of nonlinear effects in silicon engineered photonic crystal waveguides. *Optics express*, 17(4):2944–2953, 2009.

[90] Thanh-Nam Nguyen, Kevin Lengle, Monique Thual, Philippe Rochard, Mathilde Gay, Laurent Bramerie, Stefania Malaguti, Gaetano Bellanca, Sy Dat Le, and Thierry Chartier. Nondestructive method to measure coupling and propagation losses in optical guided structures. *JOSA B*, 29(12):3393–3397, 2012.

[91] Masao Tachikura. Internal loss measurement technique for optical devices equipped with fiber connectors at both ends. *Applied optics*, 34(34):8056–8057, 1995.

[92] Elena Lopez-Lago, Valérie Messager, Frederic Louradour, Vincent Couderc, and Alain Barthelemy. Characterization of the fast component of the complex third-order nonlinearity and time response of bulk materials and waveguides. *JOSA B*, 18(8):1166–1173, 2001.

[93] Jérémy Oden. *Microcavités non linéaires en régime d'excitation cohérente*. PhD thesis, Institut d'Optique Graduate School, 2013.

[94] O. Martinez. 3000 times grating compressor with positive group velocity dispersion: Application to fiber compensation in 1.3-1.6 μm region. *Quantum Electronics, IEEE Journal of*, 23(1):59 – 64, jan 1987.

[95] Cl Froehly, B Colombeau, and M Vampouille. Shaping and analysis of picosecond light pulses. *Progress in optics*, 20:63–153, 1983.

[96] Govind Agrawal. *Applications of nonlinear fiber optics*. Academic press, 2010.

[97] Takanori Sato, Shuntaro Makino, Yuhei Ishizaka, Takeshi Fujisawa, and Kunimasa Saitoh. A rigorous definition of nonlinear parameter γ and effective area a eff for photonic crystal optical waveguides. *JOSA B*, 32(6):1245–1251, 2015.

[98] M Dinu, F Quochi, and H Garcia. Third-order nonlinearities in silicon at telecom wavelengths. *Applied Physics Letters*, 82(18):2954–2956, 2003.

[99] R. M. Osgood, N. C. Panoiu, J. I. Dadap, Xiaoping Liu, Xiaogang Chen, I-Wei Hsieh, E. Dulkeith, W. M.J. Green, and Y. A. Vlasov. Engineering nonlinearities

in nanoscale optical systems: physics and applications in dispersion-engineered silicon nanophotonic wires. *Adv. Opt. Photon.*, 1(1):162–235, Jan 2009.

[100] Nick K Hon, Richard Soref, and Bahram Jalali. The third-order nonlinear optical coefficients of si, ge, and si1- xgex in the midwave and longwave infrared. *Journal of Applied Physics*, 110(1):011301, 2011.

[101] M Ferhat, A Zaoui, B Khelifa, and H Aourag. Band structure calculations of ge x si 1- x. *Solid state communications*, 91(5):407–411, 1994.

[102] Jeff M Harbold, Fö Ilday, FW Wise, JS Sanghera, VQ Nguyen, LB Shaw, and Ishwar D Aggarwal. Highly nonlinear as–s–se glasses for all-optical switching. *Optics Letters*, 27(2):119–121, 2002.

[103] Marcel Spurny. *Photonic crystal waveguides in chalcogenide glasses.* PhD thesis, University of St Andrews, 2011.

[104] Michael RE Lamont, Barry Luther-Davies, Duk-Yong Choi, Steve Madden, and Benjamin J Eggleton. Supercontinuum generation in dispersion engineered highly nonlinear (γ= 10/w/m) as 2 s 3 chalcogenide planar waveguide. *Optics Express*, 16(19):14938–14944, 2008.

[105] David J Moss, Roberto Morandotti, Alexander L Gaeta, and Michal Lipson. New cmos-compatible platforms based on silicon nitride and hydex for nonlinear optics. *Nature Photonics*, 7(8):597–607, 2013.

[106] R Halir, Y Okawachi, JS Levy, MA Foster, M Lipson, and AL Gaeta. Ultrabroadband supercontinuum generation in a cmos-compatible platform. *Optics letters*, 37(10):1685–1687, 2012.

[107] M. Soljačić and JD Joannopoulos. Enhancement of nonlinear effects using photonic crystals. *Nature materials*, 3(4):211–219, 2004.

[108] Q. Xu and M. Lipson. All-optical logic based on silicon micro-ring resonators. *Optics express*, 15(3):924–929, 2007.

[109] F Raineri, Crina Cojocaru, P Monnier, A Levenson, R Raj, C Seassal, X Letartre, and P Viktorovitch. Ultrafast dynamics of the third-order nonlinear response in a two-dimensional inp-based photonic crystal. *Applied physics letters*, 85:1880, 2004.

[110] Chad Husko, Alfredo De Rossi, Sylvain Combrié, Quynh Vy Tran, Fabrice Raineri, and Chee Wei Wong. Ultrafast all-optical modulation in gaas photonic crystal cavities. *Applied Physics Letters*, 94(2):021111, 2009.

[111] V. Eckhouse, I. Cestier, G. Eisenstein, S. Combrié, G. Lehoucq, and A. De Rossi. Kerr-induced all-optical switching in a gainp photonic crystal fabry-perot resonator. *Opt. Express*, 20(8):8524–8534, Apr 2012.

[112] Z. K. Ioannidis, P. M. Radmore, and I. P. Giles. Dynamic response of an all-fiber ring resonator. *Opt. Lett.*, 13(5):422–424, May 1988.

[113] Yannick Dumeige, Stéphane Trebaol, Laura Ghişa, Thi Kim Ngan Nguyen, Hervé Tavernier, and Patrice Féron. Determination of coupling regime of high-q resonators and optical gain of highly selective amplifiers. *JOSA B*, 25(12):2073–2080, 2008.

[114] Dragan Vujic and Sajeev John. Pulse reshaping in photonic crystal waveguides and microcavities with kerr nonlinearity: Critical issues for all-optical switching. *Physical Review A*, 72(1):013807, 2005.

[115] Nirit Dudovich, Barak Dayan, Sarah M Gallagher Faeder, and Yaron Silberberg. Transform-limited pulses are not optimal for resonant multiphoton transitions. *Physical Review Letters*, 86(1):47, 2001.

[116] Wayne V Sorin and Rodney S Tucker. Optical pulse storage, shaping, and wavelength conversion in resonators with controllable input coupling. *Journal of Lightwave Technology*, 27(14):2587–2594, 2009.

[117] S. Sandhu, M.L. Povinelli, and S Fan. Enhancing optical switching with coherent control. *Applied Physics Letters*, 96(23):231108, 2010.

[118] D. Meshulach and Y. Silberberg. Coherent quantum control of two-photon transitions by a femtosecond laser pulse. *Nature*, 396(6708):239–242, 1998.

[119] Andrew M Weiner. Femtosecond pulse shaping using spatial light modulators. *Review of scientific instruments*, 71(5):1929–1960, 2000.

[120] Sebastien Zamith, Jérôme Degert, Sabine Stock, Béatrice De Beauvoir, Valérie Blanchet, M Aziz Bouchene, and Bertrand Girard. Observation of coherent transients in ultrashort chirped excitation of an undamped two-level system. *Physical Review Letters*, 87(3):033001, 2001.

[121] Philip Trøst Kristensen, Mikkel Heuck, and Jesper Mørk. Optimal switching using coherent control. *Applied Physics Letters*, 102(4):041107, 2013.

[122] Akitoshi Chen-Jinnai, Wataru Yoshiki, and Takasumi Tanabe. Broad-bandwidth pulse propagation through ultrahigh-quality-factor microcavity with chirped pulse. *Japanese Journal of Applied Physics*, 54(12):122201, 2015.

[123] Jérémy Oden, Stephane Trebaol, Philippe Delaye, and Nicolas Dubreuil. Coherent excitation of a nonlinear microcavity. *Journal of the European Optical Society-Rapid publications*, 8, 2013.

[124] S. M. Hendrickson, A. C. Foster, R. M. Camacho, and B. D. Clader. Integrated nonlinear photonics: emerging applications and ongoing challenges [invited]. *J. Opt. Soc. Am. B*, 31(12):3193–3203, Dec 2014.

[125] P. Velha, J. C. Rodier, P. Lalanne, J. P. Hugonin, D. Peyrade, E. Picard, T. Charvolin, and E. Hadji. Ultracompact silicon-on-insulator ridge-waveguide mirrors with high reflectance. *Applied Physics Letters*, 89(17):171121, 2006.

[126] Philippe Velha, Jean-Claude Rodier, Philippe Lalanne, Jean-Paul Hugonin, D Peyrade, E Picard, T Charvolin, and E Hadji. Ultra-high-reflectivity photonic-bandgap mirrors in a ridge soi waveguide. *New Journal of Physics*, 8(9):204, 2006.

[127] Eric Silberstein, Philippe Lalanne, Jean-Paul Hugonin, and Qing Cao. Use of grating theories in integrated optics. *JOSA A*, 18(11):2865–2875, 2001.

[128] Amy C Turner, Christina Manolatou, Bradley S Schmidt, Michal Lipson, Mark A Foster, Jay E Sharping, and Alexander L Gaeta. Tailored anomalous group-velocity dispersion in silicon channel waveguides. *Optics express*, 14(10):4357–4362, 2006.

[129] Paul Barclay, Kartik Srinivasan, and Oskar Painter. Nonlinear response of silicon photonic crystal microresonators excited via an integrated waveguide and fiber taper. *Opt. Express*, 13(3):801–820, Feb 2005.

[130] Vilson R. Almeida, Carlos A. Barrios, Roberto R. Panepucci, Michal Lipson, Mark A. Foster, Dimitre G. Ouzounov, and Alexander L. Gaeta. All-optical switching on a silicon chip. *Opt. Lett.*, 29(24):2867–2869, Dec 2004.

[131] N. Dubreuil, J. Oden, S. Serna, M. Hanna, C. Caer, X. Le Roux, C. Sauvan, S. Trebaol, P. Delaye, and E. Cassan. Coherent excitation of a nonlinear silicon microcavity. In *2014 The European Conference on Optical Communication (ECOC)*, pages 1–3, Sept 2014.

[132] S. Serna, J. Oden, M. Hanna, C. Caer, X. Le Roux, C. Sauvan, P. Delaye, E. Cassan, and N. Dubreuil. Nonlinear enhancement in a coherently excited microcavity. In *2015 European Conference on Lasers and Electro-Optics (CLEO) - European Quantum Electronics Conference*, pages CD–P–34. Optical Society of America, 2015.

[133] Samuel Serna, Jérèmy Oden, Marc Hanna, Charles Caer, Xavier Le Roux, Christophe Sauvan, Philippe Delaye, Eric Cassan, and Nicolas Dubreuil. Enhanced nonlinear interaction in a microcavity under coherent excitation. *Opt. Express*, 23(23):29964–29977, Nov 2015.

[134] V.R. Almeida, C.A. Barrios, R.R. Panepucci, and M. Lipson. All-optical control of light on a silicon chip. *Nature*, 431(7012):1081–1084, 2004.

[135] M Castellanos Muñoz, A Yu Petrov, and M Eich. All-optical on-chip dynamic frequency conversion. *Applied Physics Letters*, 101(14):141119, 2012.

[136] Richard S Judson and Herschel Rabitz. Teaching lasers to control molecules. *Physical Review Letters*, 68(10):1500, 1992.

[137] Eiichi Kuramochi, Kengo Nozaki, Akihiko Shinya, Koji Takeda, Tomonari Sato, Shinji Matsuo, Hideaki Taniyama, Hisashi Sumikura, and Masaya Notomi. Large-scale integration of wavelength-addressable all-optical memories on a photonic crystal chip. *Nature Photonics*, 8(6):474–481, 2014.

[138] Laurent Vivien and Lorenzo Pavesi. *Handbook of silicon photonics*. Taylor & Francis, 2016.

[139] Bill Corcoran, Christelle Monat, Christian Grillet, David J Moss, Benjamin J Eggleton, TP White, Liam O'Faolain, and Thomas F Krauss. Green light emission in silicon through slow-light enhanced third-harmonic generation in photonic-crystal waveguides. *Nature photonics*, 3(4):206–210, 2009.

[140] Yurii A Vlasov, Martin O'Boyle, Hendrik F Hamann, and Sharee J McNab. Active control of slow light on a chip with photonic crystal waveguides. *Nature*, 438(7064):65–69, 2005.

[141] A Yu Petrov and M Eich. Zero dispersion at small group velocities in photonic crystal waveguides. *Applied physics letters*, 85(21):4866–4868, 2004.

[142] Thomas F Krauss. Slow light in photonic crystal waveguides. *Journal of Physics D: Applied Physics*, 40(9):2666, 2007.

[143] RJP Engelen, Yoshimasa Sugimoto, Yoshinori Watanabe, Jeroen P Korterik, Noaki Ikeda, Niek F van Hulst, Kiyoshi Asakawa, and Laurens Kuipers. The effect of higher-order dispersion on slow light propagation in photonic crystal waveguides. *Optics express*, 14(4):1658–1672, 2006.

[144] Simon Mazoyer, Jean-Paul Hugonin, and Philippe Lalanne. Disorder-induced multiple scattering in photonic-crystal waveguides. *Physical review letters*, 103(6):063903, 2009.

[145] Simon Mazoyer, Philippe Lalanne, Jean-Claude Rodier, Jean-Paul Hugonin, M Spasenović, L Kuipers, DM Beggs, and TF Krauss. Statistical fluctuations of transmission in slow light photonic-crystal waveguides. *Optics express*, 18(14):14654–14663, 2010.

[146] Lars H Frandsen, Andrei V Lavrinenko, Jacob Fage-Pedersen, and Peter I Borel. Photonic crystal waveguides with semi-slow light and tailored dispersion properties. *Optics Express*, 14(20):9444–9450, 2006.

[147] Juntao Li, Thomas P White, Liam O'Faolain, Alvaro Gomez-Iglesias, and Thomas F Krauss. Systematic design of flat band slow light in photonic crystal waveguides. *Optics Express*, 16(9):6227–6232, 2008.

[148] Juntao Li, Liam O'Faolain, Isabella H Rey, and Thomas F Krauss. Four-wave mixing in photonic crystal waveguides: slow light enhancement and limitations. *Optics Express*, 19(5):4458–4463, 2011.

[149] Chad Husko, Pierre Colman, Sylvain Combrié, Alfredo De Rossi, and Chee Wei Wong. Effect of multiphoton absorption and free carriers in slow-light photonic crystal waveguides. *Optics letters*, 36(12):2239–2241, 2011.

[150] Chad Husko, Sylvain CombriÚ, Quynh V Tran, Fabrice Raineri, Chee Wei Wong, and Alfredo De Rossi. Non-trivial scaling of self-phase modulation and three-photon absorption in iii-v photonic crystal waveguides. *Optics express*, 17(25):22442–22451, 2009.

[151] Jana Jágerská. *Dispersion Properties of Photonic Crystals and Silicon Nanostructures Investigated by Fourier-Space Imaging.* PhD thesis, EPFL, 2011.

[152] Ran Ding, Tom Baehr-Jones, Woo-Joong Kim, Xugang Xiong, Richard Bojko, Jean-Marc Fedeli, Maryse Fournier, and Michael Hochberg. Low-loss strip-loaded slot waveguides in silicon-on-insulator. *Optics express*, 18(24):25061–25067, 2010.

[153] Ran Ding, Tom Baehr-Jones, Woo-Joong Kim, Bryan Boyko, Richard Bojko, Alexander Spott, Andrew Pomerene, Craig Hill, Wesley Reinhardt, and Michael Hochberg. Low-loss asymmetric strip-loaded slot waveguides in silicon-on-insulator. *Applied Physics Letters*, 98(23):233303, 2011.

[154] Zhechao Wang, Ning Zhu, Yongbo Tang, Lech Wosinski, Daoxin Dai, and Sailing He. Ultracompact low-loss coupler between strip and slot waveguides. *Optics letters*, 34(10):1498–1500, 2009.

[155] R Palmer, L Alloatti, D Korn, W Heni, PC Schindler, J Bolten, M Karl, M Waldow, T Wahlbrink, W Freude, et al. Low-loss silicon strip-to-slot mode converters. *IEEE Photon. J*, 5(1):2200409, 2013.

[156] Valentyn S Volkov, Sergey I Bozhevolnyi, Lars H Frandsen, and Martin Kristensen. Direct observation of surface mode excitation and slow light coupling in photonic crystal waveguides. *Nano letters*, 7(8):2341–2345, 2007.

[157] TP White, LC Botten, C Martijn De Sterke, KB Dossou, and RC McPhedran. Efficient slow-light coupling in a photonic crystal waveguide without transition region. *Optics letters*, 33(22):2644–2646, 2008.

[158] Jean-Paul Hugonin, Philippe Lalanne, Thomas P White, and Thomas F Krauss. Coupling into slow-mode photonic crystal waveguides. *Optics letters*, 32(18):2638–2640, 2007.

[159] Charles Caer. *Cristaux photoniques a fente : vers une photonique silicium hybride a exaltation localisee du champ electromagnetique.* PhD thesis, Université Paris-Sud XI, UFR Sciences, 2013.

[160] Andrea Melloni, A Canciamilla, C Ferrari, F Morichetti, L O'Faolain, TF Krauss, Re De La Rue, A Samarelli, and M Sorel. Tunable delay lines in silicon photonics: coupled resonators and photonic crystals, a comparison. *IEEE Photonics Journal*, 2(2):181–194, 2010.

[161] Amir Hosseini, Xiaochuan Xu, Harish Subbaraman, Che-Yun Lin, Somayeh Rahimi, and Ray T Chen. Large optical spectral range dispersion engineered silicon-based photonic crystal waveguide modulator. *Optics express*, 20(11):12318–12325, 2012.

[162] Shousaku Kubo, Daisuke Mori, and Toshihiko Baba. Low-group-velocity and low-dispersion slow light in photonic crystal waveguides. *Optics letters*, 32(20):2981–2983, 2007.

[163] Yohei Hamachi, Shousaku Kubo, and Toshihiko Baba. Slow light with low dispersion and nonlinear enhancement in a lattice-shifted photonic crystal waveguide. *Optics letters*, 34(7):1072–1074, 2009.

[164] Ran Hao, Eric Cassan, Xavier Le Roux, Dingshan Gao, Laurent Vivien, Delphine Marris-Morini, Xinliang Zhang, et al. Improvement of delay-bandwidth product in photonic crystal slow-light waveguides. *Optics express*, 18(16):16309–16319, 2010.

[165] Yong Zhao, Ya-Nan Zhang, Di Wu, and Qi Wang. Wideband slow light with large group index and low dispersion in slotted photonic crystal waveguide. *Journal of Lightwave Technology*, 30(17):2812–2817, 2012.

[166] Ya-nan Zhang, Yong Zhao, and Jin Li. Theoretical research on slow light engineering of slotted photonic crystal waveguides with elliptical holes and optofluidic infiltration. *Applied Optics*, 54(7):1639–1646, 2015.

[167] Bo Meng, Ling-ling Wang, Xiao-fei Li, Wen-zhi Xiao, Liu Wang, and Dong Xiang. Novel slow-light waveguide with large bandwidth and ultra low dispersion. *Optics Communications*, 285(18):3704–3708, 2012.

[168] Charles Caër, Sylvain Combrié, Xavier Le Roux, Eric Cassan, and Alfredo De Rossi. Extreme optical confinement in a slotted photonic crystal waveguide. *Applied Physics Letters*, 105(12):121111, 2014.

[169] Jun Wu, Yanping Li, Chao Peng, and Ziyu Wang. Wideband and low dispersion slow light in slotted photonic crystal waveguide. *Optics Communications*, 283(14):2815–2819, 2010.

[170] Samuel Serna, Pierre Colman, Weiwei Zhang, Xavier Le Roux, Charles Caer, Laurent Vivien, and Eric Cassan. Experimental gvd engineering in slow light slot photonic crystal waveguides. *Scientific reports*, 6:26956, 2016.

[171] Steven G Johnson and John D Joannopoulos. Block-iterative frequency-domain methods for maxwell's equations in a planewave basis. *Optics express*, 8(3):173–190, 2001.

[172] N Le Thomas, H Zhang, J Jágerská, V Zabelin, R Houdré, I Sagnes, and A Talneau. Light transport regimes in slow light photonic crystal waveguides. *Physical Review B*, 80(12):125332, 2009.

[173] N Le Thomas, Z Diao, H Zhang, and R Houdré. Statistical analysis of subnanometer residual disorder in photonic crystal waveguides: Correlation between slow light properties and structural properties. *Journal of Vacuum Science & Technology B*, 29(5):051601, 2011.

[174] Mark Patterson, Stephen Hughes, Sylvain Combrié, N-V-Quynh Tran, Alfredo De Rossi, Renaud Gabet, and Yves Jaouën. Disorder-induced coherent scattering in slow-light photonic crystal waveguides. *Physical review letters*, 102(25):253903, 2009.

[175] Bing Wang, Simon Mazoyer, Jean-Paul Hugonin, and Philippe Lalanne. Backscattering in monomode periodic waveguides. *Physical Review B*, 78(24):245108, 2008.

[176] N Le Thomas and R Houdré. Group velocity and energy transport velocity near the band edge of a disordered coupled cavity waveguide: an analytical approach. *JOSA B*, 27(10):2095–2101, 2010.

[177] Juraj Topolancik, B Ilic, and Frank Vollmer. Experimental observation of strong photon localization in disordered photonic crystal waveguides. *Physical review letters*, 99(25):253901, 2007.

[178] Eiichi Kuramochi, Masaya Notomi, S Hughes, Akihiko Shinya, T Watanabe, and L Ramunno. Disorder-induced scattering loss of line-defect waveguides in photonic crystal slabs. *Physical Review B*, 72(16):161318, 2005.

[179] Momchil Minkov and Vincenzo Savona. Effect of hole-shape irregularities on photonic crystal waveguides. *Optics letters*, 37(15):3108–3110, 2012.

[180] Simon Mazoyer, Alexandre Baron, Jean-Paul Hugonin, Philippe Lalanne, and Andrea Melloni. Slow pulses in disordered photonic-crystal waveguides. *Applied optics*, 50(31):G113–G117, 2011.

[181] René Matzen, Jakob S Jensen, and Ole Sigmund. Systematic design of slow-light photonic waveguides. *JOSA B*, 28(10):2374–2382, 2011.

[182] R Ferrini, B Lombardet, B Wild, R Houdre, and G-H Duan. Hole depth-and shape-induced radiation losses in two-dimensional photonic crystals. *Applied physics letters*, 82(7):1009–1011, 2003.

[183] Liam O'Faolain, Sebastian Andreas Schulz, Daryl Matthew Beggs, Tom P White, M Spasenović, L Kuipers, F Morichetti, Andrea Melloni, Simon Mazoyer, Jean-Paul Hugonin, et al. Loss engineered slow light waveguides. *Optics express*, 18(26):27627–27638, 2010.

[184] Alberto Parini, Philippe Hamel, Alfredo De Rossi, Sylvain Combrié, Yaneck Gottesman, Renaud Gabet, Anne Talneau, Yves Jaouen, Giovanni Vadala, et al. Time-wavelength reflectance maps of photonic crystal waveguides: a new view on disorder-induced scattering. *Journal of Lightwave Technology*, 26(23):3794–3802, 2008.

[185] Sylvain Combrié, Evelin Weidner, Alfredo De Rossi, Simone Cassette, Philippe Hamel, Yves Jaouën, Renaud Gabet, Anne Talneau, et al. Investigation of group delay, loss, and disorder in a photonic crystal waveguide by low-coherence reflectometry. *Applied physics letters*, 90(23):231104, 2007.

[186] Pierre Colman. *Circuits nanophotoniques pour le traitement optique du signal*. PhD thesis, Paris 6, 2011.

[187] Nishan Mann, Sylvian Combrié, Pierre Colman, Mark Patterson, Alfredo De Rossi, and Stephen Hughes. Reducing disorder-induced losses for slow light photonic crystal waveguides through bloch mode engineering. *Optics letters*, 38(20):4244–4247, 2013.

[188] Christian Koos, Philipp Vorreau, Thomas Vallaitis, Pieter Dumon, Wim Bogaerts, Roel Baets, Bweh Esembeson, Ivan Biaggio, Tsuyoshi Michinobu, François Diederich, et al. All-optical high-speed signal processing with silicon–organic hybrid slot waveguides. *Nature photonics*, 3(4):216–219, 2009.

[189] Tom W Baehr-Jones and Michael J Hochberg. Polymer silicon hybrid systems: A platform for practical nonlinear optics†. *The Journal of Physical Chemistry C*, 112(21):8085–8090, 2008.

[190] Kimberly A Drenser, Rulon J Larsen, Friedrich P Strohkendl, and Larry R Dalton. Femtosecond, frequency-agile, phase-sensitive-detected, multi-wave-mixing nonlinear optical spectroscopy applied to π-electron photonic materials. *The Journal of Physical Chemistry A*, 103(14):2290–2301, 1999.

[191] M Asobe, I Yokohama, T Kaino, S Tomaru, and T Kurihara. Nonlinear absorption and refraction in an organic dye functionalized main chain polymer waveguide in the 1.5 μm wavelength region. *Applied physics letters*, 67(7):891–893, 1995.

[192] CA Barrios. High-performance all-optical silicon microswitch. *Electronics Letters*, 40(14):1, 2004.

[193] Charles Caer, Xavier Le Roux, and Eric Cassan. Enhanced localization of light in slow wave slot photonic crystal waveguides. *Optics letters*, 37(17):3660–3662, 2012.

[194] Pierre Colman, Chad Husko, Sylvain Combrié, Isabelle Sagnes, Chee Wei Wong, and Alfredo De Rossi. Temporal solitons and pulse compression in photonic crystal waveguides. *Nature Photonics*, 4(12):862–868, 2010.

[195] A Willinger, S Roy, M Santagiustina, S Combrié, A De Rossi, and G Eisenstein. Narrowband optical parametric amplification measurements in ga 0.5 in 0.5 p photonic crystal waveguides. *Optics express*, 23(14):17751–17757, 2015.

[196] Pierre Colman, Isabelle Cestier, Amnon Willinger, Sylvain Combrié, Gaëlle Lehoucq, Gadi Eisenstein, and Alfredo De Rossi. Observation of parametric gain due to four-wave mixing in dispersion engineered gainp photonic crystal waveguides. *Optics letters*, 36(14):2629–2631, 2011.

[197] Samuel Serna, Weiwei Zhang, Pierre Colman, Xavier Le Roux, Rene Coudevylle, Laurent Vivien, and Eric Cassan. Experimental investigation of top cladding on properties of silicon slotted photonic crystal waveguides. *IEEE Journal of Selected Topics in Quantum Electronics*, 22(6), nov 2016.

[198] A Casas Bedoya, S Mahmoodian, C Monat, S Tomljenovic-Hanic, C Grillet, P Domachuk, EC Mägi, BJ Eggleton, and RW Van der Heijden. Liquid crystal dynamics in a photonic crystal cavity created by selective microfluidic infiltration. *Optics express*, 18(26):27280–27290, 2010.

[199] A. Casas Bedoya, P. Domachuk, C. Grillet, C. Monat, E.C. Mägi, E. Li, and B. J. Eggleton. Reconfigurable photonic crystal waveguides created by selective liquid infiltration. *Opt. Express*, 20(10):11046–11056, May 2012.

[200] Xiaolong Wang, Che-Yun Lin, Swapnajit Chakravarty, Jingdong Luo, Alex K-Y Jen, and Ray T Chen. Effective in-device r 33 of 735 pm/v on electro-optic polymer infiltrated silicon photonic crystal slot waveguides. *Optics letters*, 36(6):882–884, 2011.

[201] Weiwei Zhang, Samuel Serna, Nicolas Dubreuil, and Eric Cassan. Nonlinear optimization of slot si waveguides: Tpa minimization with fom tpa up to 4.25. *Optics letters*, 40(7):1212–1215, 2015.

[202] Tsuyoshi Michinobu, Joshua C May, Jin H Lim, Corinne Boudon, Jean-Paul Gisselbrecht, Paul Seiler, Maurice Gross, Ivan Biaggio, and François Diederich. A new class of organic donor–acceptor molecules with large third-order optical nonlinearities. *Chemical communications*, (6):737–739, 2005.

[203] Bweh Esembeson, Michelle L Scimeca, Tsuyoshi Michinobu, François Diederich, and Ivan Biaggio. A high-optical quality supramolecular assembly for third-order integrated nonlinear optics. *Advanced Materials*, 20(23):4584–4587, 2008.

[204] C Koos, L Jacome, C Poulton, J Leuthold, and W Freude. Nonlinear silicon-on-insulator waveguides for all-optical signal processing. *Optics Express*, 15(10):5976–5990, 2007.

[205] Paul Muellner, Markus Wellenzohn, and Rainer Hainberger. Nonlinearity of optimized silicon photonic slot waveguides. *Optics express*, 17(11):9282–9287, 2009.

[206] N. A. R. Bhat and J. E. Sipe. Optical pulse propagation in nonlinear photonic crystals. *Phys. Rev. E*, 64:056604, Oct 2001.

[207] A Di Falco, L O'Faolain, and TF Krauss. Photonic crystal slotted slab waveguides. *Photonics and Nanostructures-Fundamentals and Applications*, 6(1):38–41, 2008.

[208] Charles Caer, Xavier Le Roux, Samuel Serna, Weiwei Zhang, Laurent Vivien, and Eric Cassan. Large group-index bandwidth product empty core slow light photonic crystal waveguides for hybrid silicon photonics. *Frontiers of Optoelectronics*, 7(3):376–384, 2014.

[209] Junfei Xia, Samuel Serna, Weiwei Zhang, Laurent Vivien, and Eric Cassan. Hybrid silicon slotted photonic crystal waveguides: how does third order nonlinear performance scale with slow light? *Photon. Res.*, 4(6), 2016.

[210] Nicolae C Panoiu, James F McMillan, and Chee Wei Wong. Theoretical analysis of pulse dynamics in silicon photonic crystal wire waveguides. *IEEE Journal of Selected Topics in Quantum Electronics*, 16(1):257–266, 2010.

[211] Spyros Lavdas and Nicolae C Panoiu. Theory of pulsed four-wave mixing in one-dimensional silicon photonic crystal slab waveguides. *Physical Review B*, 93(11):115435, 2016.

[212] M. Santagiustina, C. G. Someda, G. Vadalà, S. Combrié, and A. De Rossi. Theory of slow light enhanced four-wave mixing in photonic crystal waveguides. *Opt. Express*, 18(20):21024–21029, Sep 2010.

[213] C Monat, P Domachuk, and BJ Eggleton. Integrated optofluidics: A new river of light. *Nature photonics*, 1(2):106–114, 2007.

[214] M Ebnali-Heidari, C Monat, C Grillet, and MK Moravvej-Farshi. A proposal for enhancing four-wave mixing in slow light engineered photonic crystal waveguides and its application to optical regeneration. *Optics express*, 17(20):18340–18353, 2009.

[215] Pedro Damas, Xavier Le Roux, David Le Bourdais, Eric Cassan, Delphine Marris-Morini, Nicolas Izard, Thomas Maroutian, Philippe Lecoeur, and Laurent Vivien. Wavelength dependence of pockels effect in strained silicon waveguides. *Optics express*, 22(18):22095–22100, 2014.

[216] Stefano Grillanda and Francesco Morichetti. Light-induced metal-like surface of silicon photonic waveguides. *Nature communications*, 6, 2015.

[217] Jiangwei Wang, Mansour Sheik-Bahae, AA Said, David J Hagan, and Eric W Van Stryland. Time-resolved z-scan measurements of optical nonlinearities. *JOSA B*, 11(6):1009–1017, 1994.

[218] Jean-Claude Diels and Wolfgang Rudolph. *Ultrashort laser pulse phenomena*. Academic press, 2006.

[219] C Xiong, Christelle Monat, Alex S Clark, Christian Grillet, Graham D Marshall, MJ Steel, Juntao Li, Liam O'Faolain, Thomas F Krauss, John G Rarity, et al. Slow-light enhanced correlated photon pair generation in a silicon photonic crystal waveguide. *Optics letters*, 36(17):3413–3415, 2011.

[220] Nobuyuki Matsuda and Hiroki Takesue. Generation and manipulation of entangled photons on silicon chips. *Nanophotonics*, 2016.

ÉCOLE DOCTORALE
Physique et ingénierie : électrons, photons, sciences du vivant (EOBE)

Titre: Conception et caractérisation de structures photoniques sur silicium pour les effets nonlinéaires du troisième ordre

Mots clés : Optique intégrée; optique non linéaire; silicium; techniques de caractérisation; plates-formes d'intégration hybrides; mise en forme d'impulsions.

Résumé:

Le traitement tout-optique des signaux sur puce est une option de rupture technologique s'inscrivant dans la continuité des récentes percées de la photonique sur silicium et de sa co-intégration progressive avec l'électronique CMOS. Dans cette perspective, l'optique est principalement introduite dans l'objectif de lever des verrous technologiques de débit/bande passante sur puce et de puissance consommée. Compte tenu de la miniaturisation poussée des guides silicium, dont les sections sont typiquement de l'ordre de $0.1\mu\text{m}^2$, une réduction considérable de la puissance optique nécessaire pour atteindre les effets non linéaires est obtenue en comparaison des fibres optiques. Bien que le silicium non-contraint ne présente pas de réponse non-linéaire du second ordre ($\chi^{(2)}$) en raison de la centrosymétrie de son réseau, les effets de troisième ordre ($\chi^{(3)}$) y sont particulièrement forts mais néanmoins minorés en raison de l'impact de l'effet d'absorption à deux photons (TPA) dans la fenêtre des longueurs d'onde télécoms ($\lambda \sim 1.55\mu\text{m}$), qui génère à son tour des porteurs libres induisant de l'absorption supplémentaire et des variations d'indice de réfraction.

Cette thèse est une contribution à l'exploration théorique et expérimentale d'une voie visant à s'affranchir de ces difficultés et reposant sur l'intégration hybride des matériaux actifs à faible indice de réfraction sur silicium. Dans cette approche, la plateforme photonique silicium est utilisée pour ses propriétés extraordinaires de guidage de la lumière tandis que les matériaux rapportés, luminescents ou présentant des propriétés optiques non linéaires absentes dans le silicium, voient leurs propriétés décuplées par l'exaltation du champ électromagnétique venant des structures photoniques silicium.

Plus précisément, le présent travail a été consacré à l'étude des nonlinéarités de troisième ordre dans des structures intégrées à base de silicium exploitant des configurations de cavités à miroir de Bragg (nanobeam) et guides à cristaux photoniques à modes lents. Tout d'abord, nous avons développé une méthode non destructive à

faisceau unique pour caractériser les effets de troisième ordre instantanés, c'est à dire la quantification de la susceptibilité complexe effective dans les guides d'ondes. La méthode a été dénommée "Top-hat D-Scan bi-directionnelle" et constitue un analogue temporel de la méthode Top-hat Z-Scan développée précédemment. Nous avons établi un modèle analytique et numérique et nous rendons compte de la première mesure d'un guide d'ondes en silicium utilisant une impulsion mis en forme dans un étireur et complétée par une procédure d'injection bi-directionnelle. L'ensemble instrumental développé constitue une expérience de métrologie des effets non-linéaires dans des guides d'ondes silicium au meilleur niveau de l'état de l'art.

Forts de cet outil métrologique, nos travaux d'exploration des interactions non linéaires lumière-matière ont été consacrés à deux grandes familles de nanostructures photoniques : des microcavités optiques et guides d'ondes en régime de lumière lente. Dans la première des deux situations, les variations d'indice provoquées par les nonlinéarités sont responsables d'un décalage des fréquences de résonance excluant sa coïncidence avec la fréquence du signal d'excitation et diminuant ainsi l'efficacité de l'injection optique de manière drastique. Afin de maintenir le bénéfice de localisation de la lumière tout au long de l'excitation pulsée, nous avons expérimentalement et numériquement étudié le comportement d'une cavité en silicium conçue, fabriquée, et enfin excitée par une impulsion présentant une puissance crête élevée. En contrôlant temporellement la phase des composantes spectrales injectée, la relation de phase spectrale compensant la dérive de fréquence non linéaire de la résonance de la cavité, nous avons effectué une étude exhaustive sur l'excitation cohérente des micro-cavités silicium non linéaire.

Enfin, nous avons consacré des efforts importants pour concevoir, fabriquer et caractériser des guides d'ondes à cristaux photoniques (SPhCW) en silicium à fente, matrice d'une intégration hybride de matériaux optiques non-linéaires sur silicium. Les résultats rapportés fournissent la première preuve expérimentale d'un contrôle précis des propriétés de dispersion de guides à cristaux photoniques à fente propres à être remplis par des matériaux souples comme des polymères ou des couches minces dopées. La dispersion de groupe des modes lents guidés est contrôlable en signe et en amplitude et correspond à des bandes passantes optiques exploitables ($\sim$10nm). Ces résultats démontrent l'intérêt direct pour le traitement des données tout-optique sur puce des guides à modes lents à cœur creux utilisant des effets optiques non linéaires d'ordre trois pour le traitement tout-optique des données sur puce.

universite PARIS-SACLAY
ÉCOLE DOCTORALE
Physique et ingénierie : électrons, photons, sciences du vivant (EOBE)

Title: Design and characterization of Silicon Photonic structures for third order nonlinear effects

Keywords: Integrated optics; nonlinear optics; silicon; characterization techniques; hybrid integration platforms; pulse shaping.

Abstract:

All-optical signal processing implemented in silicon photonics is considered as a promising route to solve several bottlenecks for the realization of future dense and mixed integrated electronic and photonic chips including ultrahigh data bit rate issues and power consumption constraints. The control of optical signals by using light intrinsically brings the advantage of removing electrooptical conversions and opens the path to a large number of functions inherited from the telecommunication field by using nonlinear optical processes, which yet traditionally need high optical powers and long interaction lengths in optical fibers. In the context of the planar silicon photonics technology, a dramatic reduction of the needed power to reach optical nonlinear effects is obtained due to the sub-micrometer size of silicon wires ($\sim$450 nm$\times$260 nm) in the telecommunication wavelength window, although silicon does not exhibit second-order response ($\chi^{(2)}$) due to the centrosymmetry of its lattice. Moreover, third-order effects ($\chi^{(3)}$) are partially spoiled in this material due to the strength of the two-photon-absorption (TPA) effect, which in turn generates free-carriers inducing additional absorption and refractive index changes.

One way to overcome this limitation is the hybrid integration on silicon of low index soft materials with luminescence or nonlinear optical properties lacking to silicon. In this context, the present work is devoted to the study of third order nonlinearities in silicon-based integrated structures exploiting enhanced electromagnetic field effects (e.g. in Si resonators and slow light waveguides). First, we have developed a dedicated single beam non-destructive method to characterize the instantaneous third order effects though the quantification of complex effective waveguide susceptibility. The method is named “Bi-directional top-hat D-Scan” and consists in a temporal analogous of the top-hat Z-Scan. We have established an analytical and numerical model and we report the first measurement of a silicon waveguide by using a pulse shaping set-up and a bi-directional procedure. The originality of our method stands in the capability to measure in two steps: the 3rd order nonlinear Figure-Of-Merit

(FOM_{TPA}) independently of the injection losses, and the effective nonlinear waveguide parameters (Kerr and TPA) taking into account measured coupling losses at each facet . Furthermore, we have used the method to characterize other integrated novel materials including Ge-rich GeSi alloys, and chalcogenide waveguides.

Additionally, two further enhancements of light-matter nonlinear interactions have been explored within this work: optical microcavities and slow light waveguides. In the first picture, index variations caused by non-linearities shift the resonance frequencies precluding the coincidence with the excitation signal frequency, thereby decreasing the injection efficiency. In order to maintain the benefit of light localization throughout the pulsed excitation, we have experimentally and numerically studied the behavior of a designed and fabricated silicon nanobeam cavity excited by a high power tailored chirped pulse whose spectral phase relation compensates for the nonlinear frequency drift of the cavity resonance. We report a numerical and experimental study of the coherent excitation of a nonlinear micro-cavity, leading to enhanced intra-cavity nonlinear interactions.

Finally, we have dedicated efforts to engineer, fabricate and characterize silicon slot photonic crystal waveguides (SPhCW) in order to compensate their strong dispersion present in the slow light regime while taking benefit from large group index light propagation. Dispersion controls the dynamics of nonlinear effects so we aimed at a way to tailor it. We experimentally demonstrated that low-index materials can be incorporated in 700 μm long slot photonic crystal waveguides, and hence can benefit from both slow-light field enhancement effect and slot-induced ultra-small effective areas ($<0.1\mu\text{m}^2$). We showed that their frequency dispersion properties can be engineered from anomalous to normal dispersion, along with zero group velocity dispersion (ZGVD) crossing points exhibiting a Normalized Delay Bandwidth Product (NDBP) as high as 0.156. The reported results provide the first experimental evidence for an accurate control of the dispersion properties of fillable periodical slotted structures in silicon photonics, which is of direct interest for on-chip all-optical data treatment using nonlinear optical effects in hybrid-on-silicon technologies.

universite
PARIS-SACLAY

ÉCOLE DOCTORALE
Physique et ingénierie :
électrons, photons,
sciences du vivant (EOBE)

Título: Diseño y caracterización de estructuras a base de silicio para efectos no-lineales de tercer orden

Palabras clave: óptica integrada; óptica no lineal; silicio; técnicas de caracterización; plataformas híbridas de integración; armonización de impulsos.

Resumen: Debido al incremento en la rata de intercambio de datos, se hace necesaria una solución que facilite la comunicación rápida sin altos requerimientos energéticos. El procesamiento de señales con el uso exclusivo de luz e implementados en la plataforma de silicio es considerado como una ruta llamativa para resolver dicho problemas en escalas sub-milimétricas con miras a la realización de futuros chips integrados que sólo usen fotónica. El control de las señales ópticas mediante el uso de la luz lleva intrínseca la ventaja de eliminar las conversiones electro-ópticas y abre el camino a un gran número de funciones en el campo de las telecomunicaciones. En particular, el uso de procesos ópticos no lineales, usualmente requiere altas potencias ópticas y extensas longitudes de interacción en fibras ópticas. En el contexto de la tecnología plana de silicio (*on-chip*), una reducción drástica de la potencia necesaria para alcanzar los efectos no lineales ópticos se obtiene debido al tamaño sub-micrométrico de las guías de onda fabricadas en silicio (~450 nm×260 nm) en la ventana de longitudes de onda de las telecomunicaciones ($\lambda \sim 1550$ nm). El silicio no presenta respuestas no lineales de segundo orden ($\chi^{(2)} = 0$) debido a la centrosimetría de su malla cristalina, así que los efectos nolineales de tercer orden ($\chi^{(3)}$) son los que requieren menores energías para ser explotados. Estos últimos son parcialmente degradados debido a la alta probabilidad de absorción a dos fotones (*Two-photon absorption*: TPA), que a su vez genera portadores libres que inducen absorción y cambios en el índice de refracción adicionales.

Una forma de superar esta limitación es la integración híbrida del silicio con materiales de bajo índice de refracción que presenten propiedades ópticas nolineales y de luminiscencia, interesantes para funciones integradas alrededor de $\lambda \sim 1550$ nm. En este contexto, el presente trabajo está dedicado al estudio de la no linealidad de tercer orden en estructuras integradas basadas en silicio que explotan efectos de confinamiento adicional del campo electromagnético (por ejemplo, cavidades ópticas y guías de onda operadas en el régimen de luz lenta). En primer lugar, se ha desarrollado un método no destructivo que requiere un único haz. Este método ha sido usado

para caracterizar los efectos instantáneos (<1ps) de tercer orden, a saber: Kerr y TPA. La medida consiste en la cuantificación de la susceptibilidad compleja efectiva de una guía de onda. El método se denomina "Barrido en Dispersión con pulsos de sombrero de copa" (*Top-hat D-Scan* por su nombre en inglés) y consiste en un análogo temporal del conocido método de barrido en posición Z-Scan. Hemos establecido un modelo semi-analítico y hemos reportado la primera medición de una guía de onda de silicio usando impulsos armonizados (*chirped pulses*) y un procedimiento de inyección bidireccional. La originalidad del mencionado método se encuentra en la capacidad de medir en dos pasos diversos parámetros como: la figura de mérito de nolinealidades de tercer orden (FOM_{TPA}), independientemente de las pérdidas de inyección, los parámetros nolineales efectivos de la guía de onda (Kerr y TPA) y la medida precisa de las pérdidas de acoplamiento en cada faceta. Por otra parte, hemos aplicado el método a guías de onda en otros materiales integrados incluyendo aleaciones SiGe ricas en Germanio, calcogenuros y nitruro de silicio.

Además, otras opciones para mejorar la interacción no-lineal entre la luz y la materia han sido exploradas en el marco de esta disertación, a saber: el uso de microcavidades ópticas y de guías de onda en el régimen de luz lenta. En el primer caso, las variaciones del índice causados por pulsos de altas energías cambian las frecuencias de resonancia de la cavidad excluyendo la coincidencia con la frecuencia de la señal de excitación, lo que disminuye, entre otras, la eficiencia en el acoplamiento. A fin de mantener el beneficio de la localización de la luz a lo largo de la excitación pulsada, se ha estudiado experimental y numéricamente el comportamiento de una cavidad *nanobeam* en silicio excitada por un pulso adaptado de alta intensidad óptica cuya relación de fase espectral compensa la deriva de frecuencia no lineal de la resonancia de la cavidad. Este procedimiento demuestra un mejoramiento en la interacción luz-materia intra-cavidad.

Finalmente, se han dedicado esfuerzos para diseñar, fabricar y caracterizar guías de ondas de cristal fotónico a ranura (SPhCW por *Slot Photonic Crystal Waveguides*) en silicio con el fin de compensar la fuerte dispersión presente en el régimen de luz lenta mientras se aprovecha la propagación de la luz a un índice de grupo elevado. La dispersión controla la dinámica de los efectos no lineales, por lo que es crucial estudiar una forma de gestionarla. Hemos probado que las propiedades de dispersión en *SPhCW* de 700 μm de largo pueden ser controladas precisamente, siendo esta la primera demostración experimental manejando este tipo de guías. Los resultados presentados proporcionan una opción para el diseño de guías híbridas, pudiéndose llenar las ranuras con diversos materiales.